VNIVERSITAT DE VALÈNCIA

Facultat de Física

DEPARTAMENT D'ÒPTICA I OPTOMETRIA I CIÈNCIES DE LA VISIÓ

Spatially multiplexed interferometric microscopy: from basic principles to advanced arrangements

por

José Ángel Picazo Bueno

Tesis presentada para optar al grado de
Doctorado en Física

Bajo la supervisión de
Dr. Vicente Micó Serrano

Valencia, septiembre 2019

VNIVERSITAT DE VALÈNCIA **Departament d'Òptica**

Dr. Vicente Micó Serrano, Profesor Contratado Doctor del Departament d' Òptica i Optometria i Ciències de la Visió de la Facultat de Física de la Universitat de València,

CERTIFICA

que la presente memoria, titulada "**Spatially multiplexed interferometric microscopy: from basic principles to advanced arrangements**", corresponde al trabajo realizado bajo su dirección por el alumno **José Ángel Picazo Bueno**, para su presentación como Tesis Doctoral en el Programa de Doctorado en Física de la Universitat de València.

Y para que así conste, firma el presente certificado.

Valencia, 26 de septiembre de 2019

Fdo:

Dr. Vicente Micó Serrano

Agradecimientos

En estas líneas, me gustaría expresar mi enorme gratitud por todo el apoyo brindado a toda esa gente que me ha ayudado de manera directa o indirecta a lo largo del periodo de realización del trabajo presentado en esta memoria.

En primer lugar, agradecer al Profesor Vicente Micó, director de esta tesis doctoral, ya que sin su ayuda no habría sido posible llegar a realizar este trabajo. Muchas gracias por guiarme a lo largo de todos estos años, por enseñarme todo lo necesario sobre el tema presentado aquí y muchos otros, y por todos los buenos resultados obtenidos y momentos vividos durante este periodo.

En segundo lugar, me gustaría agradecer a todos y cada uno de los compañeros del GPOEI, (Ricardo, Martín, Luis, Vicente, Javier y Carlos), por ayudarme en todo momento, por su paciencia y, sobre todo, por hacer del GPOEI un grupo inigualable a todos los niveles.

Asimismo, me gustaría dar las gracias al responsable de la estancia de investigación, Dan Cojoc, realizada en SISSA (Trieste) durante la tesis, cuya experiencia me ha servido mucho tanto profesional como personalmente. Como no, agradecer también a Maciej Trusiak su colaboración en varias de las contribuciones aquí presentadas.

Por último, me gustaría agradecer de todo corazón a las personas que, aunque no han contribuido directamente en este trabajo, sí lo han hecho y de qué manera indirectamente: a mis padres (Basilio y Paqui) y a mi hermano (Juan Francisco), por darme su apoyo incondicional a lo largo de todos estos años y por creer siempre en mí, a mis abuelos (Juan, Francisco, Josefa y Ángeles) y mis tíos, por haberme enseñado tanto desde niño, a mi chica Andrea por haberme acompañado desde el inicio de la tesis y haber compartido tantos momentos buenos. También ha sido un placer haber estado acompañado todos estos años de unos muy buenos amigos tanto de Tarazona de la Mancha (Albacete) como de la facultad de Física.

A todos ellos, muchas gracias por todo.

List of publications

This thesis is based on following list of peer-reviewed research articles.

[Picazo-Bueno-2016] J. A. Picazo-Bueno, Z. Zalevsky, J. García, C. Ferreira, and V. Micó, "Spatially multiplexed interferometric microscopy with partially coherent illumination," J. Biomed. Opt. **21**(10), 106007 (2016).

[Picazo-Bueno-2017] J. A. Picazo-Bueno, Z. Zalevsky, J. García, and V. Micó, "Superresolved spatially multiplexed interferometric microscopy," Opt. Lett. **42**(5), 927-930 (2017).

[Picazo-Bueno-2018A] J. A. Picazo-Bueno, D. Cojoc, F. Iseppon, V. Torre, and V. Micó, "Single-shot, dual-mode, water-immersion microscopy platform for biological applications," Appl. Opt. **57**(1), A242-A249 (2018).

[Picazo-Bueno-2018B] J. A. Picazo-Bueno, M. Trusiak, J. García, K. Patorski, and V. Micó, "Hilbert–Huang single-shot spatially multiplexed interferometric microscopy," Opt. Lett. **43**(5), 1007-1010 (2018).

[Picazo-Bueno-2019A] J. A. Picazo-Bueno and V. Micó, "Opposed-view spatially multiplexed interferometric microscopy," J. Opt. **21**(3), 035701 (2019).

[Picazo-Bueno-2019B] J. A. Picazo-Bueno, M. Trusiak, and V. Micó, "Single-shot slightly off-axis digital holographic microscopy with add-on module based on beamsplitter cube," Opt. Express **27**(4), 5655-5669 (2019).

[Trusiak-2019] M. Trusiak, J. A. Picazo-Bueno, Krzysztof Patorski, Piotr Zdankowski, and V. Micó, "Single-shot two-frame π-shifted spatially multiplexed interference phase microscopy," J. Biomed. Opt. **24**(9), 096004 (2019).

Other peer-reviewed research articles not included in this thesis but closely related to it, and published during this period.

[Sanz-2015] M. Sanz, J. A. Picazo-Bueno, J. García, and V. Micó, "Improved quantitative phase imaging in lensless microscopy by single-shot multi-wavelength illumination using a fast convergence algorithm," Opt. Express 23(16), 21352 (2015).

[Perucho-2016] B. Perucho, J. A. Picazo-Bueno, and V. Micó, "A Novel Marking Reader for Progressive Addition Lenses Based on Gabor Holography," Optom. Vis. Science 93(5), 534-542 (2016).

[Sanz-2017] M. Sanz, J. A. Picazo-Bueno, L. Granero, J. García, and V. Micó, "Compact, cost-effective and field-portable microscope prototype based on MISHELF microscopy," Sci. Rep. 7, 43291 (2017).

[Sanz-2018A] M. Sanz, J. A. Picazo-Bueno, L. Granero, J. García, and V. Micó, "Multi-illumination single-holographic-exposure lensless Fresnel (MISHELF) microscopy using 4 channels," Opt. Las. Eng. 110, 341-347 (2018).

[Sanz-2018B] M. Sanz, J. A. Picazo-Bueno, J. García, and V. Micó, "Dual-mode holographic microscopy imaging platform," Lab Chip 18(7), 1105-1112 (2018).

[Soler-2018] C. Soler, J. A. Picazo-Bueno, V. Micó, A. Valverde, D. Bompart, F. J. Blasco, J. G. Álvarez, and A. García-Molina, "Effect of counting chamber depth on the accuracy of lensless microscopy for the assessment of boar sperm motility," Reproduction Fertil. Dev. 30(6), 924-934 (2018).

List of acronyms

The following list includes the abbreviations used along the different chapters of the presented report.

1D	One Dimensional
2D	Two Dimensional
3D	Three Dimensional
4D	Four Dimensional
AFM	Atomic Force Microscope
BS	Beam Splitter
CCD	Charged Coupled Device
CGH	Computer Generated Holography
CMOS	Complementary Metal-Oxide Semiconductor
CPI	Common-Path Interferometer
DVD	Digital Versatile Disc
DH	Digital Holography
DHM	Digital Holographic Microscopy
DHT	Digital Holographic Tomography
DIC	Differential Interference Contrast
DOF	Depth Of Field
DPM	Diffraction Phase Microscopy
EFEMD	Enhanced Fast Empirical Mode Decomposition
EMD	Empirical Mode Decomposition
FFT	Fast Fourier Transform
FOV	Field Of View
FPM	Fourier Phase Microscopy
FT	Fourier Transform

FT^{-1}	inverse Fourier Transform
FWMH	Full Width at Maximum Height
H2PM	Hilbert-Huang Phase Microscopy
H2S2MIM	Hilbert-Huang Single-Shot Spatially Multiplexed Interferometric Microscopy
HHT	Hilbert-Huang Transform
HPM	Hilbert Phase Microscopy
HST	Hilbert Spiral Transform
HT	Hilbert Transform
IMF	Intrinsic Mode Function
LD	Laser Diode
LED	Light-Emitting Diode
MIL	Michelson Interferometer Layout
NA	Numerical Aperture
OV	Opposed-View
OV-DHM	Opposed-View Digital Holographic Microscopy
OV-SMIM	Opposed-View Spatially-Multiplexed Interferometric Microscopy
P-S	Phase-shifting
PSF	Point-Spread Function
PZT	PieZoelectric Transducer
QLSI	Quadriwave Lateral Shearing Interferometry
QP-DHM	Quantitative Phase Digital Holographic Microscopy
QPI	Quantitative Phase Imaging
RBC	Red Blood Cells
R-G	Reference-Generation
RI	Refractive Index
ROI	Region Of Interest
S2H2PM	Single-Shot Hilbert-Huang Phase Microscopy
S2MIM	Superresolved Spatially Multiplexed Interferometric Microscopy
SA	Synthetic Aperture
SA SR	Synthetic Aperture SuperResolution
S-I	Self-Interference

SL	Stokes Lens
SLD	SuperLuminescent Diode
S-M	Spatially-Multiplexed
SMIM	Spatially Multiplexed Interferometric Microscopy
SNR	Signal-to-Noise Ratio
SO	Slightly Off-axis
SO-DHM	Slightly Off-axis Digital Holographic Microscopy
SR	SuperResolution
SS	Swine Sperm
STD	STandard Deviation
TIE	Transport of Intensity Equation
TL	Tube Lens
USAF	United States Air Force
VCSEL	Vertical-Cavity Surface-Emitting Laser
VID	Variational Image Decomposition
ZPC	Zernike Phase Contrast
π-SMIM	Single-shot two-frame π-shifted Spatially Multiplexed Interference phase Microscopy

Preface

This thesis is mainly divided into three parts:

Part I consists of four chapters including the scientific description of all the presented work. An introductory Chapter 1, in which a brief overview about quantitative phase imaging by digital holographic microscopy is done, and the objectives and structure of the thesis are specified. In Chapter 2, we present a survey on digital holographic microscopy, including an historical introduction, several interferometric layouts, reconstructions procedures, and imaging modalities. Chapter 3 includes a comprehensive description of the proposed technique as well as an overview of the experimental validations performed in this thesis. To conclude, Chapter 4 summarizes the main results and conclusions reached from the scientific research, and the outlooks derived from it. In addition, useful references are included afterwards.

In Part II, we present a copy of the research articles included in this study, as published in the different journals during the development of this thesis.

Por último, la parte III consiste en un resumen detallado en castellano de los objetivos, motivación, metodología, resultados y conclusiones de esta tesis.

Contents

Chapter 1

Introduction, objectives and structure of the thesis

1.1. Introduction

The possibility of visualizing and analysing transparent microscopic objects in a non-invasively manner was one of the addressed challenges during 20th century. Several microscopy techniques were developed to convert small phase differences into intensity ones, thus making such objects visible to the naked eye. Among all techniques created for that purpose, we must highlight both *Zernike phase contrast* (*ZPC*) *microscopy* and *differential interference contrast* (*DIC*) *microscopy*, developed by Zernike [Zernike-1942A, Zernike-1942B] and Nomarski [Nomarski-1952, Nomarski-1960], respectively. Nevertheless, such microscopy techniques only provided qualitative information about the object, since the nonlinearity between phase and intensity changes, so that the analysis with those techniques were just limited to simple visualization. In that way, the quantitative analysis of the phase differences induced by samples was not feasible.

Nonetheless, more recently in 21st century, several attempts to provide *quantitative phase imaging* (*QPI*) were reported employing different non-invasively microscopy techniques [Popescu-2004, Popescu-2006, Lue-2007, King-2008, Fu-2010, Gao-2011A], such as quantitative *ZPC* [Gao-2011A] and *DIC* [King-2008, Fu-2010], *Fourier phase microscopy* (*FPM*) [Popescu-2004, Lue-2007], or *diffraction phase microscopy* (*DPM*) [Popescu-2006], among others. However, such techniques required delicate and expensive optical elements and their precise alignment, and *QPI* was not always a trivial issue.

By contrast, there exist other microscopy techniques based on *interferometry* that provides *QPI* in an easier and direct way. Perhaps the quintessential interferometric technique for such a purpose is *digital holographic microscopy* (*DHM*) [Cuche-1999A, Cuche-1999B, Cuche-2000, Mann-2005, Charrière-2006A, Ferraro-2006, Chalut-2007]. Briefly, *DHM* arises from the application of *digital holography* (DH) to *microscopy*, and it is therefore an imaging technique that enables *QPI* of phase samples using a non-invasive (no need for labelling), full-field (non-scanning), real-time (single-frame acquisition), non-contact (no sample damage), and static (no moving components) operation principle [Kim-2011, Picart-2015]. The application of *DHM* to *QPI* is commonly denoted as *quantitative phase digital holographic microscopy* (*QP-DHM*). Figure 1.1 shows an image provided by *QP-DHM* during this thesis.

QP-DHM enables quantitative analysis of structure and dynamics of micrometric specimens, since it provides the phase-delay distribution of the optical field transmitted through or reflected by an object as a set of numerical values [Kemper-2006A, Langeha-2009]. From such retardations, it is possible to calculate extremely useful information of inspected micrometric specimens such as physical thickness and refractive index (RI) with high accuracy[1] [Rappaz-2005, Lin-2010, Wang-2012, Memmolo-2014]. In the particular case of dealing with cellular processes, those parameters are in turn related to physical density or chemical concentration properties [Kim-2011]. For those reasons, *QP-DHM* has becoming a powerful and versatile technique applied to many fields of knowledge, such as Biophotonics, Life Sciences and Medicine.

Hence, *QP-DHM* has relevant applications in cell biology: for instance, *QP-DHM* was successfully employed to three-dimensional (3D) analysis and monitoring of cell migration [Dubois-2006B, Mann-2006, Daneshpanah-2007, Sun-2008, Choi-2009, Langeha-2009, Javidi-2010, Memmolo-2012, Merola-2012], 3D tracking of micro and nanoparticles[2] [Xu-2003, Antkowiak-2008, Warnasoo-2010], automated cell counting, recognition and classification [Moon-2007, Mölder-2008, Seo-2010, Anand-2011, Liu-2011, Memmolo-2011, Mihailescu-2011, Moon-2012, Yi-2013], RI characterization [Rappaz-2005, Lin-2010, Wang-2012], and manipulating and testing biomechanical properties of cells [DaneshPanah-2010, Cardenas-2011, Esseling-2012, Kemper-2013]. Thus, *QP-DHM* can be very appealing in extremely important fields as cancer research [Mann-2005, Janeckova-2009, Wang-2010] or assisted reproduction [Crha-2011, Memmolo-2011, Merola-2013].

[1] Axial nanometer or sub-nanometer accuracy [Kemper-2008A, Kühn-2008].
[2] The use of nanoparticles is highly promising in medical fields such as tumor detection and treatment, drug carrier, and gene therapy.

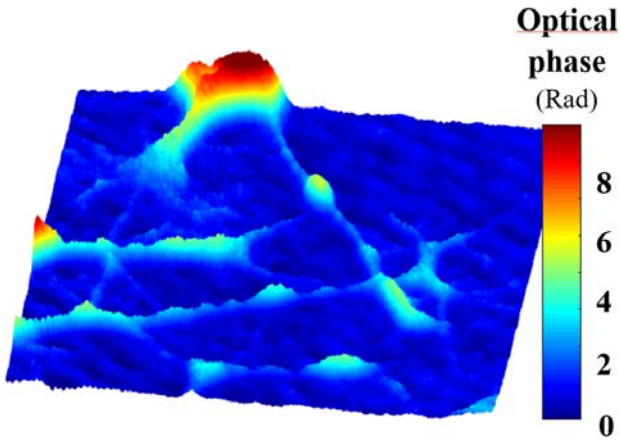

Figure 1.1. Perspective view of a quantitative phase image obtained in this thesis by *DHM* for the case of hippocampal neuron cells.

In recent years, many novel *QP-DHM* approaches have been successfully developed in order to improve their capabilities in terms of robustness, simplicity, usability, accuracy, and price [Bon-2009, Tearney-2010, Fu-2010, Merola-2011, Kemper-2011, Chhaniwal-2012, Singh-2012, Shaked-2012, Girshovitz-2013, Guo-2013, Bhaduri-2014, Karepov-2015, Roitshtain-2016, Yang-2016]. Indeed, one of the goals to achieve nowadays consists in equipping regular microscopes with coherence sensing capabilities [Kemper-2008, Bon-2009, Cui-2010]. For that purpose, several techniques were reported, such as *DPM* [Popescu-2006], *quadriwave lateral shearing interferometry* (*QLSI*) [Bon-2009], and *Michelson interferometer layout* (*MIL*) [Kemper-2011]. In short, *DPM* is based on the generation of a common-path architecture in which the reference beam is synthesized from the imaging beam by spatial filtering, and then both beams coherently interfere at the recording plane. On the other hand, *MIL* approach is also assembled following a common-path architecture, but it is more related to the idea of self-interference between two duplicated and shifted imaging beams achieved by using a Michelson layout, so that it requires sparse samples. By contrast, *QLSI* is based on a completely different concept from *holography*. In that technique, a wavefront is digitally sensed with the help of a modified Hartmann mask.

In line with those techniques, Micó *et al.* created a new technique to equip standard broadband illumination microscopes with QPI capabilities [Micó-2014]. The technique, called *spatially multiplexed interferometric microscopy* (*SMIM*), appears as a stable, non-complex and cost-effective way to convert a commercially available regular microscope into a holographic one. *SMIM* introduces minimal modifications in the microscope embodiment to implement a common-path interferometric architecture in which the reference beam is achieved by leaving a clear region in the input plane, i.e., by spatially multiplexing the object plane. Thus, *SMIM* benefits from such architectures regarding robustness, simplicity and easiness of integration in a

microscope. In addition, *SMIM* presents some advantages when compared to both *DPM* and *MIL* techniques: on one hand, *SMIM* does not require the inclusion of any pinhole mask for reference beam generation unlike *DPM* and, on the other hand, *SMIM* differs from *MIL* in the ability of dense samples inspection, with the unique constraint of leaving a clear region at the input plane for reference beam transmission.

The concept of *SMIM* was first validated at the laboratory for superresolution (SR) purposes [Micó-2006B, Micó-2008, Micó-2009] and then implemented in a regular microscope [Micó-2014] to achieve *QPI*, giving rise to *SMIM* technique itself. Such experimental validations demonstrated that *SMIM* is a powerful technique to achieve *QPI* with regular microscopes in a non-invasive, real-time, full-field, non-contact and static manner.

1.2. Objectives and structure of the thesis

Following the research line started in [Micó-2014], the main goal of this work is related to the development and improvement of *SMIM* technique. *SMIM* introduces minimal modifications in the embodiment of a conventional bright field microscope in order to convert it into a holographic one in an extremely simple, low-cost and highly-stable way. In that way, the microscope can provide not only conventional intensity images but also *QPI* by means of holographic methods. Such an improvement will be achieved by designing and developing new experimental *SMIM* approaches capable of enhancing it in terms of phase images quality, single-shot capability and versatility.

More concretely, we shall be focused on providing noise-reduced, superresolved and transflective amplitude and phase images as well as real-time analysis without an *off-axis* holographic configuration requirement. We shall reach the proposed objectives by performing several experiments. Firstly, we shall implement a dual-mode microscope platform combining both broadband (white light) and *QP-DHM* imaging modes as a first method to approach the basic principles in *QP-DHM* [Picazo-Bueno-2018A], included in Section 3.1. Then, in Section 3.2, we shall get started with *SMIM* technique by qualitatively describing and mathematically analysing it. Thereafter, we shall explain in detail the *SMIM* advanced arrangements conducted and the most important results and conclusions obtained from it (Sections 3.3-3.8). We shall start *SMIM* improvements with the performance of an experiment in which we shall reduce the coherent noise in retrieved phase distributions by replacing the coherent light source with partially coherent illumination [Picazo-Bueno-2016] and presented in Section 3.3. In that experiment, we shall additionally design an optical scheme for enlarging the useful field of view (FOV). Afterwards, we shall increase the spatial resolution of recovered images by applying SR imaging

techniques [Picazo-Bueno-2017]. The experimental validation will be overviewed in Section 3.4. Subsequently, *SMIM* will be supplied with single-shot capability even though partially coherent illumination is used and *slightly off-axis* or *quasi on-axis* holographic configurations are defined [Picazo-Bueno-2018B]. That will be accomplished by using Hilbert-Huang transform (HHT) for phase retrieval (Section 3.5). Then, *SMIM* concept will be generalized by implementing not only reflective but also transflective imaging modes [Picazo-Bueno-2019A]. Transflective *QPI* will be achieved by wavelength multiplexing and RI of homogeneous samples will be reached (Section 3.6). After that, we shall implement a single-shot *slightly off-axis SMIM* approach, which will be carried out by inserting, at the output port of the microscope, an add-on module composed of a beam splitter (BS) cube and a Stokes lens (SL) for dynamic samples analysis [Picazo-Bueno-2019B]. The experimental validation will be summarized in Section 3.7. Finally, we shall present in Section 3.8 a *SMIM* architecture which will overcome astigmatism problems presented in [Picazo-Bueno-2019B] and will provide single-shot operating principle when defining a *quasi on-axis* holographic configuration [Trusiak-2019].

Additionally, an introductory chapter (Chapter 2) will expose all basic concepts presented in this work regarding *DHM* and its application to *QPI*. Issues as types of interferometers, reconstruction procedures and imaging modes employed in the experiments performed along the thesis will be introduced in Chapter 2. Finally, two ways of enhancing the quality of phase images provided by *DHM* will be introduced. Concretely, we shall discuss the improvements related to the coherent noise reduction caused by the use of partially coherent sources and the resolution enhancement achieved from the application of SR approaches. Note that Chapter 2 presents a structure which is consistent with the work presented in this thesis; so the different sections have been arranged according to the concepts involved in this memory.

To conclude, in Chapter 4, we shall collect the general conclusions of the reported dissertation, highlighting the advantages and drawbacks of each one of the proposed *SMIM* approaches. Furthermore, we shall briefly point future feasible works which may be derived from the objectives reached during this thesis.

Chapter 2

Survey on digital holographic microscopy

2.1. Historical introduction

2.1.1. Holography

Holography is a two-step imaging technique composed by, firstly, a recording stage of an interference pattern (hologram) and, secondly, a later reconstruction procedure of such a hologram founded on diffraction. During the recording stage, a light wave transmitted through, or reflected by, an object (object wave) interferes with another wave whose features[3] are well-known (reference wave), creating an interference pattern at a given plane (recording plane). Such a pattern is then recorded by an intensity-sensitive medium, generating a hologram. Later, during the reconstruction process, the hologram is again illuminated with the reference wave, producing several diffracted waves. One of them forms an image which reproduces the original object wave, not only in amplitude, but also in phase. Phase retrieval gives rise to a multitude of unique properties and applications of *holography*, in contrast to *photography*, which can only reproduce the intensity distribution of the optical field.

[3] Complex amplitude distribution (amplitude and phase). Typically, reference waves are spherical or plane waves.

Holography was invented by the Hungarian physicist Dennis Gabor[4] in 1948, while attempting to improve the resolution of the electron microscope, avoiding electron lens aberrations [Gabor-1948]. Instead of trying to correct such aberrations, he proposed *holography* as a two-step and lensless imaging process. That idea was inspired by Bragg's research in *X-ray crystallography* [Bragg-1939, Bragg-1942]. In Gabor's approach, the diffracted electron wave of the object was first recorded, and then, its image was reconstructed optically, i.e., employing visible light.

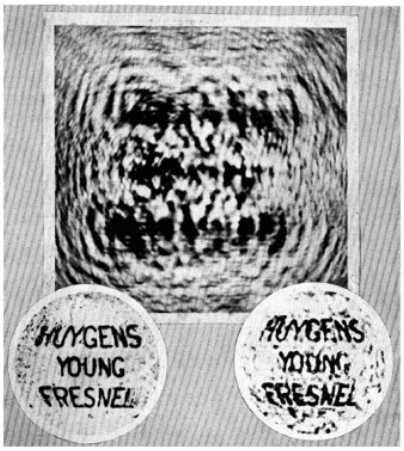

Figure 2.1. A hologram created by D. Gabor. Top: hologram; lower left: original object; lower right: reconstructed image. [Gabor-1949].

Gabor continued with his original proposal with two more papers [Gabor-1949, Gabor-1951], establishing the theoretical foundation, anticipating important features and considering its application to *microscopy* (Fig. 2.1 shows one of the first holograms created by Gabor [Gabor-1949]). However, the poor quality of holographic images made *holography* unsuccessful at the beginning, despite the efforts of several authors --- including Rogers [Rogers-1950], El-Sum [El-Sum-1952], and Lohmann [Lohmann-1965] --- for trying to understand and extend it. The reasons for the poor quality of the images obtained were, on one hand, the lack of light sources of sufficiently high coherence and intensity [Rogers-1950, El-Sum-1952] and, on the other hand, the overlapping of the reconstructed image with a background caused by the twin image and the direct beam

In the 1960s, two inventions were critical in the successful development of *holography*, one of them was technological whereas the other was rather conceptual. Technologically, the most significant improvement came from the invention of lasers. Lasers are powerful coherent light sources which provide high-quality interference contrast [Leith-1964], thus enhancing the resolution of holographic processes and allowing the creation of holograms for larger objects. Conceptually, Leith and

[4] Dennis Gabor was awarded with the Nobel prize in 1971 "for his invention and development of the holographic method"

Upatnieks introduced the off-axis reference wave technique to *holography* [Leith-1962, Leith-1963, Leith-1964]. In Gabor's (*on-axis* configuration) holographic configuration, both the object and reference electron waves arrive in parallel to the photographic plate. Such a configuration produces the spatial overlapping of all diffracted waves in the reconstruction process, significantly deteriorating the quality of the images. In addition, the requirement for a clear background, for reference wave transmission, restricted *holography* to sparse objects. Those problems were resolved by introducing a separate reference wave. Such a wave fell on the photographic plate with an appreciable angle with respect to the object wave. Thus, when the hologram was illuminated again for wave reconstruction, the image appeared spatially separated from the twin image and the direct beam. In such a way, the reconstruction and visualization of the object image without overlapping images was possible.

In parallel to those experiments, the Soviet physicist Yuri Denisyuk [Denisyuk-1962, Denisyuk-1963, Denisyuk-1965] achieved the reconstruction of images of acceptable quality (like those usually obtained with monochromatic illumination) from a hologram illuminated with white light produced by the interference of the opposite incidence the object and reference beams on the photographic emulsion. Those advances, accompanied by the quality and realism of three dimensional (3D) images obtained by *holography*, were responsible of a huge growth of scientific activity as well as general public interest in such a field of knowledge.

Soon after, many new techniques and applications were developed, making *holography* a well-established field with many valuable applications in several directions [Hariharan-1996]. Some of these applications were holographic microscopy [Gabor-1966, Knox-1966], imaging through diffusing and aberrating media [Kogelnik-1965, Leith-1966], high-resolution imaging of aerosols [Thompson-1967], computer-generated holograms [Lohmann-1967], production and correction of optical elements [Upatnieks-1966], and multiple imaging [Lu-1968, Groh-1968], just to cite a few. In the field of information storage and information processing, image deblurring [Stroke-1965] and pattern recognition [Vander Lugt-1965, Colling-1988] are two examples. And perhaps the most significant engineering application was holographic interferometry [Brooks-1965, Burch-1965, Collier-1965, Haines-1965, Powell-1965, Abramson-1980].

However, despite all advances and applications, *holography* still presented difficulties when dealing with real-time analysis (critical in many application areas), since photographic plates required long exposure times and had to be developed after recording processes, preventing the possibility of instantaneous hologram reconstruction. Nonetheless, in 1967, Joseph Goodman took the first steps to solve such an issue by making *holography* became "digital". Since diffraction theory perfectly described the propagation of an optical field, numerical reconstructions were

feasible. In Goodman's work [Goodman-1967], the interference pattern between the object and reference waves was detected by a vidicon detector instead of a photographic film as usual, and the image was numerically reconstructed employing a two dimensional (2D) Fast Fourier Transform (FFT) algorithm (the digital hologram recording, and its numerical image reconstruction are presented in Fig. 2.2). Thus, the "analog" recording/decoding of the object was replaced with a "digital" recording/recovering, giving rise to *digital holography* (*DH*).

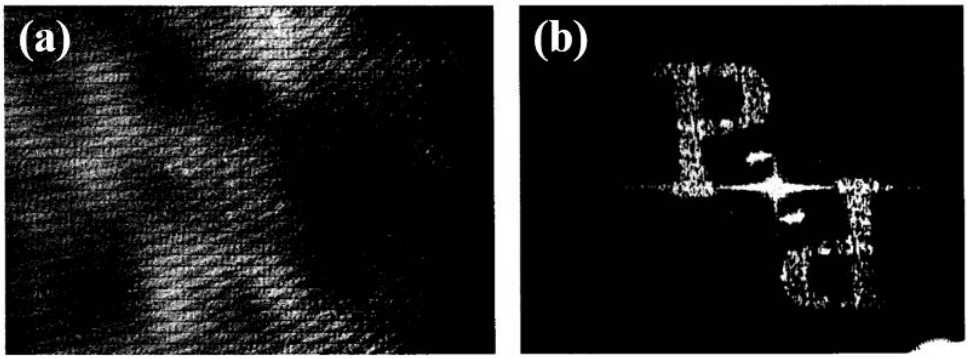

Figure 2.2. (a) Digital hologram recorded by J. Goodman, and (b) its digital image reconstruction. [Goodman-1967].

2.1.2. Digital holography

After Goodman, several researchers including Huang [Huag-1971] and Kronrod [Kronrod-1972] stablished the foundations of *DH*. As recent as the 1990s, Haddad developed a Fourier-transform holographic microscope [Haddad-1992]. Soon after, Schnars and Jüptner gave a big step forward by reporting several experiments based on the direct recording of Fresnel off-axis holograms with a Charged Coupled Device (CCD) and further numerical reconstruction [Fig. 2.3], thus allowing the use of *DH* in metrology of macroscopic objects [Schnars-1994A, Schnars-1994B, Schnars-1994C]. Hence, *DH* progresses came from some technological advances such as the creation of image sensors with numerous miniaturized pixels, the appearance of powerful processors and the increase of storage capacities. Currently, both CCD cameras and computing technologies allow a rapid and efficient application of *DH*.

In *DH*, an optically-generated interference pattern is electronically recorded by either a CCD or a Complementary Metal-Oxide Semiconductor (CMOS), creating a digital hologram. Then, the information is transferred to a computer as an array of numbers from which successful numerical image reconstruction is possible by diffraction theory. Finally, the image is presented as an array of complex number representing the complex amplitude distribution of the optical field.

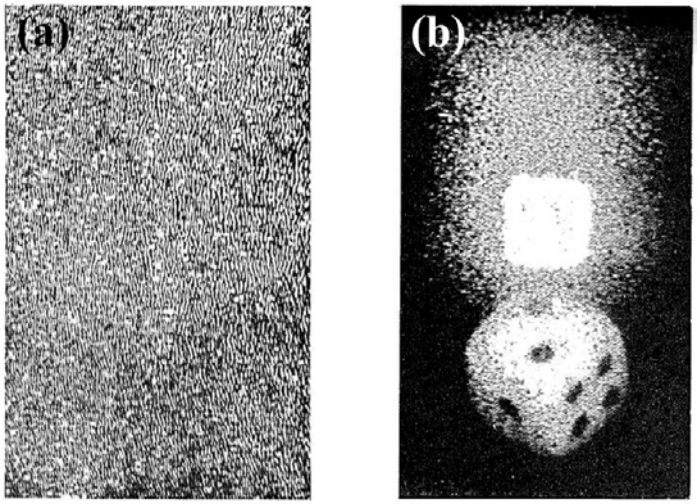

Figure 2.3. (a) One of the first digital holograms recorded with a CCD by Schnars, (b) its numerical reconstruction. [Schnars-1994A].

DH presents many significant advantages regarding time processing, simplicity, robustness, price and versatility in comparison with conventional *holography*. For instance, *DH* is capable of acquiring holograms rapidly (at video rate) and retrieving the image in a fraction of a second (considering a modest computer and applying 2D FFT). By contrast, many minutes are required for recording and photochemical procedures in conventional *holography*. That enables *DH* to real-time analysis and substantially reduces the requirements on the apparatus stability against vibrations and other disturbances [Kim-2011]. Moreover, the digital process is more economical in the long term, since dark rooms, chemical supplies and photo-processing labor are not necessary, whereas heavy optical tables with vibration isolation are often not as critical as in conventional *holography*. Another major advantage of *DH* is the representation of the complex amplitude distribution as an array of complex numbers, so that a direct access to the amplitude and phase values is achieved as soon as the optical field is calculated. In conventional *holography*, on the contrary, one must implement another interferometric experiment to extract phase information. That numerical diffraction of optical fields allows the application of a wide range of powerful numerical techniques in *DH*, difficult or infeasible in conventional *holography*, which can be applied once the hologram is transmitted to a computer. Thus, numerical focusing and auto-focusing of holographic images [Grilli-2001, Langeha-2008], automatic aberration compensation from a single hologram [Colomb-2006], and multiwavelength optical phase unwrapping [Gass-2003, Warnasoo-2007], are just a few examples of achievable applications.

However, the main constraint of *DH* is the pixel count and resolution of the imaging devices. A typical CCD or CMOS pixel may be two orders of magnitude larger than the grains of a traditional photographic emulsion[5]. That limits the spatial frequency of the fringes to those values that fulfil the sampling theorem[6] for the spatial sampling of a hologram. In such a way, the angular size of the object becomes restricted to a few degrees, in contrast to 180º available for conventional *holography*. Consequently, holographic recording with parallax effect is more difficult/restricted in *DH* [Nakatsuji-2008]. Furthermore, in *DH* the quality of reconstructed images may be also influenced by the algorithms implemented for such a purpose [Verrier-2011].

Nevertheless, *DH* has become a multidisciplinary subject with a huge amount of applications in diverse fields as biomedicine, biophotonics, nanomaterials, nanophotonics, and scientific and industrial metrologies [Kim-2011, Picart-2015]. Some of these applications are: metrology of deformations and vibrations [Schnars-2002, Yamaguchi-2003], four dimensional (4D) particle tracking [Xu-2003], pattern recognition and encryption [Matoba-2009], *computer generated holography* (CGH) [Yaroslavsky-2004], fluid and structural mechanics [Desse-2012] and analysis of live cell dynamics [Marquet-2013].

2.1.3. Digital holographic microscopy

Microscopy is one of the main application fields of *DH*. The combination of *holography* with *optical microscopy* in the digital domain is referred as *digital holographic microscopy* (*DHM*). *DHM* includes in a single platform all advantages of whole-object wavefront recovery, high-quality imaging and numerical processing [Marquet-2005, Ferraro-2005, Charrière-2006, Kemper-2008A]. Furthermore, in comparison to *DH*, *DHM* avoids the limited resolution imposed by the finite number and size of the pixels in digital sensors because of microscope lens magnification, resulting in less demanding sampling requirements of the digital sensor [Cuche-1999A].

DHM enables visualization of phase samples using a non-invasive[7], full-field[8], real-time[9], non-contact[10], and static[11] operating principle [Marquet-2005, Kemper-2008A, Kim-2010, Kim-2011]. Moreover, *DHM* does not require the focused recording of an image projected from the object onto the detector plane, since the

[5] Typically, the pixel size of a digital sensor is around few microns, whereas the grains of a photographic emulsion are about 25 nm.
[6] The Nyquist-Shannon sampling theorem states that the minimum sampling frequency of an analog signal should be at least double of its highest frequency component to avoid losing signal information **[Shannon-1949]**.
[7] No need for labelling.
[8] Non-scanning.
[9] Single-frame acquisition.
[10] No sample damage.
[11] No moving components.

focus can be digitally adjusted during the reconstruction process [Ferraro-2005, Dubois-2006A, Dubois-2006B, Dubois-2006C, Yourassowsky-2014]. In this way, *DHM* increases the limited depth of field (DOF) in high numerical aperture (NA) lenses in comparison with conventional *microscopy*, where the DOF is very narrow and shrinks inversely with the square of the NA. With *DHM*, the entire volume of an object can be recorded on a single hologram. Such a hologram is used to numerically focus on the holographic image at any distance [Grilli-2001, Langeha-2008]. In such a way, there is a direct access to the phase information with nanometer sensitivity of transparent or reflective phase objects [Cuche-1999B, Mann-2005, Kemper-2008A, Kühn-2008]. Furthermore, since the whole complex amplitude is retrieved, it is possible to manipulate the numerical representation to achieve other imaging modes normally generated by other microscopy techniques [see Fig. 2.4], such as dark field, ZPC or DIC modalities [Liu-2008].

DHM has becoming in a powerful and versatile tool in many significant fields of Biophotonics, Life Sciences and Medicine [Kim-2011, Picart-2015]. Since the first evidence on *DHM* [Zhang-1998, Cuche-1999A, Dubois-1999], it has been successfully applied to aberration lens compensation [Ferraro-2003], micro-electromechanical systems inspection [Coppola-2004], polarization microscopy imaging [Colomb-2005], real-time quantitative phase contrast imaging [Marquet-2005], 3D analysis of cells in a label-free manner [Dubois-2006B], or particle tracking [Sheng-2006], among others.

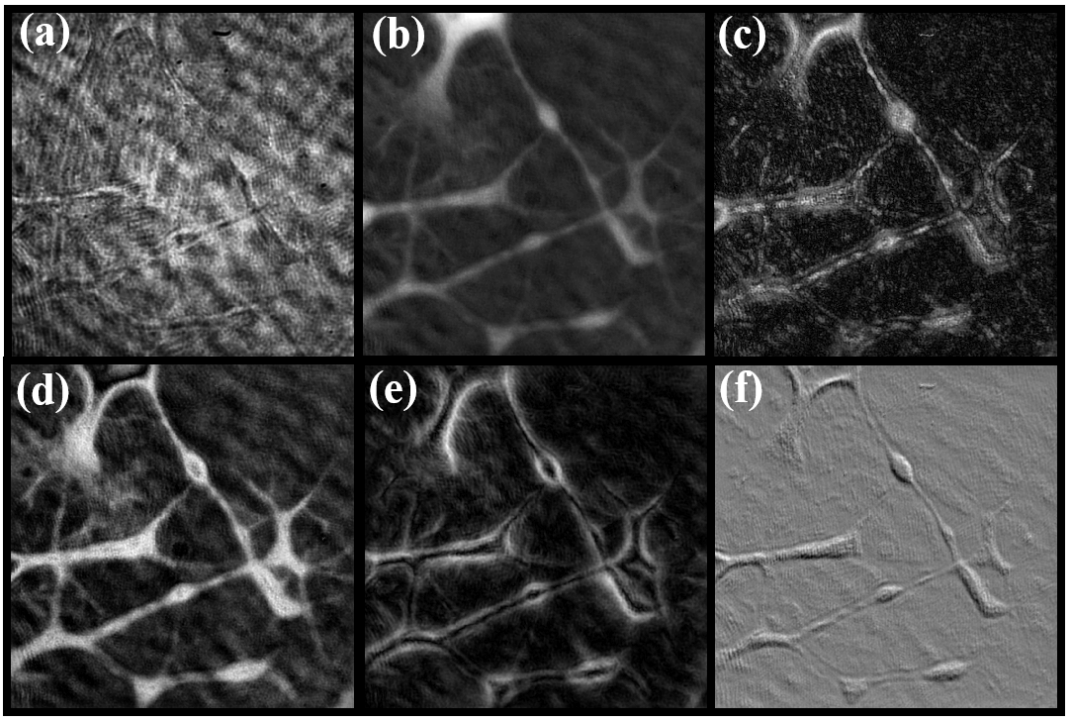

Figure 2.4. Multimode imaging capability of *DHM*: (a) amplitude contrast, (b) quantitative phase contrast, (c) dark field, (d) ZPC, (e) spiral ZPC, and (f) DIC visualizations.

2.2. Interferometric configurations

A basic *DHM* setup consists of a coherent light source to illuminate the sample, an interferometer to produce an interference pattern, a lenses system to obtain a magnified image of the object, a digital sensor to record the hologram and a computer with necessary programs to numerically retrieve the complex amplitude information from such a hologram [Kim-2010]. Normally, highly coherent laser sources are employed for illumination, while for holographic recording are mostly used CCD or CMOS cameras.

Regarding interferometers, different architectures have been implemented such as Mach-Zehnder [Zhang-1998, Dubois-1999], Michelson [Cuche-1999B, Iwai-2004, Kemper-2011], Mirau [Kino-1990, León-Rodríguez-2013], Linnik [Gale-1996, Guo-2014], Twyman-Green [Reichelt-2005], diffraction grating [Micó-2006, Micó-2014], BS cube [Ferrari-2007, Qu-2009, Gabai-2012], Lloyd's mirror [Chhaniwal-2012], lateral shearing [Singh-2012], and Sagnac [Mahajan-2015, Ma-2017] interferometers. Among them, Mach-Zehnder interferometric layout is the most commonly used for transmissive configurations [Zhang-1998, Dubois-1999, Mann-2005, Marquet-2005, Charrière-2006, Kemper-2008A], whereas Michelson arrangement is the main type of interferometer assembled for reflective objects [Cuche-1999B, Iwai-2004, Kemper-2008B, Kemper-2011, Jeon-2016, Cho-2018].

Briefly, interferometers are optical instruments responsible for producing interference patterns. They may include diverse optical elements, such as mirrors, BS cubes, diffraction gratings, lenses, apertures, attenuators, polarizers, etc., to guide, control and manipulate waves. There exist several criteria for their classification. One criterion distinguishes them depending on the path followed by the interferometric beams, making differentiation between double-path and common-path interferometers (CPI). In double-path configurations, the reference and object beams travel along divergent paths and then are recombined by any optical element after passing through the sample[12]. Examples of double-path interferometric configurations are Mach-Zehnder, Michelson, or Twyman-Green interferometers, among others. On the other hand, in CPIs, both beams travel in parallel along the same optical path, going through the same optical elements. CPIs based on lateral shearing, diffraction grating, and BS cube are only three examples.

[12] Typically a BS cube.

Among all those existing interferometers, we shall now focus on describing the two interferometric configurations implemented throughout this thesis for *QP-DHM*. Hence, Mach-Zehnder and common-path (based on diffraction gratings and BS cubes) interferometers will be described in detail as follows.

2.2.1. Mach-Zehnder interferometer

An example of a typical Mach-Zehnder architecture implemented in *DHM* is schematized in Fig. 2.5. A collimated beam[13] coming from a laser source is divided into two beams by a first BS cube (BS1). One of them, the imaging beam, is directed towards the sample (S) by a mirror (M1), passes through it, and is magnified by a microscope objective. The other one, the reference beam, does not interact with the sample, but goes through a lens (L1), which matches the wavefront curvatures between both beams[14], and with a mirror (M2) it is folded towards a second BS cube (BS2), where is recombined with the imaging beam. After BS2, a second lens (L2) is placed to produce the magnified image of the object together with the microscope lens, acting as a tube lens. Then, both beams arrive at the detector plane conforming a given angle (θ) and interfering each other. Such an interference pattern is recorded by a digital sensor creating a digital hologram. Since the sensor is placed at the image plane of the imaging system, the recorded pattern will be an image plane digital hologram.

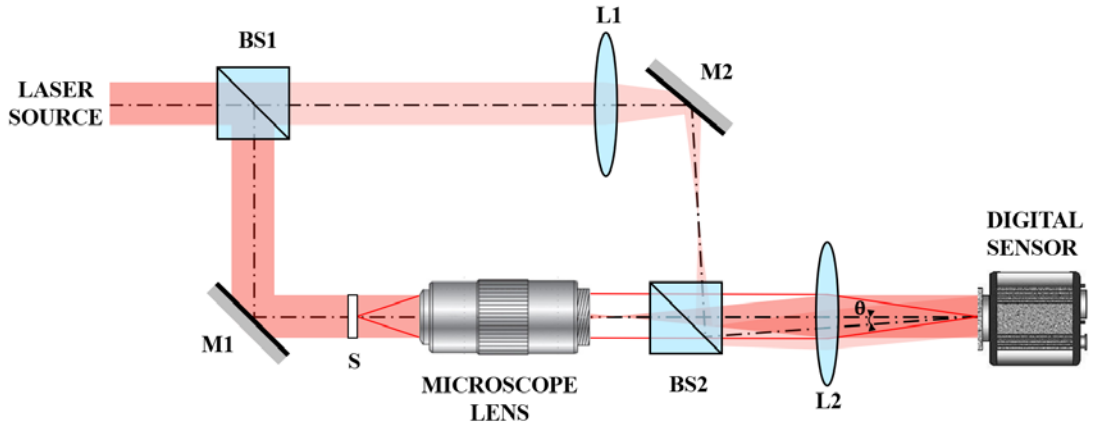

Figure 2.5. A typical DHM layout based on a Mach-Zehnder interferometric architecture. S, M_i, L_i and BS_i, being i = 1,2, denote sample, mirrors, lenses and BS cubes, respectively. θ is the interference angle formed by both reference and imaging beams.

[13] Normally, the laser beam is transversely expanded before entering to the Mach-Zehnder interferometer with a beam expander in order to illuminate the whole FOV.
[14] Note that there exist many other digital techniques to compensate the curvature mismatch between such wavefronts in DHM.

If we now consider that the imaging beam arrives perpendicular to the sensor plane, the complex amplitude distribution of its electric field in such a plane can be expressed as ($i = \sqrt{-1}$):

$$O(x,y) = O_0(x,y)e^{-i\Phi_O(x,y)} \tag{2.1}$$

being O_0 the amplitude, Φ_O the phase, and (x, y) the spatial coordinates transversal to the direction of propagation[15].

On the other hand, we can assume that the reference beam is a tilted[16] plane wave with constant amplitude and phase, so its complex amplitude in that plane is given by

$$R(x,y) = R_0 e^{-i2\pi vy} \tag{2.2}$$

where $v = \frac{\sin\theta}{\lambda}$ is the spatial frequency of the reference beam.

Thus, the intensity distribution across the recording plane produced by a Mach-Zehnder interferometer and recorded by the digital sensor is

$$I(x,y) = |O(x,y) + R(x,y)|^2 = |O_0(x,y)|^2 + |R_0|^2 + \\ + R_0 O_0(x,y)e^{-i\Phi_O(x,y)}e^{i2\pi vy} + R_0 O_0(x,y)e^{i\Phi_O(x,y)}e^{-i2\pi vy} \tag{2.3}$$

As we can notice in Eq. (2.3), the digital hologram includes three diffraction orders: the first two terms on the right-hand side comprise the 0th order (DC term), while the third and fourth terms represent the +1st and -1st orders, respectively. The third term (+1st order) is directly related to the real image provided by the imaging system. Frequently, the last term (-1st order) is referred as the twin image.

Perhaps the main advantage of a Mach-Zehnder architecture is its versatility to integrate optical components, offering high-flexibility in alignment, especially when microscope lenses are used as in *DHM*. In addition, it allows easy variation of the interference angle θ, and thus the fringe pattern frequency[17] by rotating either M2 or BS2, which provides high versatility to change between holographic configurations[18]. By contrast, its arrangement requires many optical elements, and the different optical paths followed by the beams might make Mach-Zehnder interferometers sensitive to mechanical vibrations and thermal changes.

[15] We assume that the direction of propagation of the waves is along the axis z.
[16] For simplicity, we suppose that the tilt of the reference beam is just along the direction y.
[17] We shall understand the importance of changing the period of fringe patterns in an easy way in Section 1.7.
[18] We shall explain in detail the different holographic configurations existing in DHM in Section 1.7.

2.2.2. Common-path interferometer

Nevertheless, those issues can be overcomed by employing CPIs instead of Mach-Zehnder interferometers. CPIs present some advantages in comparison with other interferometric configurations regarding stability, simplicity and robustness [Micó-2006B, Micó-2009, Ding-2010, Shaked-2010, Chhaniwal-2012, Singh-2012, Micó-2014]. Indeed, since in CPIs both the imaging and reference beams follow nearly the same optical path and pass through the same optical elements, they minimize the required components and can be assembled in a more compact way. Furthermore, the instabilities[19] of the system do not alter the obtained results, because they affect equally both beams.

Depending on the way of creation of the reference beam, one can distinguish between three different types of CPIs: reference-generation (R-G), self-interference (S-I) and spatially-multiplexed (S-M) approaches. In R-G CPIs, the reference beam is synthesized by spatially filtering[20] one of the two imaging beams after passing the microscope lens at an intermediate Fourier plane [Popescu-2006, Micó-2006A, Gao-2010, Shaked-2012A, Girshovitz-2013]. That was reached with Mach-Zehnder [Micó-2006, Micó-2007] as well as Michelson [Shaked-2012A, Girshovitz-2013, Guo-2013] architectures. In such a way, the FOV is fully preserved, but a relatively complex opto-mechanical stage must be assembled instead.

In S-I CPIs, the clear region in the surroundings of sparse samples is used as reference beam, since do not alter the light passing through it, so the imaging beam interferes with a shifted version of itself [Fu-2010, Kemper-2011, Chhaniwal-2012, Singh-2012]. To do so, there were proposed, for instance, Lloyd's mirror [Chhaniwal-2012], and lateral shearing plate [Singh-2012] arrangements, among others. Such a CPI requires fewer optical elements, and its configuration is more compact and simpler than R-G CPI, but its applicability is restricted only to sparse samples. Nonetheless, biosamples fulfil such a condition in many cases.

Finally, S-M CPIs leave a clear region at the input plane for reference beam transmission by means of a spatial distribution of the FOV, being in side-by-side configuration with the sample region. After the microscope lens, both beams are overlapped by using minimal optical components, such as a diffraction grating [Micó-2006B, Micó-2009, Micó-2014], a BS cube [Ferrari-2007, Gabai-2012, León-Rodríguez-2018], or a Fresnel biprism [Ebrahimi-2018]. Such an architecture enables inspection of dense samples[21], but the useful FOV is halved.

[19] Such as mechanical vibrations or thermal changes between both paths.
[20] Using a pinhole mask with a proper diameter to block just the spatial frequency information of the sample.
[21] Unlike S-I CPI.

In line with that, we have successfully implemented two types of S-M CPIs for *QP-DHM* along the present work. One of them makes use of a diffraction grating to produce interferences, while the other employs a BS cube as interferometric element.

2.2.3. Common-path interferometer by using a diffraction grating

As mentioned above, it is possible to achieve an interferometric configuration by spatially multiplexing the FOV and placing a one dimensional (1D) diffraction grating, for instance, behind the imaging lens, as depicted in Fig. 2.6. Here, a collimated laser beam illuminates both the sample, which takes only one half of the whole FOV, and a clear region with the same extension, located immediately adjacent to it. Then, the imaging system composed of a microscope objective and a lens (L) projects a magnified image of the input plane onto the sensor plane[22]. By inserting a sinusoidal 1D diffraction grating[23] (G) behind L, three laterally shifted replicas of the image are produced at the recording plane, corresponding with the diffraction orders of the grating (-1^{st}, 0^{th}, and $+1^{st}$). Now, we can properly select the grating period to overlap the clear region of -1^{st} order with the sample region of the 0^{th} order, thus producing an interference pattern suitable for digital recording and further numerical reconstruction.

Figure 2.6. Scheme and ray tracing of a CPI based on a diffraction grating employed in *DHM*. S, L, and G denote sample, lens, and 1D diffraction grating.

Since both imaging and reference beams arrive at the sensor plane in the same conditions as in Mach-Zehnder case[24], the intensity distribution recorded by the digital sensor will be described by Eq. (2.3). In this case, the interference angle θ will depend on both the spatial period and axial position of the grating. A more detailed treatment of such an interferometer will be done in Section 3.2, where it will be widely described and mathematically analysed.

[22] In the absence of the grating.
[23] For simplicity, we consider a sinusoidal 1D diffraction grating.
[24] The imaging beam falls perpendicular upon the CCD sensor, whereas the reference beam arrives forming an angle θ with the normal to the camera.

2.2.4. Common-path interferometer by using a beam splitter cube

A BS cube can also act as an interferometer by placing it in a proper way. Normally, when an input beam goes through a BS cube, both reflected and transmitted components propagate along orthogonal directions each other, and they do not interfere unless we introduce other optical components, such as mirrors, to redirect and recombine both beams. However, by placing the BS cube in a manner that its semireflecting mirror is quasi-parallel to the optical axis of the system, then it will behave like a single element S-M CPI [Ferrari-2007].

A general scheme of a CPI based on a BS cube in *DHM* is shown in Fig. 2.7. A BS cube is placed with its semireflecting mirror along the optical axis, so that an incident beam will be divided into two beams. By defining a S-M FOV, one half of the beam will be used for reference beam transmission, while the other will pass through the sample. After crossing the imaging system formed by a microscope objective and a lens (L), such two beams enter to the BS cube, in which its semireflecting layer splits both beams into two laterally shifted replicas (reflected and transmitted ones), thus having four beams behind the BS cube. Finally, these beams are overlapped by pairs to simultaneously produce two interferograms (I_1 and I_2) in a side by side configuration at the recording plane. Essentially, such interferograms will be almost identical, except that they are mirror images each other with a relative phase shift.

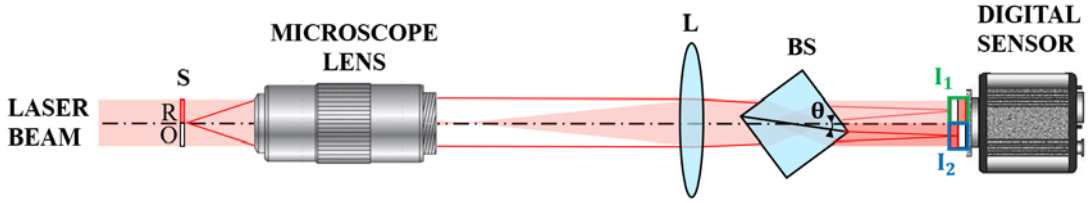

Figure 2.7. Scheme and ray tracing of a DHM layout based on a BS cube interferometer.

The relative phase shift between the interferograms can be easily calculated. Let assume that a collimated laser beam passes through the S-M FOV, composed of two regions (the sample and clear regions), thus conforming the object and reference beams, respectively, as described above. After being magnified by the imaging system and before entering the BS cube, the imaging beam can be perfectly described by Eq. (2.1), and the reference beam can be expressed as (assuming an *on-axis* configuration)

$$R(x,y) = R_0 \tag{2.4}$$

Once inside the BS cube, the semireflecting layer provides transmitted (O_t and R_t) and reflected (O_r and R_r) replicas of such beams. In addition, assuming a lossless BS cube, the conservation of energy condition [Degiorgio-1980] requires that the phase relation between both transmitted and reflected replicas is given by

$$\varphi_r = \varphi_t + \frac{\pi}{2} \tag{2.5}$$

Then, at the exit of the BS cube, such four beams will therefore be defined as

$$\begin{aligned} O_t(x,y) &= O_0(x,y)e^{-i\Phi_o(x,y)} \\ O_r(x,y) &= O_t(x,y)e^{i\pi/2} \\ R_t(x,y) &= R_0 \\ R_r(x,y) &= R_t(x,y)e^{i\pi/2} \end{aligned} \tag{2.6}$$

Hence, the intensity distribution of both interferograms can be calculated from Eqs. (2.6). Looking at Fig. 2.7, we realise that I_1 is generated by the interference between O_r and R_t, whereas the coherent overlapping of O_t and R_r defines I_2, thus having

$$\begin{aligned} I_1 &= \left|O_0(x,y)e^{-i\Phi_o(x,y)}e^{i\pi/2} + R_0\right|^2 \\ I_2 &= \left|O_0(x,y)e^{-i\Phi_o(x,y)} + R_0e^{i\pi/2}\right|^2 \end{aligned} \tag{2.7}$$

If we now consider that the transmission/reflection ratio of the BS cube is 50:50 and the sample is a pure phase object[25]

$$O_0(x,y) = R_0 \tag{2.8}$$

On the other hand, taking into account the trigonometric relationships $\cos(\Phi + \pi/2) = -\sin(\Phi)$ and $\cos(\Phi - \pi/2) = \sin(\Phi)$, I_1 and I_2 can be eventually expressed as

$$\begin{aligned} I_1 &= |R_0|^2\left[1 - \sin\left(\Phi_o(x,y)\right)\right] \\ I_2 &= |R_0|^2\left[1 + \sin\left(\Phi_o(x,y)\right)\right] \end{aligned} \tag{2.9}$$

Equations 2.9 shows that the relative phase shift between both interferograms is π rad[26] coming from the interaction between the beams and the semireflecting mirror of the BS cube.

Such a CPI based on a BS cube has the advantage of generating controllable interference fringes by rotating it with respect to the optical axis. Depending on the angle θ between the semireflecting layer and the optical axis, the interferograms will adopt a different holographic configuration. The higher the rotation angle θ, the higher frequency of the fringes ranging from fully *on-axis* to *off-axis* configurations.

[25] It does not modify the modulus of the complex amplitude distribution.
[26] Since $e^{i\pi} = -1$.

2.3. Reconstruction procedures

In *DHM*, the interference angle between both interferometric beams defines the holographic configuration [see Fig. 2.8]. Thus, we can distinguish between three main configurations: *on-axis*, *slightly off-axis*, and *off-axis* holographic configurations.

When both beams arrive parallel each other to the sensor plane ($\theta = 0^{\circ}$), an *on-axis* configuration is defined [Fig. 2.8 (a1)]. In such a configuration, the hologram does not present a fringe pattern since the fringe period is infinite [Fig. 2.8 (a2)], and the Fourier transform (FT) of the digital hologram will therefore present all diffraction orders overlapping one another [Fig. 2.8 (a3)]. On the other hand, in a *slightly off-axis* configuration (a specific situation of *off-axis* case), both interferometric beams fall upon the digital sensor forming a small interference angle θ [Fig. 2.8 (b1)]. In that case, the hologram will present a fringe pattern [Fig. 2.8 (b2)] whose spatial frequency will not be enough to separate all diffraction orders at the Fourier domain. In this configuration, both -1^{st} and $+1^{st}$ orders will overlap with the 0^{th} order but they will appear separated each other [Fig. 2.8 (b3)]. Finally, when both interferometric beams form an interference angle θ at the recording plane [Fig. 2.8 (c1)] big enough to produce a fringe pattern whose spatial frequency [Fig. 2.8 (c2)] separates completely all orders one another [Fig. 2.8 (c3)], an *off-axis* holographic configuration is defined.

The suitability of implementing each configuration will be related to the experimental requirements. Depending on the configuration chosen in the DHM layout, a different approach for complex amplitude retrieval will be demanded. Below, we describe the reconstruction procedures employed in this thesis according to the holographic configuration. Thus, we present approaches based on the spectral domain such as Fourier filtering and Fourier filtering after hologram subtraction, and methods carried out considering spatial domain such as phase-shifting (P-S) and HHT.

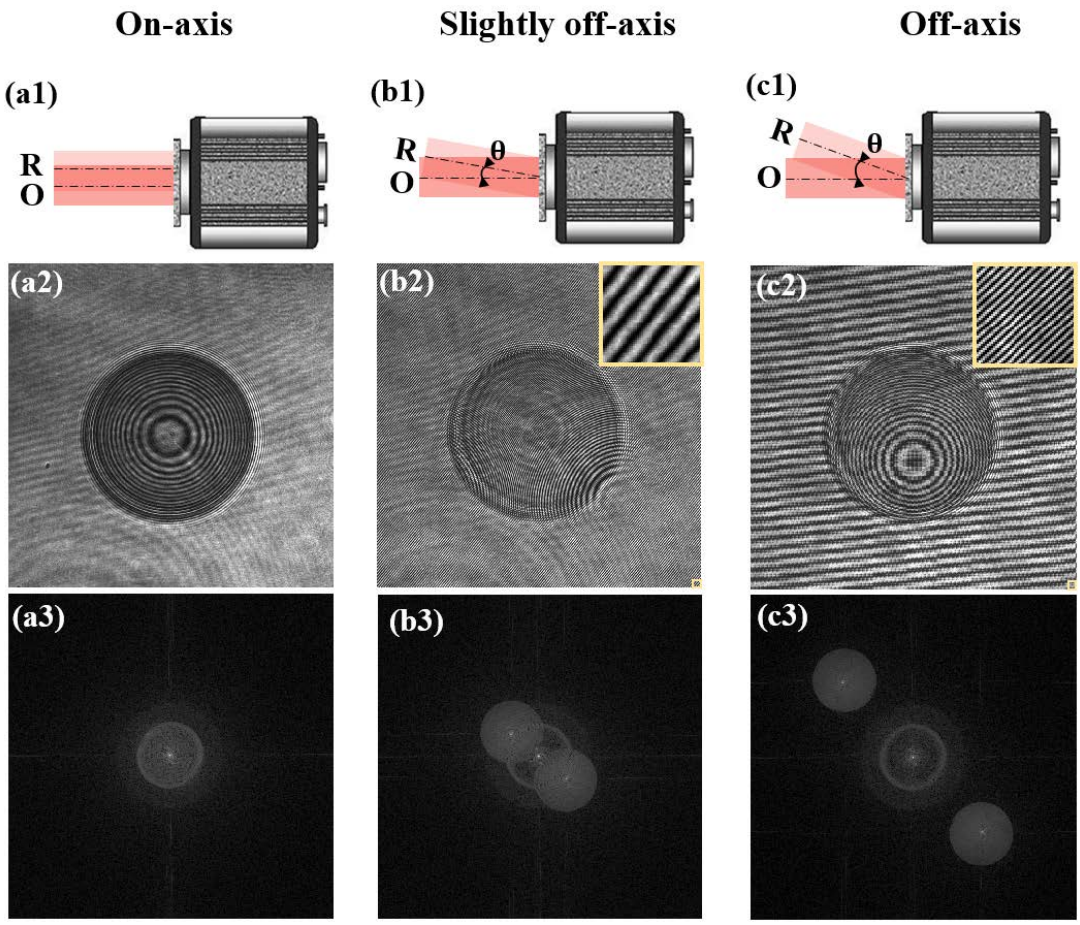

Figure 2.8. Holographic configurations in *DHM*, where columns (a), (b) and (c) depict *on-axis*, *slightly off-axis* and *off-axis* configurations, respectively, and rows (1), (2), and (3), represent the dependence of such configurations with the interference angle θ, the fringe pattern of the hologram and its FT, respectively.

2.3.1. Fourier filtering method

In an *off-axis* configuration, a reference beam is introduced with a spatial carrier frequency in order to separate the propagation of the different diffraction terms encoded in the hologram (DC term, real image and virtual image). Thus, it is possible to reconstruct only the real image (or virtual image), without any perturbation coming from the other terms. In that case, in the spatial frequency spectrum, there is a three-modal distribution related to the three diffraction orders (FT and FT^{-1} means, respectively, 2D Fourier transform and 2D inverse Fourier transform), which can be expressed as [Picart-2015]

$$FT[I](u,v) = C_0(u,v) + C_{+1}(u+u_0, v+v_0) + C_{-1}(u-u_0, v-v_0) \qquad (2.10)$$

where C_0 is the FT of the 0^{th} order and $C_{\pm 1}$ are the FTs of the $\pm 1^{st}$ orders. If the three orders are well separated one another in the Fourier space, the $+1^{st}$ order (or -1^{st} order) can be extracted from the whole Fourier spectrum as depicted in Fig. 2.9.

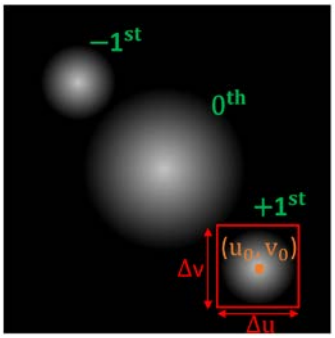

Figure 2.9. Spectral distribution of the orders in an *off-axis* holographic configuration and spectral filtering of the real image.

The spatial frequencies (u_0,v_0) localize the useful information (center of the coherent aperture) and they must be adjusted to minimize the overlapping of the three diffraction orders. By applying a rectangular bandwidth-limited filter ($\Delta u \times \Delta v$ width) around the spatial frequency (u_0,v_0), and after filtering and FT^{-1}, we get the complex amplitude of the imaging beam as

$$O(x,y) = FT^{-1}[C_{+1}(u-u_0, v-v_0)] \cong R_0\left\{O_0(x,y)e^{i\Phi_o(x,y)}e^{i2\pi(u_0x+v_0y)}\right\} * h(x,y) \tag{2.11}$$

where the symbol $*$ means the convolution and h is the impulse response corresponding to the filtering applied in the Fourier domain, being

$$h(x,y) = \Delta u \Delta v e^{i2\pi(u_0x+v_0y)} \mathrm{sinc}(\pi\Delta u x)\mathrm{sinc}(\pi\Delta v y) \tag{2.12}$$

The spatial resolution is then related to $1/\Delta u$ and $1/\Delta v$, respectively, in the x-y axis. In addition, the phase recovered from Eq. (2.11) includes the spatial carrier modulation that must be removed. This can be achieved by multiplying O by $e^{-i2\pi(u_0x+v_0y)}$. Note that a circular bandwidth-limited filter (instead of a rectangular one) can also be used [Cuche-1999A]. In that case, the impulse response of the filter is proportional to a J_0 Bessel function.

Then, the optical phase of the imaging beam at the hologram plane can be estimated from the relation

$$\Phi_o(x,y) = \tan^{-1}\left(\frac{\mathrm{Im}[O(x,y)]}{\mathrm{Re}[O(x,y)]}\right) \tag{2.13}$$

while the object amplitude is given by

$$O_0(x,y) = \sqrt{\mathrm{Re}[O(x,y)]^2 + \mathrm{Im}[O(x,y)]^2} \tag{2.14}$$

In Eqs. (2.13) and (2.14), Re[…] and Im[…], mean the real and imaginary parts of the complex value, respectively.

2.3.2. Fourier filtering method with DC term suppression by hologram subtraction

Fourier filtering method can be also applied in case of having a *slightly off-axis* holographic configuration. Since $\pm 1^{st}$ terms overlap with 0^{th} order but not each other, it is possible to retrieve the complex amplitude of the imaging beam from $+1^{st}$ (or -1^{st}) order by subtracting somehow the DC term from the digital hologram [Kreis-1997, Demoli-2003]. Several approaches were developed for such a DC term removal. Thus, DC term can be easily removed by subtracting the average intensity I from the hologram [Kreis-1997]. However, the reference beam may contain nonuniformities in real experiments causing a non-successful DC suppression. Another way of completely removing the 0^{th} order is by separately recording both the imaging and reference beams as well as the digital hologram [Kim-2011]. Nonetheless, such a method is limited when dealing with dynamic objects. By contrast, it is also possible to achieve DC suppression by recording only the reference intensity and the hologram [Chen-2007], but some assumptions are required that might not be always present in the experiments.

Another appealing method for DC removal is based on the recording of two holograms phase shifted by π rad each other [Gao-2011B, Picazo-Bueno-2019], which can be expressed as

$$I_1(x,y) = |O(x,y)|^2 + |R|^2 + R^*O(x,y) + RO^*(x,y)$$

$$I_2(x,y) = |O(x,y)|^2 + |R|^2 - R^*O(x,y) - RO^*(x,y) \qquad (2.15)$$

As we have previously mentioned, the first two terms at the right hand in Eqs. (2.15) compose the 0^{th} order. Thus, by subtracting both interferograms, we can reach the complete suppression of these two terms, thus having a subtracted hologram given by

$$I = I_1 - I_2 = 2R^*O(x,y) + 2RO^*(x,y) \qquad (2.16)$$

When a *slightly off-axis* configuration is selected, these two terms at the right hand in Eq. (2.16) will appear completely separated each other in the Fourier spectrum. In such a way, we can apply Fourier filtering method to retrieve the complex amplitude distribution of the imaging beam from the $+1^{st}$ order (or -1^{st}) [Fig. 2.10]. Note that a BS cube interferometer provides simultaneously I_1 and I_2 of Eqs. (2.15), so the DC term can be removed in a single acquisition, making this method suitable for dynamic analysis when a *slightly off-axis* holographic configuration is selected.

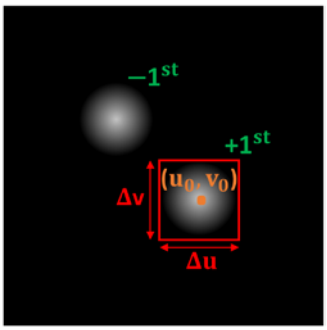

Figure 2.10. Fourier filtering method applied to a subtracted digital hologram, whose DC term is previously removed.

2.3.3. Phase-shifting method

Complex amplitude information can also be directly retrieved from spatial domain when an *on-axis* configuration is implemented by using P-S methods in the temporal domain [Creath-1988, Dorrio-1999]. Such an approach was described by Yamaguchi in 1997 [Yamaguchi-1997, Yamaguchi-2001A, Yamaguchi-2001B] and led to the reconstruction of a holographic image free of 0^{th} order and twin image.

The intensity distribution of an *on-axis* interferogram at the recording plane can be written as follows

$$I(x,y) = |R_0|^2 + |O_0(x,y)|^2 + 2R_0O_0(x,y)\cos(\Phi_O(x,y)) \qquad (2.17)$$

In Eq. (2.17), we should consider three unknows: the DC term formed by the first two terms at the right hand of the equation, the modulation term $2R_0O_0(x,y)$, and the phase of the cosine function $\Phi_O(x,y)$. Hence, if we record at least three values of I linearly independents, we should be able to solve those three unknows. That can be done by introducing a phase shift in the cosine function with the insertion of a phase modulator in the DHM layout. Typically, a piezoelectric transducer (PZT) is used to achieve P-S[27] by time multiplexing [Creath-1988, Dorrio-1999]. Briefly, a PZT is stamped to a mirror[28] on which can produce slightly axial displacements by means of the application of small voltages on it. In such a way, the optical phase of one beam changes respect to the other, thus generating a phase shift between both beams. With at least three positions of the mirror, the imaging beam can be reconstructed [Yamaguchi-2001]. However, the robustness of the method increases with increasing the number of phase-shifted holograms. If we consider a hologram with a phase-shift being an integer division of 2π, i.e. $2\pi/P$, with P an integer, we will have

$$I_P(x,y) = |R_0|^2 + |O_0(x,y)|^2 + 2R_0O_0(x,y)\cos\left(\Phi_O(x,y) - \frac{2(p-1)\pi}{P}\right) \qquad (2.18)$$

[27] Although there exist other components or methods.
[28] Normally, such a mirror is placed in the reference arm.

with p = 1, 2, …, P. For P ≥ 3, the phase of the imaging beam at the detector plane may be calculated by [Greivenkamp-1984]

$$\Phi_o(x,y) = \tan^{-1}\left\{\frac{\sum_{n=1}^{P} I_P(x,y)\sin\left(\frac{2\pi(p-1)}{P}\right)}{\sum_{n=1}^{P} I_P(x,y)\cos\left(\frac{2\pi(p-1)}{P}\right)}\right\} \quad (2.19)$$

whereas the amplitude is given by:

$$O_0(x,y) = \frac{1}{2R_0}\sqrt{\left(\sum_{n=1}^{P} I_P(x,y)\sin\left(\frac{2\pi(p-1)}{P}\right)\right)^2 + \left(\sum_{n=1}^{P} I_P(x,y)\cos\left(\frac{2\pi(p-1)}{P}\right)\right)^2} \quad (2.20)$$

If the reference beam is plane or spherical, that is, free from aberrations, the phase $\Phi_O(x,y)$ may be determined without ambiguity and compensated, and the imaging beam may be directly reconstructed.

2.3.4. Hilbert-Huang transform method

Hilbert transform (HT) was previously proposed as a technique for *QPI* [Ikeda-2005, Popescu-2005, Lue-2009, Srivastava-2012]. The technique, named *Hilbert phase microscopy* (*HPM*), extended the concept of complex analytic signal from temporally to spatially varying fields. In contrast to temporal P-S processes, *HPM* allows single-shot operation principle by retrieving the phase distribution from a single hologram.

However, *HPM* used a 1D HT approach, so the analysis was performed row-by-row (or column-by-column) and the fringes direction was supposed to be perpendicular to the analysis direction. In addition, there were some other constraints such as the requirements of sinusoidal fringes and constant hologram background. On the other hand, neither closed nor significantly bent fringes were allowed. Furthermore, noise was transferred from hologram to phase. To overcome such restrictions, Trusiak *et al.* [Trusiak-2012, Trusiak-2014, Trusiak-2016A] proposed an approach based on HHT. HHT is a method used for nonlinear and non-stationary data analysis and consists of two parts: empirical mode decomposition (EMD) and Hilbert spiral transform (HST).

The crucial part of the HHT is the EMD method in which any complicated data is decomposed into a finite and often small number of intrinsic mode functions (IMF) that admit well-behaved HT [Huang-1998]. Such a decomposition is intuitive, direct, *a posteriori*, adaptive, highly efficient, and with its basis based on, and derived from, the local characteristic spatial scales of the data, which makes the method feasible for analysis of nonlinear and non-stationary processes. The aim of EMD approach is to identify empirically the intrinsic oscillatory modes by their

characteristic spatial scales in the data, and then decompose them accordingly into several IMFs. An IMF must fulfil two conditions: 1) the number of zero crossings and extrema must be either equal or different not more than one in the full data set, and 2) the envelope defined by the combination of the envelopes coming from the local maxima and the local minima, separately, has a mean value of zero at any point.

There exists a systematic method for IMFs extraction named sifting process [Huang-1998]. In that method, the first step is to define the spatial scales directly from, for instance, the spatial interval between the successive alternations of local maxima and minima in a hologram. Then, the extrema are founded, and all the local maxima are linked by using a cubic spline line providing an upper envelope, while a lower envelope is generated from the same connection between local minima. After that, a mean envelope $m_1(x,y)$ is calculated from both upper and lower ones. Subsequently, the difference between the data I(x,y), for instance, a hologram, and $m_1(x,y)$ is the first component $h_1(x,y)$:

$$I(x,y) - m_1(x,y) = h_1(x,y) \tag{2.21}$$

Ideally, $h_1(x,y)$ should be an IMF. However, during the process, it could be generated new extrema, and shift or exaggerate the existing ones. For that reason, the process must be repeated more times. In the second sifting process, $h_1(x,y)$ is treated as the data, then

$$h_1(x,y) - m_{11}(x,y) = h_{11}(x,y) \tag{2.22}$$

We can repeat the process *k* times, until $h_{1k}(x,y)$ is an IMF, that is

$$h_{1(k-1)}(x,y) - m_{1k}(x,y) = h_{1k}(x,y) \tag{2.23}$$

After the considered *k* repetitions, we eventually obtain the first IMF component from the data set as

$$c_1(x,y) = h_{1k}(x,y) \tag{2.24}$$

The process must be carefully applied since a high number of *k* repetitions could make the IMF a pure frequency modulated signal of constant amplitude. In such a way, we must determine a criterion to stop it guaranteeing that the IMF components retains enough physical sense of both amplitude and frequency modulations. That can be accomplished by limiting the size of the standard deviation (STD), computed from the two consecutive sifting results as

$$STD = \sum_{x,y=0}^{X,Y} \left[\frac{\left| h_{1(k-1)}(x,y) - h_{1k}(x,y) \right|^2}{h_{1(k-1)}^2(x,y)} \right] \tag{2.25}$$

A typical value for STD can be set between 0.2 and 0.3 [Huang-1998].

Normally, $c_1(x,y)$ contains the finest scale or the shortest period component of the signal. We can separate $c_1(x,y)$ from the rest of the data by

$$I(x,y) - c_1(x,y) = r_1(x,y) \tag{2.26}$$

Since the residue $r_1(x,y)$ still contains information of longer period components, it is treated as new data and subjected to the same sifting process as described above. Such a procedure can be repeated on all the subsequent residues and the result is

$$r_1(x,y) - c_2(x,y) = r_2(x,y), \dots, r_{n-1}(x,y) - c_n(x,y) = r_n(x,y) \tag{2.27}$$

The sifting process can be stopped by any of the following predetermined criteria: either when the component $c_n(x,y)$ or the residue $r_n(x,y)$ becomes so small that it is less than a predetermined value of substantial consequence, or when the residue $r_n(x,y)$ becomes a monotonic function from which no more IMF can be extracted. Even for data with zero mean, the final residue can still be different from zero; and for data with a trend, then the final residue should be that trend. By considering Eqs. (2.26) and (2.27) we obtain

$$I(x,y) = \sum_{i=1}^{n} c_i(x,y) + r_n(x,y) \tag{2.28}$$

Hence, the data is decomposed into n-empirical modes and a residue, which can be either the mean trend or a constant.

Now, we shall assume that the data is a hologram that can be mathematically expressed in the form

$$I(x,y) = b(x,y) + a(x,y)\cos(\Phi_o(x,y)) + n(x,y) \tag{2.29}$$

where b, n, a, and Φ_O represent background, noise, amplitude and phase, respectively. Such an interference pattern is decomposed into IMFs by using EMD as above described. After that, we must efficiently manage the set of extracted IMFs that define the hologram I(x,y) by discarding spurious and preserving informative ones. Indeed, the first and the latest ones are normally removed since they are related to high frequency noise and hologram background, thus providing a filtered interference pattern as follows

$$I_F(x,y) = \sum_{n_1}^{n_2} c_i(x,y) = a(x,y)\cos(\Phi_o(x,y)) \tag{2.30}$$

where $n_1 > 1$ and $n_2 < n$, and defines the first and last IMFs used for compounding the filtered hologram.

Complex amplitude reconstruction is achieved by applying HST [Larkin-2001] to Eq. (2.30). HST is a natural and isotropic way to generalize HT to 2D and it is primarily based on the combination of two multiplicative operators: 1) a spiral phase operator defined in spatial-frequency domain to create the quadrature component and 2) an orientational phase spatial operator. Such a spiral phase function is defined as

$$\mathrm{SPF}(u,v) = \frac{u+iv}{\sqrt{u^2+v^2}} \tag{2.31}$$

where u and v are spatial frequencies. The quadrature component is calculated employing the HST by

$$\mathrm{QI_F}(x,y) = -ie^{-i\beta(x,y)}\mathrm{FT}^{-1}\left[\mathrm{SPF}(u,v)\mathrm{FT}[\mathrm{I_F}(x,y)]\right] = -a(x,y)\sin(\Phi_o(x,y)) \tag{2.32}$$

where β(x,y) represents the fringe local direction map. β(x,y) can be calculated using principal component analysis [Trusiak-2016A].

Finally, a 2D analytic signal is defined considering $I_F(x,y)$ and $QI_F(x,y)$ in the form

$$\mathrm{AFP}(x,y) = \mathrm{I_F}(x,y) + i\mathrm{QI_F}(x,y) = a(x,y)e^{i\Phi_o(x,y)} \tag{2.33}$$

where the amplitude and the phase of the imaging beam are eventually calculated as

$$\begin{aligned} a(x,y) &= \sqrt{\mathrm{I_F^2}(x,y) + \mathrm{QI_F^2}(x,y)} \\ \Phi_o(x,y) &= \tan^{-1}\left(\frac{QI_F(x,y)}{I_F(x,y)}\right) \end{aligned} \tag{2.34}$$

2.4. Imaging modalities

Different imaging modalities can be performed in *DHM*, mainly depending on the optical characteristics of the sample to be inspected. In such a way, *DHM* setups can be implemented in transmissive [Dubois-2004, Marquet-2005, Charrière-2006, Garcia-Sucerquia-2006, Langeha-2009, Pavillon-2012], reflective [Iwai-2004, Kühn-2007, Kemper-2008A, Shaked-2010, Yaqoob-2011, Guo-2013], and transflective [Reichelt-2005, Lin-2010, Biener-2011, Faridian-2013, Zheng-2017A, Zheng-2017B] configurations. In addition, *DHM* layouts can also be combined with other imaging techniques such as fluorescence microscopy [Park-2006, Pavillon-2010, Kühn-2013] and Raman spectroscopy [Kang-2011, Pavillon-2013, McReynolds-2017], thus allowing multianalysis of specimens.

2.4.1. Transmissive modality

DHM layouts are often defined using transmissive imaging mode. When light passes through a transparent object, it contains valuable information about both its RI and morphology. Several layouts such as Mach-Zehnder [Javidi-2005, Dubois-2006, Shaked-2009, Liu-2011], diffraction grating [Micó-2006A, Micó-2008, Micó-2014], and BS cube [Ferrari-2007, Qu-2009, Gabai-2012] interferometers were assembled in *DHM* considering transmission. In addition, all holographic configurations were implemented with such an imaging mode [Javidi-2005, Kemper-2006, Micó-2008, Langeha-2009, Shaked-2009, Min-2011]. For instance, an *on-axis* configuration was employed for 3D visualization and recognition of microorganisms [Javidi-2005] and for superresolved imaging of red blood cells (RBCs) [Micó-2008]. On the other hand, *slightly off-axis* arrangements allowed visualization of living human skin cancer cells by using a two-step-only P-S approach [Shaked-2009], as well as extension of the axial measurement range to the micrometer scale by means of wavelength-multiplexing [Min-2011], just to cite a few examples. Finally, an *off-axis* configuration was used for investigation of living pancreas tumor cells [Kemper-2006] and for 3D tracking of cell migrations [Langeha-2009].

A scheme of a CPI in *DHM* using a diffraction grating and working in a transmissive modality is depicted in Fig. 2.11. In that scheme, a collimated laser beam goes through a S-M FOV, and the optical system composed by a microscope lens, a lens (L) and a 1D diffraction grating (G) produces an image plane hologram at the CCD sensor area.

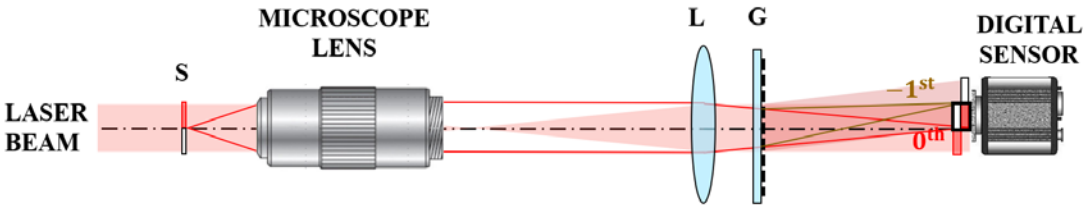

Figure 2.11. *DHM* layout working in a transmissive imaging mode.

Then, the optical phase of the imaging beam can be retrieved from the digital hologram by means of the application of any of the reconstruction procedures previously described in Section 2.3 and according to the established configuration. Such phase differences will be directly related to both the RI differences between the object and the surrounding medium $\Delta n(x,y) = n_o(x,y) - n_m$, and the thickness $t(x,y)$ of the object, in the following way

$$\Phi_o(x,y) = \frac{2\pi}{\lambda}\Delta n(x,y)\, t(x,y) \tag{2.35}$$

Eq. (2.35) shows the dependence of the optical phase changes with RI and thickness variations. Thus, RI as well as thickness modifications can be calculated by analyzing the phase variations between different recorded holograms. However, phase variations are commonly caused by both parameters and it is difficult to distinguish between them. Furthermore, transmissive mode is useless when dealing with opaque objects[29], so a reflective imaging mode is necessary to inspect those samples.

2.4.2. Reflective modality

In reflective mode, a light beam is directed onto the target surface and eventually returned by either specular or diffused reflection. Reflective imaging mode was previously reported in *DHM* [Iwai-2004, Kühn-2007, Warnasoo-2007, Kemper-2008A, Kemper-2008B, Kühn-2008, Remmer-2009, Shaked-2010, Yaqoob-2011, Guo-2013, Castañeda-2018] where different arrangements such as modified Michelson interferometers in Linnik arrangement [Iwai-2004, Warnasoo-2007, Kemper-2008A, Remmer-2009, Guo-2013], by external introduction of the reference beam at the recording plane [Kühn-2007, Kemper-2008B, Kühn-2008, Yaqoob-2011, Castañeda-2018] as well as in a close-to-common-path geometry [Shaked-2010] were implemented.

Reflective imaging mode was widely implemented in *DHM* for topography measurements with nanometer accuracy [Iwai-2004, Kemper-2008A, Kemper-2008B, Kühn-2008, Guo-2013, Castañeda-2018], for removing 2π ambiguities in unwrapping phase profiles by using multi-wavelength phase imaging [Kühn-2007, Kühn-2008, Warnasoo-2007], for investigation on cells [Remmer-2009, Shaked-2010, Yaqoob-2011], and for imaging of dense samples (such as histopathology/tissue slides) [Biener-2011], which are challenging for lensfree transmission imaging in general [Seo-2010].

An example of a common-path geometry working in reflection imaging modality and using a 1D diffraction grating for holographic recording is presented in Fig. 2.12. An expanded laser beam is focused and directed towards the back focal plane of a microscope objective by a first lens (L1) and a BS cube, respectively. Then, the beam passes through the objective, it is reflected or scattered by the sample (S) and goes back to the microscope lens. Finally, an image plane hologram is generated at the sensor plane with the help of a microscope lens, a second lens (L2) acting as a tube lens, and a diffraction grating (G), as in the case of the example presented in transmissive imaging modality.

[29] The number of non-transparent specimens is enormous, including most metals, ceramics, many polymers or semiconductors, among others.

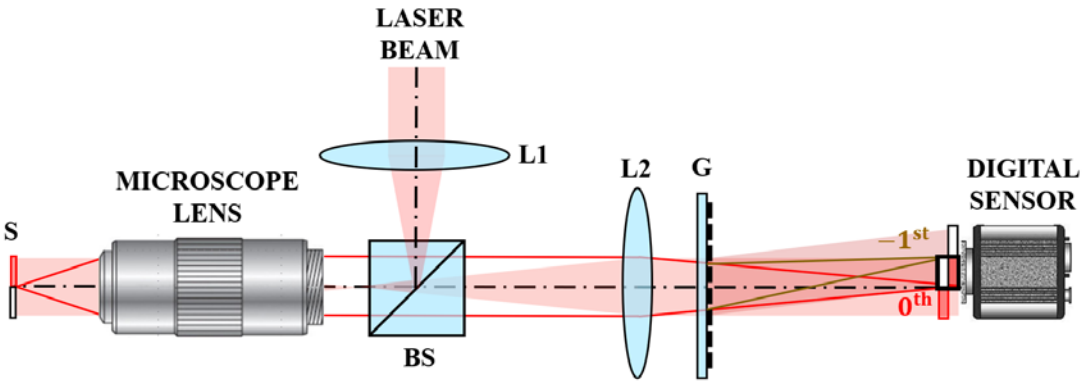

Figure 2.12. Reflective imaging mode implemented in a *DHM* setup.

In that case, the phase distribution retrieved from the digital hologram is directly related to the topography t(x,y) of the target, and can be generally calculated with the equation

$$t(x,y) = \frac{\lambda \cdot \Phi_o(x,y)}{4\pi \cdot n_m} \tag{2.36}$$

where λ is the illumination wavelength, n_M is the RI of the surrounding medium, and $\Phi_o(x,y)$ is the phase delay introduced by the geometry of the target surface. However, in the particular case of a reflective object composed of both metallic and dielectric surfaces, Eq. (2.36) becomes

$$t(x,y) = \frac{\lambda(\Phi_o(x,y)+\Phi_t-\pi)}{4\pi \cdot n_m} \tag{2.37}$$

being Φ_t the phase change introduced by the light reflection at metallic layers [Born-1999]. In Eq.(2.37), π rad factor comes from the light reflection at dielectric interfaces.

2.4.3. Transflective modality

Reflective imaging mode can be implemented in a single imaging modality or combined with transmission mode in *DHM*, thus defining a transflective imaging modality [Reichelt-2005, Lin-2010, Lim-2011, Faridian-2014, Zheng-2017A, Zheng-2017B]. A transflective *DHM* setup can be performed as in Fig. 2.13. In that scheme, both the imaging and interferometric parts are analogous to the previously presented in Figs. 2.11 and 2.12. Nonetheless, in this case, two laser beams illuminate the sample, one of them in a transmissive way (laser beam 1), whereas the other (laser beam 2) is reflected onto its surface, defining a reflective mode. Finally, two image plane digital holograms are recorded by the digital sensor.

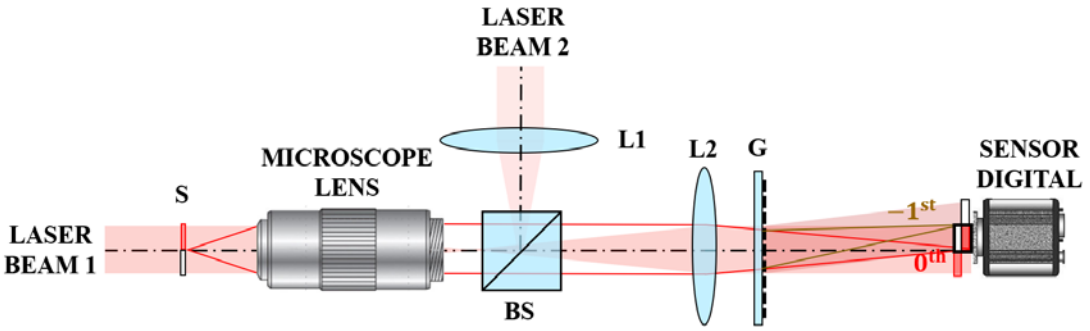

Figure 2.13. Transflective imaging mode implemented in a *DHM* setup.

A transflective imaging mode using both a Twyman-Green (reflective mode) and a Mach-Zehnder (transmission mode) interferometers was generated for microlenses testing [Reichelt-2005]. In addition, plasmonic light beaming was probed by using transflective *DHM* [Lim-2011]. Furthermore, dark-field transflective imaging mode was proposed to improve the contrast of internal structures and the signal-to-noise ratio (SNR) [Faridian-2014]. Moreover, both autofocusing and FOV extension capabilities were also demonstrated by means of transflective *DHM* [Zheng-2017A]. Finally, a transflective mode was applied for RI measurements [Lin-2010, Zheng-2017B].

The RI of biological samples gives fundamental information about its organizational structure and composition [Curl-2005]. Different strategies to measure the RI of biosamples were reported in *DHM* [Curl-2005, Rappaz-2005, Charrière-2006, Kemper-2006, Kemper-2007, Rappaz-2008, Zheng-2017B], such as digital holographic tomography [Charrière-2006]. There, an illumination beam in an angular range of [0,180º] was used to scan a pollen cell. In addition, *QPI* of living cells was applied to separately measure both the integral RI and cellular thickness by means of an experimental protocol named “decoupling procedure” [Rappaz-2005]. Another strategy involved a comparison of the cell RI with the RI of an air bubble by sandwiching them between two cover slips and assuming the same thickness [Kemper-2006, Kemper-2007]. Furthermore, cell thickness and phase difference were separately measured combining confocal microscopy with transport-of-intensity-based phase retrieval [Curl-2005]. Moreover, the RI of cells was achieved by means of the dispersion of the surrounding medium using a dual-wavelength approach [Rappaz-2008]. Finally, a transflective imaging mode was also used to analyse the RI of cells, after considering a spheroidal model with constant cross-sectional aspect ratio derived from confocal microscopy measurements for the cells [Zheng-2017B].

Transflective modality enables itself the determination of the RI of certain homogeneous objects. Such a mode provides both transmission and reflection phase distributions, so that it is possible to combine Eqs. (2.35) and (2.36) in order to calculate the RI of some homogeneous objects as follows

$$n_o = \frac{2\,\Phi_{oT}(x,y)\,n_m}{\Phi_{oR}(x,y)} + n_m \tag{2.38}$$

being $\Phi_{oT}(x,y)$ and $\Phi_{oR}(x,y)$ the phase distributions of the light transmitted and reflected by the object, respectively. In case of using different wavelengths for transmissive and reflective illuminations, Eq. (2.38) becomes

$$n_{oT} = \frac{2\,\lambda_T\,\Phi_{oT}(x,y)\,n_{mR}}{\lambda_R\,\Phi_{oR}(x,y)} + n_{mT} \tag{2.39}$$

where λ_T, λ_R, n_{mT} and n_{mR} are the illumination wavelengths and the RIs of the surrounding medium for transmission/reflection modes, respectively. Note that the RI is only calculated for the wavelength used in the transmissive mode, since it is the only one that passes through the object.

2.4.4. Multimodal imaging

As previously mentioned, *DHM* can obtain information about the RI and morphology of different types of samples. Such an information can be complemented with other analysis provided by diverse imaging techniques for a better understanding of certain processes that take place in samples as living cells, for instance. Since cell processes are multifaceted, multiple imaging techniques are sometimes required to obtain as many relevant biophysical parameters as possible, ideally at the same time.

To provide such a multianalysis, *DHM* layouts[30] were implemented in combination with other microscopy techniques [Picart-2015], such as *fluorescence microscopy* [Park-2006, Pavillon-2010], *Raman spectroscopy* [Kang-2011, McReynolds-2017], or conventional (incoherent) *bright field microscopy* [Langeha-2009, Rommel-2010, Bettenworth-2014], among others.

The combination of *fluorescence microscopy* with *DHM* in a multimodal approach enables the simultaneous analysis of intracellular phenomena and 3D morphology in real time [Picart-2015]. In such a way, a CPI-based interference microscope was incorporated into a conventional fluorescence microscope to compose a phase-fluorescence imaging mode used for mitotic kidney cells imaging [Park-2006]. In addition, such a multimodal technique was used for simultaneously analysis of both intracellular calcium homeostasis and cell volume regulation, quite important relationship in many cell progression including cell death processes [Pavillon-2010].

[30] In any imaging modality previously described.

Concerning multimodal *Raman spectroscopy DHM*, the approach has the capability of providing, not only the dynamic of the morphological changes of cells, but also their intracellular molecular content (lipids, DNA, proteins, etc.) at video rates [Kang-2011, McReynolds-2017]. As consequence, those two imaging techniques were joined together to investigate healthy and diseased RBCs in [Kang-2011], where *DHM* approach was used for searching malaria infection signs, whereas *Raman spectroscopy* was conducted for validation. In addition, the identification and discrimination between some immune cell populations was reached by using such a dual-mode approach [McReynolds-2017].

Conventional[31] *bright field microscopy* was mainly implemented in conjunction with *DHM* for comparison purposes [Langeha-2009, Rommel-2010, Bettenworth-2014]. In [Langeha-2009], both imaging modes were utilized for qualitative and quantitative 3D monitoring of migration of human fibrosarcoma HT-1080 tumor cells in collagen. On the other hand, Rommel *et. al.* added a *DHM* module on an inverse fluorescence microscope to study the effect of intracellular injection of glycerol in human pancreatic cells by using *DHM* for quantitative analysis and conventional microscopy as reference visualization [Rommel-2010]. Furthermore, *DHM* monitoring of epithelial wound healing was compared against white light visualization, showing the low contrast obtained in conventional images [Bettenworth-2014]. In Fig. 2.14. we can see an optical scheme of a platform which includes both imaging techniques.

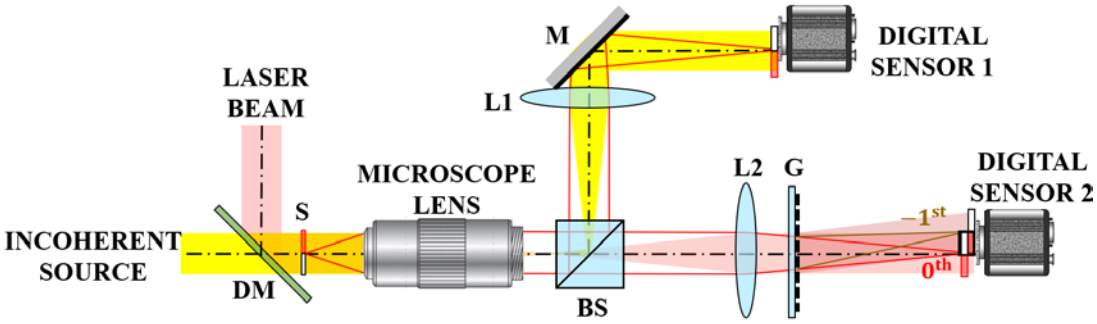

Figure 2.14. Optical system which combines *DHM* with conventional *bright field microscopy*.

[31] Incoherent or broadband light sources.

2.5. Improvements in digital holographic microscopy

2.5.1. Partially coherent illumination

Coherent sources are typically employed for interference pattern generation in *DHM*. However, DHM arrangements with high-coherence sources are suitable to present some problems regarding coherent noise that can severely reduce both the resolution and quality of retrieved images. For that reason, low-coherence sources are becoming an alternative more and more popular in DHM layouts.

Briefly, coherence defines a phase relation between two points of a wave in time or space to allow interference. Coherence is strongly related to the ability of light to exhibit visible interference effects [Saleh-1991]. Temporal coherence is linked to the capability of interfering a wave with a delayed version of itself, whereas spatial coherence concerns to the ability of two points of a wave to keep the phase relation in space constant for all times.

Temporal coherence is quantified by the coherence time (t_C), which is defined as the temporal shift between two versions of a wave to reduce significantly the autocorrelation function. Similarly, the coherence length ($L_C = ct_C$) also quantifies temporal coherence, being L_C the distance covered by the wave during t_C. In addition, temporal coherence is inversely related to the spectral bandwidth $\Delta\nu$ of a light source which can be specified as

$$L_C = \frac{k\lambda^2}{\Delta\lambda} \tag{2.40}$$

where k = 0.66 for Gaussian spectrum [Born-1999], λ is the central wavelength and $\Delta\lambda$ is the spectral bandwidth of the light source. As we can see in Eq. (2.40), temporal coherence is directly affected by the monochromaticity of the light source. On the other hand, spatial coherence depends on other characteristics such as the light-emitting area, among others.

In *DHM*, coherent noise could be derived from a combination of speckle, coherent artefacts and multiple reflections. Speckle is a random granular pattern produced when a coherent beam is scattered by a rough surface or an inhomogeneous medium. Coherent artefacts arise from unwanted diffraction patterns originated by the presence of dust or defect in the optical elements of an optical system. And multiple reflections appear as residual fringe patterns coming from the interference of back reflections produced by some interfaces of the optical elements that form the optical system.

Coherent noise can be reduced by using different strategies such as image averaging [Baumbach-2006, Micó-2012, Micó-2013], digital processing capabilities [Frauel-2001, Ozcan-2007, Bianco-2013], or by using specific optical components [Moon-2009, Kubota-2010, Ouyang-2010]. Speckle, coherent artefacts, and multiple reflections are directly related to the temporal coherence of the light source. Thus, another way to reduce coherent noise resides in the use of light sources with temporally reduced coherence. In line with that, partially coherent sources are frequently used in *DHM* [Dubois-1999, Dubois-2004, Dubois-2006C, Kemper-2008B, Remmer-2009, Kolman-2010, Dubois-2012, Slabý-2013].

Superluminescent diodes (SLDs) are partially coherent sources which provide interesting capabilities to *DHM*. SLDs combine the advantages of both laser diode (LD) and light-emitting diode (LED) sources. On one hand, SLDs provide a high degree of spatial coherence, since they are similar in geometry to LDs, but without optical feedback mechanism for laser light emission. On the other hand, SLDs yield a broadband spectrum as LEDs, which produce low temporal coherence illumination. As a result, SLDs provide partially coherent (temporally incoherent) quasi-point illumination that reduces coherent noise while allow interference according to its coherent length.

However, the use of SLDs might derive in other issues related to their coherence lengths. The main drawback of using SLDs is the prevention of *off-axis* recording, since the optical path mismatch between interferometric beams in a CPI is higher than the coherence length in most cases. Consequently, it is necessary to adopt either *on-axis* or *slightly off-axis* holographic configurations where the optical paths of the imaging and reference beams are fine matched each other.

2.5.2. Superresolution techniques

Another feature of DHM images that can be improved is the spatial resolution. Since Ernst Abbe realised that the resolution of an optical imaging system is limited by diffraction [Abbe-1873], there have been developed many techniques to go beyond that limit. The resolution of an optical system is defined as the minimal separation distance of fine details in the input object that can still be resolved in the output image. According to Rayleigh's criterion, two close point sources are well-resolved by an optical system when their images are separated by a distance greater than or equal to the distance between the central maximum and the first minimum in the intensity point-spread function (PSF) of such a system. The Rayleigh resolution distance can be expressed as

$$\rho = k\frac{\lambda}{NA} \tag{2.41}$$

where λ is the illumination wavelength, NA is the numerical aperture of the imaging, system composed of NA_{ilum} + NA_{lens}, and k = 0.82 for the case of coherent imaging systems having circular apertures [Born-1999, Cotte-2010]. The resolving power of an imaging system is defined as the inverse of the Rayleigh resolution distance.

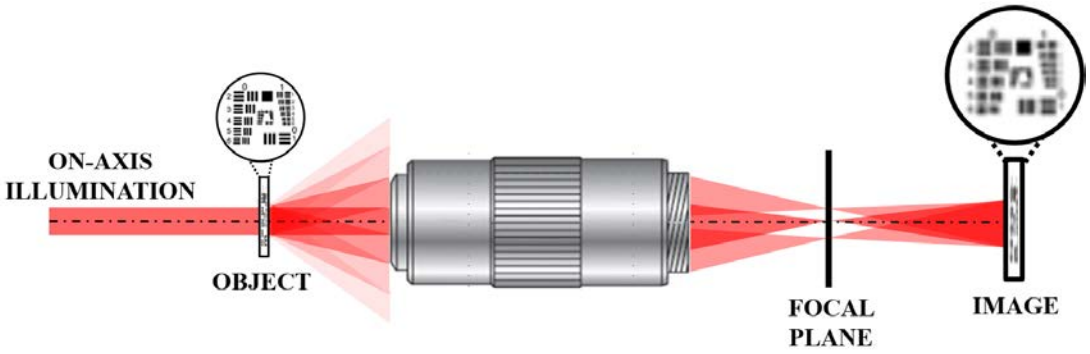

Figure 2.15. Imaging through an optical system according to Abbe's theory.

In concordance with Abbe's theory, filter theory applied to the spatial-frequency domain suggests that an optical imaging system acts as a low bandpass filter [see Fig. 2.15] that selects the spatial-frequency range of the final image [Goodman-2005]. Thus, the imaging system can be represented in the spatial-frequency domain as a limited aperture that blocks part of the object spectrum, limiting the resolution. The resolution of the system will depend on how wide its aperture is. Such an aperture is demarcated by a cutoff frequency which is defined as

$$f_C = \frac{NA}{n\lambda} \tag{2.42}$$

where n is the RI of the medium between the object and the imaging lens.

According to Eqs. (2.41) and (2.42), and aside of replacing the RI medium at the object space, it is possible to increase the resolution by either decreasing the illumination wavelength or increasing the NA of the imaging system. In cases where the illumination wavelength is fixed, a NA increment will be directly related to a resolution gain. However, high NA lenses are costly and not always practical, since they present working distances of few hundred microns and highly-reduced FOVs. On the other hand, low NA lenses present longer working distances, larger FOVs, larger DOF and low cost in comparison with high NA lenses, but they define lower resolution limits.

There are many times in which a resolution gain is required, but it is not possible neither to change the illumination wavelength nor to increase the NA optical system without changing the physical properties of the imaging system. In those cases, it is necessary to use other techniques. Those techniques of improving the resolution are named *SR* techniques. Such *SR* techniques are based on the generation of a

synthetic aperture (SA) higher than the aperture defined by diffraction in an optical system and are commonly called as *synthetic aperture superresolution* (*SA SR*) techniques. Such techniques are very appealing in fields like microscopy, astronomy, optical data storage or holography, among others.

SA SR techniques are based on a certain *a priori* knowledge about the object. For example, wavelength [Kartashev-1960, Armitage-1965], polarization [Gartner-1963, Zlotnik-2005, Micó-2007], or time [Françon-1952, Lukosz-1966, Micó-2008] invariances were three properties of the objects utilized in *SR* techniques. All those properties are included in an invariance theorem provided by the information capacity theory [Toraldo-1955, Toraldo-1969, Lukosz-1967]. That theorem states that is the information capacity[32] what remains constant in an optical system and gives the number of degrees of freedom on such systems. Thus, the spatial bandwidth can be extended by encoding and decoding additional information employing other unused parameters of the system. For instance, the spatial bandwidth of temporally restricted objects can be broadened by time multiplexing, since the complex amplitude of such objects does not change in time[33]. Time multiplexing means that different spatial-frequency slots of the object spectrum pass through the limited aperture of the imaging system sequentially in time. The object must be therefore static at least when the time multiplexing process is being implemented.

SA SR techniques are carried out by performing at least two steps. First, an encoding stage is required to transmit through the aperture of the imaging system the higher spatial-frequency content of the object spectrum. Then, a decoding stage allows us to retrieve and replace such a frequency content to its original position in the spectrum, thus generating the SA and achieving the final SR image. Sometimes, a final digital post-processing stage might be required for proper relocation of such a content.

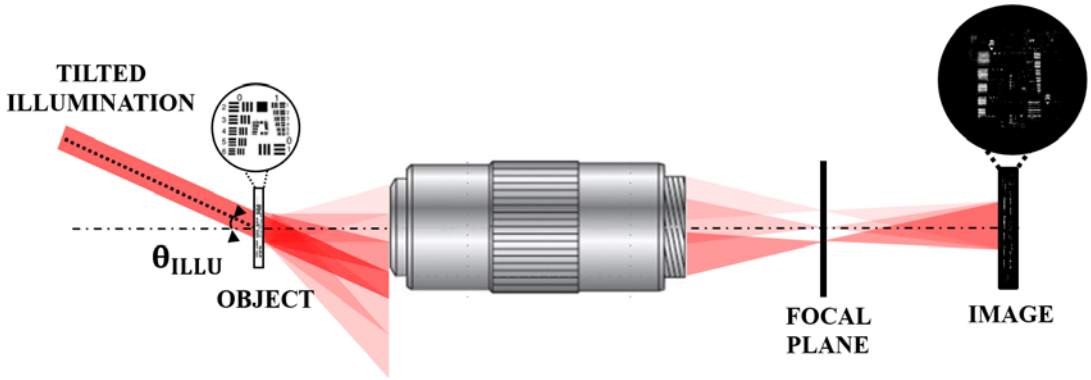

Figure 2.16. Imaging through an optical system under tilted illumination.

[32] And not the spatial bandwidth.
[33] At least during the encoding process.

During the encoding stage, the higher spatial-frequency content must be somehow downshifted to low spatial-frequency ones by encoding it into the temporal dimension. One way of obtaining such a frequential downshift is by using titled beam illumination [see Fig. 2.16]. By employing different tilted beams, that is, by angular multiplexing, it is possible to transmit the frequency components that initially were diffracted out and blocked by the limited aperture of the imaging system. Off-axis illumination makes that spatial frequency bands, which are normally diffracted at high angles under conventional on-axis illumination, thus falling outside the limited aperture of the imaging system, will be diffracted at lower ones thus passing through the optical system aperture. The time multiplexing encoding stage will be therefore defined by the number of illumination beams, not only on-axis but also off-axis, that will impinge on the temporally restricted object to transmit the extra spectral content. Typically, 2 or 4/8 tilted beams are used for generating a SA in 1D or 2D, respectively, depending on the *a priori* available object information and the overlapping of the additional apertures in the spatial-frequency domain. The illumination angle (θ) of each tilted beam will define the transmitted frequency bandpass.

After passing through the limited imaging lens aperture, the additional info must be rearranged to its original position at the object spectrum. That is, off-axis illumination downshifts those frequencies diffracted at high angles and they must be properly replaced at their original diffraction angle to get the SR image. A widely used approach to retrieve complex amplitude information of each tilted beam is by using holographic methods [Ueda-1973]. Nowadays, the decoding stage starts with a holographic recording in the digital domain and then each retrieved additional aperture is shifted to the correct spectral position by using a digital post-processing stage. Finally, all of them are coherently superimposed to synthesize the SA and FT^{-1} provides the final superresolved image.

An example of the application of *SA SR* techniques to DHM layouts was included in [Micó-2008]. There, SR imaging of static 3D objects[34] was achieved by angular multiplexing as illumination strategy and time multiplexing to retrieve information from different spatial-frequency content. A S-M CPI based on a diffraction grating[35] was implemented for an *on-axis* holographic recording, and a vertical-cavity surface-emitting-laser (VCSEL) array was employed to provide the tilted beam illuminations. In addition, another 1D diffraction grating was located at the clear region of the input plane to redirect the reference beam towards the system aperture. Then, a temporal P-S algorithm was applied for frequency bandpass retrieval, and the SA was generated after reallocating and adding each spatial-frequency content.

[34] Fixed human RBCs.
[35] Placed at the Fourier plane and placed onto a linear translation stage for linear movement.

Chapter 3

Scientific research

In this chapter, all experimental arrangements implemented and validated during this thesis are overviewed [Picazo-Bueno-2016, Picazo-Bueno-2017, Picazo-Bueno-2018A, Picazo-Bueno-2018B, Picazo-Bueno-2019A, Picazo-Bueno-2019B, Trusiak-2019]. In order to provide a solid guiding structure where the different sections are deduced one from the previous ones, the scientific contributions included in this thesis are not presented in chronological order of publication. Thus, as a first approach to *DHM*, a multimodal imaging platform combining *QP-DHM* with broadband illumination is first presented [Picazo-Bueno-2018A]. Then, a *QP-DHM* technique named *spatially multiplexed interferometric microscopy* (*SMIM*), which is employed to convert a conventional bright field microscope into a holographic one, is explained in detail. After that, a set of different SMIM approaches using a diffraction grating as interferometric component is included [Picazo-Bueno-2016, Picazo-Bueno-2017, Picazo-Bueno-2018B, Picazo-Bueno-2019A, Trusiak-2019], in which: 1) a partially coherent source is introduced and an optimized FOV is presented [Picazo-Bueno-2016]; 2) a *SA SR* technique is applied [Picazo-Bueno-2017]; 3) a HHT method is used for phase retrieval [Picazo-Bueno-2018B]; and 4) reflective and transflective modalities are implemented [Picazo-Bueno-2019A]. Finally, two SMIM arrangements employing a BS cube to produce interferences are also included [Picazo-Bueno-2019B, Trusiak-2019].

3.1. Single-shot, dual-mode, water-immersion microscopy platform for biological applications

The aim of this preliminary experiment is to provide us a better understanding of QP-DHM layouts and their capabilities. A multimodal imaging approach combining *QP-DHM* with broadband (white light) illumination imaging is implemented [Picazo-Bueno-2018A]. The approach is based on a lab-built platform operating under a single-shot and water-immersion working principle. The system allows simultaneously real-time conventional incoherent visualization as well as *QPI* at a diffraction-limited resolution level. In that case, the incoherent mode is used not only for general imaging purposes, such as selecting the interesting FOV and layout optimization, but also for coherent illumination alignment. On the other hand, the DHM arrangement enables quantitative optical thickness analysis at video rate without damaging the cell physiology due to the selected wavelength and the *off-axis* holographic configuration.

3.1.1. Layout description

The experimental layout uses an incoherent white light source (high-power plasma light source HPLS343, Thorlabs, USA) and a coherent infrared CWA laser (780 nm, 120 mW maximum optical power, 10 mW estimated used optical power, 10 cm coherence length, Omicron-Laser) for sample illumination, whose optical paths are merged by a first dichroic mirror (DM1) just before the sample (S) and separated by a second one (DM2) behind the tube lens. Both illumination beams pass through an imaging system composed of a water-immersion microscope lens (100X, 1.0 NA, Olympus, 1mm WD, 1.8 mm focal length) and a tube lens (200 mm focal length), which provides a global magnification of M ≈ 110, according to the ratio of the focal lengths. After DM2, and in absence of the interferometric part, both the incoherent and coherent images (see images enclosed in yellow and red rectangles, respectively, included in Fig. 3.1) are recorded by two digital sensors (CCD1 and CCD2) placed at the back focal plane of the tube lens. Such cameras are a Thorlabs DCC1240C (5.3 μm pixel size, 25.8 fps, 1280 x 1024 pixels), and a Fastec Imaging HiSpec 4 (8 μm pixel size, 523 fps, 1696 x 1710 pixels), which record the incoherent and coherent images, respectively. A scheme of the proposed setup without including the interferometric part is depicted in Fig. 3.1.

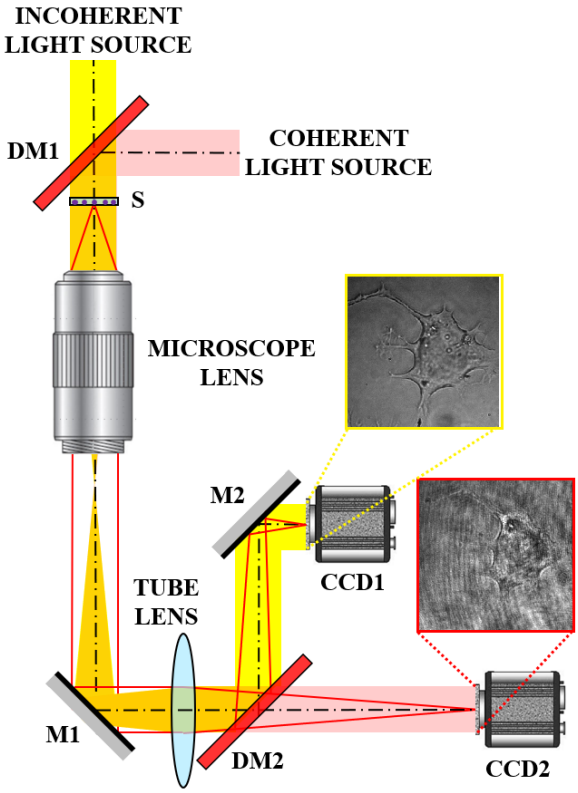

Figure 3.1. Scheme of the proposed experimental setup without considering the interferometric part. S, sample; DM1 and DM2, dichroic mirrors; M1 and M2, silvered mirrors; CCD1 and CCD2, digital cameras. Incoherent and coherent images (enclosed in the yellow and red rectangles, respectively) are produced at the back focal plane of the tube lens and recorded by two digital sensors (CCD1 and CCD2, respectively).

Then, just behind DM2, a lab-built interferometric architecture based on a R-G CPI architecture is assembled. As a result, the sensitivity to vibrations and/or thermal changes become reduced since the reference beam is generated from the imaging beam, after passing through the imaging system. In the interferometric part [see Fig. 3.2], a BS cube (BS1) divides the imaging beam into two beams. One of them is used for reference beam synthesis by using a focussing lens (L1) and a spatial filter (SP). The spatial filter (SP) is properly selected (a pinhole with 10 μm diameter) and placed at the Fourier plane of L1 to block the high-frequency components of the image and to transmit only the DC term, thus generating a clear reference beam from the imaging beam. By contrast, the other beam crosses another lens (L3), identical to L1, to make equal the beam divergences. Then, both beams are combined by using another BS cube (BS2), and a final lens (L2) introduces the same divergence in both beams as leaving the tube lens. Additional silvered mirrors (M1, and M2) complete the interferometric architecture guiding the light path along proper directions. Since CCD2 is placed at the back focal plane of the tube lens, image plane holograms are recorded (see image enclosed in the red rectangle included in Fig. 3.2). Finally, an *off-axis* holographic configuration is achieved by tilting M1 to introduce a large enough relative angle θ between both interferometric beams at sensor plane.

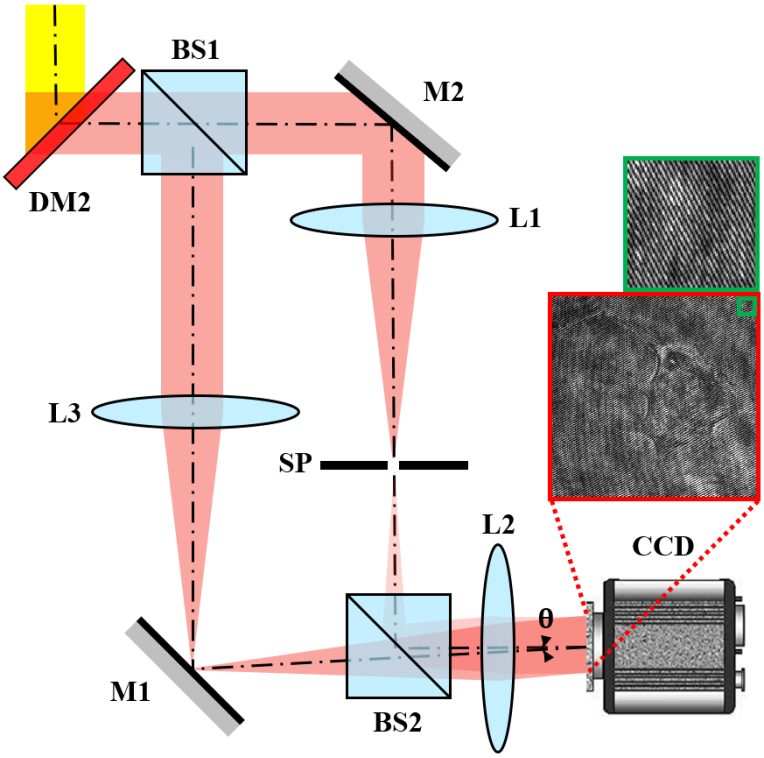

Figure 3.2. Interferometric layout implemented behind the second dichroic mirror (DM2) in [Picazo-Bueno-2018A]. BS1 and BS2, BS cubes; M1 and M2, silvered mirrors; L1, L2 and L3, converging lens; SP, spatial filter. A digital hologram of a NG108 neuroblastoma cell is enclosed in a red rectangle.

3.1.2. Experimental results

Experimental validation is composed of two parts: 1) a calibration stage of the QP-DHM layout, and 2) a validation of the dual-mode platform using both imaging modes. In all cases, off-axis image holograms are recorded, and Fourier filtering methods are used to retrieve the complex amplitude of the imaging beam.

Calibration procedure involves different types of microbeads (45 μm, 3 μm, and conical) as well as a simulated movement of a biosample. The microspheres are made of a single material (silica or polystyrene) and have a well-known RI at the near-infrared (780 nm). As consequence, once the phase distribution is retrieved, the thickness can be straightforward calculated from Eq. (2.35). After that, such a thickness is compared with the theoretical value provided by the manufacturer to quantitatively validate the DHM platform.

One of the experiments performed for calibration involves a 45 μm silica sphere deposited in aqueous suspension. The experimental results are shown in Fig. 3.3, where (a) is the recorded hologram, (b) the FT of (a), (c) the FT after applying Fourier filtering, (d) the filtered FT after correcting the linear phase, (e) and (f) the retrieved amplitude and phase (wrapped) after applying FT^{-1} to (d), (g) the unwrapped

phase map coming from (f), and (h) a perspective view of the thickness distribution computed according to Eq. (2.35). Such a thickness distribution is calculated assuming that the RIs of silica and water are n_{sample} = 1.454 and n_{medium} = 1.333 at 780 nm, respectively. As we can see in Fig. 3.3 (h), the maximum thickness value experimentally obtained is between 44 and 49 μm, showing a high concordance with the theorical value provided by the manufacturer for the microbead diameter. As consequence, the QP-DHM platform becomes validated in a quantitative way.

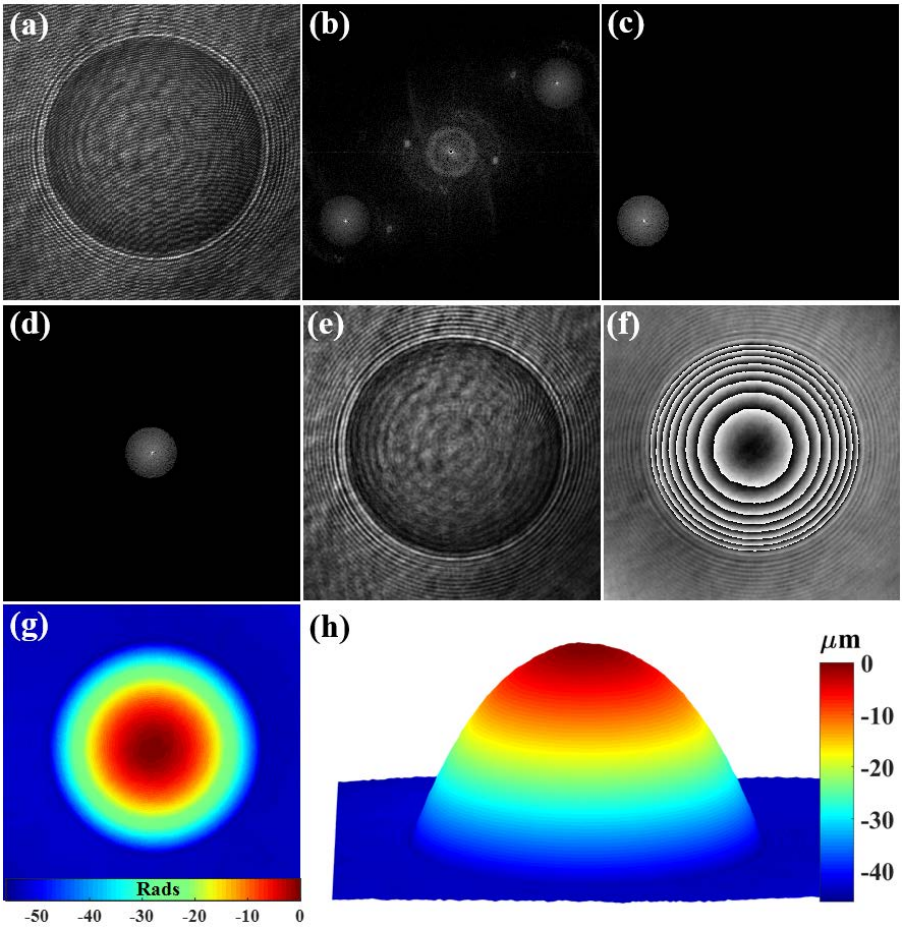

Figure 3.3. Experimental results involving a 45 μm microbead employing the QP-DHM platform: (a) the recorded hologram; (b) its FT; (c) the Fourier filtering application to (b); (d) the result of multiplying (c) by a linear phase factor; (e) the retrieved amplitude after applying FT^{-1} to (d); (f) the retrieved phase (wrapped) distribution after applying Fourier filtering method; (g) the unwrapped phase distribution coming from (f); (h) a perspective view of thickness distribution calculated from Eq. (2.35).

Another calibration experiment is conducted to demonstrate single-shot capability of the DHM layout by simulating a dynamic biological process. The experiment involves a sample consisting of fixed and prepared hippocampal neuron cells, which are in continuous movement induced by a piezo-mirror. Such a piezo-mirror continuously shifts the coverslip during the whole recording time (10 s). In Fig.

3.4, the digital holograms recorded in two-time lapses (t = 0 s, and t = 10 s) [see Fig. 3.4 (a1) and (b1)], the wrapped phase distributions retrieved after Fourier filtering [see Fig. 3.4 (a2) and (b2)], and the perspective views of unwrapped phase distributions [see Fig. 3.4 (a3) and (b3)] are included.

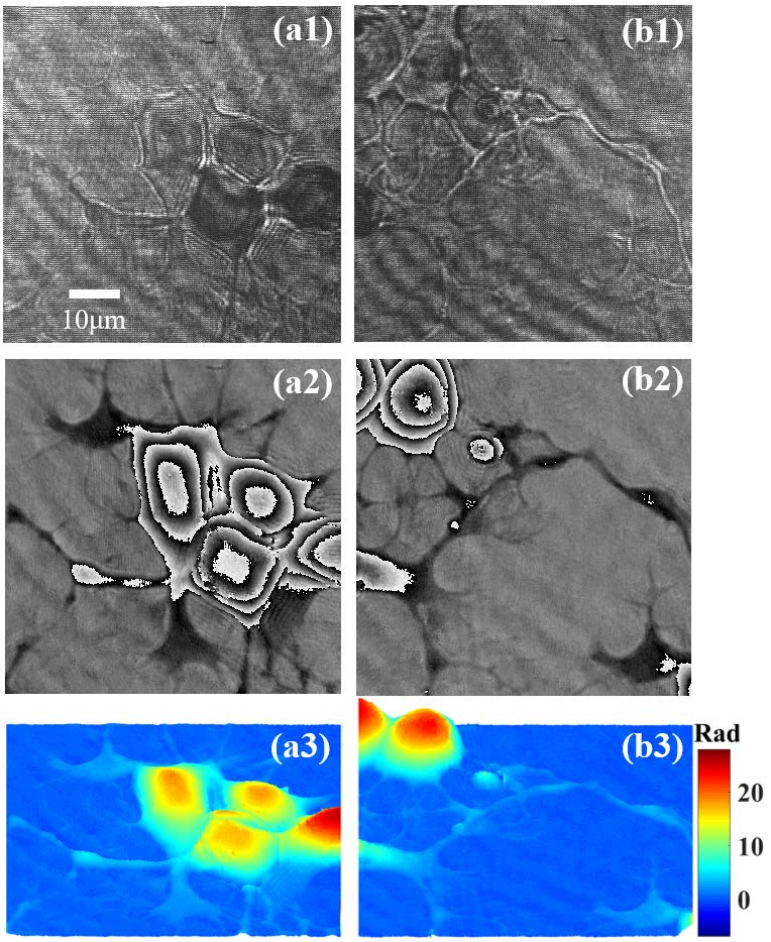

Figure 3.4. Experimental results involving a simulated dynamic process employing fixed hippocampal neuron cells, where columns (a) and (b) include the results for the time lapses of t = 0 s and t = 10 s, respectively. Recorded digital holograms are presented in row (1); row (2) depicts the wrapped phase distributions retrieved after Fourier filtering; and row (3) shows the perspective views of unwrapped phase distributions.

After the calibration process, validation of the multimodal approach is performed by using a wide variety of static biosamples including NG108 neuroblastoma cells, breast cancer cells, and hippocampal neuron cells. Figure 3.5 presents the results for NG108 neuroblastoma cells, where (a) shows a bright field image provided by white light illumination, (b) includes a digital hologram produced by DHM layout, (c) and (d) qualitative *ZPC* and *DIC* visualizations generated from retrieved complex amplitude distribution, and (e) perspective view of unwrapped quantitative phase image supplied by *DHM*.

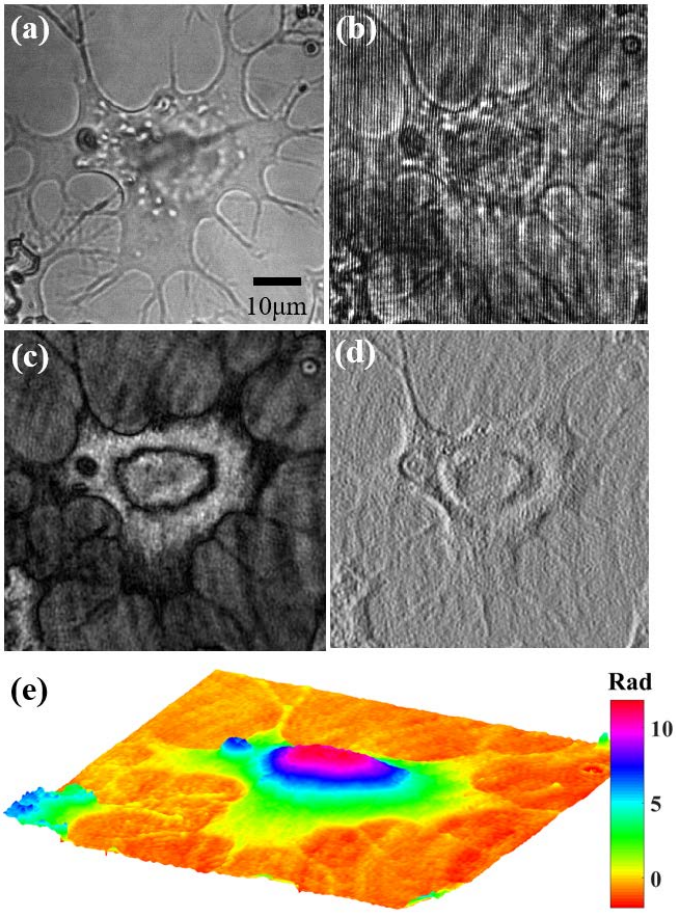

Figure 3.5. Experimental validation of multimodal layout for fixed NG108 neuroblastoma cells: (a) intensity image provided by incoherent illumination; (b) digital hologram recorded with QP-DHM platform; (c) ZPC visualization; (d) DIC imaging mode; and (e) perspective view of unwrapped quantitative phase distribution provided by *QP-DHM*.

Finally, the capability of single-shot operation principle of such a dual-mode imaging system is demonstrated by analyzing the movement of a live hippocampal neuron cell. Figure 3.6 includes two frames (first and last) of the whole video movie (total recording time 100 s) including both intensity images provided by incoherent illumination [column (a)] and quantitative phase images provided by DHM platform [column (b)]. Since it is difficult to appreciate the cell movement due to its slowness, the averaged intensity and phase distributions are plotted [see Figs. 3.6 (a3) and (b3)]. The profiles for all images are calculated along the white solid lines [see Figs. 3.6 (a1)-(b2)]. The averages, which are computed along the dashed green, blue and red lines included in Figs. 3.6 (a1)-(b2), are performed since the profile along just one section is dominated by noise. As we can see in Figs. 3.6 (a3) and (b3), there exists a cell contraction movement generated by a slight displacement of the right cell's wall during the recording time. Such a shift is about 0.75 μm, so that the neuron cell contraction presents an average speed of 7.5 nm/s during the observation time.

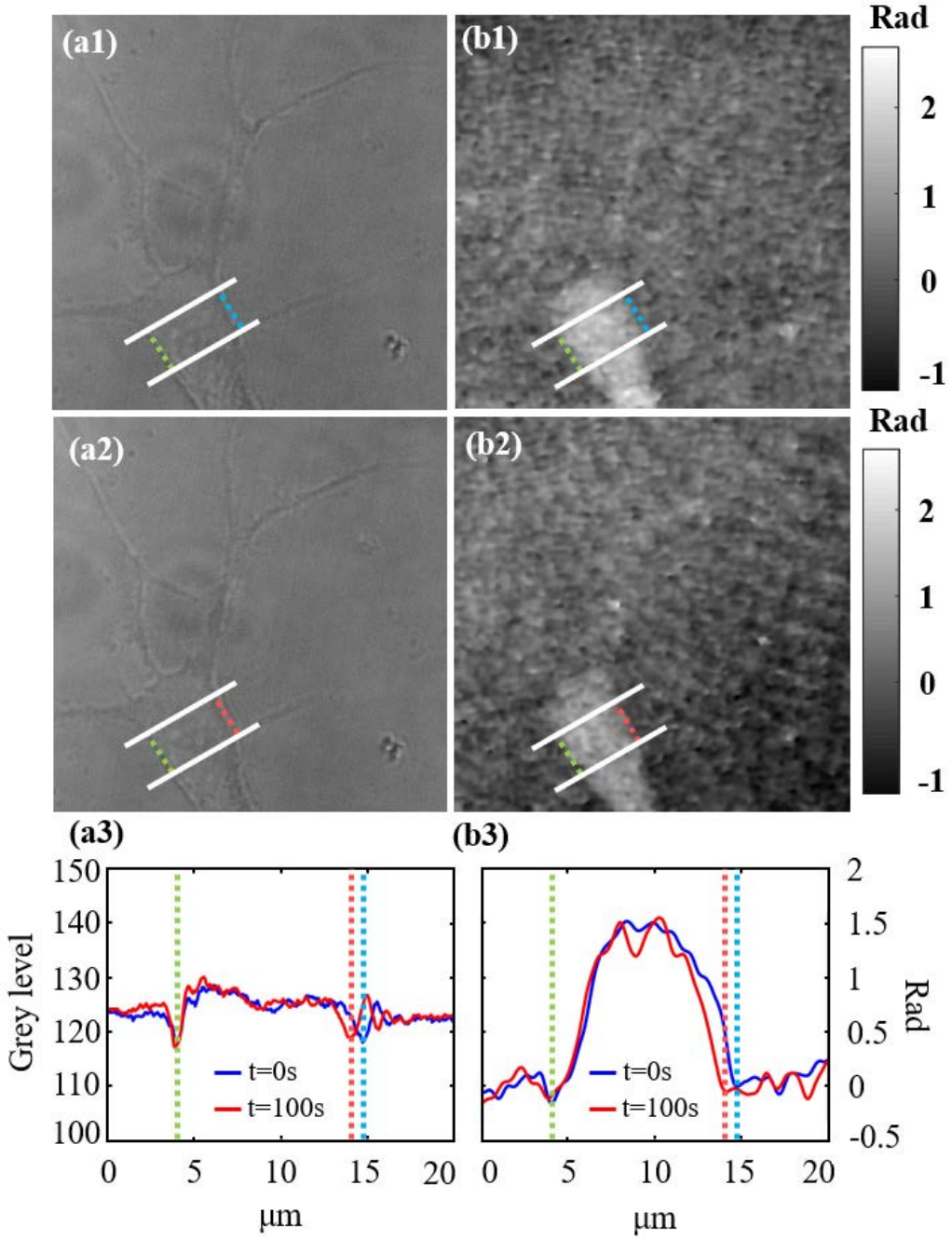

Figure 3.6. Experimental results for a dynamic process involving a living hippocampal neuron cell. Rows (1) and (2) present the results for t = 0 s and t = 100 s, respectively. In column (a) the intensity images from incoherent illumination are depicted, and column (b) shows the quantitative phase distributions provided by DHM mode. Finally, row (3) includes the intensity (a) and phase (a) plots of the averaged profiles along the white solid lines included in (a1)-(b2). Green, blue and red dashed lines mark the left and right walls of the cell, respectively.

3.2. Spatially multiplexed interferometric microscopy

The previous dual-mode imaging platform including a *DHM* layout has served to reach a better understanding of the optical processes and phase retrieval procedures involved in *QP-DHM*. From now until the end of the dissertation, we will be focus on a *QP-DHM* technique developed during the present thesis. Such a technique, named *spatially multiplexed interferometric microscopy* (SMIM), has the main goal of turning a standard bright field microscope into a holographic one.

The cornerstone of *SMIM* is to introduce minimal modifications on a conventional microscope to supply it with the capability of *QPI*. In the *SMIM* case, *QPI* is achieved by assembling a *DHM* layout in the embodiment of such a microscope. Such a layout employs a CPI architecture to provide digital holograms. According to the classification of CPIs done in Section 2.4.2, *SMIM* utilizes a S-M approach for reference beam generation.

The concept of *SMIM* was previously validated as demonstrator at the lab by Micó *et al.* [Micó-2006B, Micó-2008, Micó-2009]. In those contributions, the authors pursued a resolution enhancement by generating a SA using a time multiplexing strategy. For instance, a resolution gain factor of 2.5 was achieved for the case of an USAF resolution test target in [Micó-2006B]. There, a VCSEL source array was employed to sequentially provide both on-axis and off-axis illuminations, and the input plane was divided into two regions including: 1) the sample, and 2) a 2D holographic grating to redirect off-axis illuminations towards on-axis direction. In order to reach interferometric recording, a 1D diffraction grating was introduced behind the microscope lens.

After a few years, Micó *et al.* implemented such a concept in a regular microscope, giving rise to *SMIM* technique itself [Micó-2014]. There, a conventional microscope was equipped with holographic capabilities by introducing three minimal changes: 1) the replacement of incoherent illumination by a coherent light source, 2) the definition of a spatially multiplexed input plane, which was split into three regions (object, reference, and blocking), for reference beam transmission, and 3) the introduction of a 1D diffraction grating behind the microscope lens for interferometric recording. However, the main drawback of that approach was the division into three areas of the input plane, leaving just one third of whole FOV available for containing the sample. Nevertheless, *SMIM* can additionally admit other less restrictive input plane spatial distributions as the partition of the input plane into two regions, object and reference, thus avoiding the blocking region. The optical configuration required for such a configuration is slightly different to the proposed in [Micó-2014]. For that reason, a detailed explanation not only qualitative but also mathematical of SMIM architecture with an input plane division into two regions is given in this section, while experimental validations are overviewed in the subsequent sections.

3.2.1. Qualitative description

SMIM is carried out by simply introducing minimal modifications on a conventional microscope. Thus, the microscope can be transformed into a holographic one by means of three non-complex changes in its configuration. First of all, let consider a standard bright field microscope composed of: an incoherent light source (halogen lamp), a XYZ translation stage (where samples are placed and manipulated), an infinity-corrected objective lens, a tube lens system, and a CCD digital sensor. It is also worth considering two planes, the planes where: 1) samples are located, and 2) images are produced by the microscope. Those planes are conjugated planes and are denoted as input and output planes, respectively. Figure 3.7 includes both optical system and ray tracing schemes of such a microscope working under transmission imaging mode. Note that the eyepieces are not considered here since the images employed for *QPI* are digitally recorded.

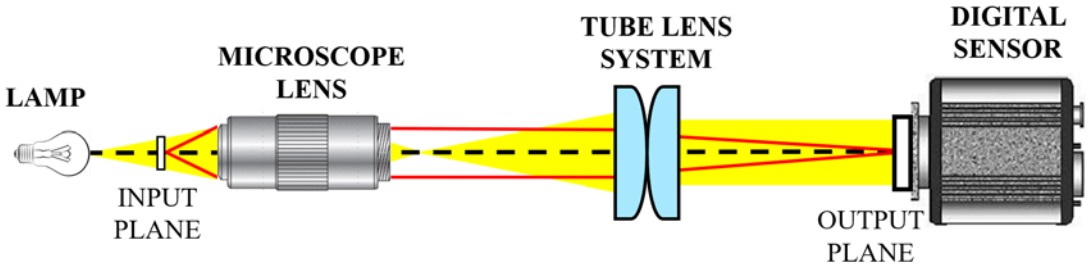

Figure 3.7. Optical system and ray tracing scheme of a conventional bright field optical microscope, where the main planes and components are clearly indicated.

The microscope depicted in Fig. 3.7 provides incoherent intensity images of samples, so no information about complex amplitude phase distribution can be extracted from them. Nevertheless, through the design of an interferometric architecture, it is possible the recording and reconstruction of digital holograms. For that purpose, three minimal modifications are required over the scheme included in Fig. 3.7. The first modification consists in the replacement of the broadband illumination by a light source with enough coherence to produce interferences.

The second change is related to the reference beam transmission. The input plane must be divided into, at least, two regions. One of them contains the sample, whereas the other one must be a clear region, i.e., without any kind of object information. Thus, the reference beam is generated by means of a S-M CPI architecture. Such a spatial multiplexing can be achieved by using a specially designed chamber or by using samples with large clear areas next to them. Let us call O the region that includes the sample, and R the clear region. As we can see in Fig. 3.8, both O and R areas are presented in a side-by-side configuration. Such an input plane is magnified and imaged by the imaging system, thus defining a spatially multiplexed output plane, formed by the images of both O and R regions, denoted as O’ and R’,

respectively. Then, by properly selecting of both magnification and CCD dimensions, both regions can easily cover the whole sensitive area of the CCD. At that point, the modified microscope will behave as a regular microscope working under coherent illumination with a reduction of 2 in the useful FOV due to the spatial multiplexing.

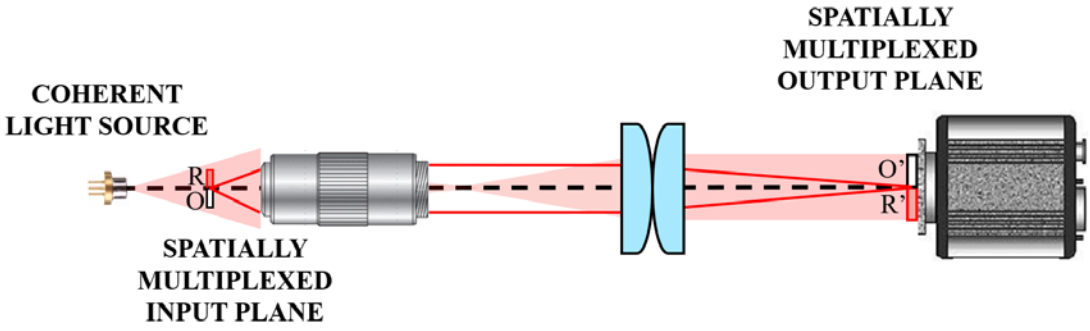

Figure 3.8. Optical scheme of the microscope after light source replacement and FOV multiplexing by *SMIM*, but before inserting the diffraction grating.

Finally, a third and final modification is required to produce interferometric recording between the light passing through both regions. Since both object and reference beams travel in parallel and side-by-side through the imaging system, they are not suitable to produce interference patterns, unless any optical element is additionally introduced. Such a component must either change the propagation direction of those beams or generate several replicas of the beams travelling in different directions. For such purposes, there exist several optical components, such as diffraction gratings, BS cubes, or Fresnel biprism, among others. Both diffraction gratings and BS cubes provide several replicas of a beam when going through them, whereas a Fresnel biprism deflects both beams from their original paths. Since most of the experiments developed in the present thesis are performed using a diffraction grating, we will now describe in detail such a scenario. In the following, we will assume a 1D sinusoidal diffraction grating, just to simplify the description and further calculations.

A 1D sinusoidal diffraction grating produces three diffracted beams travelling along three different directions[36], which are three replicas of an incident beam[37]. Each diffracted beam has associated a diffraction order according to the propagation angle. One of them (0^{th} diffraction order) passes through the grating without suffering any deviation in its direction, whereas the other two beams (corresponding to $\pm 1^{st}$ diffraction orders) are propagated forming a certain angle with respect to the original direction. Such an angle is directly related to the grating basic frequency and the illumination wavelength [as we will see in the mathematical analysis done in Section 3.2.2]. Hence, for a given wavelength, it is possible to select a grating whose spatial

[36] Contained in the plane perpendicular to the longer side of the diffracting structures.
[37] Leaving aside the diffraction efficiency of the grating.

frequency generates proper overlapping of the diffracted beams at the output plane. As we can notice in Fig. 3.9, such an adequate configuration is achieved when the images of the input plane are shifted half image one another at the output plane. Under that condition, the O' region of one order overlaps with the R' region of the contiguous one, thus producing the desired interference patterns. Such three diffraction orders provide two interference patterns at the output plane. One of them is produced by the coherent overlapping of the R' region incoming from -1st order with the O' region of the 0th order (recorded hologram digitally processed for further complex amplitude retrieval), whereas the other (not used) is created by the interference between both R' and O' regions of the 0th and +1st orders, respectively. Note that such R' and O' regions are not specified in Fig. 3.9, just to simplify the scheme.

For a better understanding of SMIM implementation, a real situation involving an Olympus BX60 upright compound microscope is presented in Fig. 3.9, in which the changes introduced to the microscope are highlighted. On the left, we show a picture of such a microscope after *SMIM* modifications, whose optical scheme is included on the right in the same figure.

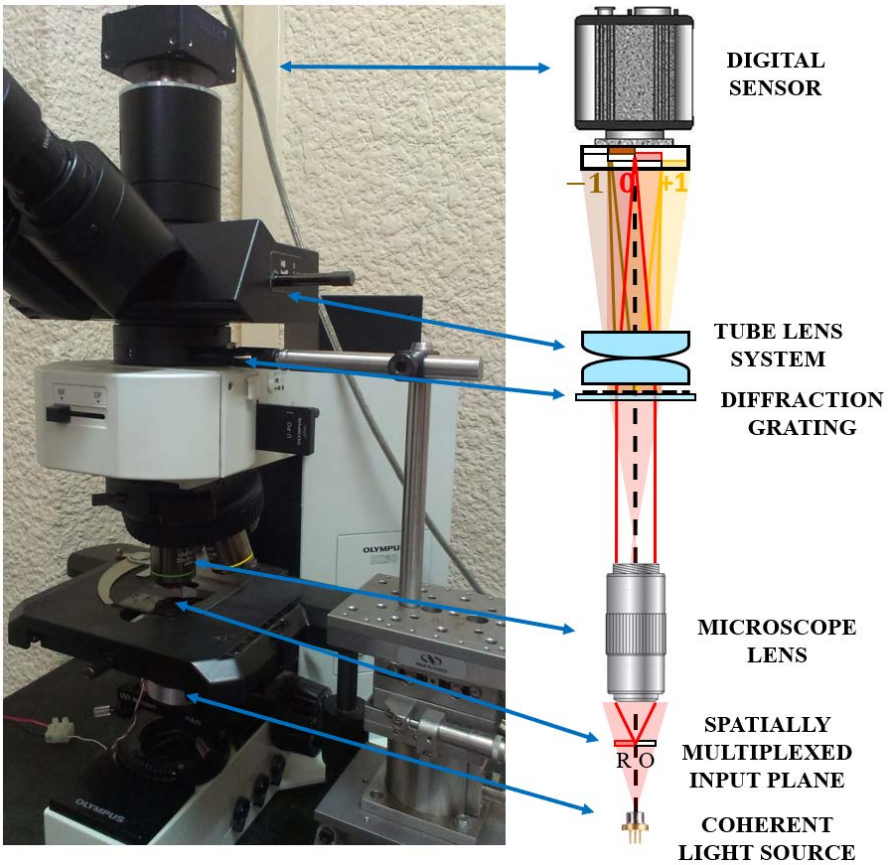

Figure 3.9. Picture of the experimental layout (left) and scheme (right) of the proposed *SMIM*, highlighting the changes introduced.

A digital sensor is placed at the output plane for holographic recording. Since just one hologram[38] is of interest for phase retrieval, the sensor can be placed in two different ways [see Fig. 3.10]. On one hand, whole sensitive area of the sensor can be used to just record the useful hologram. Nevertheless, the sensor must be laterally shifted with respect to the optical axis, since such a hologram is produced in one side of the optical axis [see Fig. 3.10(a)]. On the other hand, we can avoid such an off-axis recording configuration by placing the sensor centered with the optical axis. Indeed, the implementation of such an on-axis configuration is easier due to the exit port of any microscope is designed for such a purpose [see Fig. 3.10(b)]. However, that configuration forces to record not only the useful hologram but also the unusable by symmetry. Consequently, one half of the sensitive area is wasted, being the main drawback of the configuration. Nonetheless, that is the configuration employed in the experiments performed in the present thesis.

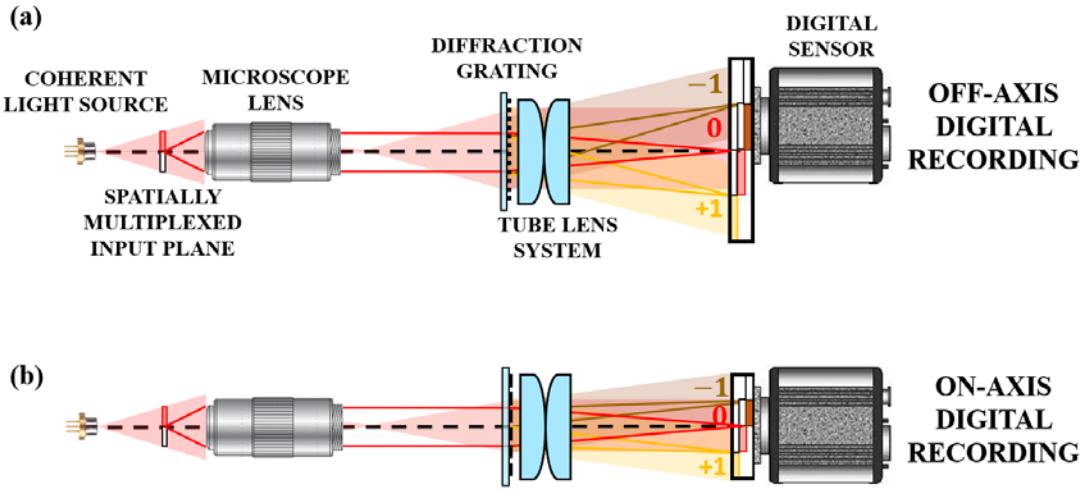

Figure 3.10. Two proposed *SMIM* configurations for holographic recording: (a) off-axis recording (only the useful interference pattern is recorded), and (b) on-axis recording (both useful and unusable interference patterns are recorded).

Another crucial aspect to take into account is the axial location of the diffraction grating. For efficient holographic recording, such a position is critical and additionally determines the grating frequency to be selected. In fact, the mismatch between both parameters can derive in a wrong (or even absent) overlapping between orders. Moreover, the axial position has a non-negligible influence when implementing a holographic configuration. Thus, two main scenarios can be described depending on the grating location [Micó-2006, Micó-2008, Micó-2009, Micó-2014]: 1) placed at or close to the Fourier plane, and 2) located far enough from it.

[38] Composed of the O' region of the 0th order and the R' region of the -1st order.

When the grating is placed at the Fourier plane, both O' (0^{th}) and R' (-1^{st}) regions travel along the same optical path with the same propagation angle. Because of the absence of a bias carrier frequency between both interferometric beams, they define an *on-axis* holographic configuration at the recording plane. In such a configuration, a low grating frequency will not produce a desired overlapping of those regions, but O' (0^{th}) region will interfere with a shifted version of itself. On the other hand, a too high frequency would diffract R' (-1^{st}) region outside the tube lens aperture, preventing the holographic recording.

On the other hand, the longer is the distance between the Fourier plane and the axial position of the grating, the larger is the bias carrier frequency that provides optimum holographic conditions. In such a way, it is possible to find an axial distance far enough from the Fourier plane to achieve *off-axis* holographic configuration. However, we must consider two parameters: first, such a distance between the grating and the Fourier plane, and second, the grating frequency. The former because the objective lens selected for imaging produces slight modifications of the Fourier plane. Nevertheless, the effects of such modifications can be negligible when the axial distance is big enough. The latter due to the grating frequency defines the shift between replicas at the output plane. Such a parameter becomes crucial since a too low frequency will produce overlapping of the hologram orders at the Fourier domain, whereas a too high frequency will derive in aliasing problems, both cases preventing an accurate retrieval of the complex amplitude.

When inserting a grating in a microscope embodiment, only few axial positions can be defined. Looking at the picture presented in Fig. 3.9, we realise that the grating can be only inserted in the analyser insertion slot of the microscope, located just before the tube lens system. The grating is therefore placed far from the Fourier plane in the experiments presented in this thesis.

3.2.2. Mathematical analysis

In this section, the grating basic frequency required for optimum holographic recording is mathematically discussed. For such a purpose, we assume that the digital sensor is located at the exit port and centered with the optical axis of the microscope [case presented in Fig. 3.10 (b)].

A SMIM layout can be represented by the scheme depicted in Fig. 3.11. Figure 3.11 includes both an optical diagram and a ray tracing schemes for the theoretical analysis of SMIM architecture. Let start the analysis assuming that a spherical wave is originated at a point source S located at a distance *a* from the objective. The input plane coincides with the front focal plane of the objective due to an infinity corrected configuration. Such an objective and the tube lens system are symbolised by two thin lenses of focal lengths f_1 and f_2, respectively. A 1D diffraction grating with a spatial

frequency of N line pairs/mm (lp/mm) is placed just before the tube lens system (assuming no distance between them). As mentioned above, the grating is regarded as a 1D sinusoidal grating, so it produces three replicas overlapping one another at the output plane. Efficient holographic recording depends on both the sensor features (pixel size and number of pixels) and the grating frequency. Ideal holographic conditions are obtained when the interference pattern produced by both O' (0^{th}) and R' (-1^{st}) regions covers exactly one half of the digital sensor. To do so, N must be selected taking into account that the propagation angle of -1^{st} order must redirect its R' region towards the O' region of the 0^{th} order, as presented in Fig. 3.11.

For the theoretical analysis, let us make some assumptions. The detector is placed at the back focal plane of the tube lens system, and its width is extended 2z, from -z to +z since it is centered with the optical axis. In the object space, both R and O regions extends a distance r. The R region is delimited by points 1 and 2, and the O region covers the distance between points 1 and 3. In addition, for the sake of simplicity but without lack of generality in the calculations, let us consider $a = -2f_1$, so that $a' = 2f_1$. Finally, anti-clockwise angles are defined as positives.

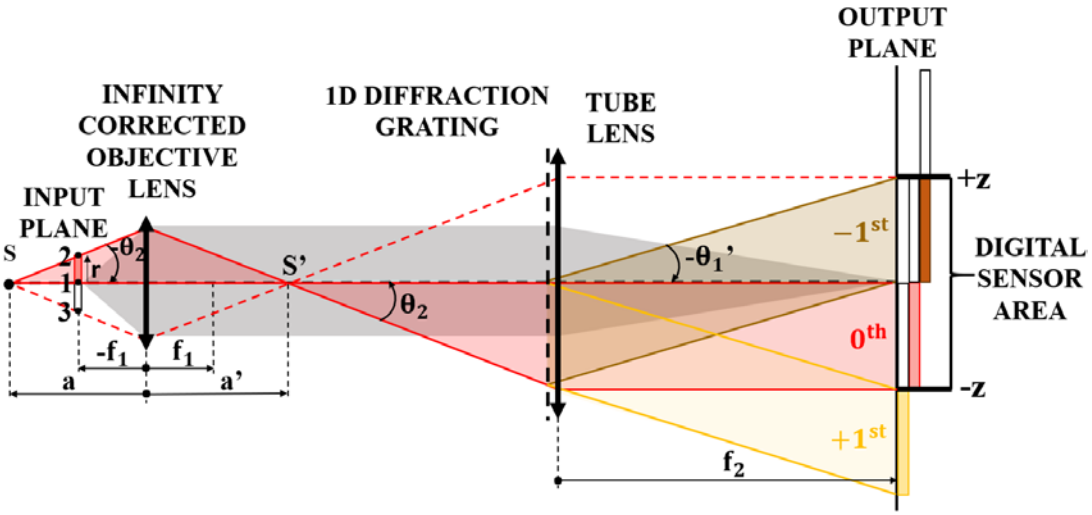

Figure 3.11. Optical diagram and ray tracing schemes for the theorical analysis of the proposed *SMIM* architecture.

First, we analyse the trajectory of a ray emerging from S and passing through the point 1, that is, a ray travelling along the optical axis. Such a ray impinges on the grating with a normal incidence ($\theta_1 = 0^0$). Behind the grating, the diffracted ray related to the -1^{st} order is diffracted forming an angle $-\theta_1'$ with respect the original direction. In addition, to ensure efficient interferometric recording, such a ray must reach the position +z at the output plane. Since the grating is assumed to be placed just before the tube lens (almost touching it), the ray deviation due to the refraction inside the tube lens can be negligible, and the distance between the grating and the output plane can be approximated by f_2. Hence, the propagation angle of the ray $-\theta_1'$ can be calculated as

$$\tan(-\theta_1') = \frac{z}{f_2} \tag{3.1}$$

On the other hand, the equation of the diffraction grating for the -1st diffraction order states that

$$\sin(-\theta_1') - \sin(\theta_1) = -N\lambda \Rightarrow \sin(-\theta_1') = -N\lambda \tag{3.2}$$

where λ is the illumination wavelength.

Finally, Eqs. (3.1) and (3.2) can be combined considering the paraxial approximation, that is, $\tan(-\theta_1') \approx \sin(-\theta_1')$ thus obtaining a mathematical expression that relates the grating frequency to the parameters of the layout

$$N = \frac{z}{\lambda f_2} \tag{3.3}$$

Second, the trajectory of a ray coming from S and passing through the point 2 is studied. Such a ray presents an angle $-\theta_2$ with the optical axis according to

$$\tan(-\theta_2) = \frac{r}{-f_1} \tag{3.4}$$

Once passed through the objective lens, the refracted ray crosses the optical axis at S' point (place where the point source is imaged by the objective lens) and arrives to the grating with the same angle θ_2. Behind the grating, we expect that the --1st order redirects the ray towards the back focal point of the tube lens or, in other words, that the ray crosses again the optical axis at the output plane. To satisfy that condition, such a ray must be diffracted in parallel ($\theta_2' = 0^o$) with the optical axis. Thus, applying the equation of the diffraction grating for the -1st diffraction order

$$\sin(\theta_2') - \sin(\theta_2) = -N\lambda \Rightarrow -\sin(\theta_2) = -N\lambda \tag{3.5}$$

Then, taking into account the paraxial approximation [$\tan(-\theta_2) \approx \sin(-\theta_2)$], we can reach an expression to calculate the width of the R (or O, by symmetry) region at the input plane depending on the system parameters

$$r = N\lambda f_1 \tag{3.6}$$

As a checking mode, we can combine Eqs. (3.3) and (3.6) to obtain a relation between the width r and the layout magnification M, achieving

$$r = z\frac{f_1}{f_2} = \frac{z}{M} \tag{3.7}$$

as could be expected.

According to the proposed symmetric scheme and considering Eq. (3.7), the largest O region that can be imaged is confined to the interval [-r, 0] at the input plane. At the output plane, the O' region incoming from the 0^{th} order term extends along the interval [0, r'=Mr]. In the case that |r'| > |z|, only the object area closer to the R region and included in the interval [0, -z/M] can be used for recording the hologram.

To conclude the mathematical analysis, we calculate the spatial frequency N_{max} of the grating above which aliasing errors begin to appear in the system. Let call d the pixel size of the digital sensor. In addition, we can assume that the digital hologram acts as a sinusoidal diffraction grating of frequency N'. In such a way, when considering a ray travelling along the optical axis that passes through such a grating, the -1^{st} order is diffracted with the angle $-\theta_1'$, so that the equation of the diffraction grating will be

$$\sin(-\theta_1') = -N'\lambda \tag{3.8}$$

We can therefore combine Eqs. (3.2) and (3.8) to relate the diffraction grating frequency N to the hologram spatial frequency N', obtaining

$$\sin(-\theta_1') = -N\lambda = -N'\lambda \Rightarrow N' = N \tag{3.9}$$

Equation (3.9) shows that both spatial frequencies are identical.

On the other hand, considering the Nyquist-Shannon sampling theorem, the condition to avoid aliasing can be expressed as

$$2d \leq \frac{1}{N'} = \frac{1}{N} \Rightarrow N \leq \frac{1}{2d} \tag{3.10}$$

Hence, the diffraction grating basic frequency N will be numerically calculated following the Eq. (3.3) and its value must never be larger than

$$N_{max} \leq \frac{1}{2d} \tag{3.11}$$

3.3. Spatially multiplexed interferometric microscopy with partially coherent illumination

In Section 3.2, we pointed that *SMIM* was initially implemented using a coherent source to illuminate the samples, and a FOV restriction of one third was applied for *QPI* [Micó-2014]. In this contribution, the capabilities of previous *SMIM* arrangement are improved by both reducing the coherent noise of retrieved phase images and increasing the useful FOV from one third to one half. As consequence, the approach provides higher quality images, coming from the reduction in speckle noise, multiple reflections, and coherent artifacts, as well as bigger inspected regions because the FOV multiplexing is less restrictive. The former is obtained by replacing the LD by a SLD as light source, and the latter is achieved by selecting the spatially multiplexed input plane described in Section 3.2.

3.3.1. Layout description

Such a *SMIM* approach is implemented using the embodiment of a BX60 Olympus upright microscope. Figure 3.12 shows a scheme of the modifications performed in the microscope for *SMIM* implementation. In addition, the spatial multiplexing of the input plane, output plane, and the recorded intensity are clarified. Here, a SLD source from Exalos (Model EXS6501-B001, 10 mW optical power, 650 nm central wavelength, 6 nm spectral bandwidth) is externally inserted just below the microscope's XY translation stage. The FOV is divided into two regions, R and O, while the CCD is centered with the optical axis. In such a way, there is no need of modifying the microscope exit port. We have used two different infinity corrected microscope lenses (UMPlanFl): 10X/0.30NA and 20X/0.46NA. A Ronchi grating (N = 20 lp/mm) is placed on a motorized linear translation stage for P-S application (Newport, model ESP300) and introduced in the microscope's analyzer insertion slot. Finally, a commercial grade CCD camera (Basler A312f, 582x782 pixels, 8.3 μm pixel size, 12 bits/pixel) is used as recording device.

There are two reasons for using a grating frequency of N = 20 lp/mm. On one hand, such a value is the optimum to ensure the proper shift of the replicas at the output plane, according to Eq. (3.3). And on the other hand, this frequency introduces a mismatch in the distance travelled by the interferometric beams around d ≈15 μm, lower than the SLD's coherence length ($L_C \approx 50$ μm, calculated by using Eq. (3.1)), thus allowing interferometric recording. The frequency value is also far away from the maximum value ($N_{max} \approx 60$ lp/mm) before deriving in aliasing errors, according to the CCD features.

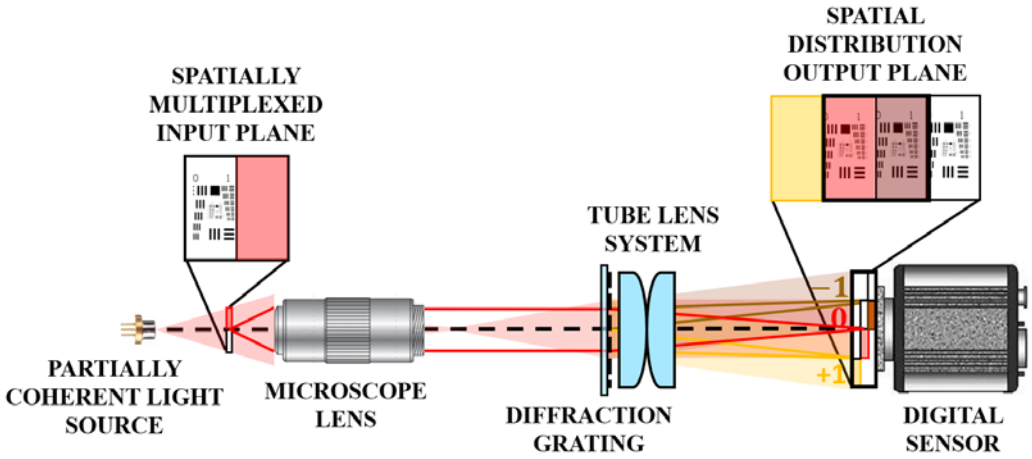

Figure 3.12. Scheme of the proposed *SMIM* with partially coherent illumination where the main components can be identified.

The short coherence length of the SLD prevents an *off-axis* configuration in our case. Thus, a *slightly off-axis* configuration is adopted, and a temporal P-S method is performed to recover the complex amplitude information. We have selected a full P-S cycle of 20 images, so that the grating motion step is 2.5 μm between consecutive holograms.

3.3.2. Experimental results

The experimental validation is divided into three parts: i) a calibration process, ii) an imaging process of static cells, and iii) a coherent noise analysis. The first one involves synthetic samples, while the second part is performed by using static biosamples. Finally, a STD analysis is performed for all samples.

One of the calibration experiments involves microbeads (Polybead® Microspheres, 45 μm mean diameter, standard monodisperse polystyrene microspheres) imaged with a 10X/0.30NA microscope lens. Such microbeads, immersed in water, are presented in a sparse mode to ensure clear areas around them. Figure 3.13 includes the experimental results, in which (a) is an image of the whole FOV recorded before grating insertion to clearly show the spatial multiplexing of the input plane. Here, the dashed white line separates both reference (upper half) and object (lower half) multiplexed regions. (b) shows the intensity distribution recorded by the CCD after grating introduction, where the dashed white line means the upper limit of the digital hologram to be reconstructed (lower half). Two frames captured at two different moments during the P-S recording process are presented in (c) and (d). Note that it is only shown the region inside the solid red rectangle included in (b). On the other hand, (e), (f) and (g) include the FT of the digital hologram, the FT after P-S algorithm application, and the FT after linear phase correction, respectively. Finally, (h), (i) and (j) present the amplitude, wrapped and unwrapped phase distributions retrieved by P-S method, respectively.

Then, in order to properly calibrate the proposed setup for *QPI*, the unwrapped phase images provided by the SMIM layout are compared with the provided ones by a conventional DHM platform. The DHM setup is composed of a He-Ne laser as light source, the same 10X/0.30NA microscope lens for imaging the microbeads, and a Mach-Zehnder interferometer assembled at the lab. In such an approach, phase images are obtained by Fourier filtering of an *off-axis* digital hologram. Figure 3.14 includes a picture of the DHM platform in (a), and perspective views of the unwrapped phase distributions provided by DHM layout and SMIM approach in (b) and (c), respectively. Looking at Figs. 3.14 (b) and (c), we realize that the microbeads are not the same in both cases. Nevertheless, they are also 45 μm spheres, so that their phase profiles must be quite similar. Indeed, leaving aside the phase unwrapping errors, the results are in good agreement each other, since the phase delays retrieved are almost the same in both cases, thus validating the *SMIM* approach for *QPI*.

Once calibrated, the SMIM layout is validated for both microscope lenses using different types of fixed cells, such as RBCs, swine sperm (SS) cells, and prostate cancer (PC-3) cells. Figure 3.15 includes the experimental results involving RBCs, structured in columns (1)-(2) and rows (a)-(c). Here, columns (1) and (2) depict the results obtained with the 10X/0.30NA and 20X/0.46NA lenses, respectively. On the other hand, row (a) includes the intensity images of the whole FOV before grating insertion, where the dashed white line separates the reference (upper) and object (lower) regions. Row (b) presents the direct intensity images of the group of cells marked with a solid square in row (a), and column (c) shows a perspective view of the quantitative phase distributions after complex amplitude retrieval.

Finally, a coherent noise analysis has been performed by means of STD values analysis. The STD values provided by this *SMIM* approach are compared with the obtained by *SMIM* technique with coherent illumination [Micó-2014]. To allow a direct comparative, the STD values for the phase distributions of the USAF test are computed, since it is the unique object imaged under the same conditions in both cases. Thus, the STD values calculated for the same clear region are 0.31 and 0.033 rad, when considering *SMIM* with coherent illumination [Micó-2014] and partially coherent illumination, respectively. An improvement factor around 10 is therefore achieved in phase spatial stability because of using partially coherent illumination.

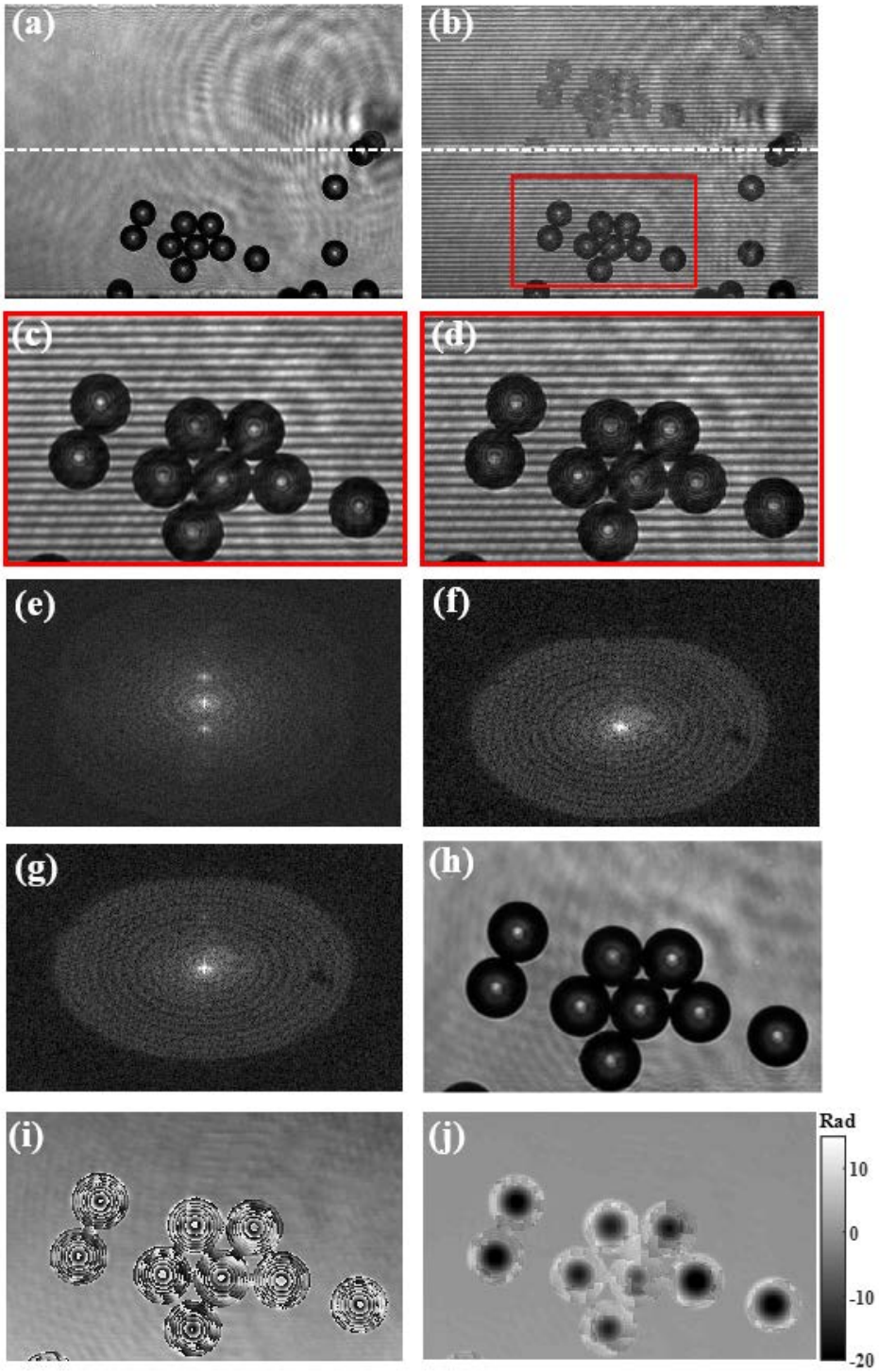

Figure 3.13. Experimental results for 10X/0.30NA microscope lens involving microbeads: (a) whole FOV before inserting the grating, in which a dashed white line separates both reference (upper) and object (lower) areas; (b) intensity distribution recorded by the digital sensor, in which the dashed solid line represent the upper border of the digital hologram to be reconstructed; (c)-(d) two frames recorded at different times during P-S recording process of the region inside the red rectangle included in (b); (e) FT of (c); (f) FT after P-S implementation; (g) FT after linear phase correction; (h), (i), and (j) retrieved amplitude, wrapped, and unwrapped phase distributions.

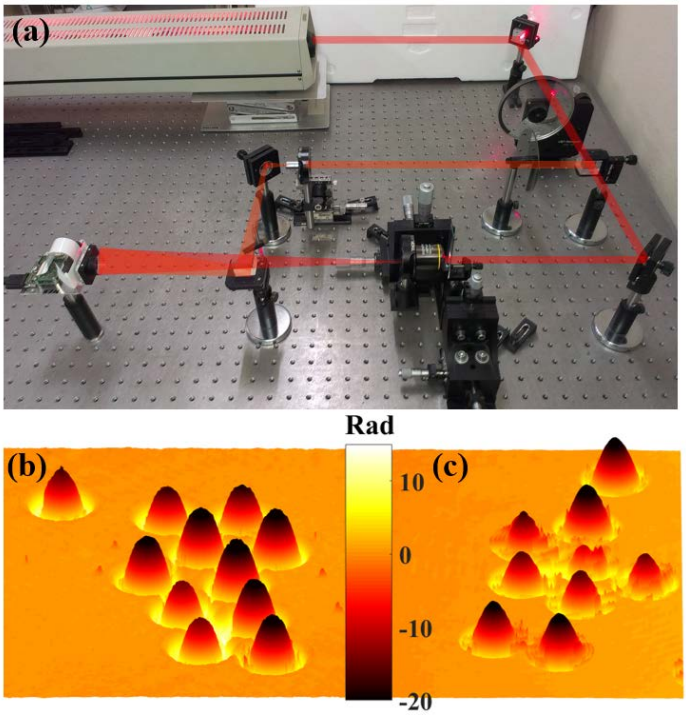

Figure 3.14. *QPI* validation of *SMIM* approach for microbeads. (a) DHM platform assembled at the lab; (b)-(c) perspective views of unwrapped phase distributions retrieved by *DHM* and *SMIM* architectures, respectively.

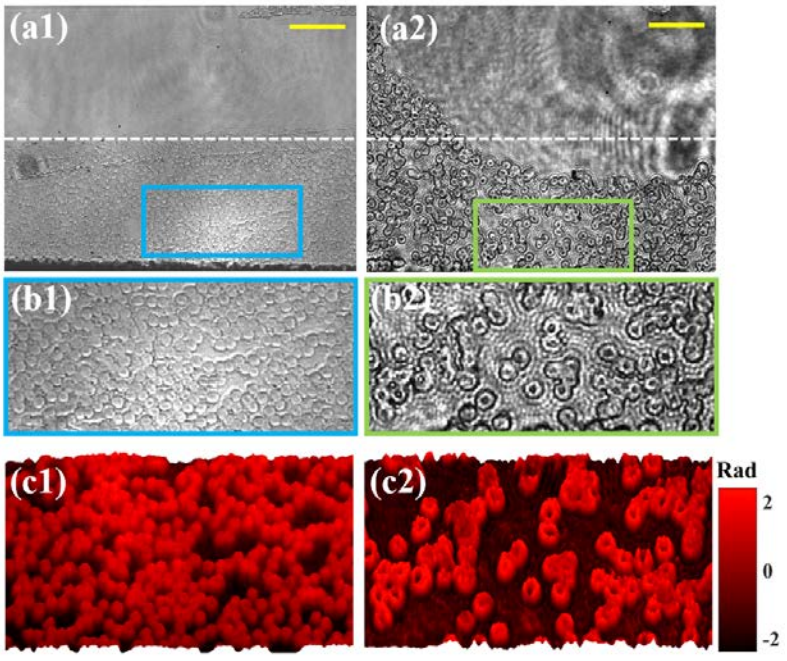

Figure 3.15. Experimental results involving RBCs. Columns (1) and (2): results for 10X and 20X objectives, respectively. Row (a): direct intensity images without the grating showing the S-M FOV; row (b) direct intensity images of some cells enclosed in blue and green squares in (a); and row (c) perspective views of phase distributions after applying P-S procedure. Scale bars: solid yellow lines at the upper right corner of (a1), and (a2) represent 100 and 50 μm, respectively.

3.4. Superresolved spatially multiplexed interferometric microscopy

As previously mentioned, *SMIM* was implemented in two ways: first, working under coherent light in an *off-axis* configuration and using a Fourier filtering method for phase retrieval [Micó-2014]; and second, with a partially coherent source in a *slightly off-axis* mode and applying a temporal P-S method for *QPI* [Picazo-Bueno-2016]. Thus, *SMIM* has been demonstrated to be a low-cost, simple and versatile way to convert a regular microscope into a holographic one. However, the main drawback of *SMIM* approaches is the FOV restriction because of the necessity to leave a clear region for reference beam transmission. As a result, modest/low NA objectives, which usually provides larger FOVs than higher NA ones, are additionally restricted in FOV. Nonetheless, such a FOV limitation (one-half the least restrictive) can be somehow compensated with an improvement of the spatial resolution, so that the characteristics of retrieved phase images are similar to the ones provided by a higher NA lens.

In line with that, a *SMIM* arrangement with SR capabilities is implemented. Such a technique, denoted as *superresolved spatially multiplexed interferometric microscopy* (*S2MIM*), enables a resolution gain factor of 2 compared with regular *SMIM* approaches. *SA SR* technique is applied by time (for temporally restricted objects) and angular (tilted beam illumination) multiplexing.

3.4.1. Layout description

S2MIM is implemented in the embodiment of an Olympus BX-60 upright microscope. The setup is a mix between both previously reported *SMIM* configurations: as in [Micó-2014], the input plane, which is spatially multiplexed in three regions (reference, object, and blocking area), is illuminated by a LD. On the other hand, a *slightly off-axis* holographic configuration and a P-S algorithm are employed as in [Picazo-Bueno-2016]. Two experiments are performed using different low NA microscope lenses: a 2X/0.05NA and a 5X/0.15NA Olympus objectives. For the case of the 2X lens, a VCSEL source (1 mW optical power, 850 nm) and a 1D Ronchi grating of 80 lp/mm are employed for illumination and holographic recording, respectively, whereas the experimental validation for the 5X objective is performed using a DVD LD source (5mW optical power, 650nm) and a 1D Ronchi grating of 50 lp/mm basic frequency. In both cases, a commercial grade CCD camera (Basler A312f, 582x782 pixels, 8.3 μm pixel size, 12 bits/pixel) is used for interference pattern recording.

Figure 3.16 includes an optical scheme to illustrate the implementation of *S2MIM*. Figure 3.16 (a) describes the imaging conditions before inserting the grating when an off-axis illumination is considered. Here, we can see that tilted beams are

achieved by laterally shifting the divergent light source to different off-axis positions. In such a way, a tilted beam forms an angle θ_{ILLU} with the optical axis of the imaging system. After grating insertion, the optical scheme remains as presented in Fig. 3.16 (b).

The divergence of the light source allows oblique illuminations by lateral displacement of the source. Five bandpass are encoded sequentially in time in five slightly off-axis holograms, corresponding to an on-axis and four off-axis illumination positions, and decoded by the application of a P-S algorithm (full cycle of 20 holograms). Then, all such a decoded information is properly phase corrected and coherently added to generate a SA and to provide SR images.

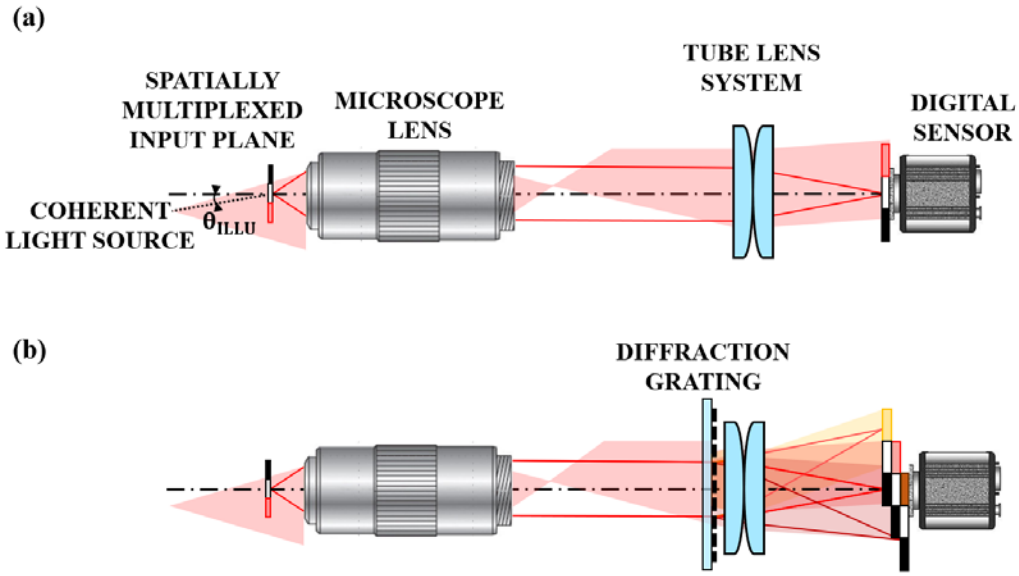

Figure 3.16. *S2MIM* implementation when an off-axis illumination is considered. (a) without grating and (b) after grating insertion.

3.4.2. Experimental results

The experimental validation is composed of two experiments. The first one involves a 2X/0.05NA objective and a NBS1963A resolution test target, while the second one is performed for a 5X/0.15NA microscope lens and an USAF resolution test target. Figure 3.17 shows the results for the 5X objective. The intensity distributions recorded by the CCD before and after the grating insertion are included in Figs. 3.17(a) and (b). On the other hand, Fig. 3.17(c) presents the FT of the hologram, in which three diffraction orders are clearly identified. After temporal P-S application, the intensity images retrieved for the cases of on-axis, horizontal, and vertical off-axis illuminations are included in Figs. 3.17 (d), (e), and (f), whereas the decoded coherent apertures corresponding to such images are depicted in Figs. 3.17 (g), (h), and (i), respectively. The generated SA incoming from the addition of the five retrieved coherent pupils is presented in Fig. 3.17 (j), and the superresolved image achieved by FT application to such a SA is depicted in Fig. 3.17 (k).

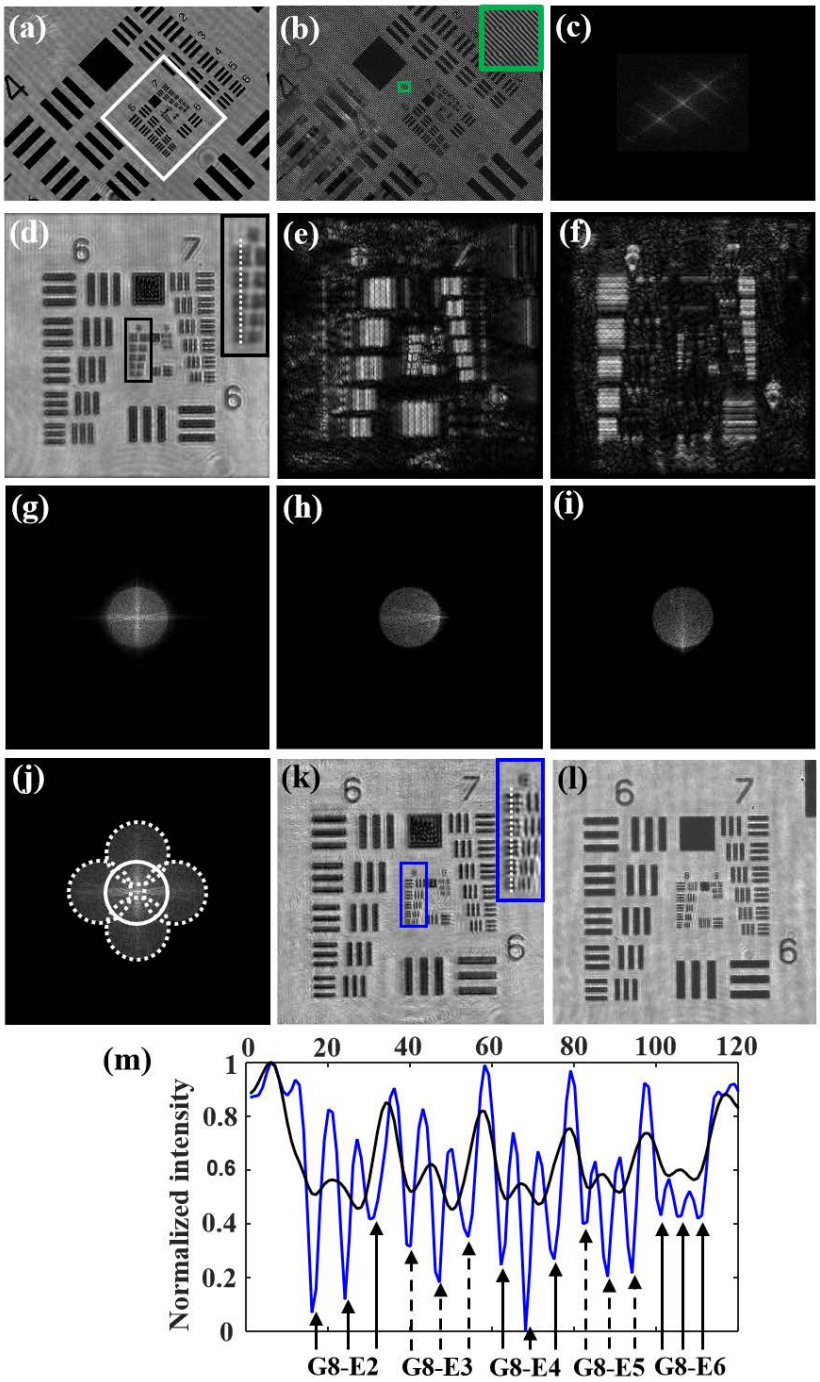

Figure 3.17. Experimental validation of *S2MIM* involving a 5X/0.15NA objective and an USAF resolution test target: (a) full frame intensity image of O region without grating; (b) hologram after grating insertion; (c) FT of (b); (d), (e), and (f) intensity images retrieved of the region enclosed in the white rectangle included in (a) after P-S algorithm for on-axis, horizontal, and vertical off-axis illuminations, respectively; (g), (h), and (i) coherent apertures of (d), (e), and (f), respectively; (j) generated SA coming from the coherent addition of the five retrieved apertures including (g), (h) and (i); (k) superresolved image provided by *S2MIM*; (l) intensity image provided by a 10X/0.30NA objective using *SMIM* with on-axis illumination; (m) plots for *S2MIM* (blue line) and *SMIM* (black line) along the dashed white lines included in (d) and (k).

From a direct comparison between Figs. 3.17 (d) and (k), we can see that a resolution gain factor around 2 is achieved by using *S2MIM* approach, since the last resolved element by *S2MIM* [Fig. 3.17 (k)] is the Group 9-Element 1 (G9-E1, 512 lp/mm or 1.95 μm), whereas by *SMIM* [Fig. 3.17 (d)] is the element G8-E1 (256 lp/mm or 3.91 μm). On the other hand, Fig. 3.17 (m) is included to clearly demonstrate the resolution improvement in the intensity distributions provided by *S2MIM* (blue line) in comparison with *SMIM* images (black line). In addition, such a new resolution limit is compared against the provided by *SMIM* technique when a 10X/0.30NA microscope lens and an on-axis illumination are considered [see Fig. 3.17 (l)]. A resolution limit of 1.95 μm is achieved in both cases. Hence, it is demonstrated that an image obtained with a 5X/0.15NA microscope lens under *S2MIM* presents a similar FOV and spatial resolution than an image provided by *SMIM* employing a 10X/0.30NA objective.

3.5. Hilbert-Huang single-shot spatially multiplexed interferometric microscopy

The use of partially coherent illumination in *SMIM* approaches significantly reduces the presence of coherent noise in retrieved phase images[39] [Picazo-Bueno-2016]. However, short L_C in such light sources does not often allow the implementation of an *off-axis* holographic configuration, so that it usually forces to use temporal P-S procedures for phase retrieval, thus preventing real-time analysis. Nevertheless, there exist other phase retrieval approaches capable to overcome such a limitation [Tahara-2010, Abdelsalam-2012, Trusiak-2016B]. Among such methods, *single-shot Hilbert-Huang phase microscopy* (*S2H2PM*) appears as a single-shot, robust, fast, and accurate technique for *QPI* even though a *slightly off-axis* holographic configuration is defined [Trusiak-2016B].

Hence, in this experiment, *SMIM* is combined with a modified version of *S2H2PM* to allow single-shot operation principle working under partially coherent illumination, thus creating the technique named *Hilbert-Huang single-shot spatially multiplexed interferometric microscopy* (*H2S2MIM*). The optical arrangement is identical to the reported in [Picazo-Bueno-2016], that is, a partially coherent illumination is employed, the input plane is multiplexed into two regions[40], a diffraction grating is used, and a *slightly off-axis* holographic configuration is implemented. On the other hand, several improvements are introduced to *S2H2PM* approach to efficiently analyse objects with cumbersome fringe patterns.

[39] One order of magnitude.
[40] Object and reference.

3.5.1. System description

The implementation of the proposed *H2S2MIM* approach is performed using the embodiment of an Olympus BX60 upright compound microscope. A scheme of the arrangement is presented in Fig. 3.18. A SLD (from Exalos, Model EXS6501-B001, 10mW of optical power, a 650 nm central wavelength, a 6 nm spectral bandwidth) is used as partially coherent illumination and emitting divergent light towards the input plane. Such an input plane (S) is spatially multiplexed into object (O) and reference (R) regions. The imaging system consists of an Olympus UMPlanFl 20X/0.46NA objective lens and a tube lens (TL) which magnifies and images the input plane at the output port of the microscope, where a CCD camera (Basler A312f, 582 x 782 pixels, 8.3 μm pixel size, 12 bits/pixel) is placed. The holographic recording is achieved by inserting a 1D Ronchi grating (G) (20 lp/mm basic frequency) in the analyser insertion slot just before the tube lens.

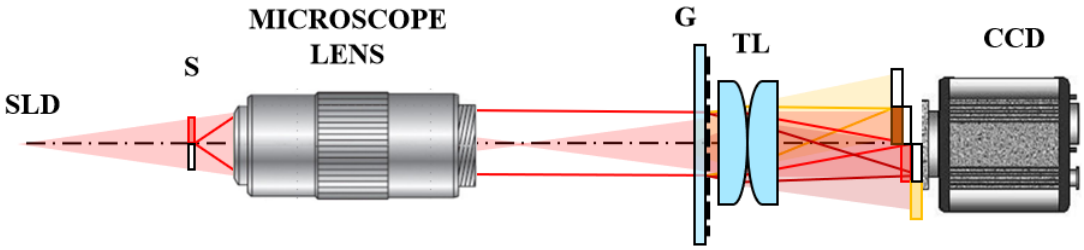

Figure 3.18. Scheme of the proposed *H2S2MIM* where the main components are identified.

On the other hand, the reconstruction algorithm is an improved version of the previously reported *S2H2PM* algorithm [Trusiak-2016B]. In this case, the modified *S2H2PM* approach begins with the application of an adaptive filtering to the hologram. Such a filtering consists in an automatic masking algorithm based on variational image decomposition (VID) [Zhu-2013] and Otsu binarization. Other steps such as local fringe direction map estimation, phase unwrapping and filtering, are modified accordingly with the samples.

Such modifications are especially useful for microbeads analysis. The microbeads are difficult to retrieve from single fringe pattern analysis point of view since: 1) they present a spurious circular diffraction pattern in their surrounding areas; 2) the period and orientation of the fringes vary significantly inside the bead; and 3) there appear fringe discontinuities along the bead edges.

H2S2MIM removes the hologram background by using the automatic masking algorithm. Then, an adaptative EMD technique [Trusiak-2014] is utilized for fringe period difference compensation. In addition, two global parameters (mean amplitude and mean spectral energy) are considered to enhance SNR into the reconstructions.

After that, the method employs a HST algorithm for phase estimation of a bandpass filtered fringe pattern with local oscillations around zero value, achieved by means of EMD application. The crucial part of HST is the correct estimation of the local fringe direction map that includes also the difficult fringe orientation variations. For that reason, we employ an EMD adaptive filtering of the first-estimate direction map (very noisy) to a fringe direction estimator previously reported in [Trusiak-2016B] to achieve an accuracy and smoothness estimated fringe direction map.

The result of applying the modified HST is a wrapped phase map. We use an iterative phase unwrapping algorithm recently introduced by [Martinez-Carranza-2017], which is based on the transport of intensity equation (TIE) and with the advantage of considering Poissonian smooth solutions, especially useful in noisy areas with fringe discontinuities. Hence, such an algorithm enables *QPI* from a single hologram, thus providing of a single-shot operation principle to *H2S2MIM* technique.

3.5.2. Experimental results

Experimental validation of *H2S2MIM* is divided into three parts: 1) an initial calibration process involving microbeads is performed to validate the approach, 2) a validation involving static biosamples, and 3) an analysis of a dynamic process to demonstrate the single-shot capability of *H2S2MIM*.

In all experiments, a *slightly off-axis* holographic configuration is adopted. On the other hand, the holographic P-S recording is performed by placing the grating on a motorized linear translation stage (Newport, model ESP300). A grating motion step of 2.5 μm is selected, so that 20 images integrate a full P-S cycle according to the grating frequency. However, 80 images are recorded to perfectly select the appropriate frames thus minimizing errors in phase retrieval.

In the calibration process, the phase distribution of a microbead of 90 μm in diameter is retrieved by both *H2S2MIM* and temporal P-S procedures, to validate the novel method by direct comparison with a well-established technique. Figure 3.19 presents the experimental results and includes two rows and three columns. Each row shows the results provided by *H2S2MIM* [row (a)] and P-S algorithm [row (b)], respectively, whereas column (1) includes two holograms of whole P-S recording process, and columns (2) and (3) depict the wrapped and perspective unwrapped visualizations of the retrieved phase distributions. By comparing the phase distributions provided by both methods, we can see that the experimental results are in good agreement each other, leaving aside the background differences, thus validating the proposed technique.

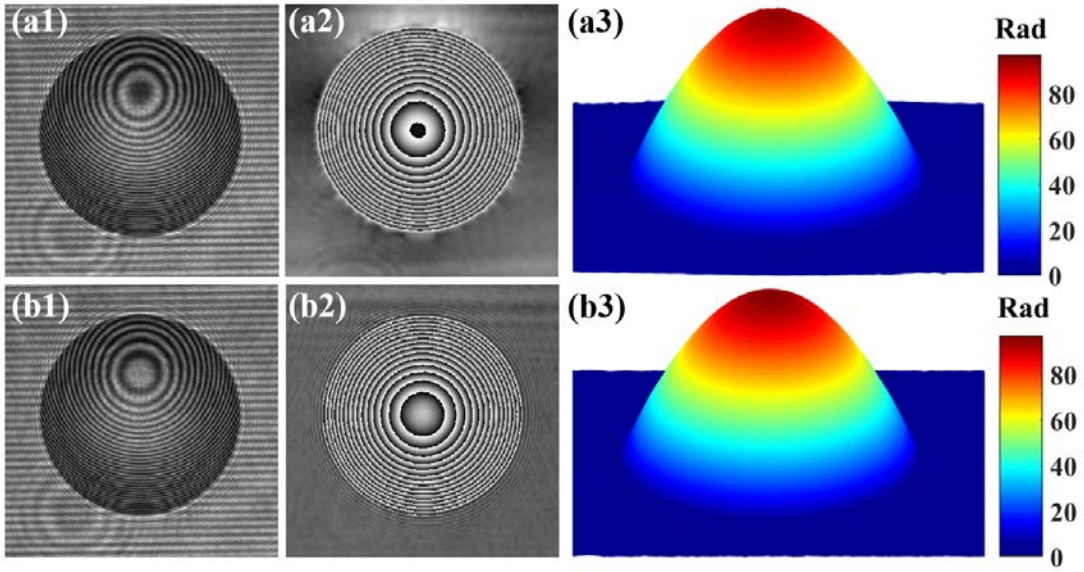

Figure 3.19. Experimental validation involving a 90 μm spherical bead: row (a)-(b) results incoming from *H2S2MIM* and P-S approaches, respectively; column (1) ROI of two different frames acquired during the P-S recording process; column (2) wrapped phase distributions; and column (3) perspective view of unwrapped phase distributions.

Another similar experiment is performed for more complex samples, such as static biosamples. In that case, the phase distributions retrieved by both *H2S2MIM* and P-S algorithms are compared each other for two different lines (LNCaP and PC-3) of prostate cancer cells. Figure 3.20 includes the experimental results for the case of LNCaP cells. The ROI of the hologram to be reconstructed is shown in Fig. 3.20 (a), while perspective visualizations of the unwrapped phase distributions retrieved from *H2S2MIM* and P-S algorithms are presented in Fig. 3.20 (b) and 3.20 (c), respectively. As before, the phase distributions are in good agreement.

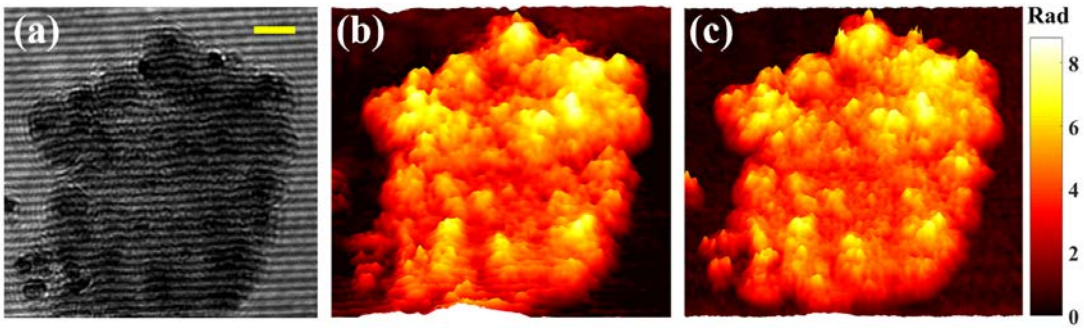

Figure 3.20. Experimental validation using prostate cancer cells: (a) ROI of a hologram; (b) perspective view of unwrapped phase distribution incoming from *H2S2MIM*; (c) perspective view of unwrapped phase distribution after applying P-S algorithm. Yellow scale bar in (a) represents 20 μm.

Finally, the single-shot operation principle of the proposed *H2SMIM* approach is demonstrated by monitoring two 45 μm microbeads flowing within a 100 μm thickness counting chamber filled with an aqueous medium. Figure 3.21 includes four perspective visualizations of unwrapped phase distributions provided by *H2S2MIM* for four different moments (0, 2, 4, and 6 s) of all recording sequence (6 s). Looking at Fig. 3.21, we can appreciate such a movement of the microbeads, so that the capability of real-time QPI analysis of *H2S2MIM* is perfectly confirmed, therefore demonstrating that our proposed technique presents single-shot capability even though a *slightly off-axis* holographic configuration is defined.

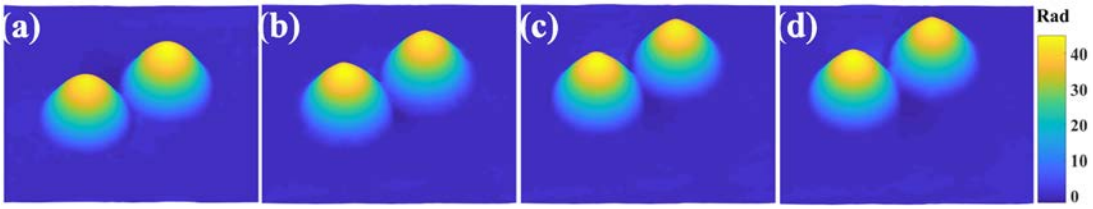

Figure 3.21. Experimental validation of *H2S2MIM* for dynamic samples. (a)-(d): perspective views of unwrapped phase images retrieved by *H2S2MIM* at four different moments (0, 2, 4, 6 s, respectively) of a full movie of 6 s.

3.6. Opposed-view spatially multiplexed interferometric microscopy

On previous experiments, *SMIM* technique was implemented working under partially coherent illumination for coherent noise reduction [Picazo-Bueno-2016], with SR capabilities to overcome FOV restrictions [Picazo-Bueno-2017], and employing an algorithm based on HHT to achieve single-shot operational principle [Picazo-Bueno-2018B]. However, all those approaches were performed in transmission imaging mode, thus restricting *SMIM* to transparent objects. Nonetheless, *SMIM* is not limited only to transmission modes, since it can be also conducted in reflective modality, or even both transmission and reflection modes simultaneously (transflective modality).

Hence, in this experiment, *SMIM* is validated for reflective sample inspection. In addition, reflective imaging mode is combined with transmission modality to define transflective mode. Such a technique, named *opposed-view spatially multiplexed interferometric microscopy* (*OV-SMIM*), increases the range of samples to be inspected by *SMIM*, thus generalizing the *SMIM* concept. Following *SMIM* characteristics, *OV-SMIM* provides a low-cost, stable and simple way to convert a conventional microscope into a holographic one with transmission/reflection imaging modes. In addition, *OV-SMIM* simultaneously provides both axial nanometer accuracy and RI measurements of the samples.

3.6.1. System description

The experimental layout assembled in the embodiment of a BX60 Olympus microscope, and its optical scheme is depicted in Fig. 3.22. Two fiber-coupled LDs illuminate the input plane in transflective mode by wavelength multiplexing. In transmission mode, a green illumination is emitted by an OSI LD (TCW RGBS-400R, 520 nm central wavelength, 3 mW optical power), whereas a LD from Blue Sky Research (SpectraTec 4, 635 nm central wavelength) is selected as red light source in reflective configuration. The input plane is multiplexed into three regions: i) a central object region, ii) a right transmission reference (and reflection blocking) region, and iii) a left reflection reference (and transmission blocking) region. The transmission mode is implemented as in previous SMIM approaches [Micó-2014, Picazo-Bueno-2017], while the reflective mode uses the transmission blocked region as mirror surface to provide reference beam reflection. A 1D Ronchi grating of 40 lp/mm basic frequency produces the interference pattern, and a colour CMOS camera is used for holographic recording (Mightex USB 3.0 SMN-CO50-U, 2560x1920 pixels, 2.2 µm pixel size, 24 bits/pixel). Due to the setup characteristics, a *slightly off-axis* holographic configuration is adopted, and a temporal P-S method is used for phase retrieval. For that reason, a motorized linear translation stage (Newport ESP300) is additionally employed to laterally shift the 1D grating for P-S application (25 holograms/cycle).

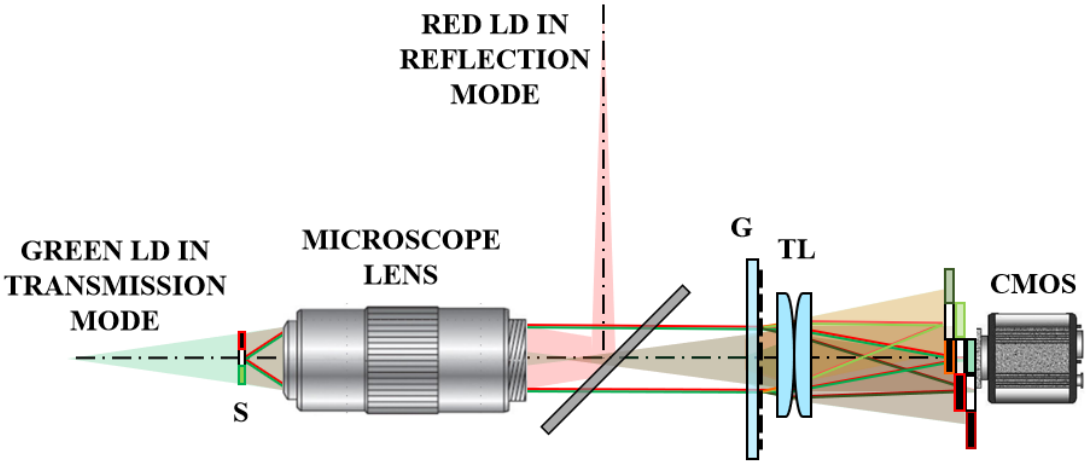

Figure 3.22. Optical scheme and ray tracing of the proposed *OV-SMIM* approach.

3.6.2. Experimental results

The experimental validation is composed of two parts: i) calibration of the *SMIM* reflective mode involving a reflective sample and a 5X/0.15NA microscope lens, and ii) *OV-SMIM* validation employing a resolution test target as well as microspheres for inspection with a 5X/0.15NA and a 10X/0.30NA microscope lenses, respectively.

Regarding the reflective imaging mode validation, a 1D Ronchi grating of 20 lp/mm basic frequency is used as reflective sample. Figure 3.23 presents the experimental results for such a case. Intensity images before (intensity image) and after (hologram) inserting the grating are included in Figs. 3.23 (a) and (b), respectively. After applying P-S algorithm, the complex amplitude is retrieved, whose intensity and phase distributions are shown in Figs. 3.23 (c) and (d), respectively. Such a phase distribution can be utilized to obtain the height profile of the chromium layer of the grating by using Eq. (2.37). Figure 3.23 (e) includes a 3D visualization of such a profile calculated within the region marked with a solid orange line in Fig. 3.23 (d). In order to confirm the validity of the thickness values provided by *SMIM*, the region inside the solid brown square in Fig. 3.23 (d) is imaged with a Cervantes Multimode Atomic Force Microscope (*AFM*) [see Fig. 3.23 (f)]. Then, the height profiles along solid blue and black lines included in Figs. 3.23 (e) and (f) are plotted in Figs. 3.23 (g) and (h), respectively. The mean height differences between the dielectric and chromium layers provided by both *SMIM* and *AFM* techniques are around 82 and 85 nm, respectively, being in good agreement each other, thus validating reflective *SMIM* imaging mode.

Concerning *OV-SMIM* validation, a NBS 1963A resolution test target as well as a group of microbeads are characterized. Transflective holograms are directly separated into two holograms (transmission and reflection holograms) by the Bayer filter mosaic of the colour CMOS camera. Then, a P-S procedure is independently applied to each one of them, thus retrieving two complementary complex amplitude distributions.

Experimental results involving the resolution test target are presented in Fig. 3.24. The recorded transflective hologram is included in Fig. 3.24 (a), where the dashed white line indicates the border of the useful hologram (left part). Figures 3.24 (b) and (c) show the transmissive and reflective holograms of the solid brown rectangle included in Fig. 3.24 (a), respectively. After applying the P-S technique, phase distributions are retrieved from both imaging modes. Figures 3.24 (d) and (e) present perspective visualizations of quantitative phase images obtained in the regions delimited by solid white squares (element 114 lp/mm) included in Figs. 3.24 (b) and (c), respectively. Then, phase profiles along solid white lines present in Figs. 3.24 (d) and (e) are performed, and two comparison plots are depicted in Figs. 3.24 (f) and (g). Figure 3.24 (f) represents the phase profiles directly calculated from Figs. 3.24 (d) and (e). As we can see, the phase delay provided by the reflection imaging mode is approximately twice the induced in transmission modality, since the reflected light goes through the same optical path in air twice. Once compensated such an effect [Fig. 3.24 (g)], a high concordance between both reflection/transmission modes is observed (leaving aside the resolution limits).

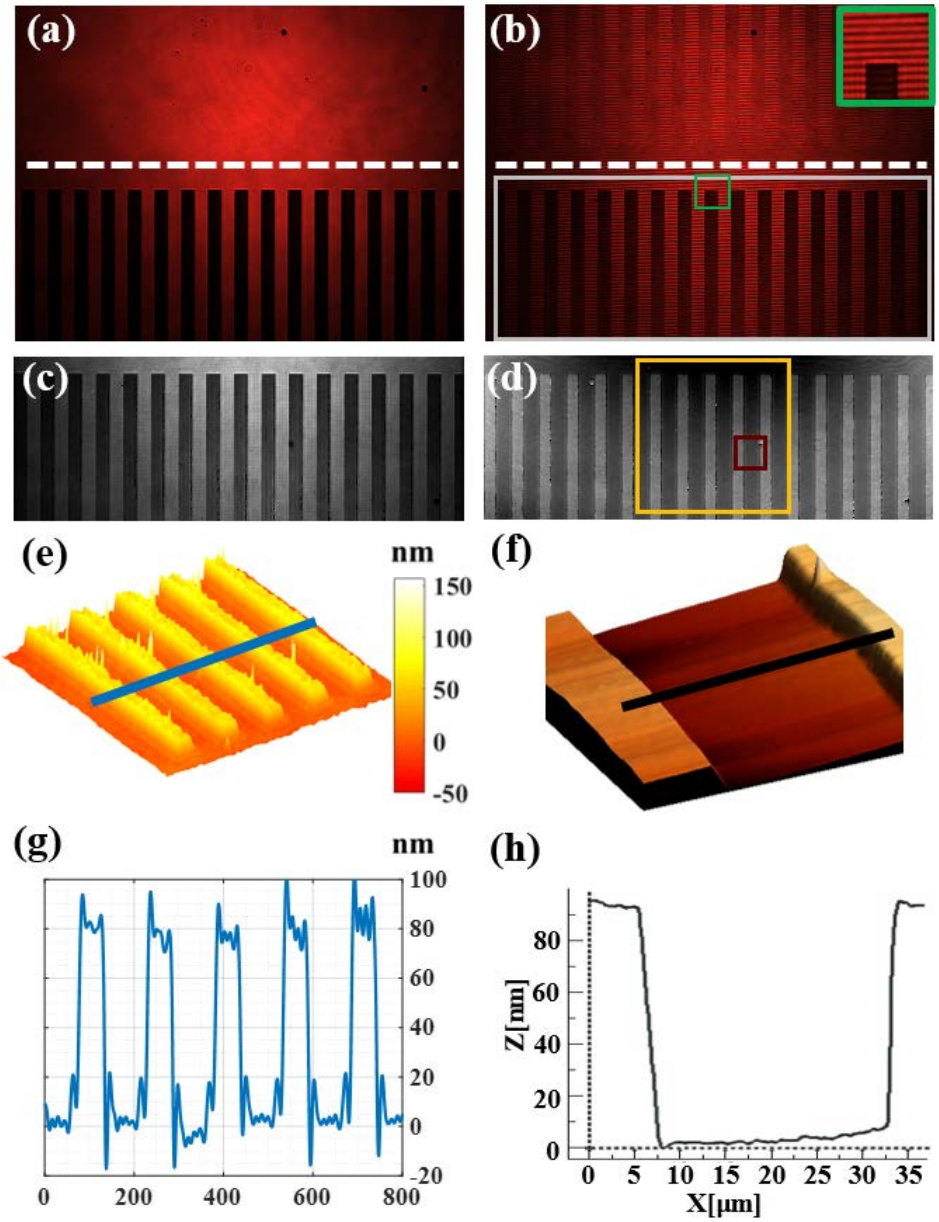

Figure 3.23. Experimental validation of *OV-SMIM* for reflective imaging mode: (a) direct intensity image of the grating; (b) reflective hologram; (c) and (d) retrieved intensity and phase images of the region enclosed in solid grey rectangle included in (b) after applying temporal P-S method, respectively; (e) and (f) 3D views of thickness distributions of the regions marked with solid orange and brown squares in (d) provided by *SMIM* and *AFM*, respectively; (g) and (h) thickness profiles along solid blue and black lines included in (e) and (f), respectively.

Finally, the proposed *OV-SMIM* approach is also validated for a 10X/0.30NA microscope lens by imaging a set of water-immersed microspheres of 45 μm in diameter. In that situation, a mirrored surface is placed on the left region of the input plane (blocking transmission zone) to provide a reflective reference beam. The phase retrieval procedure is analogous to the case of NBS resolution test target. Figure 3.25 presents the results obtained for two microbeads. Thickness distributions are calculated by applying Eqs. (2.35) and (2.36) to the phase delays retrieved after applying P-S method to both transmissive and reflective holograms, respectively [see Figs. 3.25 (a) and (b), respectively]. To allow easy comparison, thickness profiles along solid green and red lines included in Figs. 3.25 (a) and (b) are plotted together in Fig. 3.25 (d). Looking at Fig. 3.25 (d), one can notice that the thickness profiles provided by both reflection and transmission modes are in good agreement each other, since a value of $t_{b,exp} \sim 7.4$ μm is achieved in both cases. Nevertheless, such a value is far away from the real thickness value ($t_{b,theo} = 45$ μm). Since the microspheres are imaged with a 0.30NA objective lens, the whole cone of light focused by the bead is not captured, so that the retrieved phase distributions are more related to two spherical caps than to the entire sphere. Nonetheless, despite such thickness values, it is possible to calculate the RI distribution of the microbeads [see Fig. 3.25 (c)] from the two simultaneous holographic measurements by employing Eq. (2.39). A RI profile along the solid black line included in Fig. 3.25 (c) is plotted in Fig. 3.25 (e). For the green illumination wavelength, an averaged RI value of $n_{b,exp} \sim 1.59$ is obtained for the analysed microbeads, a value close to the theoretical one ($n_{b,theo} = 1.6$) for such a wavelength. Note that such a value is computed considering the central RI values delimited by the full width at maximum height (FWMH), represented by two shadowed rectangles in Figs. 3.25 (d) and (e).

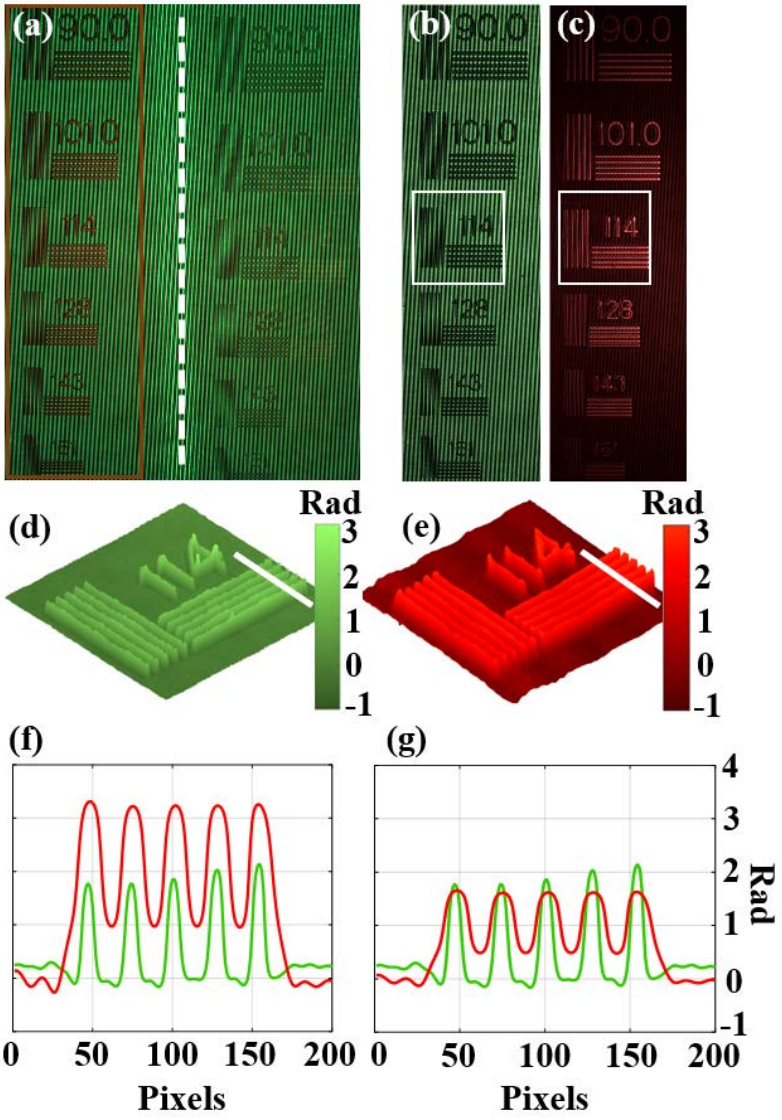

Figure 3.24. Experimental validation of the proposed *OV-SMIM* approach involving a resolution test target: (a) transflective hologram; (b) and (c) transmissive and reflective holograms, respectively, after demosaicing of the region within solid brown rectangle included in (a); (d) and (e) perspective views of retrieved phase distributions after applying P-S method to the regions within solid white squares included in (b) and (c), respectively; (f) phase profiles along solid white lines included in (d) and (e); and (g) comparison plot of such profiles once reflective phase is compensated from twice the optical path.

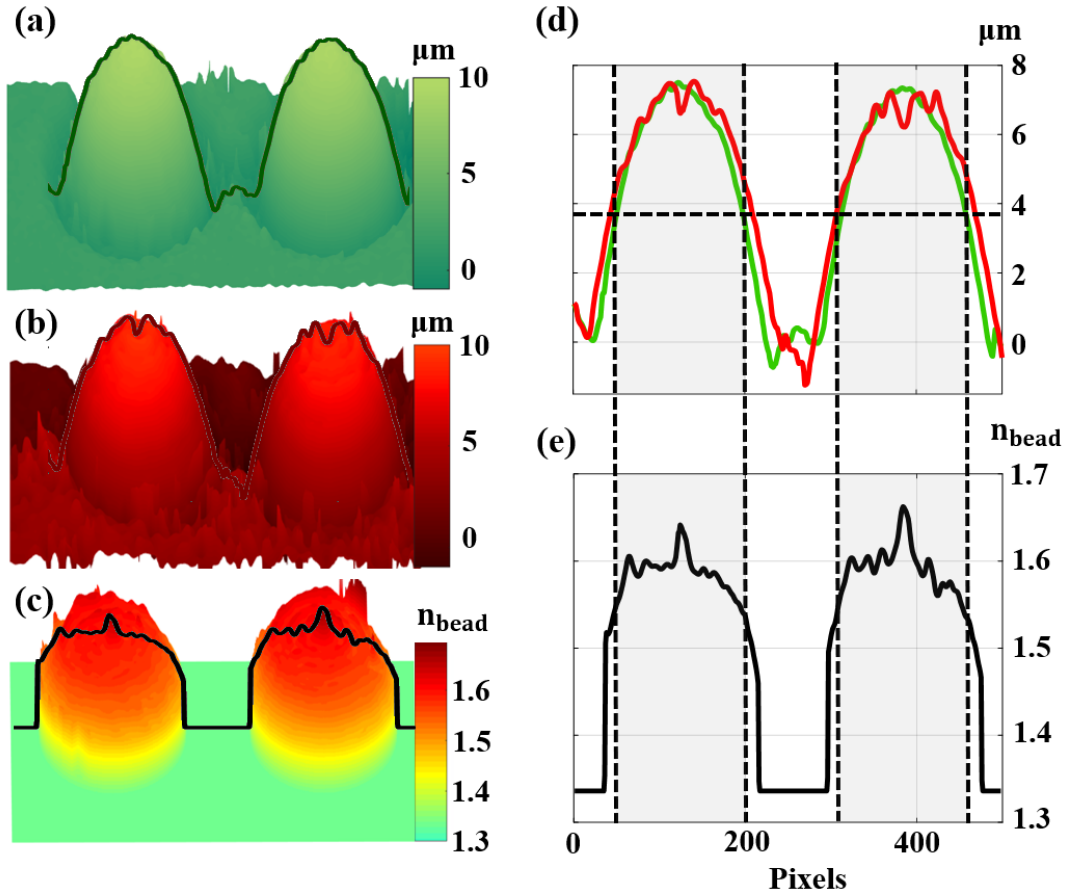

Figure 3.25. Experimental results of *OV-SMIM* involving microspheres in aqueous medium: (a) and (b) perspective views of thickness distributions provided by transmission and reflection imaging modes, respectively; (c) perspective view of RI distribution of the beads calculated using Eq. (2.39); (d) comparative thickness plot along the solid green and red lines included in (a) and (b); and (e) plot along the solid black line in (c) for averaged RI calculation. Shadowed rectangles in (d) and (e) indicate the microbead regions used for averaged RI computation.

3.7. Single-shot slightly off-axis digital holographic microscopy with an add-on module based on a beam splitter cube

A common issue in all previous *SMIM* approaches is the use of a 1D diffraction grating for the interferometric recording [Micó-2014, Picazo-Bueno-2016, Picazo-Bueno-2017, Picazo-Bueno-2018B, Picazo-Bueno-2019A]. Nevertheless, in those arrangements, both the optical and holographic configurations are highly influenced by the basic frequency of such a grating, which must be properly selected and placed for correct overlapping of the diffraction orders. By contrast, a CPI based on a BS cube interferometer enables easy variation of the holographic configuration by slightly rotating the BS cube.

Hence, in this experiment, we employ a CPI based on a BS cube instead of a grating[41] for interferometric recording. Such an interferometer is mounted in an add-on module and placed at the output port of a conventional upright microscope. To compensate the astigmatism introduced by the orientation of the BS cube, a Stokes lens (SL) is additionally included in the module. Such a *SMIM* arrangement generates two holograms phase shifted by π rad each other. By slight rotation of the BS cube, a *slightly off-axis* holographic configuration can be easily implemented, and the complex amplitude distribution can be retrieved in a single-shot by employing both subtraction algorithm[42] and Fourier filtering method. As a result, the proposed *single-shot slightly off-axis DHM* (*single-shot SO-DHM*) approach results in a simultaneous space-bandwidth product optimization and real-time analysis capability when comparing with *off-axis* and *on-axis* configurations, respectively.

3.7.1. System description

The experimental validation of *single-shot SO-DHM* approach is performed using a regular Olympus BX-60 upright microscope. Figure 3.26 shows a scheme of the setup where the main modifications are included. For coherent illumination, a fiber coupled green diode laser (OSI LD, TCW RGBS-400R) is inserted below the microscope's XY translation stage. A linear polarizer is placed for fringe contrast and intensity equalizations, necessary for a correct reconstruction process. The trinocular head is removed from the microscope embodiment to avoid spurious reflections, but we have maintained the infinity correct configuration by putting a tube lens of f = 120 mm at the circular dovetail mount of the microscope trinocular port.

At the output port of the microscope, we have added a labmade module composed of a 45º elliptical mirror (M), a SL, a BS cube and a CMOS. M is used to deviate horizontally the light path towards the other elements of the module. SL compensates the astigmatism introduced by the BS cube, which is placed onto a tilting platform (Qioptic) defining a CPI based on a BS cube. Such an interferometer provides therefore two simultaneous *slightly off-axis* holograms which are π rad phase shifted each other, recorded by a CMOS (Mightex USB3.0 monochrome camera, 2560x1920 pixels, 2.2 µm/pixel size, 14 fps). Both the orientation and location of the BS cube may introduce not only tilt but also astigmatism aberrations[43]. Such a tilt effect does not affect to the image quality and can be easily compensated by displacing the sample. By contrast, astigmatism can fully destroy the image quality (especially the finest details) and its compensation requires more complex procedures, such as the application of digital processing methods [Colomb-2006], or the insertion of specific designed optical components [Braat-1997, Arines-2011].

[41] Conventional way of achieving interferometric recording in SMIM approach.
[42] DC term removal.
[43] Like a thick plane-parallel plate.

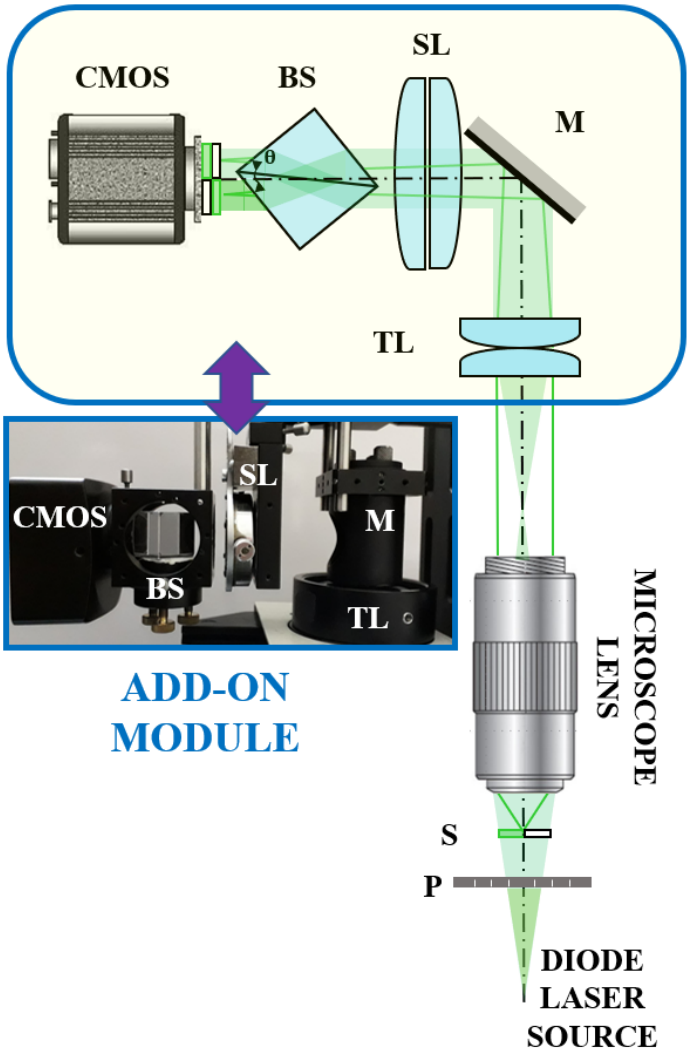

Figure 3.26. Scheme of the proposed *single-shot SO-DHM* layout, where a picture of the add-on module is included.

In this experiment, a lab-made SL is introduced to solve the astigmatism issue. Such a SL is a low-cost specific optical component composed of two pure cylindrical lenses assembled onto a Risley prism mount[44]. The dioptric power can be easily modified by changing the relative angle between the cylindrical lenses with a Risley knob. Furthermore, SL can be globally rotated to introduce the dioptric power in the correct direction. Such a SL was previously characterized for power measuring. In this case, each cylindrical lens presents a dioptric power of 1.50 D, allowing the compensation of astigmatism in a range of 3.00 D. Such a value is large enough to include the introduced by the BS cube, whose value is around 0.25 D in the experiments.

[44] SL does not introduce sphere power.

3.7.2. Experimental results

The experimental validation is carried out for both 10X/0.30NA and 20X/0.46NA microscope lenses and is divided into three parts: 1) a calibration process, 2) a validation stage involving static biosamples, and 3) a demonstration of single-shot capability. The calibration stage is performed using the 10X objective and involves a NBS 1963A resolution test target as input object. Figure 3.27 presents an example of whole process from direct image to digital hologram recording. Thus, Figure 3.27 (a) includes the intensity distribution recorded before inserting the add-on module. We can see the presence of astigmatism after placing the BS cube and blocking the reference beam path in Fig. 3.27 (b). After SL introduction, the astigmatism is compensated [see Fig. 3.27 (c)]. Finally, two image plane digital holograms are produced by unblocking the reference beam path [Fig. 3.27 (d)].

Then, the phase retrieval method employed in such a *single-shot SO-DHM* approach is compared against conventional Fourier filtering, using only a single hologram. Figure 3.28 presents the whole reconstruction process for each method. Single (right side) and subtracted hologram (left and right) are shown in Figs. 3.28 (a) and (b), respectively. FT of the single hologram is included in Fig. 3.28 (c), in which we can easily identify three diffraction orders. On the other hand, subtracted hologram [Fig. 3.28 (d)] does not contain DC term in the FT because of the subtraction procedure. After that, Fourier filtering is applied in both cases [see Figs. 3.28 (e) and (f), respectively], and the presence of the linear phase factor is removed by numerically centring the filtered orders in the FTs [Figs. 3.28 (g) and (h), respectively]. Complex amplitude distributions are retrieved performing FT^{-1}, whose intensities and phases are included, respectively, in Figs. 3.28 (i) and (k), in the case of conventional Fourier filtering, and in Figs. 3.28 (j) and (l), for the proposed *single-shot SO-DHM* approach.

Looking at Figs. 3.28 (i) and (l), we can notice a noisier and poorer quality reconstruction for the case of conventional filtering. To clearly show such an effect, the normalized intensity profiles along red and blue lines in Figs. 3.28 (i) and (j) are plotted together in Fig. 3.28 (m). The comparison between them demonstrates that the retrieved intensity by conventional Fourier filtering method is primarily noise, whereas 5 vertical bars and 4 dips related to the number “114” are clearly distinguished in the plot performed in Fig. 3.28 (j). Moreover, the proposed approach provides a smoother phase background, as we can conclude from the calculation of STD values in Figs. 3.28 (n) and (o). STD values are 0.28 and 0.17 rad for the case of conventional filtering and the proposed *single-shot SO-DHM* approach, respectively, so that the noise becomes reduced about 40%.

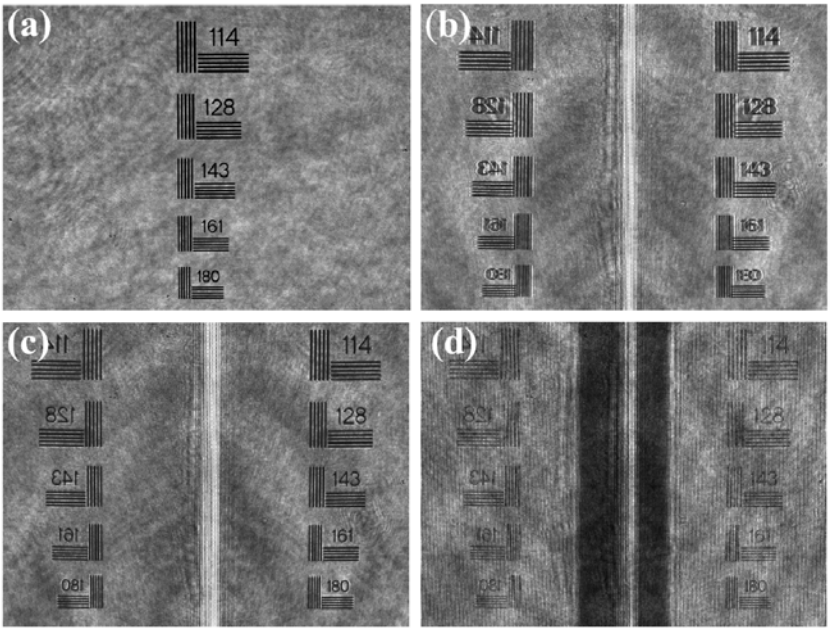

Figure 3.27. Recording sequence in the proposed *single-shot SO-DHM* approach: (a) direct intensity image without the add-on module, (b) astigmatic image when placing BS cube but without SL, (c) image after SL insertion and free of aberrations, and (d) recorded hologram by the proposed approach.

Once validated *single-shot SO-DHM* approach, the technique is employed to provide *QPI* of static biosamples. Concretely, different lines of prostate cells (PC-3, LNCaP and RWPE-1) are imaged employing a 10X microscope lens. Figure 3.29, which is structured in two rows and three columns, shows the experimental results obtained for the case of RWPE-1 prostate cancer cells. Each row (a)-(b) shows the results obtained when applying either conventional Fourier filtering (a) or subtraction algorithm and Fourier filtering (b). On the other hand, each column (1)-(3) includes the holograms (1) considered in each case, and both the retrieved intensity (2) and phase distributions (3) after applying the pertinent retrieval methods. Comparing Figs. 3.29 (a3) and (b3), we realise that a noisier phase distribution is obtained by using conventional filtering method, while a perfect phase visualization is achieved with the proposed method even though a significant number of cells are inspected.

Finally, single-shot capability of *single-shot SO-DHM* technique is demonstrated by using a 20X/0.46NA microscope lens to image microbeads (Polybead® Microspheres, standard monodisperse polystyrene microspheres) of 90 µm mean diameter flowing through an aqueous medium within a 100 µm thickness chamber. The movement of such microspheres is monitorized during 10 s, and perspective visualizations of unwrapped phase distributions are presented in Fig. 3.30 considering four different time lapses (0, 3.3, 6.6, 10 s). From Fig. 3.30, we can conclude that the novel approach also provides accurate *QPI* for real-time analysis of dynamic samples when a *slightly off-axis* holographic configuration is defined.

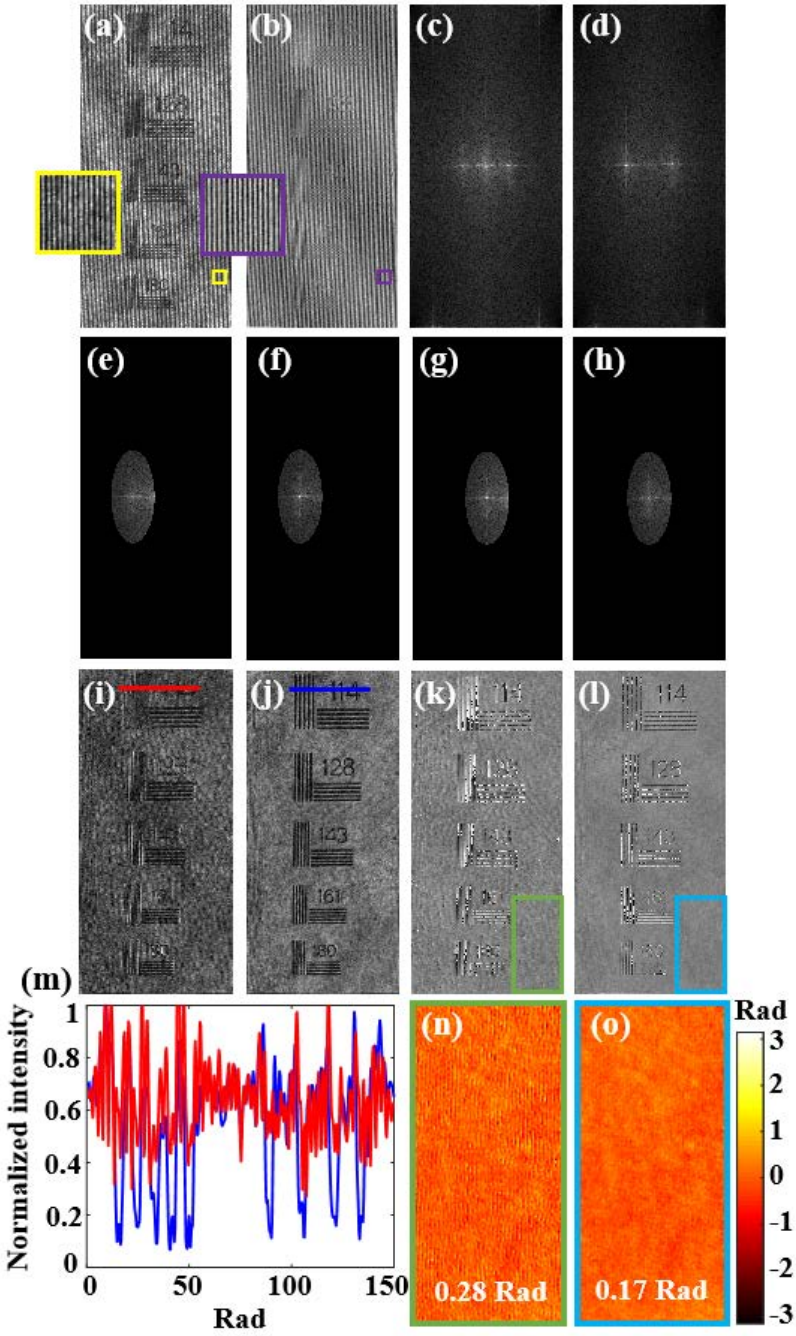

Figure 3.28. Experimental validation for a resolution test target by comparing the proposed *single-shot SO-DHM* approach and conventional Fourier filtering method. (a) single hologram for conventional filtering; (b) subtraction hologram for novel approach; (c) and (d) FTs of single and subtracted holograms, respectively; (e)-(f) filtered spatial-frequency pupils of (c) and (d), respectively; (g)-(h) centered pupils presented in (e) and (f) by linear phase factor correction; (i)-(j) retrieved intensity images from FT^{-1} of (i) and (j), respectively; (k)-(l) retrieved phase distributions from FT^{-1} of (i) and (j), respectively; (m) plot of the normalized intensity profiles along red and blue solid lines included in (i) and (j), respectively; (n)-(o) retrieved phase background images incoming from the green and cyan solid line rectangles marked in (k) and (l), respectively, including STD values.

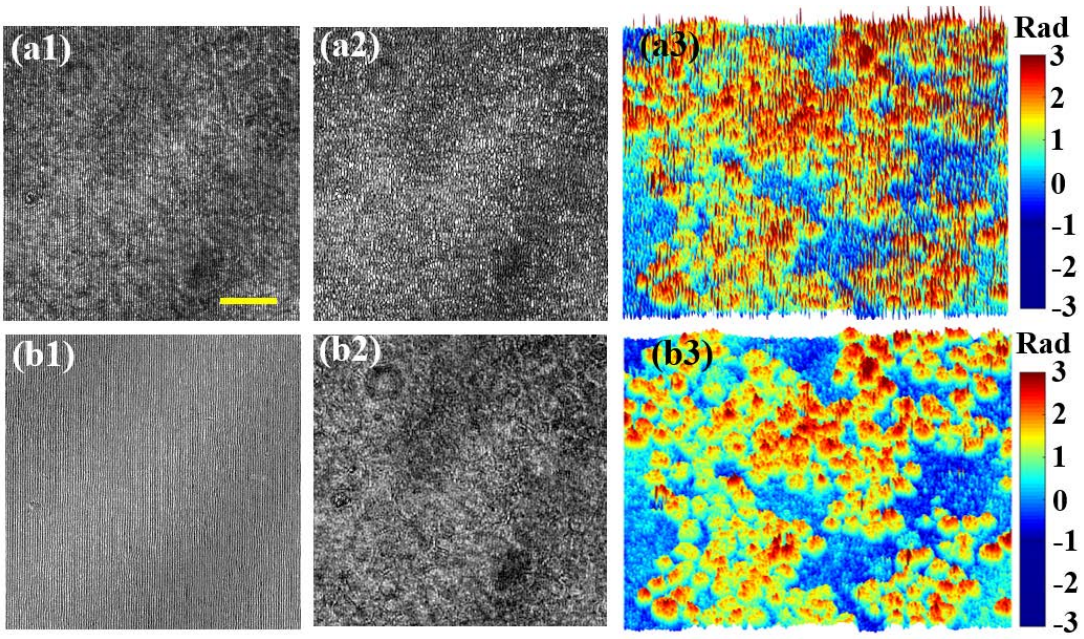

Figure 3.29. Experimental results involving RWPE-1 prostate cancer cells. Row (a) results considering conventional Fourier filtering; row (b) results for the case of the proposed *single-shot SO-DHM* approach. Column (1) single (a1) and subtracted (b1) holograms; column (2) retrieved intensity distributions; and column (3) perspective views of the retrieved phase distributions. Yellow scale bar in (a1) represents 50 μm.

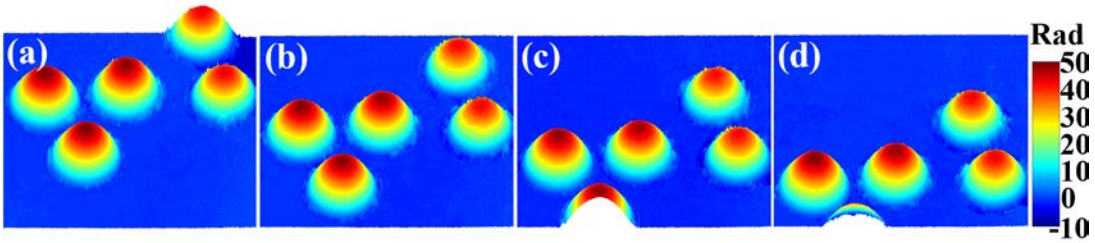

Figure 3.30. Experimental validation for dynamic processes involving flowing microbeads: (a)-(d) perspective visualizations of unwrapped phase distributions provided by the proposed *single-shot SO-DHM* approach for four (0, 3.3, 6.6, and 10 s) time lapses (full movie duration of 10s).

3.8. Single-shot two-frame π-shifted spatially multiplexed interference phase microscopy

The replacement of a diffraction grating by a BS cube to produce an interference pattern in *SMIM* approach not only allows the variation of the fringes frequency in an easier way (just rotating the BS cube), but also the possibility of real-time analysis when combining a *slightly off-axis* configuration and a subtraction algorithm. Such properties were demonstrated in the previous work [Picazo-Bueno-2019B], where an add-on module consisting in a BS cube was inserted at the output port of a compound upright microscope. However, the location and orientation of such a BS cube introduced astigmatism to the optical system, thus destroying the quality of the images, and a SL was eventually required to compensate such aberrations.

In this experiment, a novel *SMIM* arrangement is presented, named *single-shot two-frame π-shifted spatially multiplexed interference phase microscopy* (*π-SMIM*), in which a BS cube is now relocated inside the embodiment of the microscope to avoid such an astigmatism, so that the insertion of a SL is not necessary. In addition, a phase retrieval method based on the combination of subtraction algorithm and HHT employed in [Picazo-Bueno-2019B] and [Picazo-Bueno-2018B], respectively, improves the capabilities of the previous reported *H2S2MIM* when low SNR holograms are considered.

3.8.1. System description

The proposed *π-SMIM* method is implemented in a conventional upright microscope (BX60 Olympus). Figure 3.31 presents an optical scheme of such an arrangement. Here, a fiber-coupled diode laser (OSI LD, TCW RGBS-400R, 635 nm) is used to provide red divergent coherent illumination. Then, light passes through a linear polarizer (P) in order to make similar the fringe contrast of both interferograms provided by the proposed interferometric configuration[45]. The trinocular head of the microscope is removed to avoid reflections, and a tube lens (TL) of f' = 100 mm is placed to maintain the infinity corrected configuration at the circular dovetail mount of the microscope trinocular port. Between the microscope lens and the TL, a BS cube (polarizing, 25.4 mm side), which is mounted onto a tilting platform with several screws for fine adjustment, is externally inserted to produce interferometric recording. Note that such a BS cube position prevents of astigmatism to the optical system due to the light rays travel in parallel along this region. Finally, a CMOS camera (Ximea MQ042MG-CM USB3.0, 2048x2048 pixels, 5,5 μm pixel pitch) is set at the output port of the microscope for recording the two π-shifted interferograms.

[45] The more similar contrast, the better quality in retrieved phase images.

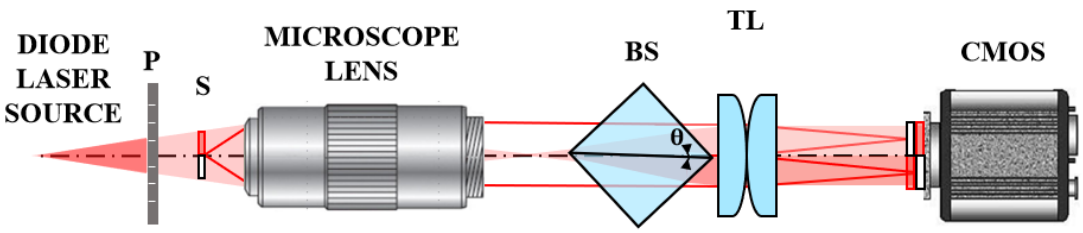

Figure 3.31. Optical scheme of the proposed π-SMIM experimental setup. P, linear polarizer; S, sample; BS, polarizing BS cube; TL, tube lens; CMOS, digital camera.

Phase retrieval algorithm is based on a conjunction of previously implemented subtraction [Picazo-Bueno-2019B] and HHT [Picazo-Bueno-2018B] methods. First, the two complementary holograms provided by the interferometric configuration are numerically matched and subtracted each other as in [Picazo-Bueno-2019B], thus generating a subtracted hologram (named π-hologram). However, such a hologram still presents some residual background due to the different background illumination. To remove that background, an enhanced fast empirical mode decomposition (EFEMD) method is applied as in [Picazo-Bueno-2018B], and the sum of two first modes is regarded as the adaptively filtered π-hologram. Then, phase retrieval is performed employing the HST [Picazo-Bueno-2018B]. Finally, phase unwrapping is conducted using TIE [Yang-2007].

3.8.2. Experimental results

Experimental validation of the proposed approach comprises three stages: 1) description of the working principle of *π-SMIM* approach, 2) validation of the technique involving samples with different sizes and densities, and 3) demonstration of the capability to analyse dynamic processes in real-time.

In the first stage, the working principle is detailed for the case of a biosample formed by prostate cancer cells (LNCaP line), and the experimental results are compared with those obtained by other previously established approaches (*H2S2MIM* and temporal P-S techniques). Figure 3.32 shows the whole process, starting from the recording of whole intensity distribution by the digital sensor [Fig. 3.32 (a)], and the selection of both left [Fig. 3.32 (c)] and right [Fig. 3.32 (d)] interferograms to be manipulated in order to achieve the adaptively filtered π-hologram [Fig. 3.32 (b)]. Successful DC term removal by subtraction process is clearly shown by the inclusion of the FTs of the right and adaptively filtered holograms [see Figs. 3.32 (e) and (f), respectively]. On the other hand, the improvement of phase images provided by the proposed method is confirmed by comparing the phase maps presented in Figs. 3.32 (g), (h), and (i). When comparing the phase maps retrieved from single hologram (left hologram) [Fig. 3.32 (g)], π-hologram [Fig. 3.32 (h)], and adaptively filtered π-

hologram [Fig. 3.32 (i)], one can notice that the phase image included in Fig. 3.32 (i) exhibits better quality than the others, since it shows more cellular details [compared with Fig. 3.32 (g)] and it does not present the periodic artefact that deteriorates the quality of Fig. 3.32 (h). Indeed, when computing the root mean square errors of such images, values of 0.86, 0.56 and 0.52 rad are obtained when considering the single hologram, π-hologram, and filtered π-hologram, respectively.

Finally, such a quantitative phase image provided by *π-SMIM* approach is compared with the provided by a conventional DHM platform [Fig. 3.32 (j)]. Such a DHM layout is based on a Mach-Zehnder interferometer, in which a He-Ne laser is used as coherent light source, and the same microscope lens is used for imaging the studied group of cells. In that case, a *quasi on-axis* holographic configuration is adopted, and a temporal P-S method is applied to retrieve the phase image from a set of six phase-shifted holograms. From a direct comparison between Fig. 3.32 (i) and (j), we can conclude that the *π-SMIM* technique yields reliable quantitative results since those results are in good agreement each other.

The versatility and robustness of the *π-SMIM* technique is corroborated by performing an experimental validation involving two additional types of biosamples consisting of prostate cancer cells (PC-3 cell line) of different sizes, on one hand, and dry RBCs presenting high density and clusters, on the other hand. Figure 3.33 includes the experimental results obtained when considering PC-3 cells. Two noisy interferograms are recorded [one of them is presented in Fig. 3.33 (a)] and combined by subtraction method to produce a hologram without background and with an improved amplitude modulation of the interference fringes.

Finally, the capability of *π-SMIM* approach to analyse dynamic processes is demonstrated by performing an experiment involving some microspheres (mean diameter of 45 μm) flowing in an aqueous medium. Figure 3.34 shows perspective views of the unwrapped phase images retrieved at 0, 5, 10, and 15 s moments [Figs. 3.34 (a)-(d), respectively]. Full recording movie presents a duration of 15 s. As we can see in Fig. 3.34, phase maps of the microspheres are well-retrieved including the regions where closed fringes are presented, thus overcoming such an issue, and demonstrating the single-shot operation principle of *π-SMIM*.

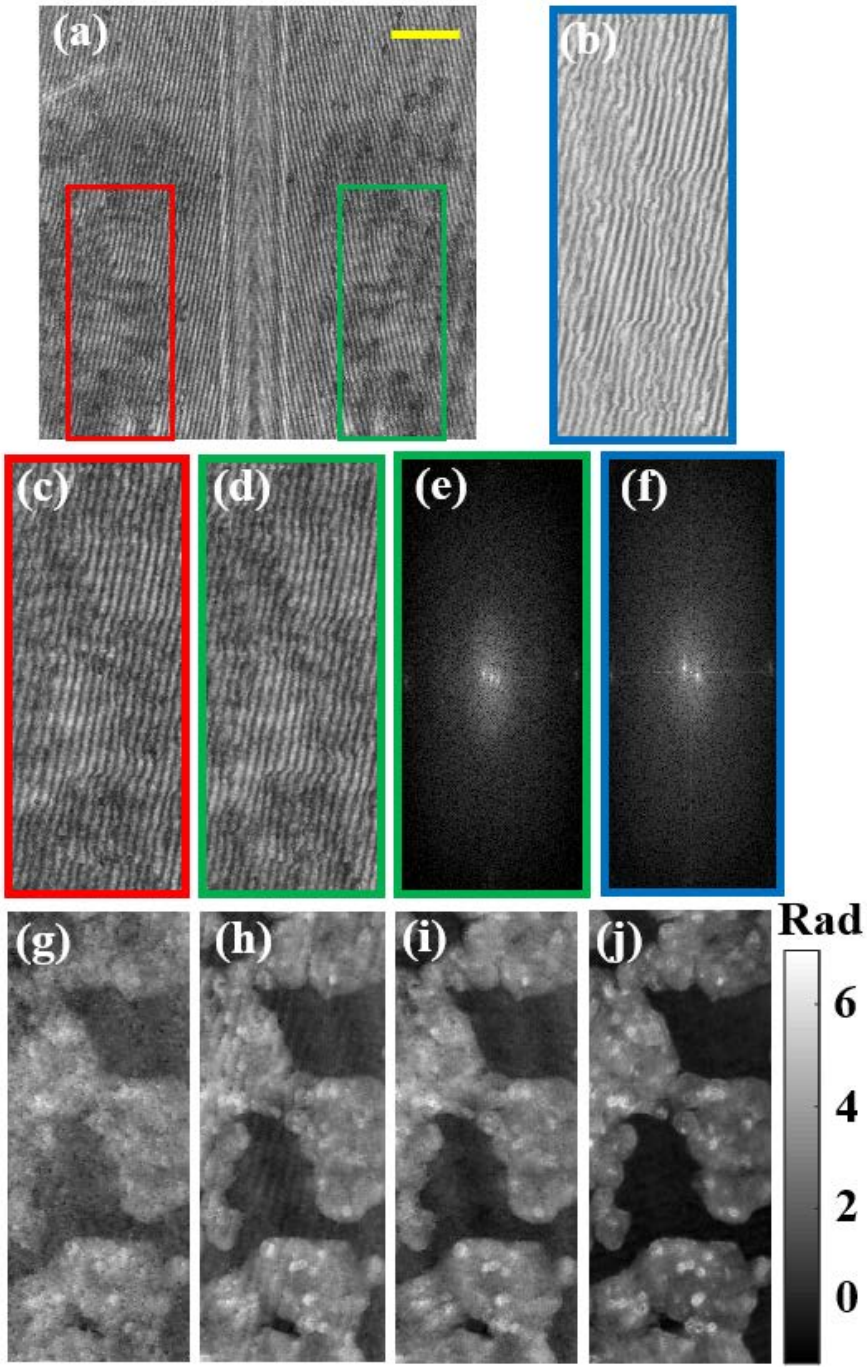

Figure 3.32. Demonstration of the working principle of the proposed *π-SMIM* approach. (a) intensity distribution recorded by the digital sensor; (b) filtered π-hologram obtained from the subtraction of left (c) and right (d) holograms and further adaptively filtering by EFEMD; (e) and (f) FTs of right hologram and filtered π-hologram, respectively; (g)-(j) quantitative phase images provided by using a single hologram, π-hologram, filtered π-hologram, and P-S algorithm, respectively. Yellow scale bar in (a) represents 100 μm.

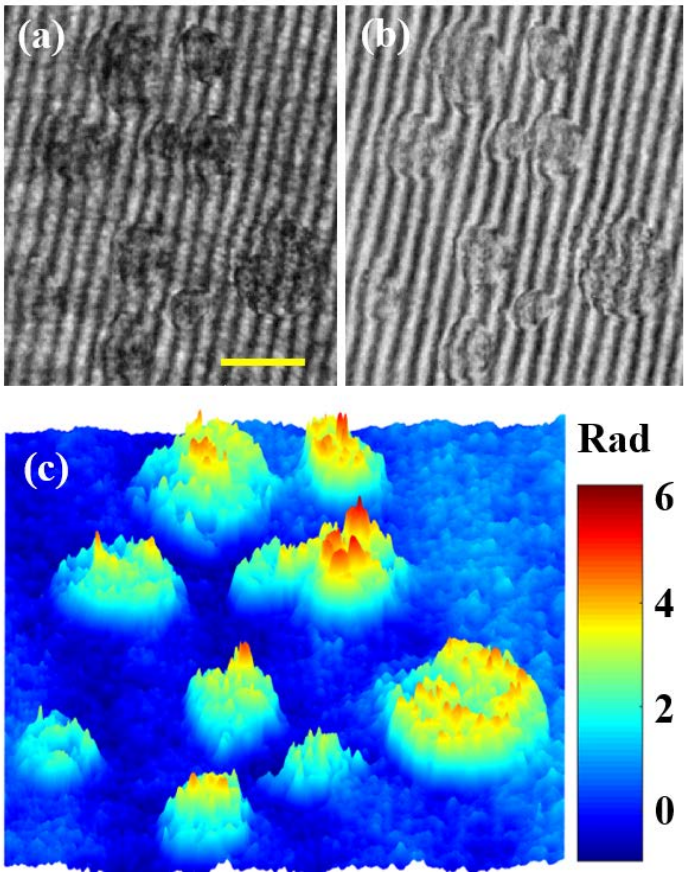

Figure 3.33. Experimental validation provided by *π-SMIM* involving PC-3 cells of different sizes. (a) recorded hologram; (b) subtracted hologram; and (c) perspective view of retrieved unwrapped quantitative phase distribution. Yellow line in (a) represents 20 μm.

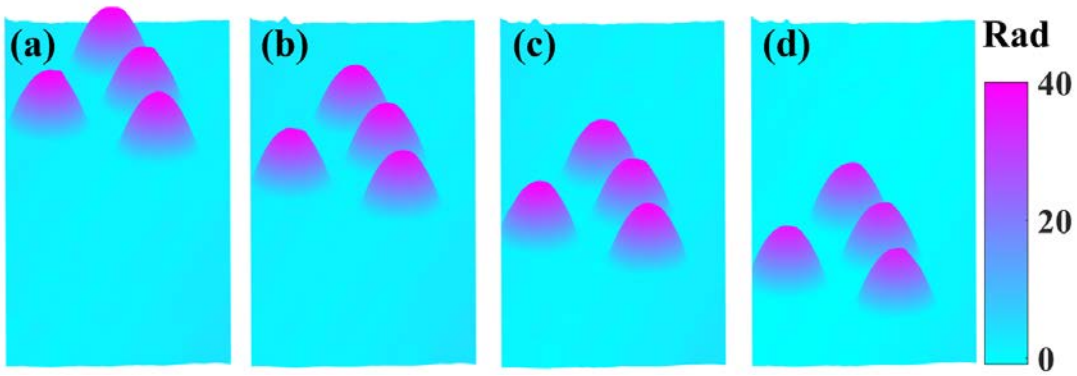

Figure 3.34. Experimental demonstration of *π-SMIM* single-shot capability involving flowing microbeads: (a)-(d) perspective visualizations of unwrapped phase distributions for four (0, 5, 10, and 15 s) time lapses (full movie duration of 15s).

Chapter 4

Summary, conclusions and outlooks

4.1. Summary and conclusions

The main goal of the present thesis has been the development and improvement of *SMIM* technique. *SMIM* is a *QP-DHM* technique based on the idea of introducing minimal modifications to a conventional bright field microscope in order to convert it into a holographic one in an easy way. Such modifications are focused on the inclusion of a CPI configuration in the microscope embodiment. That CPI architecture is based on a S-M approach.

To equip the microscope with holographic capabilities, *SMIM* implements three main changes in the microscope embodiment: 1) the replacement of the broadband illumination by a coherent one (LD, SLD, etc.), 2) the spatial multiplexing of the input plane, dividing it into two or three regions to enable reference beam transmission (leaving a clear region without sample), and 3) the insertion of an optical element (diffraction grating, BS cube, etc.) to provide interferometric recording.

First approaches to *SMIM* concept were carried out as demonstrator at the lab by Micó *et al.* [Micó-2006B, Micó-2008, Micó-2009]. Few years later, the authors implemented such a concept in a standard bright field microscope, thus giving rise to

SMIM technique itself [Micó-2014]. Following that research area, many attempts to improve the capabilities of *SMIM* approach have been validated and reported during this thesis. Thus, six different experiments have been presented in which a few or several aspects of the technique have been enhanced. More specifically, *SMIM* has been implemented:

1) under partially coherent illumination and defining a less restrictive spatial multiplexing at the input plane. As result, retrieved phase images present a reduction of the coherent noise and a larger area of inspection (Section 3.3) [Picazo-Bueno-2016];

2) using *SA SR* techniques for resolution improvement, therefore compensating the FOV limitation of *SMIM* technique (Section 3.4) [Picazo-Bueno-2017];

3) in combination with HHT for phase retrieval in a single-shot when a *slightly off-axis* configuration is defined (Section 3.5) [Picazo-Bueno-2018B];

4) in reflective and transflective imaging modes to extend the range of samples to be inspected (Section 3.6) [Picazo-Bueno-2019A];

5) by externally inserting an add-on module based on a BS cube which enables easy variation of the interferometric configuration as well as simple single-shot phase retrieval method involving a *slightly off-axis* configuration (Section 3.7) [Picazo-Bueno-2019B];

6) and introducing a BS cube inside the microscope embodiment to avoid astigmatic aberrations and using a robust and accurate phase retrieval method based on HHT for single-shot *QPI* when *quasi on-axis* and low quality holograms are considered (Section 3.8) [Trusiak-2019].

Additionally, an introductory experiment [Picazo-Bueno-2018A] has been performed to provide us a better understanding of *QP-DHM* layouts and their capabilities as well as introductory work to *QP-DHM* (Section 3.1). Essentially, a lab-built DHM platform has been combined with a broadband (white light) illumination mode to obtain simultaneously qualitative (incoherent mode) and quantitative (coherent mode) analysis of synthetic and biological samples. Since it uses an *off-axis* holographic configuration, the imaging platform has enabled the inspection and analysis of dynamic biosamples, only limited by acquisition rate of the digital camera. In addition, the use of a water-immersion objective lens has guaranteed the optimization of the resolution limit. Furthermore, the influence of vibrations and thermal changes has been reduced due to the interferometric layout has been placed behind the imaging lens.

Such a dual-mode imaging platform [Picazo-Bueno-2018A] has been validated by means of three experiments: 1) DHM layout calibration involving synthetic samples (spherical and cone tip microbeads) and tested for real-time processes by imaging the induced movement of a fixed biosample; 2) several types of fixed cells (neuroblastoma, breast cancer and hippocampal neuron cells) have been simultaneously imaged employing both incoherent and coherent illumination modes; 3) single-shot and dual-mode capabilities have been validated by the dynamic analysis of a living cell in contraction. Retrieved phase images have shown lower SNR in case of dynamic samples, since fixed cells have been sandwiched between a microscope slide and a coverslip (negligible wavefront disturbances). By contrast, living cells need water flowing to supply physiological nutrients, so considerable phase turbulences are induced thus reducing SNR (considerable wavefront disturbances).

In conclusion, the proposed dual-mode imaging platform has allowed simultaneous qualitative and quantitative analysis of dynamic phenomena by using incoherent *bright field microscopy* and *QP-DHM*. However, some live cell imaging applications may be restricted by the stabilization complexity of the system conditions, since sterile conditions, sample temperature preservation, and water evaporation in the immersed objective lens must be considered.

Moving forward, Section 3.2 describes for completeness the way of equipping a regular microscope with QPI capability by using *SMIM* approach. In particular, a *SMIM* architecture based on a diffraction grating interferometer has been qualitatively described and mathematically analysed assuming that the FOV is spatially multiplexed into two regions. In fact, the basic frequency of the diffraction grating, necessary to provide appropriate recording conditions, has been calculated as a function of several system parameters such as the wavelength, the focal length of the tube lens system and the area and pixel size of the digital sensor.

SMIM layout reported in [Micó-2014] exhibited some limitations regarding FOV restriction and coherent noise existing in retrieved phase images. In order to overcome such constraints, a new *SMIM* layout has been reported and overviewed in Section 3.3 [Picazo-Bueno-2016], which incorporates two main improvements: 1) the coherent noise reduction in phase images by replacing the coherent light source for a partially (temporally reduced) coherent source, showing better image quality in reconstructions; and 2) a less restrictive FOV limitation by defining a different spatial distribution at the input plane in which it is divided into two regions, instead of three, enlarging the inspected area.

The approach has been first validated by means of a calibration step involving a resolution test target and microbeads, and then applied to *QPI* of fixed biosamples (RBCs, SS cells and PC-3 cells). Finally, the coherent noise reduction has been calculated in phase images, therefore obtaining an improvement factor of around 10

as a result of using partially coherent light. The use of temporally reduced coherent sources is particularly relevant when implementing *DHM* with commercially available objectives and microscope embodiments containing a lot of glass-air interfaces without specific coatings for the used wavelength, thus producing several back reflections that can result in undesirable interference patterns.

Nonetheless, the main drawbacks of such an arrangement are related to the real-time analysis of dynamic processes and the use of the digital sensor. Since the coherence of the light source is temporally reduced, an *off-axis* holographic configuration is prevented and a temporal P-S algorithm is therefore employed for phase retrieval, losing single-shot capability. On the other hand, the FOV division into two regions and the digital sensor alignment with the optical axis of the microscope forces to waste half sensor area. Hence, the proposed *SMIM* can result appealing in applications where enhanced SNR and FOV are more important issues than real-time analysis.

On the other hand, a major handicap of using *SMIM* is related to the useful FOV. As a consequence of the necessity of leaving a clear region for reference beam transmission, *SMIM* reduces the useful FOV in, at least, one-half. That can be critical when dealing with high or medium NA lenses. Instead, low NA lenses provides lower resolution, present larger FOV and other appealing properties such as longer working distances, larger DOF, reduced prices, etc. that are very appealing in *microscopy*. Hence, SR techniques can be applied when working with low NA lenses in order to benefit from all those properties but without losing resolution.

For that reason, we have carried out an experiment in which *SMIM* technique is equipped with SR capability, defining *S2MIM* technique (Section 3.4) [Picazo-Bueno-2017]. *S2MIM* is based on the application of *SA SR* techniques and enables SR imaging by angular and time multiplexing with a resolution gain factor of 2. The angular multiplexing has been sequentially implemented by displacing the light source to several off-axis positions in order to recover a set of complementary spatial-frequency apertures and thus generating a SA. Experimental validations have been conducted for two different low NA microscope lenses involving two resolution test targets. Nevertheless, *S2MIM* can be theoretically applicable to higher NA lenses by considering higher illumination angles.

The setup results as a combination between both previously reported *SMIM* approaches [Micó-2014, Picazo-Bueno-2016]. On one hand, we have used a laser diode to illuminate the input plane, which has been spatially multiplexed into three regions (as in [Micó-2014]). On the other hand, a *slightly off-axis* holographic configuration has been defined and a temporal P-S algorithm has been employed for phase retrieval (as in [Picazo-Bueno-2016]). Hence, the main drawback of *S2MIM* is the prevention of single-shot operation principle, due to both time multiplexing

strategy and temporal P-S method implementations. In addition, the FOV division into three regions makes more limited the area to be inspected. However, *S2MIM* reduces such a FOV limitation by doubling the resolving power.

The use of partially coherent light sources often prevents of an *off-axis* holographic configuration, thus forcing to adopt either a *slightly off-axis* or an *on-axis* holographic configuration, as happened in two previously presented *SMIM* architectures [Picazo-Bueno-2016, Picazo-Bueno-2017]. Those configurations are generally accompanied with temporal P-S methods for phase retrieval, thus eliminating the chance of real-time analysis of dynamic processes. Thus, the sample must be static during the whole recording process. To solve such an issue, we have supplied *SMIM* with single-shot capability when working under those conditions [Picazo-Bueno-2018B]. The developed technique, named *H2S2MIM*, combines *SMIM* with a modified version of S2H2PM method reported in [Trusiak-2016]. Such an phase retrieval method is based on HHT methods to retrieve the phase using a single frame. Such modifications have been performed to enhance robustness and versatility to the approach and include: 1) an automatic masking algorithm based on VID and Otsu thresholding applied to hologram, 2) an improved fringe direction estimator based on EMD adaptive filtering, and 3) an iterative phase unwrapping algorithm based on TIE.

Experimental validations have been carried out following three steps: 1) calibration process involving microbeads, 2) *QPI* of static cells, and 3) single-shot validation by using flowing microbeads. In that way, it has been demonstrated that *H2S2MIM* enables real-time *QPI* in regular microscopes even though both partially coherent light and *slightly off-axis* configuration are employed. By contrast, perhaps the main drawback of the proposed technique is the complexity of the algorithm employed for phase retrieval.

SMIM approaches reported in [Picazo-Bueno-2016, Picazo-Bueno-2017, Picazo-Bueno-2018B] have been only validated in transmission imaging mode, so that the potential of *SMIM* for the analysis of a wide range of samples became reduced to transmissive samples. Hence, in order to extend the range of applicability, we have additionally validated *SMIM* technique not only in reflective imaging mode but also in transflective modality, thus developing the *OV-SMIM* technique (Section 3.6) [Picazo-Bueno-2019A].

The experimental validation of *OV-SMIM* has consisted of two parts: reflective and transflective experiments. Reflective modality calibration involved a diffraction grating, whose retrieved height has been successfully compared with *AFM* measurements. On the other hand, transflective imaging validation has included the use of a resolution test target as well as microbeads. Here, both retrieved phase images

(reflection and transmission) have showed high concordance each other. Furthermore, the transflective imaging mode has enabled the RI calculation of microbeads even though the thickness of such microbeads is not entirely retrieved.

In conclusion, reflective imaging mode and *OV-SMIM* have allowed the analysis of not only transmissive but also reflective samples, thus giving completeness to the *SMIM* approach. In addition, *OV-SMIM* has permitted RI inspection of homogeneous samples. However, two major drawbacks of *OV-SMIM* are related to the FOV limitation and the specific design of the chamber necessary for transflective imaging. The first one is not a big deal, since, in *microscopy*, the FOV defined by the sensor is normally smaller than the optical FOV given by the imaging system, so that we can make use of those parts that fall outside the digital sensor for reference beam transmission (something common to all *SMIM* approaches). Regarding the chamber design, nowadays customized ones can be manufactured for specific applications.

In those previous validations, *SMIM* is defined as a technique that equipped a regular microscope with QPI capability by introducing a coherent light source, a specific FOV spatial distribution and a 1D diffraction grating for interferometric recording. The use of a grating provides a single hologram which is often recorded under *slightly off-axis* configuration [Picazo-Bueno-2016, Picazo-Bueno-2017, Picazo-Bueno-2018B, Picazo-Bueno-2019A]. Such a holographic configuration prevents the application of Fourier filtering methods for phase retrieval, so temporal P-S algorithms are generally employed for that purpose. Nevertheless, we have also presented *H2S2MIM* as a technique using HHT for phase demodulation with single-shot operation principle. However, *H2S2MIM* algorithm is not trivial and requires some experience. Furthermore, since the microscope embodiment restricts the axial position of the grating (not every position is available), changes in the holographic configuration are only related to the use of different gratings with different spatial frequencies[46].

With the aims of decreasing the complexity of the reconstruction process when a *slightly off-axis* configuration is defined and enabling easy carrier frequency variation, we have experimentally validated a *single-shot SO-DHM* approach based on a compact, robust and low-cost add-on module placed at the output port of the microscope (Section 3.7) [Picazo-Bueno-2019B]. Such a module consisted on a CPI based on a BS cube, which has produced two simultaneous π-shifted holograms, and a SL to compensate astigmatism introduced by the BS cube rotation. Phase information has been retrieved by subtraction algorithm (DC term removal) and further Fourier filtering application. Experimental validation has been conducted in three steps: 1) calibration process involving resolution test targets, 2) *QPI* of fixed cells, 3) demonstration of real-time analysis capability by using flowing microbeads.

[46] After wavelength selection.

Experimental results have demonstrated that such a *single-shot SO-DHM* technique provides accurate phase retrieval even though density or dynamic samples are analysed.

Hence, the proposed *single-shot SO-DHM* approach provides single-shot *QPI* allowing the study of dynamic events even though a *slightly off-axis* holographic configuration is defined[47]. Moreover, the add-on module can modify the carrier frequency in a simpler and more versatile way than a grating by rotating the BS cube, therefore permitting all types of holographic configurations. Furthermore, the FOV reduction to one half of the available one is equal to the best conditions achieved in other *SMIM* approaches. On the other hand, maybe the main drawback of such a method is the necessity of a SL for astigmatism compensation, thus increasing the complexity of the setup. Another disadvantage to consider could be the useless region that appears between interferograms. Such a region increases with the rotation angle and the magnification, even covering all sensor area in extreme cases.

Both axial and angular positions of the BS cube presented in above *single-shot SO-DHM* technique [Picazo-Bueno-2019B] introduced a non-negligible amount of astigmatism, which reduced the quality of the images. To solve that problem, a SL was inserted just before the BS cube, forming a relatively complex module added at the output port of the microscope. However, such an issue can be easily avoided by introducing the BS cube inside the microscope embodiment, just between the infinity corrected objective and the tube lens system, i.e., where the light path of the rays is parallel. In that case, the BS cube can be essentially regarded as a thick plane-parallel plate and no astigmatism (only prismatic effect) will be introduced. Otherwise [Picazo-Bueno-2019B], nonparallel rays can cause a significant amount of astigmatism to fully destroy image quality [Zhong-2015]. In addition, the previously reported *single-shot SO-DHM* approach required a *slightly off-axis* configuration to allow correct phase retrieval, so the conjugated orders must not overlap at the Fourier domain. For those reasons, we have developed *π-SMIM* technique, which employs both a BS cube placed behind the microscope lens and phase demodulation algorithm based on subtraction and HHT methods. With those modifications, *π-SMIM* has enabled *QPI* of dynamic events even when dealing with low quality holograms and *quasi on-axis* holographic configurations.

[47] As *H2S2MIM* technique.

Experimental validation has mainly consisted in two parts: 1) a validation process of the *π-SMIM* working principle involving different types of fixed cells (clustered, variable size and density), and 2) a demonstration of the single-shot operation principle by means of the analysis of flowing microbeads. Such results have proved the capability of the proposed technique to retrieve phase information from *quasi on-axis*, single-shot, and very low quality holograms. Hence, *π-SMIM* merges all benefits from both *single-shot SO-DHM* approach presented in [Picazo-Bueno-2019B] (easy carrier frequency variation, FOV multiplexed in two halves, application of subtraction algorithm) and the *H2S2MIM* reported in [Picazo-Bueno-2018B] (single-shot operation principle under *quasi on-axis* configuration, space bandwidth optimization, phase retrieval from cumbersome holograms). On the other hand, the complexity of the HHT algorithm, the necessity of perfect overlapping between interferograms in the reconstruction stage, and the useless region present between interferograms are the main drawbacks existing in the proposed *π-SMIM* technique.

In conclusion, all those approaches performed during the present thesis have contributed to develop and improve *SMIM* technique and have demonstrated the versatility of *SMIM* to upgrade a standard bright field microscope into a holographic one with the application of a few, simple and cost-effective modifications.

4.2. Outlooks

In light of the outcomes and conclusions drawn from this thesis, there exist several ways to continue with the development of *SMIM* technique. Just to have an idea of the great number of feasible further improvements, implementations and applications of this technique, we cite some of them:

- Regarding potential improvements of the presented *SMIM* arrangements, we could move forward to the implementation of a transflective imaging modality under partially coherent illumination which employs a fast, robust, and accurate algorithm based on HHT for single-exposure working principle. This fact could provide real-time high-quality information about both RI and morphology variations of dynamic samples.

- *SMIM* can be additionally implemented in conjunction with other interferometric techniques based on wavelength multiplexing, such as *multi-wavelength DHM*, which solves the 2π ambiguity problems presented in phase unwrapping processes in *QP-DHM* when dealing with steep borders [Warnasoo-2007, Mann-2008], *single-shot super-resolved interferometric microscopy*, previously validated in lensless Gabor holography for achieving a resolution improvement [Granero-2015], or *multi-illumination single-holographic-exposure lensless Fresnel*

microscopy, which includes an extremely robust and fast iterative algorithm for high-quality phase retrieval [Sanz-2015, Sanz-2017, Sanz-2018], just to cite a few.

- On the other hand, *SMIM* technique can be also combined with other microscopy techniques, such as *fluorescence microscopy* or *conventional bright field microscopy*, thus transferring the idea presented in [Picazo-Bueno-2018A] from the optical table to a commercially available microscope. Thus, there would exist the possibility of achieving simultaneous complementary information about different dynamic processes, being especially appealing for the analysis of cellular processes.

Furthermore, in parallel with the research presented along this report, I have taken the opportunity to be actively working in additional experiments strongly related to the topic of this thesis, based on *digital in-line lensless holographic microscopy* [Sanz-2015, Sanz-2017, Sanz-2018A, Sanz-2018B], and its application to both the 4D tracking analysis of sperm motility [Soler-2018] and the development of a novel marking reader for progressive addition lenses [Perucho-2016].

References

[Abbe-1873] E. Abbe, “Beiträge zur theorie des mikroskops und der mikroskopischen wahrnehmung,” Arch. F. Microsc. Anat. 9, 413-468 (1873).

[Abdelsalam-2012] D. G. Abdelsalam, B. Yao, P. Gao, J. Min, and R. Guo, “Single-shot parallel four-step phase shifting using on-axis Fizeau interferometry,” Appl. Opt. 51(20), 4891-4895 (2012).

[Abramson-1980] N. Abramson, and H. Bjelkhagen, “Deformation displacement and vibration investigations in manufacturing applications using a new hologram interferometry technique,” Opt. Las. Eng. 1(1), 51-68 (1980).

[Anand-2011] A. Anand, V. Chhaniwal, and B. Javidi, “Imaging embryonic stem cell dynamics using quantitative 3-D digital holographic microscopy,” IEEE Photon. J. 3(3), 546-554 (2011).

[Antkowiak-2008] M. Antkowiak, N. Callens, C. Yourassowsky, and F. Dubois, “Extended focused imaging of a microparticle field with digital holographic microscopy”, Opt. Lett. 33(14), 1626-1628 (2008).

[Arines-2011] J. Arines and E. Acosta, “Low-cost adaptive astigmatism compensator for improvement of eye fundus camera,” Opt. Lett. 36(21), 4164-4166 (2011).

[Armitage-1965] J. D. Armitage, A. W. Lohmann, and D. P. Parish, “Superresolution image forming systems for objects with restricted lambda dependence,” Jpn. J. Appl. Phys. 4, 273-275 (1965).

[Awatsuji-2006A] Y. Awatsuji, T. Tahara, A. Kaneko, T. Koyama, K. Nishio, S. Ura, T. Kubota, and O. Matoba, “Parallel three-step phase-shifting digital holography,” Appl. Opt. 45(13), 2995-3002 (2006).

[Awatsuji-2006B] Y. Awatsuji, M. Sasada, A. Fujii, and T. Kubota, “Scheme to improve the reconstructed image in parallel quasi-phase-shifting digital holography,” Appl. Opt. 45(5), 968-974 (2006).

[Baumbach-2006] T. Baumbach, E. Kolenovic, V. Kebbel, and W. Jüptner, "Improvement of accuracy in digital holography by use of multiple holograms," Appl. Opt. 45(24), 6077 (2006).

[Benton-1969] S. A. Benton, "Hologram Reconstructions with Extended Incoherent Sources," J. Opt. Soc. Am. 59, 1545A (1969).

[Bernet-2006] S. Bernet, A. Jesacher, S. Fürhapter, C. Maurer, and M. Ritsch-Marte, "Quantitative imaging of complex samples by spiral phase contrast microscopy," Opt. Express 14(9), 3792-3805 (2006).

[Bettenworth-2014] D. Bettenworth, P. Lenz, P. Krausewitz, M. Brückner, S. Ketelhut, D. Domagk, and B. Kemper, "Quantitative Stain-Free and Continuous Multimodal Monitoring of Wound Healing In Vitro with Digital Holographic Microscopy," PLOS ONE 9(9), e107317 (2014).

[Bhaduri-2014] B. Bhaduri, C. Edwards, H. Pham, R. Zhou, T. H. Nguyen, L. L. Goddard, and G. Popescu, "Diffraction phase microscopy: principles and applications in materials and life sciences," Adv. Opt. Photon. 6(1), 57-119 (2014).

[Bianco-2013] V. Bianco, M. Paturzo, P. Memmolo, A. Finizio, P. Ferraro, and B. Javidi, "Random resampling masks: a non-Bayesian one-shot strategy for noise reduction in digital holography," Opt. Lett. 38(5), 619-621 (2013).

[Born-1999] M. Born, E. Wolf, A. B. Bhatia, P. C. Clemmow, D. Gabor, A. R. Stokes, A. M. Taylor, P. A. Wayman, and W. L. Wilcock, *Principles of Optics: Electromagnetic Theory of Propagation, Interference and Diffraction of Light*, 7th edition (Cambridge University Press, 1999).

[Braat-1997] J. Braat, "Analytical expressions for the wave-front aberration coefficients of a titlted plane-parallel plate," Appl. Opt. 36(32), 8459-8467 (1997).

[Bragg-1939] W. L. Bragg, "A new type of X-ray microscope," Nature 143(3625), 678-678 (1939).

[Bragg-1942] W. L. Bragg, "The X-ray microscope," Nature 149(3782), 470-471 (1942).

[Brooks-1966] L.O. Heflinger, R.F. Wuerker, and R.E. Brooks, "Holographic interferometry," J. Appl. Phys. 37(2), 642-649 (1966).

[Burch-1965] J.M. Burch, "The application of lasers in production engineering," Prod. Eng. 44(9), 431-442 (1965).

[Castañeda-2018] R. Castañeda and J. Garcia-Sucerquia, “Single-shot 3D topography of reflective samples with digital holographic microscopy,” Appl. Opt. 57(1), A12 (2018).

[Caulfield-1979] H. J. Caulfield, *Handbook of optical holography*, Academic Press, (1979).

[Charrière-2006] F. Charrière, A. Marian, F. Montfort, J. Kuehn, T. Colomb, E. Cuche, P. Marquet, and C. Depeursinge, “Cell refractive index tomography by digital holographic microscopy,” Opt. Lett. 31(2), 178-180 (2006).

[Chen-2007] G. L. Chen, C. Y. Lin, M. K. Kuo, and C. C. Chang, “Numerical suppression of zero-order image in digital holography,” Opt. Exp. 15(14), 8851-8856 (2007)

[Chhaniwal-2012] V. Chhaniwal, A. S. G. Singh, R. A. Leitgeb, B. Javidi, and A. Anand, “Quantitative phase-contrast imaging with compact digital holographic microscope employing Lloyd’s mirror,” Opt. Lett. 37(24), 5127-5129 (2012).

[Cho-2018] J. Cho, J. Lim, S. Jeon, G.-J. Choi, H. Moon, N.-C. Park, and Y.-P. Park, "Dual-wavelength off-axis digital holography using a single light-emitting diode," Opt. Express 26(2), 2123-2131 (2018).

[Collier-1965] R. J. Collier, E. T. Doherty, and K. S. Pennington, “Application of moiré techniques to holography,” Appl. Phys. Lett. 7(8), 223- (1965).

[Collier-1971] R. J. Collier, C. B. Burkhardt, and L. H. Lin, *Optical holography*, Academic Press, New York (1971).

[Collings-1988] N. Collings, *Optical pattern recognition using holographic techniques*, Addison-Wesley, (1988).

[Colomb-2005] T. Colomb, F. Dürr, E. Cuche, P. Marquet, H. G. Limberger, R.-P. Salathé, and C. Depeursinge, “Polarization microscopy by use of digital holography: application to optical-fiber birefringence measurements,” Appl. Opt. 44(21), 4461-4469 (2005).

[Colomb-2006] T. Colomb, E. Cuche, F. Charrière, J. Kühn, N. Aspert, F. Montfort, P. Marquet, and C. Depeursinge, “Automatic procedure for aberration compensation in digital holographic microscopy and applications to specimen shape compensation,” Appl. Opt. 45(5), 851-863 (2006).

[Coppola-2004] G. Coppola, P. Ferraro, M. Iodice, S. De Nicola, A. Finizio, and S. Grilli, “A digital holographic microscope for complete characterization of microelectromechanical systems,” Meas. Sci. Technol. 15(3), 529-539 (2004).

[Coquoz-1995] O. Coquoz, R. Conde, F. Taleblou, and C. Depeursinge, “Performances of endoscopic holography with a multicore optical-fiber”, Appl. Opt. 34(31), 7186-7193 (1995).

[Cotte-2010] Y. Cotte, M. F. Toy, E. Shaffer, N. Pavillon, and C. Depeursinge, “Sub-Rayleigh resolution by phase imaging,” Opt. Lett. 35(13), 2176-2178 (2010).

[Creath-1988] K. Creath, “V Phase measurement interferometry techniques,” Progress in Optics, Elsevier 26, 349-393 (1988).

[Crha-2011] I. Crha, J. Zakova, M. Huser, P. Ventruba, E. Lousova, and M. Pohanka, “Digital holographic microscopy in human sperm imaging”, J. Assist. Reprod. Genet. 28(8), 725-729 (2011).

[Cuche-1999A] E. Cuche, P. Marquet, and C. Depeursinge, “Simultaneous amplitude-contrast and quantitative phase-contrast microscopy by numerical reconstruction of Fresnel off-axis holograms”, Appl. Opt. 38(34), 6994-7001 (1999).

[Cuche-1999B] E. Cuche, F. Bevilacqua, and C. Depeursinge, “Digital holography for quantitative phase contrast imaging”, Opt. Lett. 24(5), 291-293, (1999).

[Cuche-2000] E. Cuche, P. Marquet, and C. Depeursinge, “Spatial filtering for zero-order and twin-image elimination in digital off-axis holography”, Appl. Opt. 39(23), 4070-7075 (2000).

[Curl-2005] C. L. Curl, C. J. Bellair, T. Harris, B. E. Allman, P. J. Harris, A. G. Stewart, A. Roberts, K. A. Nugent, and L. M. D. Delbridge, “Refractive index measurement in viable cells using quantitative phase-amplitude microscopy and confocal microscopy,” Cytometry Part A, 65A(1), 88-92 (2005).

[Dändliker-1980] R. Dändliker, “I Heterodyne holographic interferometry,”. in *Progress in Optics*, ed. E. Wolf, 17, 1-84 (Elsevier 1980).

[Danesh-2007] M. DaneshPanah, and B. Javidi, “Tracking biological microorganisms in sequence of 3D holographic microscopy images”, Opt. Express, 15(17), 10761-10766 (2007).

[Danesh-2010] M. DaneshPanah, S. Zwick, F. Schaal, M. Warber, B. Javidi, and W. Osten, “3D holographic imaging and trapping for non-invasive cell identification and tracking”, J. Disp. Technol. 6(10), 490-499 (2010)

[Degiorgio-1980] V. Degiorgio, “Phase shift between the transmitted and the reflected optical fields of a semireflecting lossless mirror is π/2,” Am. J. Phys. 48(81), 81-82 (1980).

[Demoli-2003] N. Demoli, J. Mestrovic, and I. Sovic, “Subtraction digital holography,” Appl. Opt. 42(5), 798-804 (2003).

[Denisyuk-1962] Y.N. Denisyuk, “Photographic reconstruction of the optical properties of an object in its own scattered radiation field,” Sov. Phys. Dokl. 7, 543-545 (1962).

[Denisyuk-1963] Y.N. Denisyuk, “On the reproduction of the optical properties of an object by the wave field of its scattered radiation,” Opt. Spectr. 15, 279-284 (1963).

[Denisyuk-1965] Y.N. Denisyuk, “On the reproduction of the optical properties of an object by the wave field of its scattered radiation,” Opt. Spectr. 18, 152-157 (1965).

[Desse-2012] J. M. Desse, P. Picart, and P. Tankam, "Digital color holography applied to fluid and structural mechanics," Opt. Las. Eng. 50(1), 18-28 (2012).

[Ding-2010] H. Ding and G. Popescu, “Instantaneous spatial light interference microscopy,” Opt. Express 18(2), 1569-1575 (2010).

[Dorrio-1999] B.V. Dorrio, J.L. Fernandez, “Phase evaluation methods in whole-field optical measurement techniques”, Meas. Sci. Technol. 10, R33-R55 (1999).

[Dubois-1999] F. Dubois, L. Joannes, and J.-C. Legros, “Improved three-dimensional imaging with a digital holography microscope with a source of partial spatial coherence”, Appl. Opt. 38(34), 7085-7094, 1999.

[Dubois-2004] F. Dubois, M.-L. N. Requena, C. Minetti, O. Monnom, and E. Istasse, “Partial spatial coherence effects in digital holographic microscopy with a laser source,” Appl. Opt. 43(5), 1131-1139 (2004).

[Dubois-2006A] F. Dubois, C. Schockaert, N. Callens, and C. Yourassowsky, “Focus plane detection criteria in digital holography microscopy by amplitude analysis,” Opt. Express 14(13), 5895-5908 (2006).

[Dubois-2006B] F. Dubois, C. Yourassowsky, O. Monnom, J. Legros, O. Debeir, P. Van Ham, R. Kiss, and C. Decaestecker, "Digital holographic microscopy for the three-dimensional dynamic analysis of in vitro cancer cell migration," J. Biomed. Opt. 11(5), 054032 (2006).

[Dubois-2006C] F. Dubois, N. Callens, C. Yourassowsky, M. Hoyos, P. Kurowski, and O. Monnom, "Digital holographic microscopy with reduced spatial coherence for three-dimensional particle flow analysis," Appl. Opt. 45(5), 864-871 (2006).

[Dubois-2012] F. Dubois and C. Yourassowsky, "Full off-axis red-green-blue digital holographic microscope with LED illumination," Opt. Lett. 37(12), 2190-2192 (2012).

[Ebrahimi-2018] S. Ebrahimi, M. Dashtdar, E. Sánchez-Ortiga, M. Martínez-Corral, and B. Javidi, "Stable and simple quantitative phase-contrast imaging by Fresnel biprism," Appl. Phys. Lett. 112(11), 113701 (2018).

[El-Sum-1952] H.M.A. El-Sum, and P. Kirkpatrick, "Microscopy by reconstructed wavefronts," Phys. Rev. 85, 763 (1952).

[Esseling-2012] M. Esseling, B. Kemper, M. Antkowiak, D. J. Stevenson, L. Chaudet, M. A. A. Neil, P. W. French, G. von Bally, K. Dholakia, and C. Denz, "Multimodal biophotonic workstation for live cell analysis," J. Biophotonics 5(1), 9-13 (2012)

[Faigel-1999] G. Faigel, and M. Tegze, "X-ray holography," Rep. Prog. Phys. 62(3), 355-393 (1999).

[Faridian-2014] A. Faridian, G. Pedrini, and W. Osten, "Opposed-view dark-field digital holographic microscopy," Biomed. Opt. Express 5(3), 728-736 (2014).

[Ferrari-2007] J.A. Ferrari, and E.M. Frins, "Single-element interferometer," Opt. Commun. 279(2), 235-239, (2007).

[Ferraro-2003] P. Ferraro, S. De Nicola, A. Finizio, G. Coppola, S. Grilli, C. Magro, and G. Pierattini, "Compensation of the inherent wave front curvature in digital holographic coherent microscopy for quantitative phase-contrast imaging," Appl. Opt. 42(11), 1938-1946 (2003).

[Ferraro-2005] P. Ferraro, S. Grilli, D. Alfieri, S. D. Nicola, A. Finizio, G. Pierattini, B. Javidi, G. Coppola, and V. Striano, "Extended focused image in microscopy by digital holography", Opt. Express 13(18), 6738-6749 (2005).

[Frauel-2001] Y. Frauel, E. Tajahuerce, M.-A. Castro, and B. Javidi, “Distortion-tolerant three-dimensional object recognition with digital holography,” Appl. Opt. 40(23), 3887-3893 (2001).

[Françon-1952] M. Françon, “Amélioration de resolution d’optique,” Nuovo Cimento Suppl. 9, 283-290 (1952).

[Fu-2010] D. Fu, S. Oh, W. Choi, T. Yamaguchi, A. Dorn, Z. Yaqoob, R. R. Dasari, and M. S. Feld, “Quantitative DIC microscopy using an off-axis self-interference approach,” Opt. Lett. 35(14), 2370-2372 (2010).

[Gabai-2012] H. Gabai and N. T. Shaked, “Dual-channel low-coherence interferometry and its application to quantitative phase imaging of fingerprints”, Opt. Express 20(24), 26906-26912 (2012).

[Gabor-1948] D. Gabor, “A new microscope principle,” Nature 161(4098), 777-778 (1948).

[Gabor-1949] D. Gabor, “Microscopy by reconstructed wavefronts,” Proc. Roy. Soc. A 197(1051), 454-487 (1949).

[Gabor-1951] D. Gabor, “Microscopy by reconstructed wavefronts: II,” Proc. Phys. Soc. B 64(6), 449-469 (1951).

[Gabor-1966] D. Gabor, and W. P. Goss, “Interference Microscope with Total Wavefront Reconstruction,” J. Opt. Soc. Am. 56(7), 849-858 (1966).

[Gale-1996] D. M. Gale, M. I. Pether, and J. C. Dainty, “Linnik microscope imaging of integrated circuit structures,” Appl. Opt. 35(1), 131-148 (1996).

[Garcia-Suc-2006] Garcia-Sucerquia, W. Xu, S. K. Jericho, P. Klages, M. H. Jericho, and H. J. Kreuzer, "Digital in-line holographic microscopy," Appl. Opt. 45(5), 836–850 (2006).

[Gartner-1963] W. Gartner, and A. W. Lohmann, “An experiment going beyond Abbe’s limit of diffraction,” Z. Phys. 174, 18 (1963).

[Gass-2003] J. Gass, A. Dakoff, and M. K. Kim, "Phase imaging without 2π ambiguity by multiwavelength digital holography.," Opt. Lett. 28(13), 1141–1143 (2003).

[Gao-2010] P. Gao, I. Harder, V. Nercissian, K. Mantel, and B. Yao, “Phase-shifting point-diffraction interferometry with common-path and in-line configuration for microscopy,” Opt. Lett. 35(5), 712–714 (2010).

[Gao-2011A] P. Gao, B. Yao, I. Harder, N. Lindlein, and F. J. Torcal-Milla, “Phase-shifting Zernike phase contrast microscopy for quantitative phase measurement”, Opt. Lett. 36(21), 4305-4307 (2011).

[Gao-2011B] P. Gao, B. Yao, J. Min, R. Guo, J. Zheng, T. Ye, I. Harder, V. Nercissian, and K. Mantel, “Parallel two-step phase-shifting point-diffraction interferometry for microscopy based on a pair of cube beamsplitters," Opt. Express 19(3), 1930–1935 (2011).

[Girshovitz-2013] P. Girshovitz and N. T. Shaked, “Compact and portable low-coherence interferometer with off-axis geometry for quantitative phase microscopy and nanoscopy,” Opt. Express 21(5), 5701–5714 (2013).

[Goodman-1967] J. W. Goodman, R. W. Lawrence, “Digital image formation from electronically detected holograms,” Appl. Phys. Lett. 11(3), 77-79 (1967).

[Goodman-2005] J. W. Goodman, *Introduction to Fourier Optics*, Roberts & Co., 3rd Ed. (2005).

[Granero-2016] L. Granero, C. Ferreira, Z. Zalevsky, J. García, and V. Micó, “Single-exposure super-resolved interferometric microscopy by RGB multiplexing in lensless configuration,” Opt. Las. Eng. 82, 104-112 (2016).

[Greivenk-1984] J. E. Greivenkamp, “Generalized data reduction for heterodyne interferometry,” Opt. Eng. 23(4), 350–352 (1984).

[Grilli-2001] S. Grilli, P. Ferraro, S. De Nicola, A. Finizio, G. Pierattini, and R. Meucci, “Whole optical wavefields reconstruction by digital holography,” Opt. Express 9(6), 294–302 (2001).

[Grim-1966] M. A. Grim, and A. W. Lohman, “Super resolution image for 1-D objects,” J. Opt. Soc. Am. 56(9), 1151-1156 (1966).

[Groh-1968] G. Groh, “Multiple imaging by means of point holograms,” Appl. Opt. 7(8), 1643-1644 (1968).

[Guo-2013] R. Guo, B. Yao, P. Gao, J. Min, J. Han, X. Yu, M. Lei, S. Yan, Y. Yang, D. Dan, and T. Ye, “Parallel on-axis phase-shifting holographic phase microscopy based on reflective point-diffraction interferometer with long-term stability,” Appl. Opt. 52(15), 3484–3489 (2013).

[Guo-2014] R. Guo, B. Yao, J. Min, M. Zhou, X. Yu, M. Lei, S. Yan, Y. Yang, and D. Dan, “LED-based digital holographic microscopy with slightly off-axis interferometry,” J. Opt. 16(12), 125408 (2014).

[Haddad-1992] W. S. Haddad, D. Cullen, J. C. Solem, J. W. Longworth, A. McPherson, K. Boyer, and C. K. Rhodes, “Fourier-transform holographic microscope,” Appl. Opt. 31(24), 4973–4978 (1992).

[Haines-1966] K.A. Haines, and B.P. Hildebrand, “Surface-deformation measurement using the wavefront reconstruction technique,” Appl. Opt. 5(4), 595-602 (1966)

[Hariharan-1983] P. Hariharan, “IV Colour holography,” in *Progress in Optics*, ed. E. Wolf 20, 263-324 (Elsevier 1983).

[Hariharan-1996] P. Hariharan, *Optical Holography: Principles, Techniques, and Applications*, Cambridge University Press, 2nd Ed. (1996).

[Huang-1971] T.S. Huang, “Digital holography,” Proc. IEEE 159, 1335–1346 (1971).

[Huang-1998] N. E. Huang, Z. Shen, S. R. Long, M. C. Wu, H. H. Shih, Q. Zheng, N.-C. Yen, C. C. Tung, and H. H. Liu, "The empirical mode decomposition and the Hilbert spectrum for nonlinear and non-stationary time series analysis," Proc. Royal Soc. A. 454(1971), 903–995 (1998).

[Ikeda-2005] T. Ikeda, G. Popescu, R.R. Dasari, and M.S. Feld, “Hilbert phase microscopy for investigating fast dynamics in transparent systems,” Opt. Lett. 30(10), 1165-1167 (2005).

[Iwai-2004] H. Iwai, C. Fang-Yen, G. Popescu, A. Wax, K. Badizadegan, R. R. Dasari, and M. S. Feld, “Quantitative phase imaging using actively stabilized phase-shifting low-coherence interferometry,” Opt. Lett. 29(20), 2399–2401 (2004).

[Janeckova-2009] H. Janeckova, P. Vesely, and R. Chmelik, “Proving tumour cells by acute nutritional/energy deprivation as a survival threat: a task for microscopy”, Anticancer Res 29(6), 2339–2345 (2009).

[Javidi-2005] B. Javidi, I. Moon, S. Yeom, and E. Carapezza, “Three-dimensional imaging and recognition of microorganism using single-exposure on-line (SEOL) digital holography,” Opt. Express 13(12), 4492-4506 (2005).

[Javidi-2010] B. Javidi, M. Daneshpanah, and I. Moon, “Three-dimensional holographic imaging for identification of biological micro/nanoorganisms,” IEEE Photon. J. 2(2), 256–259 (2010).

[Jeon-2016] S. Jeon, J. Cho, J. Jin, N. C. Park, and Y. P. Park, "Dual-wavelength digital holography with a single low-coherence light source," Opt. Express 24(16), 18408-18416 (2016).

[Johnston-2006] S. F. Johnston, *Holographic visions: a history of new science*, Oxford University Press (2006)

[Jourdain-2014] P. Jourdain, F. Becq, S. Lengacher, C. Boinot, P. J. Magistretti, and P. Marquet, “The human CFTR protein expressed in CHO cells activates aquaporin-3 in a cAMP-dependent pathway: study by digital holographic microscopy,” J. Cell Science 127(3), 546–556 (2014).

[Kang-2011] J. W. Kang, N. Lue, C.-R. Kong, I. Barman, N. C. Dingari, S. J. Goldfless, J. C. Niles, R. R. Dasari, and M. S. Feld, “Combined confocal Raman and quantitative phase microscopy system for biomedical diagnosis,” Biomed. Opt. Express 2(9), 2484–2492 (2011).

[Kartashev-1960] A. I. Kartashev, “Optical systems with enhanced resolving power,” Opt. Spectrosc. 9, 204-206 (1960).

[Kemper-2006] B. Kemper, D. Carl, J. Schnekenburger, I. Bredebusch, M. Schäfer, W. Domschke, and G. von Bally, “Investigation of living pancreas tumor cells by digital holographic microscopy,” J. Biomed. Opt. 11(3), 34005 (2006).

[Kemper-2007] B. Kemper, S. Kosmeier, P. Langehanenberg, G. von Bally, I. Bredebusch, W. Domschke, and J. Schnekenburger, “Integral refractive index determination of living suspension cells by multifocus digital holographic phase contrast microscopy,” J. Biomed. Opt. 12(5), 054009 (2007)

[Kemper-2008A] B. Kemper and G. von Bally, "Digital holographic microscopy for live cell applications and technical inspection," Appl. Opt. 47(4), A52–A61 (2008).

[Kemper-2008B] B. Kemper, S. Stürwald, C. Remmersmann, P. Langehanenberg, and G. von Bally, "Characterisation of light emitting diodes (LEDs) for application in digital holographic microscopy for inspection of micro and nanostructured surfaces," Opt. Las. Eng. 46(7), 499–507 (2008).

[Kemper-2011] B. Kemper, A. Vollmer, C. E. Rommel, J. Schnekenburger, and G. von Bally, “Simplified approach for quantitative digital holographic phase contrast imaging of living cells,” J. Biomed. Opt. 16(2), 026014 (2011).

[Kemper-2013] B. Kemper, Á. Barroso, M. Woerdemann, L. Dewenter, A. Vollmer, R. Schubert, A. Mellmann, G. von Bally, and C. Denz, "Towards 3D modelling and imaging of infection scenarios at the single cell level using holographic optical tweezers and digital holographic microscopy", J. Biophotonics. 6(3), 260–266 (2013).

[Kim-2009] T. Kim, T. C. Poon, "Autofocusing in optical scanning holography,", Appl. Opt. 48(34), H153–H159 (2009).

[Kim-2010] M. K. Kim, "Principles and techniques of digital holographic microscopy," SPIE Rev. 1, 018005 (2010).

[Kim-2011] M.K. Kim, *Digital holographic microscopy: Principles, Techniques, and Applications*, Springer (2011)

[King-2008] S. V. King, A. Libertun, R. Piestun, C. J. Cogswell, and C. Preza, "Quantitative phase microscopy through differential interference imaging", J. Biomed. Opt., 13(2), 024020 (2008).

[Kino-1990] G. S. Kino and S. S. Chim, "Mirau correlation microscope," Appl. Opt. 29(26), 3775–3783 (1990).

[Knox-1966] C. Knox, "Holographic microscopy as a technique for recording dynamic microscopic subjects," Science 153(3739), 989–990 (1966).

[Kogelnik-1965] H. Kogelnik, "Holographic image projection through inhomogeneous media," Bell Syst. Tech. J. 44(10), 2451-2455 (1965).

[Kolman-2010] P. Kolman and R. Chmelík, "Coherence-controlled holographic microscope," Opt. Express 18(21), 21990–22004 (2010)

[Kou-2010] S. S. Kou, L. Waller, G. Barbastathis, and C. J. R. Sheppard, "Transport-of intensity approach to differential interference contrast (TI-DIC) microscopy for quantitative phase imaging", Opt. Lett., 35(3), 447-449 (2010).

[Kreis-1986] T. Kreis, "Digital holographic interference-phase measurement using the Fourier-transform method", J. Opt. Soc. Am. A 3(6), 847–855 (1986).

[Kreis-1997] T. M. Kreis, and W. P. O. Jueptner, "Suppresion of the dc term in digital holography," Opt. Eng. 36(8), 2357-2360 (1997).

[Kronrod-1972] M.A. Kronrod, N.S. Merzlyakov, L.P. Yaroslavslii, "Reconstruction of a hologram with a computer," Sov. Phys. Tech. Phys. 17(2), 333–334 (1972).

[Kubota-2010] S. Kubota and J. W. Goodman, “Very efficient speckle contrast reduction realized by moving diffuser device,” Appl. Opt. 49(23), 4385–4391 (2010).

[Kühn-2007] J. Kühn, T. Colomb, F. Montfort, F. Charrière, Y. Emery, E. Cuche, P. Marquet, and C. Depeursinge, "Real-time dual-wavelength digital holographic microscopy with a single hologram acquisition," Opt. Express 15(12), 7231-7242 (2007).

[Kühn-2008] J. Kühn, F. Charrière, T. Colomb, E. Cuche, F. Montfort, Y. Emery, P. Marquet, and C. Depeursinge, “Axial sub-nanometer accuracy in digital holographic microscopy”, Meas. Sci. Technol. 19(7), 074007 (2008).

[Kühn-2013] J. Kühn, E. Shaffer, J. Mena, B. Breton, J. Parent, B. Rappaz, M. Chambon, Y. Emery, P. Magistretti, C. Depeursinge, P. Marquet, and G. Turcatti, “Label-free cytotoxicity screening assay by digital holographic microscopy”, Assay Drug Dev. Technol. 11(2), 101-107 (2013).

[Langeha-2008] P. Langehanenberg, B. Kemper, D. Dirksen, and G. von Bally, “Autofocusing in digital holographic phase contrast microscopy on pure phase objects for live cell imaging”, Appl. Opt. 47(19), D176–D182 (2008).

[Langeha-2009] P. Langehanenberg, L. Ivanova, I. Bernhardt, S. Ketelhut, A. Vollmer, D. Dirksen, G. Georgiev, G. von Bally, and B. Kemper, “Automated three-dimensional tracking of living cells by digital holographic microscopy,” J. Biomed. Opt. 14(1), 014018 (2009).

[Larkin-2001] K. G. Larkin, “Natural demodulation of two-dimensional fringe patterns. II stationary phase analysis of the spiral phase quadrature transform,” J. Opt. Soc. Am. A. 18(8), 1871–1881 (2001).

[Leith-1962] E. N. Leith, and J. Upatnieks, “Reconstructed wavefronts and communication theory,” J. Opt. Soc. Am. 52(10), 1123–1130 (1962).

[Leith-1963] E. N. Leith, and J. Upatnieks, “Wavefront reconstruction with continuous-tone objects,” J. Opt. Soc. Am. 53(12), 1377–1381 (1963).

[Leith-1964] E. N. Leith, and J. Upatnieks, “Wavefront reconstruction with diffused illumination and three-dimensional objects,” J. Opt. Soc. Am. 54(11), 1295–1301 (1964).

[Leith-1966] E.N. Leith, and J. Upatnieks, “Holographic imagery through diffusing media,” J. Opt. Soc. Am. 56(4), 523-523 (1966).

[León-2013] M. León-Rodríguez, R. Rodríguez-Vera, J. A. Rayas, and S. Calixto, "Digital holographic microscopy through a Mirau interferometric objective," Opt. Lasers Eng. 51(3), 240–245 (2013).

[León-2018] M. León-Rodríguez, J. A. Rayas, R. R. Cordero, A. Martínez-García, A. Martínez-Gonzalez, A. Téllez-Quiñones, P. Yañez-Contreras, and O. Medina-Cázares, "Dual-plane slightly off-axis digital holography based on a single cube beam splitter," Appl. Opt. 57(10), 2727-2735 (2018).

[Lim-2010] Y. Lim, S.-Y. Lee, and B. Lee, "Transflective digital holographic microscopy and its use for probing plasmonic light beaming," Opt. Express 19(6), 5202-5212 (2011).

[Lin-2010] Y. C. Lin and C. J. Cheng, "Determining the refractive index profile of micro-optical elements using transflective digital holographic microscopy," J. Opt. 12(11), 115402 (2010).

[Liu-2008] C. Liu, Y. S. Bae, W. Yang, and D. Y. Kim, "All-in-one multifunctional optical microscope with a single holographic measurement," Opt. Express 47(8), 087001 (2008)

[Liu-2011] R. Liu, D. K. Dey, D. Boss, P. Marquet, and B. Javidi, "Recognition and classification of red blood cells using digital holographic microscopy and data clustering with discriminant analysis", J. Opt. Soc. Am. A 28(6), 1204-1210 (2011).

[Lohmann-1965] A.W. Lohmann, and D.P. Paris, "Space-Variant Image Formation," J. Opt. Soc. Am. 55(8) 1007-1013 (1965).

[Lohmann-1967] A.W. Lohmann, and D.P. Paris, "Binary Fraunhofer holograms generated by computer," Appl. Opt. 6(10), 1739-1748 (1967).

[Lu-1968] S. Lu, "Generating multiple images for integrated circuits by Fourier-transform holograms," Proc. IEEE 56(1), 116-117 (1968).

[Lue-2007] N. Lue, W. S. Choi, G. Popescu, Y. Ikeda, R. R. Dasari, K. Badizadegan, and M. S. Feld, "Quantitative phase imaging of live cells using fast Fourier phase microscopy," Appl. Opt. 46(10), 1836-1842 (2007).

[Lue-2009] N. Lue, W. Choi, G. Popescu, Z. Yaqoob, K. Badizadegan, R.R. Dasari, and M.S. Feld, "Live cell refractometry using Hilbert Phase microscopy and Confocal Reflectance Microscopy," J. Phys. Chem. A 113(47), 13327-13330 (2009).

[Lukosz-1966] W. Lukosz, "Optical systems with resolving powers exceeding the classical limit," J. Opt. Soc. Am. 56(11), 1463-1471 (1966).

[Lukosz-1967] W. Lukosz, “Optical Systems with Resolving Powers Exceeding the Classical Limit. II,” J. Opt. Soc. Am. 57(7), 932-941 (1967)

[Ma-2017] C. Ma, Y. Li, J. Zhang, P. Li, T. Xi, J. Di, and J. Zhao, “Lateral shearing common-path digital holographic microscopy based on a slightly trapezoid Sagnac interferometer,” Opt. Express 25(12), 13659-13667 (2017).

[Mahajan-2015] S. Mahajan, V. Trivedi, P. Vora, V. Chhaniwal, B. Javidi, and A. Anand, “Highly stable digital holographic microscope using Sagnac interferometer,” Opt. Lett. 40(16), 3743-3746 (2015).

[Mann-2005] C. J. Mann, L. Yu, C.-M. Lo, and M. K. Kim, “High-resolution quantitative phase-contrast microscopy by digital holography,” Opt. Exp. 13(22), 8693-8698 (2005).

[Mann-2006] C. J. Mann, L. Yu, and M. K. Kim, “Movies of cellular and sub-cellular motion by digital holographic microscopy,” Biomed. Eng. Online 5, 21, (2006).

[Mann-2008] C. J. Mann, P. R. Bingham, V. C. Paquit, and K. W. Tobin, “Quantitative phase imaging by three-wavelength digital holography,” Opt. Express 16(13), 9753 (2008).

[Marquet-2005] P. Marquet, B. Rappaz, P. J. Magistretti, E. Cuche, Y. Emery, T. Colomb, and C. Depeursinge, “Digital holographic microscopy: a noninvasive contrast imaging technique allowing quantitative visualization of living cells with subwavelength axial accuracy,” Opt. Lett. 30(5), 468-470 (2005).

[Marquet-2013] P. Marquet, C. Depeursinge, and P. J. Magistretti, “Exploring neural cell dynamics with digital holographic microscopy,” Annu. Rev. Biomed. Eng. 15(1), 407-431 (2013).

[Matoba-2009] O. Matoba, T. Nomura, E. Perez-Cabre, M. S. Millan, and B. Javidi, “Optical Techniques for Information Security,” Proc. IEEE 97(6), 1128-1148 (2009).

[Mcelhinney-2008] C. Mcelhinney, B. Hennelly, T. Naughton, “Extended focused imaging for digital holograms of macroscopic three-dimensional objects”, App. Opt. 47(19) D71-D79 (2008).

[McReynolds-2017] N. McReynolds, F. G. M. Cooke, M. Chen, S. J. Powis, and K. Dholakia, “Multimodal discrimination of immune cells using a combination of Raman spectroscopy and digital holographic microscopy,” Sci. Rep. 7(1), (2017).

[Mehta-2012] D.S. Mehta, V. Srivastava, “Quantitative phase imaging of human red blood cells using phase-shifting white light interference microscopy with colour fringe analysis”, Appl. Phys. Lett. 101(20), 203701 (2012).

[Memmolo-2011] P. Memmolo, G. Di Caprio, C. Distante, M. Paturzo, R. Puglisi, D. Balduzzi, A. Galli, G. Coppola, and P. Ferraro, “Identification of bovine sperm head for morphometry analysis in quantitative phase-contrast holographic microscopy”, Opt. Express 19(23), 23215-23226 (2011).

[Memmolo-2012] P. Memmolo, M. Iannone, M. Ventre, P.A. Netti, A. Finizio, M. Paturzo, and P. Ferraro, “On the holographic 3D tracking of *in vitro* cells characterized by a highly-morphological change”, Opt. Express 20(27), 28485-28493 (2012).

[Memmolo-2014] P. Memmolo, L. Miccio, F. Merola, O. Gennari, P. A. Netti, and P. Ferraro, “3D morphometry of red blood cells by digital holography: DH for Morphometric Analysis of RBC Cells in 3D,” Cytom. A 85(12), 1030-1036 (2014).

[Merola-2011] F. Merola, L. Miccio, M. Paturzo, A. Finizio, S. Grilli, and P. Ferraro, “Driving and analysis of micro-objects by digital holographic microscope in microfluidics,” Opt. Lett. 36(16), 3079-3081 (2011).

[Merola-2012] F. Merola, L. Miccio, P. Memmolo, M. Paturzo, S. Grilli, and P. Ferraro, “Simultaneous optical manipulation, 3-D tracking, and imaging of micro-objects by digital holography in microfluidics”, IEEE Photon. J. 4(2), 451-454 (2012).

[Merola-2013] F. Merola, L. Miccio, P. Memmolo, G. Di Caprio, A. Galli, R. Puglisi, D. Balduzzi, G. Coppola, P. Netti, and P. Ferraro, “Digital holography as a method for 3D imaging and estimating the biovolume of motile cells,” Lab Chip 13(23), 4512-4516 (2013).

[Micó-2006A] V. Micó, Z. Zalevsky, P. García-Martínez, and J. García, “Synthetic aperture superresolution with multiple off-axis holograms,” J. Opt. Soc. Am. 23(12), 3162-3170 (2006).

[Micó-2006B] V. Micó, Z. Zalevsky, and J. García, “Superresolution optical system by common-path interferometry,” Opt. Express 14(12), 5168-5177 (2006).

[Micó-2007] V. Micó, Z. Zalevsky, and J. García, “Synthetic aperture microscopy using off-axis illumination and polarization coding,” Opt. Commun. 276(2), 209-217 (2007).

[Micó-2008] V. Micó, Z. Zalevsky, and J. García, “Common-path phase-shifting digital holographic microscopy: a way to quantitative phase imaging and superresolution,” Opt. Commun. 281(17), 4273-4281 (2008).

[Micó-2009] V. Micó, J. García, and Z. Zalevsky, “Quantitative phase imaging by common-path interferometric microscopy: application to super-resolved imaging and nanophotonics,” J. Nanophotonics 3(1), 031780 (2009).

[Micó-2012] V. Micó, C. Ferreira, and J. García, “Surpassing digital holography limits by lensless object scanning holography,” Opt. Express 20(9), 9382-9395 (2012).

[Micó-2013] V. Micó, C. Ferreira, and J. García, “Lensless object scanning holography for two-dimensional mirror-like and diffuse reflective objects,” Appl. Opt. 52(25), 6390-6400 (2013)

[Micó-2014] V. Micó, C. Ferreira, Z. Zalevsky, and J. García, “Spatially-multiplexed interferometric microscopy (SMIM): converting a standard microscope into a holographic one,” Opt. Express 22(12), 14929-14943 (2014).

[Mihailescu-2011] M. Mihailescu, M. Scarlat, A. Gheorghiu, J. Costescu, M. Kusko, I. A. Paun, and E. Scarlat, “Automated imaging, identification, and counting of similar cells from digital hologram reconstructions”, Appl. Opt. 50(20), 3589-3597 (2011).

[Mölder-2008] A. Mölder, M. Sebesta, M. Gustafsson, L. Gisselson, A. G. Wingren, and K. Alm, “Non-invasive, label-free cell counting and quantitative analysis of adherent cells using digital holography”, J. Microsc. 232(2), 240-247 (2008).

[Moon-2007] I. Moon and B. Javidi, “Three-dimensional identification of stem cells by computational holographic imaging,” J. Royal Soc. Interface 4(13), 305-313 (2007).

[Moon-2009] I. Moon and B. Javidi, “Three-dimensional speckle-noise reduction by using coherent integral imaging,” Opt. Lett. 34(8), 1246-1248 (2009).

[Moon-2012] I. Moon, B. Javidi, F. Yi, D. Boss, and P. Marquet, “Automated statistical quantification of three-dimensional morphology and mean corpuscular hemoglobin of multiple red blood cells”, Opt. Express 20(9), 10295-10309 (2012).

[Nakatsuji-2008] T. Nakatsuji, and K. Matsushima, “Free-viewpoint images captured using phase-shifting synthetic aperture digital holography,” Appl. Opt. 47(19), D136-D143 (2008).

[Nomarski-1952] G. Nomarski, “Interféromètre a polarisation,” Brevet français 1059(123), (1952).

[Nomarski-1955] G. Nomarski, “Interferential polarizing device for study of phase objects,” US Patent No. 2,924,142, (1960).

[Ouyang-2010] G. Ouyang, Z. Tong, M. N. Akram, K. Wang, V. Kartashov, X. Yan, and X. Chen, “Speckle reduction using a motionless diffractive optical element,” Opt. Lett. 35(17), 2852-2854 (2010).

[Ozcan-2007] A. Ozcan, A. Bilenca, A. E. Desjardins, B. E. Bouma, and G. J. Tearney, “Speckle reduction in optical coherence tomography images using digital filtering,” J. Opt. Soc. Am. A 24(7), 1901-1910 (2007).

[Park-2006] Y. Park, G. Popescu, K. Badizadegan, R. R. Dasari, and M. S. Feld, “Diffraction phase and fluorescence microscopy,” Opt. Express 14(18), 8263-8268 (2006).

[Park-2009] Y. Park, W. Choi, Z. Yaqoob, R. Dasari, K. Badizadegan, and M. S. Feld, "Speckle-field digital holographic microscopy," Opt. Express 17(15), 12285-12292 (2009).

[Parshall-2006] D. Parshall and M. K. Kim, "Digital holographic microscopy with dual-wavelength phase unwrapping," Appl. Opt. 45(3), 451-459 (2006).

[Pavillon-2010] N. Pavillon, A. Benke, D. Boss, C. Moratal, J. Kühn, P. Jourdain, C. Depeursinge, P. J. Magistretti, and P. Marquet, “Cell morphology and intracellular ionic homeostasis explored with a multimodal approach combining epifluorescence and digital holographic microscopy”, J. Biophotonics 3(7), 432-436 (2010).

[Pavillon-2012] N. Pavillon, J. Kühn, C. Moratal, P. Jourdain, C. Depeursinge, P. J. Magistretti, and P. Marquet, “Early cell death detection with digital holographic microscopy”, PLOS One 7(1), e30912 (2012).

[Perucho-2016] B. Perucho, J. A. Picazo-Bueno, and V. Micó, “A Novel Marking Reader for Progressive Addition Lenses Based on Gabor Holography,” Optom. Vis. Science 93(5), 534-542 (2016).

[Picart-2015] P. Picart, *New techniques in digital holography*, Wiley & Sons (2015).

[Picazo-Bueno-2016] J. A. Picazo-Bueno, Z. Zalevsky, J. García, C. Ferreira, and V. Micó, “Spatially multiplexed interferometric microscopy with partially coherent illumination,” J. Biomed. Opt. 21(10), 106007 (2016).

[Picazo-Bueno-2017] J. A. Picazo-Bueno, Z. Zalevsky, J. García, and V. Micó, “Superresolved spatially multiplexed interferometric microscopy,” Opt. Lett. 42(5), 927-930 (2017).

[Picazo-Bueno-2018A] J. A. Picazo-Bueno, D. Cojoc, F. Iseppon, V. Torre, and V. Micó, “Single-shot, dual-mode, water-immersion microscopy platform for biological applications,” Appl. Opt. 57(1), A242-A249 (2018).

[Picazo-Bueno-2018B] J. A. Picazo-Bueno, M. Trusiak, J. García, K. Patorski, and V. Micó, “Hilbert–Huang single-shot spatially multiplexed interferometric microscopy,” Opt. Lett. 43(5), 1007-1010 (2018).

[Picazo-Bueno-2019A] J. A. Picazo-Bueno and V. Micó, “Opposed-view spatially multiplexed interferometric microscopy,” J. Opt. 21(3), 035701 (2019).

[Picazo-Bueno-2019B] J. A. Picazo-Bueno, M. Trusiak, and V. Micó, “Single-shot slightly off-axis digital holographic microscopy with add-on module based on beamsplitter cube,” Opt. Express 27(4), 5655-5669 (2019).

[Popescu-2004] G. Popescu, L. P. Deflores, J. C. Vaughan, K. Badizadegan, H. Iwai, R. R. Dasari, and M. S. Feld, “Fourier phase microscopy for investigation of biological structures and dynamics,” Opt. Lett. 29(21), 2503-2505 (2004).

[Popescu-2005] G. Popescu, T. Ikeda, C. Best, K. Badizadegan, R. R. Dasari, and M. S. Feld, “Erythrocyte structure and dynamics quantified by Hilbert phase microscopy," J. Bio. Opt. 10(6), 060503 (2005).

[Popescu-2006] G. Popescu, T. Ikeda, R. R. Dasari, and M. S. Feld, “Diffraction phase microscopy for quantifying cell structure and dynamics,” Opt. Lett. 31(6), 775-777 (2006).

[Powell-1965] R.L. Powell, and K.A. Stetson, “Interferometric vibration analysis by wavefront reconstruction,” J. Opt. Soc. Am. 55(12), 1593-1598 (1965).

[Qu-2009] W. Qu, K. Bhattacharya, C. O. Choo, Y. Yu, and A. Asundi, "Transmission digital holographic microscopy based on a beam-splitter cube interferometer," Appl. Opt. 48(15), 2778-2783 (2009).

[Rappaz-2005] B. Rappaz, P. Marquet, E. Cuche, Y. Emery, C. Depeursinge, and P. Magistretti, “Measurement of the integral refractive index and dynamic cell morphometry of living cells with digital holographic microscopy,” Opt. Express 13(23), 9361-9373 (2005).

[Rappaz-2008] B. Rappaz, F. Charrière, C. Depeursinge, P. J. Magistretti, and P. Marquet, “Simultaneous cell morphometry and refractive index measurement with dual-wavelength digital holographic microscopy and dye-enhanced dispersion of perfusion medium,” Opt. Let. 33(7), 744-746 (2008).

[Reichelt-2005] S. Reichelt and H. Zappe, “Combined Twyman-Green and Mach-Zehnder interferometer for microlens testing,” Appl. Opt. 44(27), 5786-5792 (2005).

[Remmer-2009] C. Remmersmann, S. Stürwald, B. Kemper, P. Langehanenberg, and G. von Bally, “Phase noise optimization in temporal phase-shifting digital holography with partial coherence light sources and its application in quantitative cell imaging,” Appl. Opt. 48(8), 1463-1472 (2009).

[Rogers-1950] G.L. Rogers, “Gabor diffraction microscope: the hologram as a generalized zone plate,” Nature 166(4214), 237-237 (1950).

[Rogers-1952] G. L. Rogers, “Experiments in diffraction microscopy,” Proc. Roy. Soc. Edinburgh A 63(3), 193-221 (1952).

[Rommel-2010] C. E. Rommel, C. Dierker, L. Schmidt, S. Przibilla, G. von Bally, B. Kemper, and J. Schnekenburger, “Contrast-enhanced digital holographic imaging of cellular structures by manipulating the intracellular refractive index,” J. Biomed. Opt. 15(4), 041509 (2010).

[Saleh-1991] B. E. A. Saleh, M. C. Teich, *Fundamentals of Photonics*, New York: Wiley, 1991.

[Sanz-2015] M. Sanz, J. A. Picazo-Bueno, J. García, and V. Micó, “Improved quantitative phase imaging in lensless microscopy by single-shot multi-wavelength illumination using a fast convergence algorithm,” Opt. Express 23(16), 21352 (2015).

[Sanz-2017] M. Sanz, J. Á. Picazo-Bueno, L. Granero, J. García, and V. Micó, “Compact, cost-effective and field-portable microscope prototype based on MISHELF microscopy,” Sci. Rep. 7, 43291 (2017).

[Sanz-2018A] M. Sanz, J. Á. Picazo-Bueno, L. Granero, J. García, and V. Micó, “Multi-illumination single-holographic-exposure lensless Fresnel (MISHELF) microscopy using 4 channels,” Opt. Las. Eng. 110, 341-347 (2018).

[Sanz-2018B] M. Sanz, J. A. Picazo-Bueno, J. García, and V. Micó, “Dual-mode holographic microscopy imaging platform,” Lab Chip 18(7), 1105-1112 (2018).

[Schnars-1994A] U. Schnars, W. P. O. Jüptner, “Direct recording of holograms by a CCD target and numerical reconstruction”, Appl. Opt. 33(2), 179-181 (1994).

[Schnars-1994B] U. Schnars, and W. P. O. Jüptner, “Digital Recording and Reconstruction of Holograms in Hologram Interferometry and Shearography,” Appl. Opt. 33(20), 4373-4377 (1994).

[Schnars-1994C] U. Schnars, “Direct Phase Determination in Hologram Interferometry with Use of Digitally Recorded Holograms,” J. Opt. Soc. Am. A 11(7), 2011-2015 (1994).

[Schnars-2002] U. Schnars, and W. P. O. Jüptner, “Digital recording and numerical reconstruction of holograms," Meas. Sci. Technol. 13(9), R85-R101 (2002).

[Schnars-2015] U. Schnars, C. Falldorf, J. Watson, and W. P. O. Jüptner, *Digital holography and wavefront sensing: principles, techniques and applications*, 2nd Ed., Springer (2015)

[Seo-2010] S. Seo, S. O. Isikman, I. Sencan, O. Mudanyali, T.-W. Su, W. Bishara, A. Erlinger, and A. Ozcan, “High-throughput lens-free blood analysis on a chip”, Anal. Chem. 82(11), 4621-4627 (2010).

[Shaked-2010] N. T. Shaked, Y. Zhu, N. Badie, N. Bursac, and A. Wax, “Reflective interferometric chamber for quantitative phase imaging of biological sample dynamics,” J. Biomed. Opt. 15(3), 030503 (2010).

[Shaked-2012A] N. T. Shaked, “Quantitative phase microscopy of biological samples using a portable interferometer,” Opt. Lett. 37(11), 2016-2018 (2012).

[Shaked-2012B] N. T. Shaked, Z. Zalevsky, and L. L. Satterwhite, eds., *Biomedical Optical Phase Microscopy and Nanoscopy*, 1 edition (Academic Press, 2012).

[Shannon-1949] C. E. Shannon, “Communication in the presence of noise,” Proc. IRE 37(1), 10-21 (1949).

[Sheng-2006] J. Sheng, E. Malkiel, and J. Katz, “Digital holographic microscope for measuring three-dimensional particle distributions and motions,” Appl. Opt. 45(16), 3893-3901 (2006).

[Singh-2012] A. S. G. Singh, A. Anand, R. A. Leitgeb, and B. Javidi, “Lateral shearing digital holographic imaging of small biological specimens,” Opt. Express 20(21), 23617-23622 (2012).

[Slabý-2013] T. Slabý, P. Kolman, Z. Dostál, M. Antoš, M. Lošťák, and R. Chmelík, "Off-axis setup taking full advantage of incoherent illumination in coherence-controlled holographic microscope," Opt. Express 21(12), 14747-14762 (2013).

[Smith-1969] H. M. Smith, *Principles of holography*, Wiley, (1969).

[Solem-1982] J. C. Solem, and G. C. Baldwin, "Micro-Holography of Living Organisms," Science 218(4569), 229-235 (1982).

[Soler-2018] C. Soler, J. Á. Picazo-Bueno, V. Micó, A. Valverde, D. Bompart, F. J. Blasco, J. G. Álvarez, and A. García-Molina, "Effect of counting chamber depth on the accuracy of lensless microscopy for the assessment of boar sperm motility," Reproduction Fertil. Dev. 30(6), 924-934 (2018).

[Srivastava-2012] V. Srivastava, T. Anna, and D. S. Mehta, "Full-field Hilbert phase microscopy using nearly common-path low coherence off-axis interferometry for quantitative imaging of biological cells," J. Opt. 14(12), 125707 (2012).

[Stroke-1965] G.W. Stroke, R. Restrick, A. Funkhouser, and D. Brumm, "Resolution-retrieving compensation of source effects by correlation reconstruction in high resolution holography," Phys. Lett. 18(3), 274-275 (1965).

[Sun-2008] H. Sun, B. Song, H. Dong, B. Reid, M. A. Player, J. Watson, and M. Zhao, "Visualization of fastmoving cells *in vivo* using digital holographic video microscopy", J. Biomed. Opt., 13(1), 014007 (2008).

[Tahara-2010] T. Tahara, K. Ito, T. Kakue, M. Fujii, Y. Shimozato, Y. Awatsuji, K. Nishio, S. Ura, T. Kubota, and O. Matoba, "Parallel phase-shifting digital holographic microscopy," Biomed. Opt. Express, BOE 1(2), 610-616 (2010).

[Takeda-1982] M. Takeda, H. Ina, and S. Kobayashi, "Fourier-transform method of fringe-pattern analysis for computed-based topography and interferometry", J. Opt. Soc. Am. 72(1), 156-160 (1982).

[Toraldo-1955] G. Toraldo di Francia, "Resolving Power and Information," J. Opt. Soc. Am. 45(7), 497-501 (1955).

[Toraldo-1969] G. Toraldo di Francia, "Degrees of freedom of an image," J. Opt. Soc. Am. 59(7), 799-804 (1969).

[Török-2003] P. Török and F. J. Kao, *Optical Imaging and Microscopy: Techniques and Advanced Systems*, Springer (2013).

[Thompson-1967] B.J. Thompson, J.H. Ward, and W.R. Zinky, “Application of hologram techniques for particle size analysis,” Appl. Opt. 6(3), 519-526 (1967).

[Trusiak-2012] M. Trusiak, K. Patorski, and M. Wielgus, "Adaptive enhancement of optical fringe patterns by selective reconstruction using FABEMD algorithm and Hilbert spiral transform," Opt. Express 20(21), 23463-23479 (2012).

[Trusiak-2014] M. Trusiak, M. Wielgus, and K. Patorski, “Advanced processing of optical fringe patterns by automated selective reconstruction and enhanced fast empirical mode decomposition,” Opt. Las. Eng. 52, 230-240 (2014).

[Trusiak-2016A] M. Trusiak, Ł. Służewski, and K. Patorski, “Single shot fringe pattern phase demodulation using Hilbert-Huang transform aided by the principal component analysis,” Opt. Express 24(4), 4221-4238 (2016).

[Trusiak-2016B] M. Trusiak, V. Micó, J. Garcia, and K. Patorski, “Quantitative phase imaging by single-shot Hilbert–Huang phase microscopy,” Opt. Lett. 41(18), 4344-4347 (2016).

[Trusiak-2019] M. Trusiak, J. A. Picazo-Bueno, Krzysztof Patorski, Piotr Zdankowski, and V. Micó, “Single-shot two-frame π-shifted spatially multiplexed interference phase microscopy,” J. Biomed. Opt. **24**(9), 096004 (2019).

[Ueda-1973] M. Ueda, T. Sato, and M. Kondo, “Superresolution by multiple superposition of image holograms having different carrier frequencies,” Opt. Acta 20, 403-410 (1973).

[Upatnieks-1966] J. Upatnieks, A. Vander Lugt, and E. Leith, “Correction of lens aberrations by means of holograms,” Appl. Opt. 5(4), 589-593 (1966).

[Vander Lugt-1965] A. Vander Lugt, F.B. Rotz, and A. Klooster Jr, “Character-reading by optical spatial filtering,” (1965).

[Verrier-2011] N. Verrier and M. Atlan, "Off-axis digital hologram reconstruction: some practical considerations," Appl. Opt. 50(34), H136-H146 (2011).

[Wang-2010] P. Wang, R. K. Bista, W. E. Khalbuss, W. Qiu, S. Uttam, K. D. Staton, L. Zhang, T. A. Brentnall, R. E. Brand, and Y. Liu, “Nanoscale nuclear architecture for cancer diagnosis beyond pathology via spatial-domain low-coherence quantitative phase microscopy,” J. Biomed. Opt. 15(6), 066028 (2010).

[Wang-2012] S. Wang, L. Xue, J. Lai, and Z. Li, “Three-dimensional refractive index reconstruction of red blood cells with one-dimensional moving based on local plane wave approximation,” J. Opt. 14(6), 065301 (2012).

[Warnasoo-2007] N. Warnasooriya and M. K. Kim, “LED-based multi-wavelength phase imaging interference microscopy,” Opt. Express 15(15), 9239-9247 (2007).

[Warnasoo-2010] N. Warnasooriya, F. Joud, P. Bun, G. Tessier, M. Coppey-Moisan, P. Desbiolles, M. Atlan, M. Abboud, and M. Gross, “Imaging gold nanoparticles in living cell environments using heterodyne digital holographic microscopy”, Opt. Express 18(4), 3264-3273 (2010).

[Xu-2001] W. B. Xu, M. H. Jericho, I. A. Meinertzhagen, and H. J. Kreuzer, “Digital in-line holography for biological applications,” Proc. Natl. Acad. Sci. U.S.A. 98(20), 11301-11305 (2001).

[Xu-2003] W. Xu, M. H. Jericho, H. J. Kreuzer, and I. A. Meinertzhagen, “Tracking particles in four dimensions with in-line holographic microscopy”, Opt. Lett. 28(3), 164-166 (2003).

[Yamaguchi-1997] I. Yamaguchi, and T. Zhang, “Phase-shifting digital holography”, Opt. Lett. 22(16), 1268-1270 (1997).

[Yamaguchi-2001A] I. Yamaguchi, J. Kato, S. Ohta, and J. Mizuno, “Image formation in phase shifting digital holography and application to microscopy”, Appl. Opt. 40(34), 6177-6186 (2001).

[Yamaguchi-2001B] I. Yamaguchi, J. Kato, and S. Ohta, “Surface shape measurement by phase shifting digital holography”, Opt. Review 8(2), 85-89, (2001).

[Yamaguchi-2003] I. Yamaguchi, “Holography, speckle, and computers,” Opt. Las. Eng. 39(4), 411-429 (2003).

[Yang-2007] X. Yang, Q. Yu, and S. Fu, “A combined method for obtaining fringe orientations of ESPI,” Opt. Commun. 273(1), 60-66 (2007).

[Yaqoob-2011] Z. Yaqoob, T. Yamauchi, W. Choi, D. Fu, R. R. Dasari, and M. S. Feld, “Single-shot Full-field reflection phase microscopy,” Opt. Express 19(8), 7587-7595 (2011).

[Yaroslavsky-2004] L. Yaroslavsky, *Digital holography and digital image processing: principles, methods, algorithms*, Kluwer Academic, (2004).

[Yi-2013] F. Yi, I. Moon, B. Javidi, D. Boss, and P. P. Marquet, “Automated segmentation of multiple red blood cells with digital holographic microscopy”, J. Biomed. Opt. 18(2), 026006 (2013).

[Yourasso-2014] C. Yourassowsky and F. Dubois, “High throughput holographic imaging-in-flow for the analysis of a wide plankton size range”, Opt. Express 22(6), 6661-6673 (2014).

[Zernike-1942A] F. Zernike, “Phase contrast, a new method for the microscopic observation of transparent objects”, Physica 9(7), 686-698 (1942).

[Zernike-1942B] F. Zernike, “Phase contrast, a new method for the microscopic observation of transparent objects part II”, Physica 9(10), 974-980 (1942).

[Zhang-1998] T. Zhang and I. Yamaguchi, “Three-dimensional microscopy with phase shifting digital holography”, Opt. Lett. 23(15), 1221-1223 (1998).

[Zheng-2017A] J. Zheng, P. Gao, and X. Shao, “Opposite-view digital holographic microscopy with autofocusing capability,” Sci. Rep. 7(1), 4255 (2017).

[Zheng-2017B] J. Zheng, P. Gao, X. Shao, and G. U. Nienhaus, “Refractive index measurement of suspended cells using opposed-view digital holographic microscopy,” Appl. Opt. 56(32), 9000-9005 (2017).

[Zhong-2015] X. Zhong, T. Wang, J. Yan, and G. Jin, “Aberrations correction of tilted plane-parallel plate in convergent rays,” Appl. Opt. 54(7), 1758-1764 (2015).

[Zhu-2013] X. Zhu, Z. Chen, and C. Tang, “Variational image decomposition for automatic background and noise removal of fringe patterns,” Opt. Lett. 38(3), 275-277 (2013).

[Zlotnik-2005] A. Zlotnik, Z. Zalevsky, and E. Marom, “Superresolution with nonorthogonal polarization coding,” Appl. Opt. 44, 3705-3715 (2005).

PART II

PEER-REVIEWED

PUBLICATIONS

A242 Vol. 57, No. 1 / January 1 2018 / Applied Optics Research Article

applied optics

Single-shot, dual-mode, water-immersion microscopy platform for biological applications

José Ángel Picazo-Bueno,[1] Dan Cojoc,[2] Federico Iseppon,[3] Vincent Torre,[3] and Vicente Micó[1,*]

[1]Universidad de Valencia, Departamento de Óptica y Optometría y Ciencias de la Visión, C/Doctor Moliner 50, Burjassot 46100, Spain
[2]CNR-IOM Institute of Materials, Area Science Park—Basovizza, S.S. 14 km 163.5, Trieste 34149, Italy
[3]SISSA–International School for Advanced Studies, Via Bonomea, 265, 34136 Trieste, Italy
*Corresponding author: vicente.mico@uv.es

Received 22 June 2017; revised 24 November 2017; accepted 28 November 2017; posted 28 November 2017 (Doc. ID 300613); published 18 December 2017

A single-shot water-immersion digital holographic microscope combined with broadband (white light) illumination mode is presented. This double imaging platform allows conventional incoherent visualization with phase holographic imaging of inspected samples. The holographic architecture is implemented at the image space (that is, after passing the microscope lens), thus reducing the sensitivity of the system to vibrations and/or thermal changes in comparison to regular interferometers. Because of the off-axis holographic recording principle, quantitative phase images of live biosamples can be recorded in a single camera snapshot at full-field geometry without any moving parts. And, the use of water-immersion imaging lenses maximizes the achievable resolution limit. This dual-mode microscope platform is first calibrated using microbeads, then applied to the characterization of fixed cells (neuroblastoma, breast cancer, and hippocampal neuronal cells) and, finally, validated for visualization of dynamic living cells (hippocampal neurons).

OCIS codes: (100.0100) Image processing; (110.0180) Microscopy; (170.3880) Medical and biological imaging; (180.3170) Interference microscopy.

https://doi.org/10.1364/AO.57.00A242

1. INTRODUCTION

Dynamic process visualization at the cellular level without influencing the process itself is a particularly useful tool in biomedical imaging. In that sense, photo damage of the cells should be avoided since physiological changes induced by excessive illumination can lead to artifacts and abnormal responses [1,2]. Therefore, linear optical techniques requiring low light intensities are preferable. But even in this case, illumination with an innocuous wavelength is still important; otherwise, it can influence or disturb the behavior of the sample, thus yielding the wrong cell's dynamics and resulting in inappropriate conclusions. For example, pulsed laser light is able to modulate the growth of axons of primary neuronal cell cultures [3], and aggregation of red blood cells has been shown to be wavelength dependent [4].

Inside linear imaging modality methods, digital holographic microscopy (DHM) has become a powerful and versatile tool in many significant fields of biophotonics, life sciences, and medicine [5–7]. DHM combines into a single platform the high-quality imaging provided by microscopy, whole-object wavefront recovery provided by holography, and numerical processing capabilities provided by computers [8–12]. DHM allows visualization of phase samples using a non-invasive (no need for stained samples), full-field (non-scanning), real-time (on-line control), non-contact (no sample damage), and static (no moving components) operating principle [13,14].

DHM originates from the application of digital holography (DH) to microscopy in order to magnify an object's diffracted wavefront to be electronically sampled in the recording process. DH seems to have started approximately half a century ago [15,16] and it is based on the same holographic principles as classical holography, but replaces the holographic recording medium by electronic image recording devices (typically a CCD or a CMOS camera). Thus, a complete parallelism can be established between classical holography and DH, and the extension to DHM is straightforward.

Since the first evidence on DHM [17–19], a wide range of applications has been reported in the literature enabling DHM as a high-resolution multi-in-focus imaging method for polarization microscopy imaging [20], aberration lens compensation [21], particle tracking [22], extended depth of field (DOF) imaging [10], micro-electromechanical systems inspection [23], 3D dynamic analysis of cells [9], and refractive index characterization [24–26], just to cite a few. Because of its interferometric underlying principle, DHM has been implemented using different classical interferometric configurations [27–32]

1559-128X/18/01A242-08 Journal © 2018 Optical Society of America

Research Article Vol. 57, No. 1 / January 1 2018 / Applied Optics A243

with the most used one being the Mach–Zehnder interferometric layout [8,9,11,12,17,19]. Nevertheless, and considering illumination by transmission, the common-path interferometric (CPI) configuration [33–49] provides significant advantages over all previous architectures. In CPI, both the imaging and the reference beams follow nearly the same optical path because both are transmitted in parallel through the same microscope lens. Thus, the instabilities of the system (mechanical vibrations or thermal changes between both optical paths) do not affect the obtained results.

Roughly speaking, CPI can be divided into three general types of layouts. First, the imaging beam allows the synthesis of the reference beam after passing the microscope lens [33–37]. Once the transmitted beam is split into two beams, one of them is spatially filtered by using a pinhole mask at an intermediate Fourier plane. The filtering process allows reference beam synthesis by DC term transmission and samples information blocking. Its main advantage is that the field of view (FOV) is fully preserved while the strong drawback is the need to implement a relatively complex opto-mechanical stage at the microscope's exit port. As an additional implementation, the use of spatial light modulators for in-line generation of the reference beam has also been reported in the literature [38–40].

Second, supposing that the sample is sparse, the surroundings of the inspected sample area can act in good approximation as a clear region for reference beam transmission. Once transmitted through the objective lens, it is only a question of overlapping the imaging beam with a shifted version of itself, since it is assumed that there is a blank or clear region without sample information in the imaging beam, which does not alter the light passing through it [41–45]. This type of CPI can be easily assembled (fewer optical elements, more compact and simple configuration, etc.) than the previous one, but its applicability is restricted to sparse samples. Nevertheless, this is a common fact in many cases when imaging biosamples.

And, third, the reference beam can be transmitted in parallel with the imaging beam through the microscope lens without any approximation. Once transmitted, both beams are properly overlapped at the recording plane [46–49]. This type of parallel transmission can be accomplished by the specific constraints of the input plane design: a black region at the input plane in side-by-side configuration with the sample [46–48] or by back-reflection at the tilted coverslip of a specially designed chamber [49] for transmissive and reflective configurations, respectively. And, after that, both beams are overlapped allowing holographic recording by using minimal elements (diffraction gratings and tube lenses). This type of CPI allows reference beam transmission for all sample cases by minimal modifications in the setup with the inconvenience of a specific input plane spatial distribution design.

In this paper, we report on a home-built platform based on a single-shot immersion DHM technique in combination with broadband (white light) illumination and visualization. This double-mode imaging platform combines real-time conventional incoherent visualization with off-line quantitative phase holographic imaging at a diffraction-limited resolution level due to the use of water-immersion microscope lenses. In order to improve the robustness of the system, considering vibrations and/or thermal changes, the interferometric stage is assembled by synthesizing the reference beam after passing the objective lens. Due to the off-axis holographic recording principle, quantitative phase images of live biosamples are recorded in a single camera snapshot at full-field geometry without any moving parts. The capabilities of this dual-mode microscope platform are experimentally validated by first using microbeads for calibration, then imaging fixed cells (NG108 neuroblastoma, breast cancer (MDA-MB-231), and hippocampal neuronal cells) under different visualization modes and, finally, for visualization of dynamic samples (growth cones of hippocampal neurons).

2. DESCRIPTION OF THE IMAGING PLATFORM

The experimental layout is presented in Fig. 1. It is a dual-imaging platform containing incoherent (white light) and coherent (infrared laser source) illuminations combined by a dichroic mirror (DM1). The broadband illumination is used for general imaging purposes (centering the sample, imaging with reduced noise, etc.) and it is reflected out from the coherent path by a second dichroic mirror (DM2) after passing the tube lens, which is also used to image the sample onto the CCD plane (CCD1). The coherent illumination is aligned with the incoherent one following the same optical path until DM2, where it becomes transmitted, allows the assembly of a home-built Mach–Zehnder interferometric architecture. This optical layout is set in vertical (see Fig. 1), but the interferometric stage is built in the horizontal plane for simplicity.

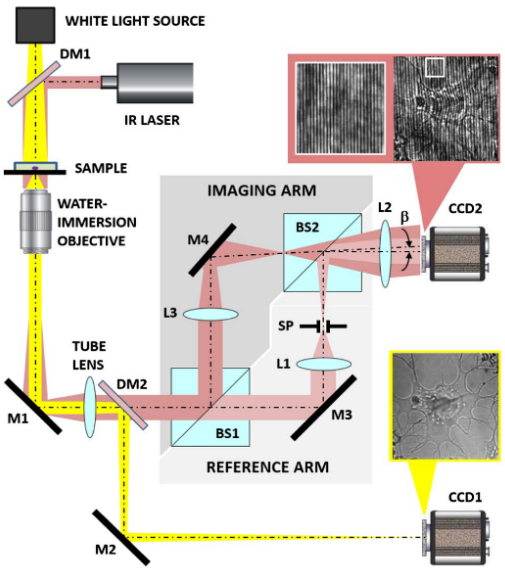

Fig. 1. Experimental layout for the proposed dual-mode microscope platform. DM1 and DM2, dichroic mirrors; M1, M2, M3, and M4, metallic mirrors; BS1 and BS2, beam splitters; L1, L2, and L3, lenses; CCD1 and CCD2, digital cameras; SP, spatial filter.

Nevertheless, and for the sake of simplicity, Fig. 1 presents such assembly also in the vertical plane.

As we have previously stated, the interferometric configuration belongs to a CPI architecture where the reference beam is synthesized from the imaging beam at the image space after passing the microscope lens. A first non-polarizing beam splitter (BS1) divides the imaging beam into two coherent beams, one following the imaging arm while the other is used for reference beam generation. In the reference arm, the first lens (L1) focusses the imaging beam, and a spatial filter (SP) is properly selected and placed in order to transmit only the DC term of the focused imaging beam. It is a conventional spatial filtering using a pinhole and permits the generation of a clear reference beam from the imaging beam. Thus assembled, the pinhole position depends on the spatial location of the transmitted DC term, which in turn directly depends on the sample's illumination direction. This fact makes the spatial pinhole position sensitive to misalignments in the laser beam propagation direction, but remains unaffected once the laser source is fixed.

The reference beam is then reflected at a second non-polarizing beam splitter (BS2), which acts as a combiner with the imaging beam coming from the imaging arm. This imaging beam is reflected at the first beam splitter (BS1) and passes through a third lens (L3), which is identical to the lens L1 to simplify the setup. After passing through the second beam splitter (BS2), an additional lens (L2) is used to make the divergence of both beams equal as they were before being split at BS1. Finally, a second CCD camera (CCD2) records the holograms incoming from the combination of the two coherent beams. But to allow off-axis interferometric recording, the mirror M4 of the imaging arm is tilted to allow a relative bias (β) between both interferometric beams when reaching the CCD2. The recorded holograms are image plane holograms since the CCD2 is placed at the focal plane of the tube lens, something that also happens with the CCD1 by setting in the layout an equal distance between both CCD cameras and the tube lens. Thus, the only restriction is to assemble the interferometric stage in the optical path length provided by the focal length of the lenses L1–L3. Additional metallic mirrors (M1, M2, M3, and M4) fold the light path into proper directions and complete the experimental layout. For example, Fig. 1 includes the images provided by both CCD cameras when using a NG108 neuroblastoma cell. The holographic image includes a magnified area to clearly show the interference fringes. The global structure of the cell is qualitatively visualized in the incoherent image while quantitative measurements will be derived from the coherent image as we will see in the experimental section.

Concerning the numerical processing for retrieving the complex amplitude distribution of the sample in the DHM imaging path, we have implemented a method based on spatial filtering at the Fourier plane from the recorded off-axis holograms [50–52]. Thus, the complex amplitude distribution of the transmitted frequency bandpass is recovered by applying a Fourier transformation over the recorded holograms and considering a circular spatial filtering mask at the distribution located at one of the diffraction orders. After the filtering and centering process at the Fourier domain, each recovered elementary pupil can be digitally manipulated for aberration compensation [21] and numerically processed in order to propagate them to different planes [10,51,52]. This issue is of particular significance provided that the sample will exhibit some axial movement, thus incurring in a retrieved blurred image that must be properly managed (as we will show in the experimental section).

3. EXPERIMENTAL RESULTS

The optical layout presented in Fig. 1 is assembled at the lab. It includes a white light source (high-power plasma light source—HPLS343, Thorlabs, USA) as incoherent illumination and an infrared CWA Laser (780 nm, 120 mW maximum optical power, 10 mW estimated used optical power, 10 cm coherence length, Omicron-Laser) as coherent illumination. Note that the use of a near-infrared laser at 780 nm drastically reduces light absorption by the sample; hence, living cell experiments are possible without damaging or influencing cell physiology. The samples are magnified and imaged by the combination of a water-immersion microscope objective (100×, 1.0 NA, Olympus, Japan, 1 mm WD, 1.8 mm focal length) with a tube lens (200 mm focal length). The interferometric stage uses lenses (L1, L2, L3) with identical focal length $f' = 100$ mm, 25 mm side beam splitters (BS1, BS2) and a pinhole of a diameter equal to 10 μm as spatial filter. Finally, two CCD cameras (Thorlabs DCC1240C, 5.3 μm pixel size, 25.8 fps, 1280 × 1024 pixels and Fastec Imaging HiSpec 4, 8 μm pixel size, 1696 × 1710 pixels) are used as digital recording devices for incoherent and coherent illuminations, respectively. Under these conditions, the DOF provided by the microscope objective is around 1 μm according to the formula $\mathrm{DOF} = \lambda n_{\mathrm{medium}}/\mathrm{NA}^2$ and the global magnification of the system built at the lab is $M \cong 110$ calculated as the ratio between the focal length of the tube lens and the one from the objective.

Now, experimental validation of the proposed dual-mode imaging platform is considered. First, we present the calibration of the DHM modality using different types of microbeads (45 and 3 μm in diameter and a conical microbead). Then, experiments involving different types (NG108 neuroblastoma, breast cancer, and hippocampal neuron cells) of static biosamples are imaged by the proposed platform.

A. Calibration of the DHM Platform

Microbeads are the perfect sample for calibration purposes since they are microspheres of a single material (silica, polystyrene, etc.) from which the refractive index at the illumination wavelength is well known. The beads are deposited in aqueous suspension and are observed under a DHM imaging modality. Figure 2 illustrates the full process when a 45 μm silica bead is imaged: (a) the recorded hologram, (b) its digital Fourier transformation (FT), (c) the retrieved (wrapped) phase distribution after filtering one of the diffraction orders at (b) and performing inverse FT, (d) the unwrapped phase distribution where the scale indicates radians of phase delay, and (e)–(f) the thickness distribution plots derived from the phase values.

Thickness information is not directly related with the 3D geometry of the inspected sample but with the phase delay

Research Article Vol. 57, No. 1 / January 1 2018 / Applied Optics A245

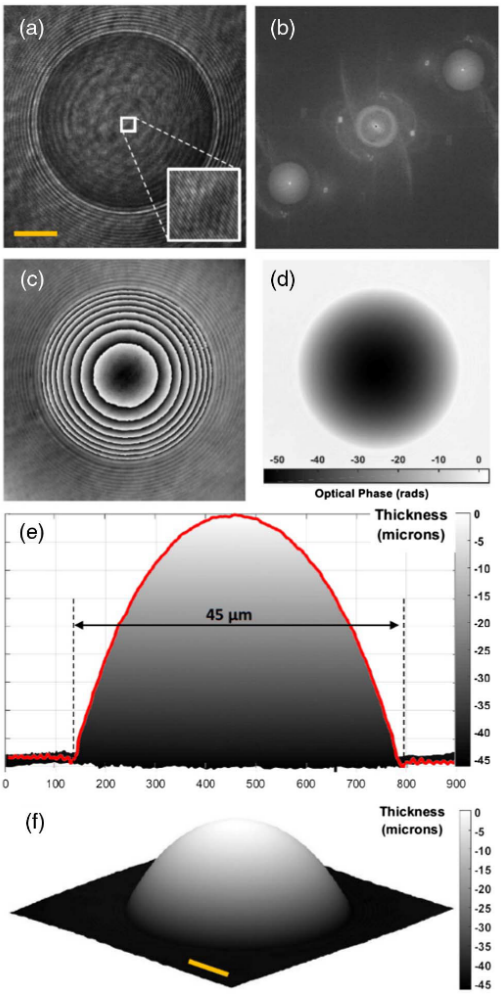

Fig. 2. Experimental results involving a 45 µm microbead imaged by DHM: (a) the recorded hologram (the inset is a magnified area to clearly show the interferometric fringes); (b) the FT of (a) showing the hologram diffraction orders; (c) the retrieved wrapped phase distribution coming from (b) after Fourier domain filtering and centering process; (d) the unwrapped phase distribution derived from (c); (e) the thickness profile from (d) and computed according to Eq. (1); and (f) 3D plot of the thickness info. Orange scale bars are 10 µm.

introduced by it—phase delay regarding the light passing through clear areas without a sample. In this way, a microbead will not appear as a ball sphere under a thickness visualization mode, but the maximum height of the thickness profile will be related with the maximum phase delay introduced by the microbead—in other words, with its diameter. So, thickness distribution retrieved from microbeads is useful to characterize the performance of DHM. Thus, once the phase distribution $\Delta\varphi(x, y)$ is retrieved and unwrapped, thickness information $\Delta t(x, y)$ is computed by knowing the refractive index step value ($\Delta n = n_{\text{sample}} - n_{\text{medium}}$) introduced by the sample (microbead) regarding the surrounding medium (aqueous solution) at the illumination wavelength by means of

$$\Delta\varphi(x, y) = \frac{2\pi}{\lambda}\Delta n \Delta t(x, y) \Rightarrow \Delta t(x, y) = \frac{\lambda}{2\pi\Delta n}\Delta\varphi(x, y). \quad (1)$$

Since we are using a silica microbead of $n_{\text{sample}} \cong 1.454$ in an aqueous-based solution ($n_{\text{medium}} \cong 1.33$), the maximum thickness value can be directly computed from Eq. (1) considering that the maximum phase delay is produced at the center of the bead. Taking a look at Fig. 2(c) and leaving aside border bead effects, there are a total number of 7 phase steps in addition to the central phase delay that does not appear to be a complete phase step. From Eq. (1), the thickness at the bead center equals 44 and 49 µm considering 7 and 7.8 phase steps, respectively. These values are in good agreement with the theoretical microbead diameter considering that there is a bead manufacturing tolerance and the fact that the refractive index values are approximated. Note that temperature and exact composition of the aqueous-based medium will slightly modify the considered values.

A second calibration experiment involving polystyrene ($n_{\text{sample}} = 1.579$) microbeads of 3 µm in diameter is performed. The results are included in Fig. 3 where the recorded hologram is included in (a) and the ROI marked with the solid line white rectangle is magnified in (b) showing also the interferometric fringes. Once FT, filtering, centering, and inverse FT is performed (not included at Fig. 3), the retrieved amplitude and unwrapped phase distributions of the ROI included in (b) are presented in (c) and (d), respectively. Finally, the thickness distribution is included in (e) showing again concordance at maximum thickness values as it corresponds with 3 µm diameter microbeads. Note that the peaks appearing in some beads are due to phase-unwrapping problems.

In a third calibration experiment, we have used a conical bead fabricated in SU-8 photoresist by a two-photon lithography (refractive index $n = 1.58$). The results are presented through Fig. 4. The conical tip has a dimension of 6 × 12 µm (cone base × height) as can be seen from Fig. 4(a) corresponding with a SEM image of the bead. The same dimensions are retrieved from the thickness information derived from the proposed DHM platform and included in Fig. 4(b). Note that the bead is flat on the cone base meaning that the retrieved thickness becomes, in this case, the 3D geometry of the bead.

Finally, an additional experiment concerning a simulated dynamic biosample is included at Fig. 5. The sample consists of hippocampal neuronal cells, which are fixed and prepared according to the procedure included in the next section, and the sample's movement is induced by a piezo-mirror that shifts the coverslip continuously in time (total recording time: 10 s). Figure 5(a) includes the 2D wrapped phase distribution retrieved by the proposed DHM platform, while Fig. 5(b) depicts the 3D unwrapped phase profile derived from (a). Those images are the first frames of two video movies named as Visualization 1 (4.4 MB) and Visualization 2 (1.9 MB)

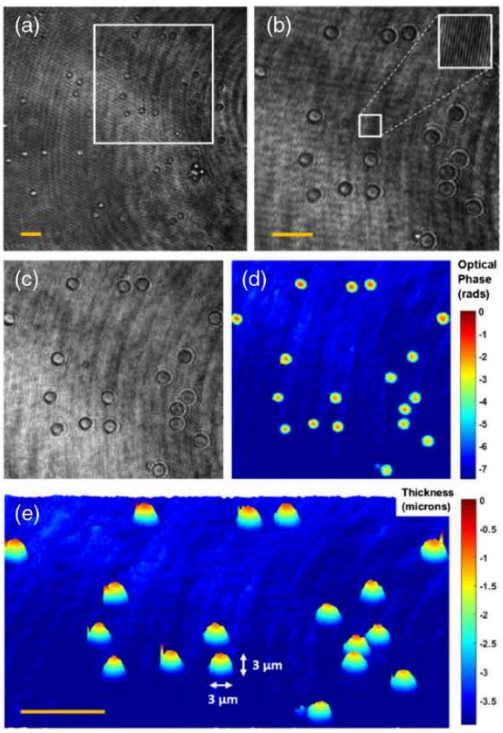

Fig. 3. Experimental results involving 3 µm diameter beads imaged by DHM: (a) the recorded hologram; (b) the ROI marked with a solid line white rectangle in (a) where the inset shows the interferometric fringes; (c) and (d) the retrieved amplitude and unwrapped phase distributions from (b), respectively; and (d) the 3D thickness plot computed from (d). Orange scale bars are 10 µm.

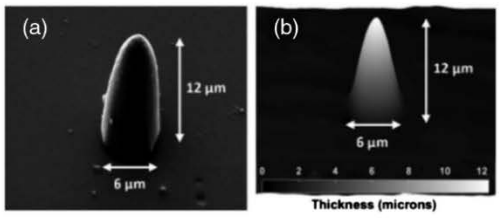

Fig. 4. Experimental results involving a conical bead: (a) SEM image and (b) thickness profile of the bead retrieved from DHM.

corresponding with Figs. 5(a) and 5(b), respectively. One can see, due to the 3D piezo-induced movement, the sample is not only transversally, but also slightly axially shifted, so the sample becomes misfocused as the time is running. But DHM uses numerical propagation to refocus the sample. We have implemented numerical refocusing at a given instant ($t = 6$s) in the video movies. The timeline of the videos is stopped, then

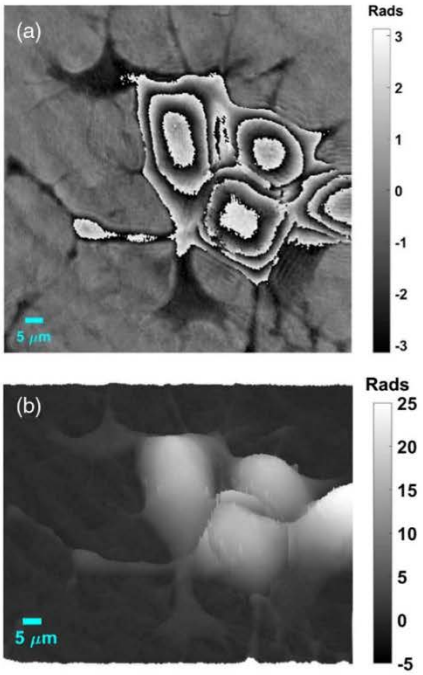

Fig. 5. Experimental results involving a simulated dynamic biosample: (a) 2D wrapped phase (Visualization 1) and (b) 3D unwrapped (Visualization 2) phase distributions retrieved from DHM.

refocusing is applied, and then the videos restart again. One can see that the thinner terminal branches of the cells are visible after refocusing.

With all of these calibration tests, it is experimentally stated that the proposed DHM imaging platform perfectly retrieves the phase values introduced by the studied samples (microbeads and neuron cells). Phase values are converted into thickness results showing good agreement, on the one hand, with the theoretical beads' dimensions and, on the other hand, with the shape of the conical bead provided by SEM. Thus, the DHM platform becomes validated from a quantitative point of view.

B. Results Using Static Samples

After validating our home-built DHM layout from a quantitative phase imaging point of view, we have performed additional experiments concerning a wide variety of static biosamples. This subsection includes as examples the simultaneous results provided by our single-shot, dual-mode, water-immersion microscopy platform.

First, all cell types are grown on glass coverslips and kept at 37°C, 5% CO2 in an incubator for 24–48 h. Coverslips are then removed from the incubator and inspected under an inverted light microscope to verify the viability and desired appearance of the cells. The cells are then rinsed with phosphate buffered saline (PBS) and subsequently fixed in 4% paraformaldehyde in the PBS solution for 15–20 min at room

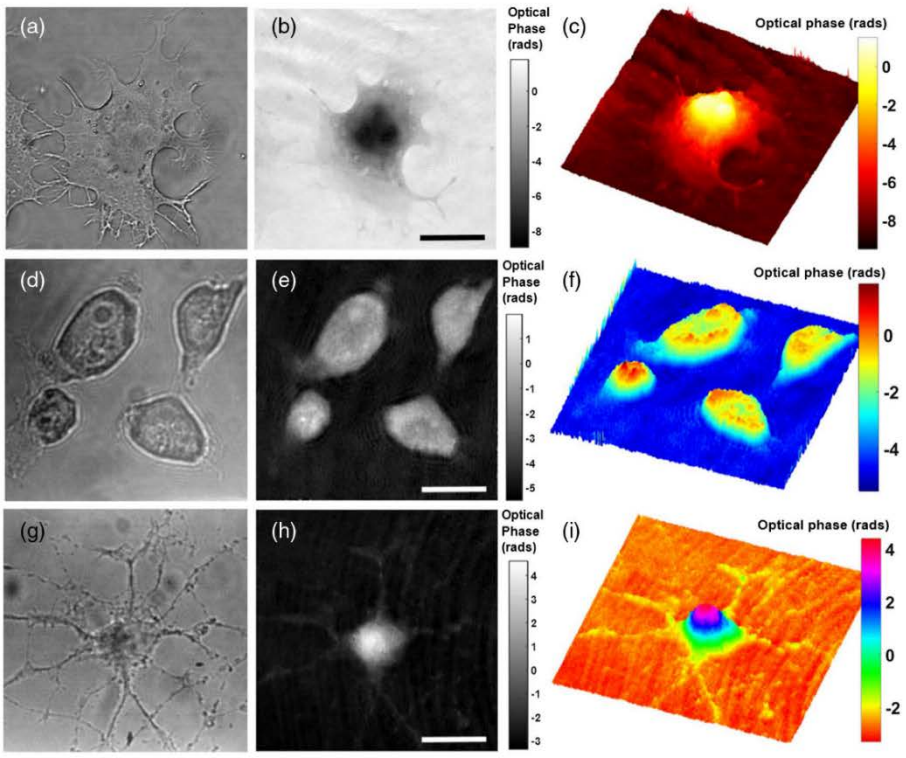

Fig. 6. Experimental results involving biosamples: (a)–(c), (d)–(f), and (g)–(i) are, in the same order, the bright field (intensity) image provided by white light illumination, the 2D quantitative phase imaging provided by DHM, and the 3D geometry computed from the phase values for NG108 neuroblastoma cells (first row), breast cancer cells MDA-MB 231 (second row), and hippocampal neuronal cells (third row), respectively. Scale bars (white solid lines) at the lower right corner of (b)–(c)–(h) represent 15 μm.

temperature. After abundant washing with PBS, the coverslips are mounted with VectaShield mounting medium and inverted onto glass slides for imaging.

Figure 6 includes the experimental images for NG108 neuroblastoma cells (upper row), breast cancer cells (central row), and hippocampal neuron cells (lower row) regarding the (a)–(d)–(g) bright field imaging modality provided by incoherent illumination and (b)–(e)–(h) and (c)–(f)–(i) the 2D and 3D, respectively, quantitative phase images incoming from the unwrapped phase distribution provided by DHM. Positive and negative visualization modes for 2D quantitative phase imaging and different colormaps for 3D views are selected to enhance image visualization.

C. Results with Dynamic Samples

Finally, to check the capability of the proposed imaging platform regarding the single-shot operating principle, Fig. 7 includes the experimental results obtained with an additional experiment involving a hippocampal neuron for investigating the cell dynamics. Figures 7(a) and 7(b) present the first frame of a video movie (Visualization 3, 6.7 MB) including the white light imaging and the retrieved phase distribution from DHM concerning the neuron cell movement, respectively. The frame rate of the camera is 12 fps and the total recording time of the movie is 100 s. However, the video movie is not displayed in real time to reduce its final size. It is difficult to observe the cell movement because of its slowness even with the increased frames per second visualization rate.

For this reason, we present in Figs. 7(c) and 7(d), the plots of the first ($t = 0$s) and last ($t = 100$s) video frames along the solid blue lines included in Figs. 7(a) and 7(b), respectively, the first corresponding with the intensity image provided by the white light imaging mode, while the second deriving from the phase distribution retrieved from DHM. Note that we have included the averaged plots included in between the solid blue lines (plot along the white arrows) because plotting a single section is mainly dominated by noise. By paying attention to the averaged points 1 and 2 at the plots, one can see the contraction of the cell's wall after the recording time. Point 1 is at the same position along the whole movie, while point 2 is slightly shifted from the first frame to the last one. This shift can be seen at both imaging modes (dark shapes with white light and increasing phase values from the background with DHM) and it is

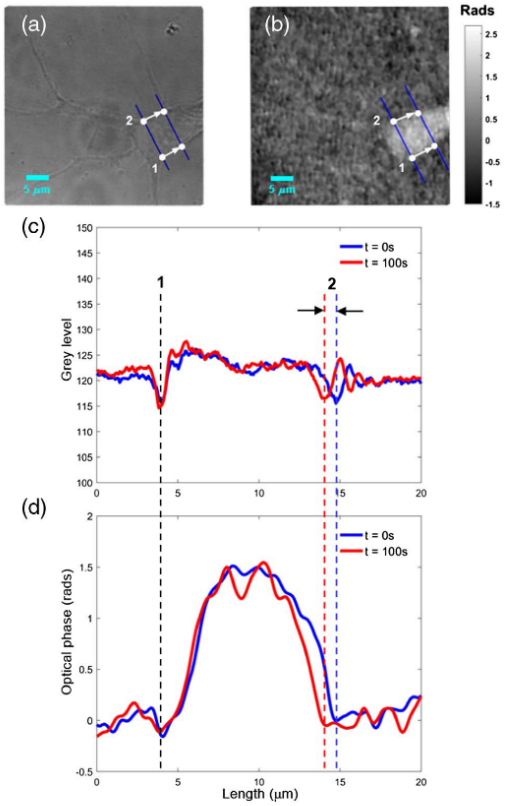

Fig. 7. Experimental results involving a dynamic biosample (hippocampal neuron): (a) intensity image provided by the white light visualization mode, (b) retrieved phase distribution from DHM, and (c) and (d) averaged plots along the points 1 and 2 of the intensity and phase images, respectively, and for the first ($t = 0$ s) and the last ($t = 100$ s) frames of the whole video sequence. Visualization 3 includes image sequences presented in (a) and (b).

approximately quantified in 0.75 μm of cell contraction, thus defining an averaged cell's contraction speed of 7.5 nm/s during the total recording time.

4. CONCLUSIONS

We have presented a home-built microscope platform based on the combination of DHM with regular broadband imaging for quantitative and qualitative analysis of biosamples. The proposed imaging platform is capable of working in a single illumination shot, thus allowing inspection and analysis of dynamic samples with the only limitation being the acquisition rate of the camera. The resolution limit of the imaging platform is optimized by using a water-immersion objective lens and the interferometric setup is assembled after passing through the imaging lens, thus reducing the sensitivity of the DHM layout to vibrations or thermal changes. In order to prove the capabilities of the proposed dual-mode microscope platform, we have presented experimental validation of the DHM part considering different types of microbeads (spherical and one cone tip) and fixed cells (neuroblastoma, breast cancer, and hippocampal neuronal cells) for calibration and biomedical sample testing purposes.

From the reported experiments, it is noticeable that the phase image SNR is lower for the dynamic sample than the fixed one. Fixed samples are placed on a microscope slide and a coverslip is used to enclose the static sample. Thus, both sides of the chamber are optical quality glasses providing low wavefront disturbances. On the contrary, the dynamic sample experiment was implemented using water flow containing physiological nutrients for the living cells. This water flow introduces stronger phase disturbances that reduce SNR in comparison with the static experiments.

Finally, the proposed dual-mode microscope platform can present some limitations for certain live cell imaging applications. For instance, long-term time-lapse imaging is highly challenging because of the stabilization complexity of the system conditions. Thus, sterile conditions, sample temperature preservation, and liquid evaporation in the immersed microscope objective should be carefully taken into account.

Funding. Ministerio de Economía y Competitividad (MINECO); European Regional Development Fund (ERDF) (FIS2013-47548-P).

Acknowledgment. J. A. Picazo-Bueno acknowledges a postgraduate grant from SISSA. In addition, we thank Massimo Tormen and Farideh Abhari from CNR-IOM for the conical bead fabrication and SEM image, and Sulaiman Yousafzai from CNR-IOM for the breast cancer cells' preparation.

REFERENCES

1. V. Magidson and A. Khodjakov, "Circumventing photodamage in live-cell microscopy," Methods Cell Biol. **114**, 545–560 (2013).
2. S. Wäldchen, J. Lehmann, T. Klein, S. van de Linde, and M. Sauer, "Light-induced cell damage in live-cell super-resolution microscopy," Sci. Rep. **5**, 15348 (2015).
3. M. Mathew, I. Amat-Roldan, R. Andrés, S. I. Santos, D. Artigas, and E. Soriano, "Signalling effect of NIR pulsed lasers on axonal growth," J. Neurosci. Methods **186**, 196–201 (2010).
4. M. Uyuklu, M. Canpolat, H. J. Meiselman, and O. K. Baskurt, "Wavelength selection in measuring red blood cell aggregation based on light transmittance," J. Biomed. Opt. **16**, 117006 (2011).
5. G. von Bally, *Holography in Medicine and Biology* (Springer, 1979).
6. M. K. Kim, *Digital Holographic Microscopy: Principles, Techniques, and Applications*, 1st ed. (Springer, 2011).
7. N. T. Shaked, Z. Zalevsky, and L. L. Satterwhite, *Biomedical Optical Phase Microscopy and Nanoscopy* (Academic, 2012).
8. C. Mann, L. Yu, C. Lo, and M. Kim, "High-resolution quantitative phase-contrast microscopy by digital holography," Opt. Express **13**, 8693–8698 (2005).
9. P. Marquet, B. Rappaz, P. J. Magistretti, E. Cuche, Y. Emery, T. Colomb, and C. Depeursinge, "Digital holographic microscopy: a noninvasive contrast imaging technique allowing quantitative visualization of living cells with subwavelength axial accuracy," Opt. Lett. **30**, 468–470 (2005).
10. P. Ferraro, S. Grilli, D. Alfieri, S. de Nicola, A. Finizio, G. Pierattini, B. Javidi, G. Coppola, and V. Striano, "Extended focused image in microscopy by digital holography," Opt. Express **13**, 6738–6749 (2005).

1. Single-shot, dual-mode, water-immersion microscopy platform for biological applications

11. F. Charrière, F. Montfort, J. Kühn, T. Colomb, A. Marian, E. Cuche, P. Marquet, and C. Depeursinge, "Cell refractive index tomography by digital holographic microscopy," Opt. Lett. **31**, 178–180 (2006).
12. B. Kemper and G. von Bally, "Digital holographic microscopy for live cell applications and technical inspection," Appl. Opt. **47**, A52–A61 (2008).
13. M. K. Kim, "Principles and techniques of digital holographic microscopy," SPIE Rev. **1**, 018005 (2010).
14. D. Boss, J. Kühn, P. Jourdain, C. Depeursinge, P. J. Magistretti, and P. Marquet, "Measurement of absolute cell volume, osmotic membrane water permeability, and refractive index of transmembrane water and solute flux by digital holographic microscopy," J. Biomed. Opt. **18**, 036007 (2013).
15. J. W. Goodman and R. W. Lawrence, "Digital image formation from electronically detected holograms," Appl. Phys. Lett. **11**, 77–79 (1967).
16. T. Huang, "Digital holography," Proc. IEEE **59**, 1335–1346 (1971).
17. T. Zhang and I. Yamaguchi, "Three-dimensional microscopy with phase-shifting digital holography," Opt. Lett. **23**, 1221–1223 (1998).
18. E. Cuche, P. Marquet, and C. Depeursinge, "Simultaneous amplitude-contrast and quantitative phase-contrast microscopy by numerical reconstruction of Fresnel off-axis holograms," Appl. Opt. **38**, 6994–7001 (1999).
19. F. Dubois, L. Joannes, and J. C. Legros, "Improved three-dimensional imaging with a digital holography microscope with a source of partial spatial coherence," Appl. Opt. **38**, 7085–7094 (1999).
20. T. Colomb, F. Dürr, E. Cuche, P. Marquet, H. G. Limberger, R. P. Salathé, and C. Depeursinge, "Polarization microscopy by use of digital holography: application to optical-fiber birefringence measurements," Appl. Opt. **44**, 4461–4469 (2005).
21. T. Colomb, J. Kühn, F. Charrière, C. Depeursinge, P. Marquet, and N. Aspert, "Total aberrations compensation in digital holographic microscopy with a reference conjugated hologram," Opt. Express **14**, 4300–4306 (2006).
22. J. Sheng, E. Malkiel, and J. Katz, "Digital holographic microscope for measuring three-dimensional particle distributions and motions," Appl. Opt. **45**, 3893–3901 (2006).
23. G. Coppola, P. Ferraro, M. Iodice, S. De Nicola, A. Finizio, and S. Grilli, "A digital holographic microscope for complete characterization of microelectromechanical systems," Meas. Sci. Technol. **15**, 529–539 (2004).
24. B. Rappaz, P. Marquet, E. Cuche, Y. Emery, C. Depeursinge, and P. Magistretti, "Measurement of the integral refractive index and dynamic cell morphometry of living cells with digital holographic microscopy," Opt. Express **13**, 9361–9373 (2005).
25. Y. C. Lin and C. J. Cheng, "Determining the refractive index profile of micro-optical elements using transflective digital holographic microscopy," J. Opt. **12**, 115402 (2010).
26. S. Wang, L. Xue, J. Lai, and Z. Li, "Three-dimensional refractive index reconstruction of red blood cells with one-dimensional moving based on local plane wave approximation," J. Opt. **14**, 065301 (2012).
27. H. Iwai, C. Fang-Yen, G. Popescu, A. Wax, K. Badizadegan, R. R. Dasari, and M. S. Feld, "Quantitative phase imaging using actively stabilized phase-shifting low-coherence interferometry," Opt. Lett. **29**, 2399–2401 (2004).
28. R. Guo, B. Yao, J. Min, M. Zhou, X. Yu, M. Lei, S. Yan, Y. Yang, and D. Dan, "LED-based digital holographic microscopy with slightly off-axis interferometry," J. Opt. **16**, 125408 (2014).
29. V. Srivastava, T. Anna, and D. S. Mehta, "Full-field Hilbert phase microscopy using nearly common-path low coherence off-axis interferometry for quantitative imaging of biological cells," J. Opt. **14**, 125707 (2012).
30. S. Reichelt and H. Zappe, "Combined Twyman–Green and Mach–Zehnder interferometer for microlens testing," Appl. Opt. **44**, 5786–5792 (2005).
31. G. Popescu, T. Ikeda, R. R. Dasari, and M. S. Feld, "Diffraction phase microscopy for quantifying cell structure and dynamics," Opt. Lett. **31**, 775–777 (2006).
32. V. Mico, Z. Zalevsky, and J. Garcia, "Common-path phase-shifting digital holographic microscopy: a way to quantitative phase imaging and superresolution," Opt. Commun. **281**, 4273–4281 (2008).
33. V. Mico, Z. Zalevsky, P. García-Martínez, and J. García, "Synthetic aperture superresolution with multiple off-axis holograms," J. Opt. Soc. Am. A **23**, 3162–3170 (2006).
34. V. Mico, Z. Zalevsky, and J. García, "Synthetic aperture microscopy using off-axis illumination and polarization coding," Opt. Commun. **276**, 209–217 (2007).
35. P. Gao, I. Harder, V. Nercissian, K. Mantel, and B. Yao, "Phase-shifting point-diffraction interferometry with common-path and in-line configuration for microscopy," Opt. Lett. **35**, 712–714 (2010).
36. N. T. Shaked, "Quantitative phase microscopy of biological samples using a portable interferometer," Opt. Lett. **37**, 2016–2018 (2012).
37. B. Bhaduri, C. Edwards, H. Pham, R. Zhou, T. H. Nguyen, L. L. Goddard, and G. Popescu, "Diffraction phase microscopy: principles and applications in materials and life sciences," Adv. Opt. Photon. **6**, 57–119 (2014).
38. S. Bernet, A. Jesacher, S. Fürhapter, C. Maurer, and M. Ritsch-Marte, "Quantitative imaging of complex samples by spiral phase contrast microscopy," Opt. Express **14**, 3792–3805 (2006).
39. G. Popescu, L. P. Deflores, J. C. Vaughan, K. Badizadegan, H. Iwai, R. R. Dasari, and M. S. Feld, "Fourier phase microscopy for investigation of biological structures and dynamics," Opt. Lett. **29**, 2503–2505 (2004).
40. H. Ding and G. Popescu, "Instantaneous spatial light interference microscopy," Opt. Express **18**, 1569–1575 (2010).
41. D. Fu, S. Oh, W. Choi, T. Yamauchi, A. Dorn, Z. Yaqoob, R. R. Dasari, and M. S. Feld, "Quantitative DIC microscopy using an off-axis self-interference approach," Opt. Lett. **35**, 2370–2372 (2010).
42. F. Merola, L. Miccio, M. Paturzo, A. Finizio, S. Grilli, and P. Ferraro, "Driving and analysis of micro-objects by digital holographic microscope in microfluidics," Opt. Lett. **36**, 3079–3081 (2011).
43. B. Kemper, A. Vollmer, C. E. Rommel, J. Schnekenburger, and G. von Bally, "Simplified approach for quantitative digital holographic phase contrast imaging of living cells," J. Biomed. Opt. **16**, 026014 (2011).
44. V. Chhaniwal, A. S. G. Singh, R. A. Leitgeb, B. Javidi, and A. Anand, "Quantitative phase-contrast imaging with compact digital holographic microscope employing Lloyd's mirror," Opt. Lett. **37**, 5127–5129 (2012).
45. A. S. G. Singh, A. Anand, R. A. Leitgeb, and B. Javidi, "Lateral shearing digital holographic imaging of small biological specimens," Opt. Express **20**, 23617–23622 (2012).
46. V. Mico, J. Garcia, and Z. Zalevsky, "Quantitative phase imaging by common-path interferometric microscopy: application to superresolved imaging and nanophotonics," J. Nanophotonics **3**, 031780 (2009).
47. V. Mico, C. Ferreira, Z. Zalevsky, and J. García, "Spatially-multiplexed interferometric microscopy (SMIM): converting a standard microscope into a holographic one," Opt. Express **22**, 14929–14943 (2014).
48. J. A. Picazo-Bueno, Z. Zalevsky, J. García, C. Ferreira, and V. Micó, "Spatially-multiplexed interferometric microscopy with partially coherent illumination," J. Biomed. Opt. **21**, 106007 (2016).
49. N. T. Shaked, Y. Zhu, N. Badie, N. Bursac, and A. Wax, "Reflective interferometric chamber for quantitative phase imaging of biological sample dynamics," J. Biomed. Opt. **15**, 030503 (2010).
50. U. Schnars, "Direct phase determination in hologram interferometry with use of digitally recorded holograms," J. Opt. Soc. Am. A **11**, 2011–2015 (1994).
51. T. Kreis, *Handbook of Holographic Interferometry: Optical and Digital Methods* (Wiley-VCH, 2005).
52. V. Micó, Z. Zalevsky, C. Ferreira, and J. García, "Superresolution digital holographic microscopy for three-dimensional samples," Opt. Express **16**, 19260–19270 (2008).

Journal of Biomedical Optics 21(10), 106007 (October 2016)

Spatially multiplexed interferometric microscopy with partially coherent illumination

José Ángel Picazo-Bueno,[a] Zeev Zalevsky,[b] Javier García,[a] Carlos Ferreira,[a] and Vicente Micó[a,*]
[a]Universitat de Valencia, Departamento de Óptica, C/Doctor Moliner 50, Burjassot 46100, Spain
[b]Bar-Ilan University, Faculty of Engineering, Ramat-Gan 52900, Israel

Abstract. We have recently reported on a simple, low cost, and highly stable way to convert a standard microscope into a holographic one [Opt. Express 22, 14929 (2014)]. The method, named spatially multiplexed interferometric microscopy (SMIM), proposes an off-axis holographic architecture implemented onto a regular (nonholographic) microscope with minimum modifications: the use of coherent illumination and a properly placed and selected one-dimensional diffraction grating. In this contribution, we report on the implementation of partially (temporally reduced) coherent illumination in SMIM as a way to improve quantitative phase imaging. The use of low coherence sources forces the application of phase shifting algorithm instead of off-axis holographic recording to recover the sample's phase information but improves phase reconstruction due to coherence noise reduction. In addition, a less restrictive field of view limitation (1/2) is implemented in comparison with our previously reported scheme (1/3). The proposed modification is experimentally validated in a regular Olympus BX-60 upright microscope considering a wide range of samples (resolution test, microbeads, swine sperm cells, red blood cells, and prostate cancer cells). [DOI: 10.1117/1.JBO.21.10.106007]

Keywords: holography; microscopy; phase measurement; medical and biological imaging; interference microscopy.

Paper 160286PR received May 3, 2016; accepted for publication Oct. 6, 2016; published online Oct. 27, 2016.

1 Introduction

Digital holographic microscopy (DHM) rises from a combination of classical holography[1,2] with optical microscopy[3] in the digital domain.[4] DHM avoids the limited resolution imposed by the finite number and size of the pixels in the digital sensor as well as the limited depth of focus in high numerical aperture (NA) lenses. The former because of the microscope lens magnification resulting in less demanding sampling requirements of the digital sensor.[5] And the latter by allowing three-dimensional (3-D) sample imaging by numerical refocusing of a two-dimensional (2-D) image at different object planes without using any optomechanical movement.[6] But maybe more significant is its capability to allow visualization of phase samples using a noninvasive (no need for labeling), full-field (nonscanning), real-time (single-frame acquisition), noncontact (no sample damage), and static (no moving components) operating principle.[7–9] Due to its versatility, DHM has been successfully applied to real-time quantitative phase contrast imaging,[7] polarization microscopy imaging,[10] aberration lens compensation,[11] particle tracking,[12] 3-D dynamic analysis of cells,[13] and in so many other disciplines in the fields of biophotonics, life sciences, and medicine.[14–17]

DHM layouts typically use laser sources for generating interference fringes in the experimental configuration. However, coherent light is very sensitive to both the microstructure of the sample and any defect or dust in optical paths. As a result, the complex amplitudes interfering at the recording plane are strongly affected by coherent noise. And such coherent noise severely reduces the optical quality of the reconstructed fields.[18] One way to improve image reconstruction is to reduce speckle noise and coherent artifacts by using different strategies such as digital processing capabilities[19–21] or by using specific optical components[22–24] or by image averaging.[25–27] Another strategy is to use partially coherent light sources for illuminating the sample.[28–42] Partially coherent illumination allows coherent noise reduction and increased phase resolution in DHM by avoiding multiple reflections and reducing the contribution of coherent artifacts. Due to this, partially coherent illumination has been implemented in DHM[28–35] as well as in digital in-line holographic microscopy[36–42] layouts.

We have recently reported on a noncomplex way to convert a commercially available standard microscope into a DHM with only minimal modifications.[43] The method, named spatially multiplexed interferometric microscopy (SMIM), rises from our previously developed spatially multiplexed common-path interferometric layout tested on an optical table and under super-resolution purposes.[44–46] SMIM simply replaces the broadband light source of the conventional microscopy by a laser diode, it leaves a clear region at the input plane for reference beam transmission, and it properly places a one-dimensional (1-D) diffraction grating in the microscope embodiment. With these three minimal modifications, a regular microscope is converted into a holographic one working under off-axis holographic recording.[43] However, two main factors limit the proposed SMIM approach. The first relates with the field of view (FOV) restriction imposed by the need to leave a clear transparent region at the input plane for the reference beam transmission. This fact reduces the useful FOV to one-third of the available one without using SMIM but enables phase information availability. And the second one relates to the use of coherent light sources, which produce coherent noise at the reconstructed images.

*Address all correspondence to: Vicente Micó, E-mail: vicente.mico@uv.es

1083-3668/2016/$25.00 © 2016 SPIE

2. Spatially multiplexed interferometric microscopy with partially coherent illumination

In this contribution, we have avoided both previously noted drawbacks in SMIM by relaxing the FOV limitation (from one-third to one-half) and by minimizing coherent noise effects. The former is achieved by a slightly different optical design of the input plane's spatially multiplexing. And the latter is obtained by replacing the laser diode by a super luminescent diode (SLD) source with a reduced temporal coherence. However, off-axis recording is prevented since the coherence length of the SLD is lower than the optical path mismatch between both interferometric beams when considering off-axis configuration at SMIM.[43] As a consequence, quasi on-axis (or slightly off-axis) holographic recording[47 49] with temporal phase-shifting algorithm[50 52] is adopted to retrieve quantitative phase-resolved information of the sample.

SMIM is closely related with those methods implemented in regular microscopes to provide quantitative phase imaging. Diffraction phase microscopy (DPM),[53] quadriwave lateral shearing interferometry (QLSI),[54] and Michelson interferometer layout (MIL)[55] are some examples. In few words, DPM proposes common-path architecture based on splitting into tow the imaging beam and synthesizes a reference beam from one of those two beams using spatial filtering with a pinhole; then, both coherent beams are overlapped at the recording CCD plane in off-axis configuration. SMIM differs from DPM in that there is no need to add a pinhole mask at any specific location of the setup to generate the reference beam since it is transmitted by saving a clear area at the input plane. QLSI proposes phase imaging using wavefront sensing implemented with the aid of a modified Hartmann mask. QLSI is a completely different concept approach based on digital wavefront sensing and not in holography. And MIL uses a Michelson layout at the image space to perform off-axis holographic recording at the CCD plane. MIL is based on the fact that the surrounding area of the cell to be imaged is blank so holographic recording using an almost clean reference beam is produced. In other words, MIL needs sparse samples. SMIM differs to MIL since samples can be dense: the only requirement is they will be placed in a restricted area allowing clear reference beam transmission.

The paper is organized as follows. Section 2 provides a layout description of the proposed working scheme highlighting the main difference with respect to Ref. 43. Section 3 experimentally validates SMIM with SLD illumination in a regular microscope (Olympus BX-60) first with synthetic samples (USAF, United States Air Force resolution test target, and microbeads) for calibration purposes and second with complex biosamples [red blood cells (RBC), swine sperm (SS) cells, and prostate cancer (PC-3) cells] for two different objectives (10× and 20×). Sec. 4 concludes the paper.

2 Experimental Layout Considerations

SMIM was previously implemented using the embodiment of a BX60 Olympus upright microscope where three modifications were introduced.[43] The first involves the use of coherent illumination for the interferometric recording. This is accomplished in Ref. 43 by using a commercial grade laser diode. The second one defines a specific spatial multiplexing at the input plane for reference and imaging beam transmission in common-path configuration. Note that by spatial multiplexing we mean that a specific spatial distribution needs to be implemented for allowing the transmission at once of both interferometric beams. The spatial multiplexing included in Ref. 43 divides the input plane's FOV into three contiguous areas having the same width where one is for the sample, another is for the reference beam and the third is blocked. And the third modification inserts a 1-D diffraction grating for mixing both interferometric beams at the recording plane. The 1-D grating is placed at the analyzer insertion slot just before the tube lens system included in the observation tube of the microscope and it allows off-axis holographic recording at the CCD plane. All together it confers the microscope with the capability of quantitative phase imaging by using conventional image processing tools involving digital fast Fourier transform (FFT), spatial filtering, and inverse FFT operation. The experimental validation was presented using a USAF resolution test target as well as RBCs and SS cells.

Now, some modifications are provided for the basic SMIM layout for improving quantitative phase imaging and FOV. The proposed setup is presented in Fig. 1 and it resembles the one included in Fig. 1 of Ref. 43, but with the following three differences. First, the coherent light source, which is externally inserted just below the microscope's XY translation stage, is not a laser diode but an SLD source. SLDs combine the advantages of both light-emitting diode (LED) and laser diode sources since, on one hand, SLDs provide temporal incoherent illumination incoming from a broadband spectrum (such as LEDs) and, on the other hand, SLDs are similar in geometry to laser diodes but without optical feedback mechanism for laser light emission thus providing a high degree of spatial coherence. As result, SLDs provide partially coherent (temporal incoherence) quasipoint illumination that reduces noise incoming from speckle and coherent artifacts while allows interference according to its coherent length[56] that can be calculated as $Lc = k\,\lambda^2/\Delta\lambda \cong 50\ \mu$m, being $k = 0.66$ for Gaussian spectrum, and $\lambda = 650$ nm the central wavelength, and $\Delta\lambda = 6$ nm the spectral bandwidth for the SLD used in the experiments.

Second, the spatial multiplexing at the input plane does not divide the FOV into three regions but only into two ones. This fact improves the useful FOV from one-third to one-half or, in other words, it does not restrict the FOV by a factor of 3 but by a factor of 2. Notice that SMIM with only two regions at the input plane was also proposed at Ref. 43; but this possibility was not implemented because the CCD must be laterally shifted to an off-axis position to record the holograms and this fact is intended to modify the microscope exit port. Figure 2 shows for clarity a comparison between the spatial multiplexing included in Ref. 43 [Fig. 2(a)] and the one proposed in this paper [Fig. 2(b)]. In Fig. 2(a), left side, the three regions in which the FOV is separated in Ref. 43 are identified as R-O-X (initials incoming from the reference, the object, and the X-blocking areas, respectively). The O region is on-axis centered while the R and X ones are at the sides of the O region. This FOV multiplexing is imaged and magnified by the microscope system in the form of R'-O'-X' at the output plane. Since the CCD is centered with the optical axis of the microscope embodiment, only the O' region will fall in its sensitive area. But the proper selection of a 1-D diffraction grating allows a displacement between replicas equal to one-third of the FOV [see Fig. 2(a), right side]. So, the three regions R'-O'-X' will perfectly overlap one to each other at the recording plane and the CCD records an off-axis hologram incoming from the addition of the imaging beam (O') and a tilted reference beam (R') which arrives at the CCD plane with a specific off-axis propagation angle. This propagation angle is enough to separate the diffraction orders of the recorded hologram at the Fourier domain and the complex amplitude distribution of the sample

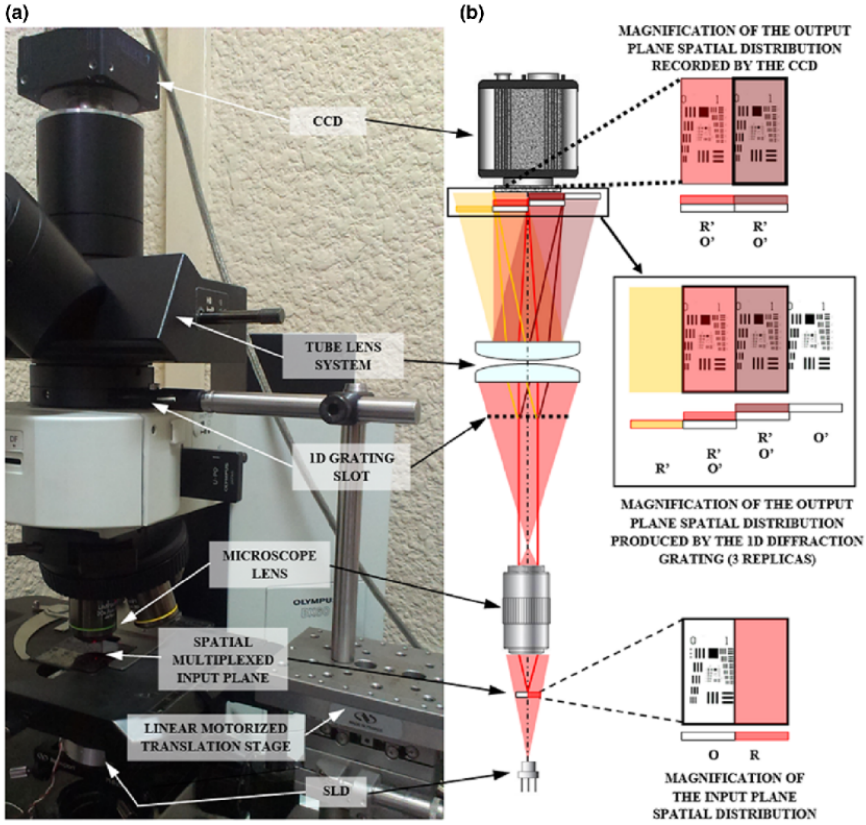

Fig. 1 Picture of (a) the experimental layout and (b) scheme of the proposed SMIM with partially coherent illumination where the main components of SMIM can be identified at both the picture and the scheme. In addition, the spatial multiplexing is included at the input plane, the output plane, and the recorded intensity by the CCD.

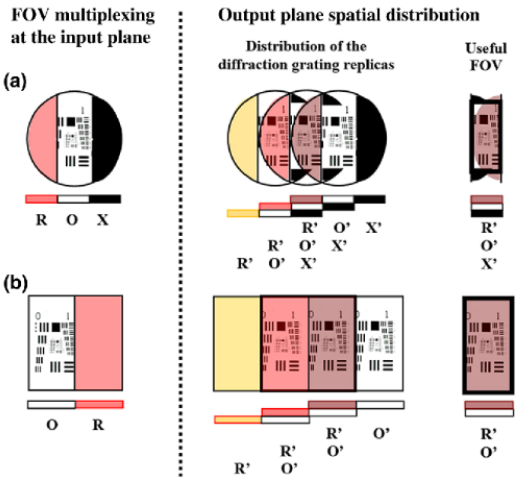

Fig. 2 FOV multiplexing according to the layouts presented in: (a) Ref. 43 and (b) this contribution.

is recovered after conventional digital image processing (FFT, Fourier filtering, and inverse FFT).

The proposed scheme layout [Fig. 2(b), left side] organizes the FOV into two regions where one is used for placing the object (O) and the other for reference beam transmission (R). Thus, by properly selection of the grating's period, overlapping of O' with R' is also provided [Fig. 2(b), right side] and the FOV becomes improved from one-third to one-half of the available one. To compute the grating's basic frequency allowing half of the FOV overlapping, Eq. (7) from Ref. 43 is adapted to the new experimental configuration. In Ref. 43, we proposed a shift of the replicas equal to $2z$ for one-third FOV limitation, being $2z$ the width of the CCD detector. Now and for one-half FOV limitation, the replicas of the grating at the CCD plane must be shifted z. Thus, under the same assumptions as were in Ref. 43 and using Fig. 3, the grating's basic frequency N can be calculated as $N = z/(\lambda f')$, where λ is the illumination wavelength and f' is the focal length of the tube lens (180 mm according to the microscope specifications). Assuming an FOV multiplexing along the shortest CCD direction (as we use in most of the cases), the resulting grating's basic frequency results in $N = 20.64$ linepairs/mm.

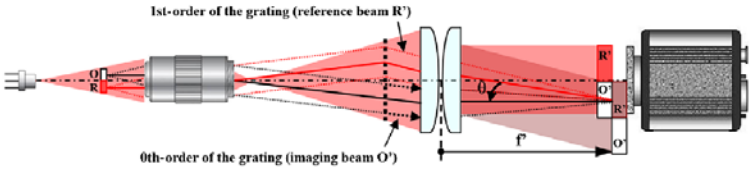

Fig. 3 Scheme of the optical beam paths for calculating mismatches in the optical paths of the reference (red raytracing) and imaging (black raytracing) beams. For clarity, we have removed the yellow raytracing included in Fig. 1 and corresponding with the +1 grating's diffraction order.

Third, and as a consequence of using a partially coherent illumination source, the 1-D diffraction grating must have a larger period than the one used in Ref. 43. Because of the lateral shift of the replicas at the recording plane produced by the 1-D grating, the reference beam optical path is higher than the imaging beam optical path (see Fig. 3). Some rapid calculations will assist with this fact. Assuming that the optical path of both beams is the same until the 1-D diffraction grating and that the grating is closely placed to the tube lens system, the change in optical path between both beams will be produced after passing the tube lens. According to the microscope specifications, the tube lens focal length (f' in Fig. 3) is 180 mm. Thus, while the nondiffracted light (zeroth-order term of the grating) travels 180 mm until reaching the CCD (central ray of the imaging beam included as the black solid ray parallel to the optical axis after the tube lens in Fig. 3), the one of the grating's diffraction orders (central ray of the reference beam included as the red solid ray after the tube lens in Fig. 3) will result in a distance equal to $d = 180/\cos\theta$, where θ is the tilted beam angle on which the reference beam arrives at the CCD plane. This θ angle is in good approximation the same as the grating's diffraction angle. Considering the 1-D grating used in Ref. 43 with a period of 12.5 μm (or 80 lp/mm basic frequency), the θ angle can be calculated from: $\sin\theta = \lambda/p = 0.65/12.5 = 0.26$; so the reference beam central ray will travel 186.41 mm until reaching the CCD. The mismatch in optical path is much higher than the coherence length of the SLD source (50 μm as we have previously calculated). So a lower basic frequency diffraction grating must be used. In the experiments, we have used a 20 lp/mm (or 50-μm period) meaning that the diffracted ray will travel 180.015 mm, which is well below the coherence length of the SLD source allowing interferometric recording. But because of this low basic frequency, off-axis holographic recording with spatial filtering in the Fourier domain is prevented and phase-shifting strategy is needed to recover the sample's complex amplitude distribution. Note that, in principle, it is possible to equalize the optical path difference using delay lines in one of the interferometric beams[57] and, thus, allow single-shot holographic recording with partially coherent sources. But this is not the case for the proposed approach since no real optical path separation happens because of the common-path interferometric architecture.

With these three simple and cost-effective modifications, SMIM implemented in a regular microscope becomes improved as previously stated although some drawbacks also arise. As a general problem in SMIM, the main shortcoming comes from the FOV spatial multiplexing needed to transmit a clear reference beam for the holographic recording. This fact can be fully achieved by designing a specific chamber for the sample. However, the experimental validation included in this paper expands its use to conventional microscope slides, provided that a clear region will be allocated in side-by-side configuration with the sample. In addition, use of the phase-shifting method presented in this paper yields a double disadvantage when comparing with the previous SMIM technique.[43] On the one hand, phase-shifting algorithm prevents the implementation of the technique to samples varying inside the phase-shifting duty cycle. Although this issue can be minimized by a two-step phase-shifting algorithm[52] and or using additional polarization multiplexing for parallel phase-shifting recordings,[58,59] it is true that additional restrictions affects the type of samples to be imaged. On the other hand, the microscope embodiment must be equipped with some sort of mechanical stage for grating movement, thus improving the complexity and pricing of the approach. Additional restriction is performed over the retrieved phase values because of the temporal incoherence of the illumination source used in the experiments.

3 Experimental Validation of SMIM with Partially Coherent Illumination

As in Ref. 43, we have used a commercial BX60 Olympus microscope for implementing the modifications involved in SMIM. We have used an SLD source from Exalos (Model EXS6501-B001, 10-mW optical power, 650-nm central wavelength, 6-nm spectral bandwidth) as a partially coherent light source, which is placed just below the manual XY translation stage of the microscope (see Fig. 1). As optics, we have used two different microscope lenses (UMPlanFl) all of them infinity corrected ones: 10 × /0.30 NA and 20 × /0.46 NA. A Ronchi ruled grating (20 lp/mm period) and a commercial grade CCD camera (Basler A312f, 582 × 782 pixels, 8.3 μm pixel size, 12 bits/pixel) are used as 1-D diffraction grating and imaging device, respectively. The grating is placed on a motorized linear translation stage (Newport, model ESP300) and it is externally introduced in the microscope embodiment in the analyzer insertion slot. We have selected a grating motion step of 2.5 μm between consecutive holograms meaning that 20 images integrate a full phase-shifting cycle. In the experiments, we have recorded a total of 40 images, so two full phase-shifting cycles are available. Note that although phase-shifting algorithm can be implemented using a lower number of images, the lower the number the higher the required precision to control the phase step between frames. Thus, a large number of images per cycle have been selected just to minimize uncertainty errors in phase determination but any other phase-shifting algorithm[52] can be implemented.

3.1 *System Calibration Involving Microbeads and a Resolution Target*

In this section, we will present the experimental results provided by the proposed method when using the USAF resolution test

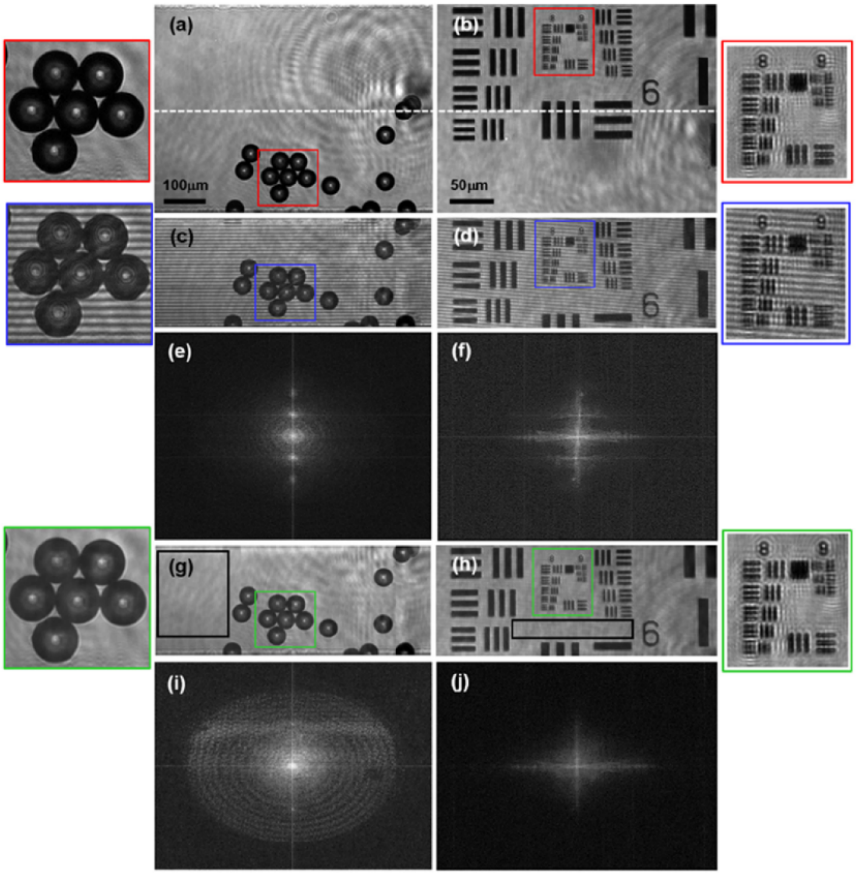

Fig. 4 Experimental results for 10×/0.30 NA (left column) and 20×/0.46 NA (right column) lenses using microbeads and USAF test, respectively: (a) and (b) the full FOV split by the dashed white lines in the two FOV's spatially multiplexed areas, (c) and (d) a single half FOV frame of the full FOV phase-shifting cycle which can be seen through (Video 1, MOV, 1.5 MB) [URL: http://dx.doi.org/10.1117/1.JBO.21.10.106007.1] and (Video 2, MOV, 2.8 MB) [URL: http://dx.doi.org/10.1117/1.JBO.21.10.106007.2], (e) and (f) the FFT of the single holograms included in (c) and (d) showing diffraction orders overlapping, (g) and (h) the retrieved images after phase-shifting algorithm implementation, and (i) and (j) the FFT of (g) and (h) showing diffraction order removal.

target and microbeads as input objects. The microbeads (Polybead® Microspheres, 45 μm mean diameter) are standard monodisperse polystyrene microspheres in aqueous suspension. The beads are deposited in a conventional microscope slide in sparse mode to assure clear areas in the surroundings of the region containing the microbeads. Regarding the USAF test, we have used the clear area separating groups 4 and 5 from 6 and 7 to pass through it the reference beam.

Figure 4 shows a mosaic of the experimental results obtained for these two types of samples where the microbeads are imaged with the 10× objective and the USAF test by the 20× lens. Figures 4(a) and 4(b) show the direct intensity images provided by the microscope without the grating and where the FOV spatial multiplexing has been marked with a dashed white line (R' in the upper part and O' at the lower one for Figs. 4(a) and viceversa for 4(b), we can see the intensity images of the interferometric fringes as a consequence of adding the 1-D diffraction grating. To save space, we have included only one-half of the FOV (the one corresponding with the useful O' area). Images presented in Figs. 4(e) and 4(f) include the FFT of a single hologram showing as the hologram's diffraction orders overlap at the Fourier domain as consequence of the slightly off-axis interferometric configuration; so, phase-shifting must be applied to recover the complex amplitude distributions. The whole phase-shifting process is included in two videos for the microbeads (Video 1) and the USAF test (Video 2). The movies correspond with the full set of recorded phase-shifted images where not only the imaging O' area can be seen [as in images included in Figs. 4(c) and (d)] but the full frame also includes the reference R' region. The intensity images obtained after phase-shifting algorithm implementation and the recovered sample's spectrum are included in Figs. 4(g) and 4(h) and 4(i)

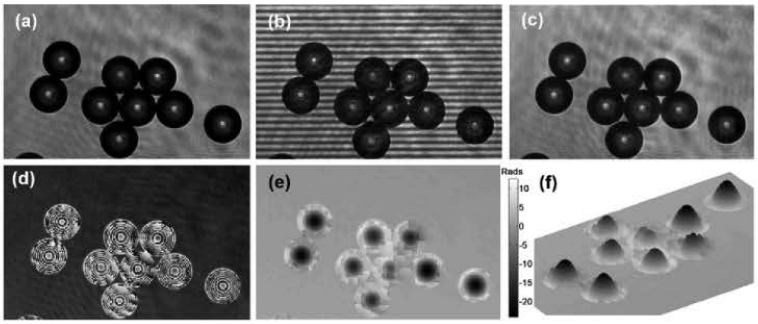

Fig. 5 Experimental results for the 10 × /0.30 NA objective lens using microbeads: (a–c) magnified images of the intensity distribution retrieved by the proposed method, and (d–f) present the retrieved phase distribution in the form of wrapped, unwrapped, and 3-D view, respectively. Scale bar depicts optical phase in radians and it corresponds with (e) and (f) images.

and 4(j), respectively, where the zeroth- and -first-order terms have been removed. In addition, RGB inner rectangles in Figs. 4(a) and 4(b), 4(c) and 4(d), and 4(g) and 4(h) show in detail a magnification of the inner parts of the images.

Figure 5 includes the experimental results obtained for the microbeads shown in Fig. 4 where only the FOV part containing the microspheres is included. As in Figs. 4(a)– 4(c) present the intensity images corresponding with the direct imaging mode

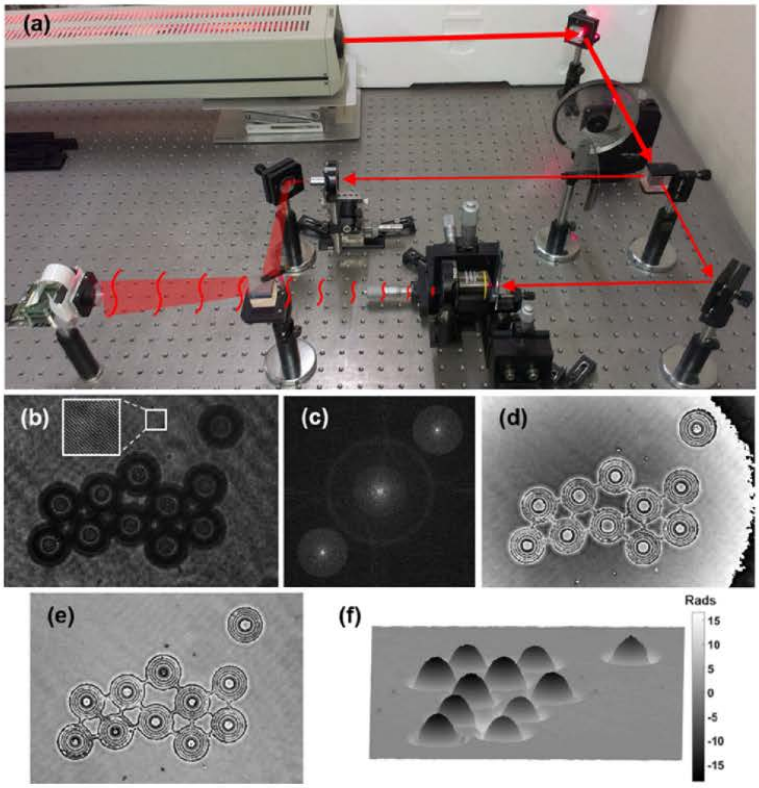

Fig. 6 Experimental results for the 10 × /0.30 NA objective lens using microbeads in a regular Mach–Zehnder interferometric configuration: (a) the experimental setup, (b) the off-axis recorded hologram, (c) its FFT, (d) the recovered phase distribution after spatial filtering one of the diffraction orders included in (c), (e) the recovered phase distribution after additional spherical and linear digital phase compensation of the image included in (d), and (f) a 3-D unwrapped phase distribution plot of the microbeads. Gray-level scale in (f) represents optical phase in radians.

(no grating in the layout), the interferometric fringes after 1-D grating insertion, and the retrieved image after phase-shifting algorithm, respectively. However, SMIM allows phase recovery and this can be checked with the phase information coming from the microbeads. Figures 4(d)–4(f) include the retrieved wrapped phase distribution, the unwrapped phase distribution, and a 3-D view of the unwrapped phase distribution, respectively.

In order to validate these results, we have assembled a conventional Mach–Zehnder interferometric configuration at the lab. Thus, a direct comparison between quantitative phase values provided by SMIM with partial coherent illumination (Fig. 5) and the obtained ones with a conventional DHM platform (Fig. 6) can be performed. For the DHM implementation, we have used a He–Ne laser as illumination source for imaging the microbeads with the same microscope objective ($10\times/0.30$ NA). The results from DHM are presented in Fig. 6 including the experimental Mach–Zehnder layout at the lab [Fig. 6(a)], the recorded hologram [Fig. 6(b)], its FFT [Fig. 6(c)], the retrieved phase distribution before [Fig. 6(d)] and after [Fig. 6(e)] phase compensation (spherical and linear factors) and unwrapping, and a 3-D view of the unwrapped phase distribution [Fig. 6(f)]. Although the imaged group of microbeads in Fig. 6 is not the same one as in Fig. 5, they are 45 μm spheres so a similar phase profile must be obtained. As one can see by comparing images in Figs. 5(f) and 6(f), the phase delay introduced by the microbeads is almost the same. This fact shows a high concordance between the unwrapped phase values provided by both methods and validates that the quantitative phase information provided by the proposed approach perfectly matches the one provided by conventional holographic methods.

3.2 *Experimental Results with Biosamples*

Now SMIM with partially coherent illumination is tested using different fixed biological samples. In particular, we have selected RBCs, SS cells, and PC-3 cells. The RBCs were stained onto the microscope slide using a specially prepared mixture of methylene blue and eosin in methanol (Wright stain), the SS cells were unstained but dried up for fixing them on a counting chamber, and the PC-3 cells were *in vivo* cultured and mounted in a microscope slide after centrifugation and resuspension into a cytopreservative solution. As in Ref. 43, we have not built a specially designed chamber for the FOV multiplexing but we are

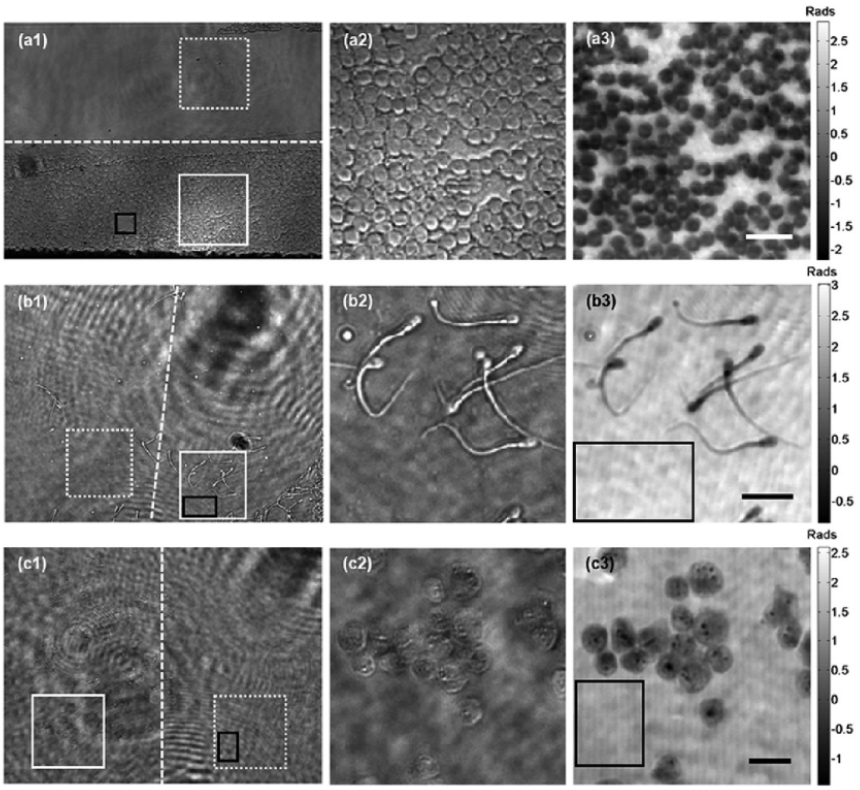

Fig. 7 Experimental results for the $10\times/0.30$ NA microscope lens using biosamples: (a) RBCs, (b) SS cells, and (c) PC-3. Images at left column (1) show the direct intensity mage without the grating showing the FOV multiplexed regions. Images at central column (2) present the direct intensity image of the group of cells marked with a solid white line square in (1). And images at right column (3) include the retrieved unwrapped phase distribution using the proposed method. Scale bars: the solid lines at the lower right corner of (a3), (b3), and (c3) represent 25 μm.

taking advantage of clear areas in the microscope slide for reference beam transmission.

Figures 7 and 8 include the experimental results for the aforementioned biosamples when using the 10× and the 20× microscope objectives, respectively. The figures are structured in rows (a-b-c) and columns (1-2-3) corresponding with a different biosample and a different image per biosample, respectively. At the left column (1) of both figures, we have included the direct intensity image without grating insertion to identify the spatially multiplexed regions at the input plane. At those images, the dashed white line separates both multiplexed regions (O and R) at the input plane; the solid white line square marks a given region of interest (ROI) including some cells which are magnified on (2) and (3); and the dotted white line square identifies the clear region which will overlap with the cells for SMIM. In addition, note as figures (b1) and (c1) at Fig. 7 include an FOV multiplexing in a different direction. This is because the experimental considerations for those biosamples suggested for us to rotate the CCD at the output port of the microscope for a better implementation of the proposed approach. At the central column (2), we have included the direct intensity image of the cells included in the ROI marked in (1). Finally, the right column (3) presents the unwrapped phase distribution (positive phase contrast images) retrieved when applying the proposed SMIM method. The gray-scale bars in (3) depict optical phase in radians.

Since SMIM performs holographic recording, the phase information is retrieved; so additional images such as negative phase contrast, DIC in different directions, and 3-D plots can be digitally processed and presented. Figures 9 and 10 include, just as examples, the negative-phase contrast images (2-D and 3-D visualizations) of the positive-phase contrast images included along Figs. 6 and 7 for the three analyzed biosamples.

3.3 *SNR Analysis in Spatially Multiplexed Interferometric Microscopy*

As a final comparative, we have included an analysis of the standard deviation (STD) of the retrieved phase distributions when using SMIM with off-axis holographic recording[43] and the proposed SMIM with partially coherent illumination. STD values are very useful to evaluate spatial noise and image quality in quantitative-phase imaging because it provides a direct value on the phase stability provided by the holographic method. STD

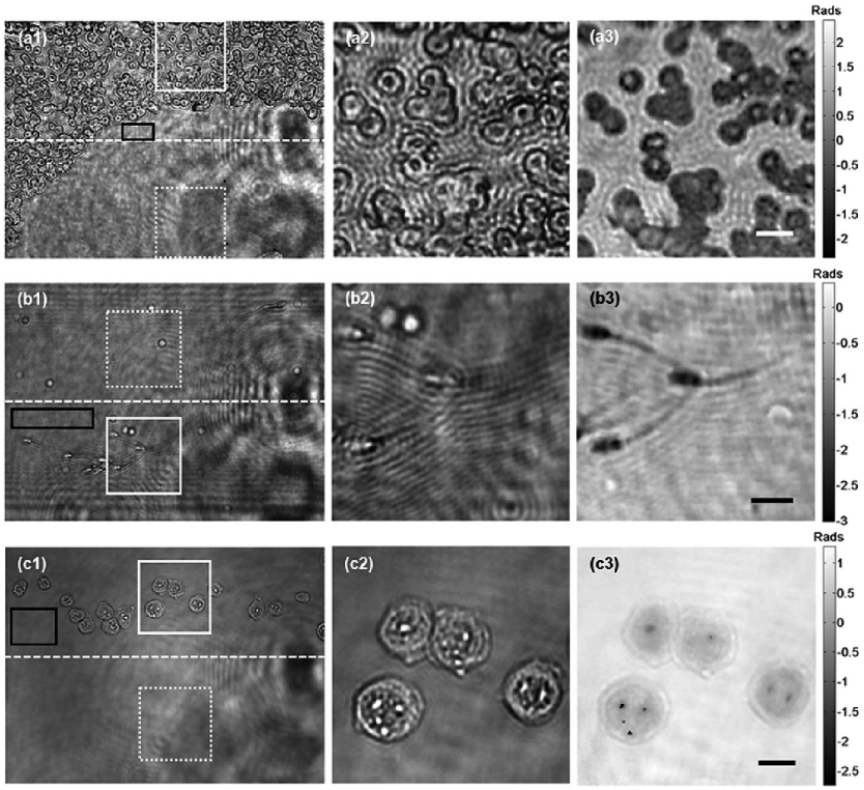

Fig. 8 Experimental results for the 20 × /0.46 NA microscope lens using biosamples: (a) RBCs, (b) SS cells, and (c) PC-3. Images at left column (1) show a direct image without the grating showing the FOV multiplexed regions. Images at central column (2) present the direct intensity image of the group of cells marked with a solid white line square in (1). And images at right column (3) include the retrieved unwrapped phase distribution using the proposed method. Scale bars: the solid lines at the lower right corner of (a3), (b3), and (c3) represent 10 μm.

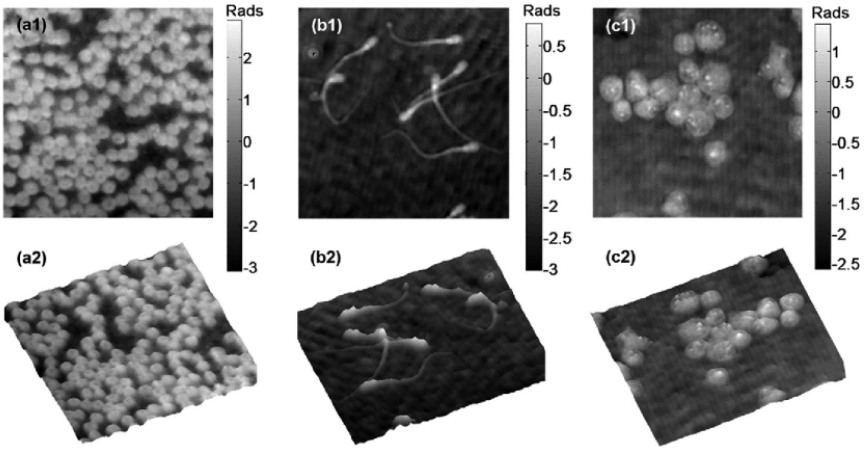

Fig. 9 Experimental results for the 10 × /0.30 NA microscope lens using biosamples: (a) RBCs, (b) SS cells, and (c) PC-3. Images in upper row (1) are the negative-phase contrast images of the ones included in Figs. 7(a3), 7(b3), and 7(c3), respectively, while the ones included in the lower row (2) include the 3-D representations of the negative-phase contrast images. Scales are equal to the images included in Fig. 7.

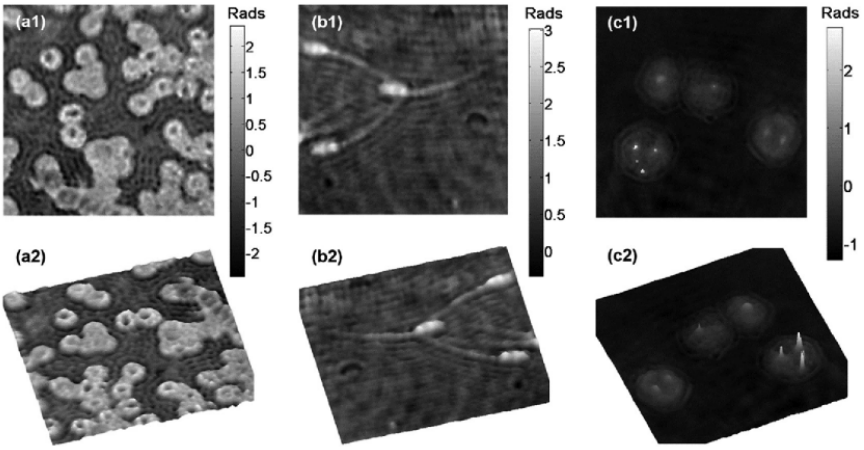

Fig. 10 Experimental results for the 20 × /0.46 NA microscope lens using biosamples: (a) RBCs, (b) SS cells, and (c) PC-3. Images in upper row (1) are the negative-phase contrast images of the ones included in Figs. 8(a3), 8(b3), and 8(c3), respectively, while the ones included in the lower row (2) include the 3-D representations of the negative-phase contrast images. Scales are equal to the images included in Fig. 8.

values are computed over some of the clear regions (background of the image) available at the retrieved phase distribution. STD is respectively computed from a single hologram and from the image resulting when considering the whole set (40 frames and 2 cycles) of temporally phase-shifted holograms for the cases of SMIM in off-axis configuration[43] and the proposed method. In the case of the proposed method, the clear area for computing the STD value is included in Fig. 4. To allow the comparative, we have selected the USAF test images since it is the unique object tested at both in Ref. 43 and in the actual paper with the same microscope objective (20 × /0.46 NA lens). Note that although an SS sample is also included in Ref. 43 and here, the counting chamber is different so the expected STD values will not be useful for direct comparison. Thus, the STD values for the USAF using SMIM with off-axis configuration[43] and with partially coherent sources are 0.31 and 0.033 rad, respectively. These values provide an improvement factor close to 10 in phase quality reconstruction as consequence of using partially coherent illumination.

In addition and for completeness, we have computed the STD values of all the retrieved images presented in this contribution. The selected clear areas for STD computation are marked with black rectangles in Figs. 4(g), 7, and 8. Note that we have selected clear areas far away from the parasitic

Table 1 STD analysis in SMIM with partially coherent illumination.

	Microbeads	RBCs	SS cells	PC-3
10×/0.30 NA STD (rad)	0.026	0.027	0.026	0.032
20×/0.46 NA STD (rad)	No data	0.06	0.028	0.025

noise due to internal dirt introduced by the illumination and this areas are sometimes inside the magnified region while other not. Results are summarized in Table 1. One can see that the background fluctuation of the retrieved phase using SMIM with partially coherent illumination is highly stable and in the order of $1/10^{th}$ of the phase stability provided by SMIM in Ref. 43.

4 Conclusions

We have presented a modification of our previously reported SMIM method[43] with improved capabilities from a quantitative phase imaging reconstruction point of view but with some penalizations when considering its applicability (slightly more complex hardware modification and useless for dynamic samples). SMIM proposes a noncomplex, low cost, and highly stable way to convert a standard microscope into a holographic one. SMIM is based on a CPI architecture using input plane spatial multiplexing and a 1-D diffraction grating to allow holographic recording. SMIM was previously validated as demonstrator at the lab[44,45] and implemented in a regular microscope.[43] In the latter validation, SMIM allows holographic imaging in a regular microscope by three small modifications: a coherent illumination source, a 1-D diffraction grating, and a specific input plane spatial distribution. The holographic recording is performed in off-axis configuration and reconstruction is achieved by spatial filtering at the Fourier domain. SMIM was validated for different samples and objectives showing a useful FOV of one-third of the available one.

In this contribution, SMIM has been validated using a partially (temporally reduced) coherent source, with a less restrictive FOV limitation (one-half instead of one-third), and for different samples and objectives. As a consequence of the reduced temporal coherence of the illumination, phase information is retrieved by phase-shifting algorithm meaning that the sample must be static during the recording time (typically a few seconds). However, spatial phase noise becomes improved and phase images show better image quality in reconstruction. The proposed SMIM modification is aimed for those cases where improved SNR and FOV will be more important issues than real time. Moreover, the use of temporally reduced coherence sources is of particular significance when implementing DHM with commercially available objectives and microscope embodiments containing a lot of glass–air interfaces without specific coatings for the used wavelength, thus generating several back reflections that can result in parasitic interference patterns. The experimental results for synthetic objects (USAF test and microbeads) as well as static biosamples (RBCs, SS cells, and PC-3) verify these assumptions. Future work will be focused on implementing the proposed technique into an inverted microscope and apply it for the analysis of live specimens using partially coherent illumination with equalized optical path difference, i.e., using a single illumination shot.

Acknowledgments

We want to thank Prof. Carles Soler and Mr. Paco Blasco from Proiser R+D S.L. for providing the swine sperm sample and Dr. José Antonio López-Guerrero from Fundación Instituto Valenciano de Oncología - FIVO for PC-3 biosample preparation. Also, part of this work has been funded by the Spanish Ministerio de Economía y Competitividad and the Fondo Europeo de Desarrollo Regional (FEDER) under the project FIS2013-47548-P.

References

1. D. Gabor, "A new microscopic principle," *Nature* **161**, 777–778 (1948).
2. G. L. Rogers, "Experiments in diffraction microscopy," *Proc. R. Soc. Edinburgh A* **63**, 193–221 (1952).
3. D. Gabor and W. P. Goss, "Interference microscope with total wavefront reconstruction," *J. Opt. Soc. Am.* **56**, 849–856 (1966).
4. J. W. Goodman and R. W. Lawrence, "Digital image formation from electronically detected holograms," *Appl. Phys. Lett.* **11**, 77–79 (1967).
5. E. Cuche, P. Marquet, and C. Depeursinge, "Simultaneous amplitude-contrast and quantitative phase-contrast microscopy by numerical reconstruction of Fresnel off-axis holograms," *Appl. Opt.* **38**, 6994–7001 (1999).
6. P. Ferraro et al., "Extended focused image in microscopy by digital holography," *Opt. Express* **13**, 6738–6749 (2005).
7. P. Marquet et al., "Digital holographic microscopy: a noninvasive contrast imaging technique allowing quantitative visualization of living cells with subwavelength axial accuracy," *Opt. Lett.* **30**, 468–470 (2005).
8. B. Kemper and G. von Bally, "Digital holographic microscopy for live cell applications and technical inspection," *Appl. Opt.* **47**, A52–A61 (2008).
9. M. K. Kim, "Principles and techniques of digital holographic microscopy," *SPIE Rev.* **1**, 018005 (2010).
10. T. Colomb et al., "Polarization microscopy by use of digital holography: application to optical-fiber birefringence measurements," *Appl. Opt.* **44**, 4461–4469 (2005).
11. P. Ferraro et al., "Compensation of the inherent wave front curvature in digital holographic coherent microscopy for quantitative phase-contrast imaging," *Appl. Opt.* **42**, 1938–1946 (2003).
12. J. Sheng, E. Malkiel, and J. Katz, "Digital holographic microscope for measuring three-dimensional particle distributions and motions," *Appl. Opt.* **45**, 3893–3901 (2006).
13. F. Dubois et al., "Digital holographic microscopy for the three-dimensional dynamic analysis of in vitro cancer cell migration," *J. Biomed. Opt.* **11**, 054032 (2006).
14. G. von Bally, *Holography in Medicine and Biology*, Springer, Berlin (1979).
15. M. K. Kim, *Digital Holographic Microscopy: Principles, Techniques, and Applications*, 1st ed., Springer, New York (2011).
16. N. T. Shaked, Z. Zalevsky, and L. L. Satterwhite, Eds., *Biomedical Optical Phase Microscopy and Nanoscopy*, Academic Press, Oxford (2012).
17. C. Mann et al., "High-resolution quantitative phase-contrast microscopy by digital holography," *Opt. Express* **13**, 8693–8698 (2005).
18. P. Chavel, "Optical noise and temporal coherence," *J. Opt. Soc. Am.* **70**, 935–943 (1980).
19. Y. Frauel et al., "Distortion-tolerant three-dimensional object recognition with digital holography," *Appl. Opt.* **40**, 3887–3893 (2001).
20. A. Ozcan et al., "Speckle reduction in optical coherence tomography images using digital filtering," *J. Opt. Soc. Am. A* **24**, 1901–1910 (2007).
21. V. Bianco et al., "Random resampling masks: a non-Bayesian one-shot strategy for noise reduction in digital holography," *Opt. Lett.* **38**, 619–621 (2013).
22. I. Moon and B. Javidi, "Three-dimensional speckle-noise reduction by using coherent integral imaging," *Opt. Lett.* **34**, 1246–1248 (2009).
23. S. Kubota and J. W. Goodman, "Very efficient speckle contrast reduction realized by moving diffuser device," *Appl. Opt.* **49**, 4385–4391 (2010).
24. G. Ouyang et al., "Speckle reduction using a motionless diffractive optical element," *Opt. Lett.* **35**, 2852–2854 (2010).

25. T. Baumbach et al., "Improvement of accuracy in digital holography by use of multiple holograms," *Appl. Opt.* **45**, 6077–6085 (2006).
26. V. Micó, C. Ferreira, and J. García, "Surpassing digital holography limits by lensless object scanning holography," *Opt. Express* **20**, 9382–9395 (2012).
27. V. Micó, C. Ferreira, and J. García, "Lensless object scanning holography for two-dimensional mirror-like and diffuse reflective objects," *Appl. Opt.* **52**, 6390–6400 (2013).
28. F. Dubois, L. Joannes, and J.-C. Legros, "Improved three-dimensional imaging with a digital holography microscope with a source of partial spatial coherence," *Appl. Opt.* **38**, 7085–7094 (1999).
29. F. Dubois et al., "Partial spatial coherence effects in digital holographic microscopy with a laser source," *Appl. Opt.* **43**, 1131–1139 (2004).
30. F. Dubois et al., "Digital holographic microscopy with reduced spatial coherence for three-dimensional particle flow analysis," *Appl. Opt.* **45**, 864–871 (2006).
31. B. Kemper et al., "Characterisation of light emitting diodes (LEDs) for application in digital holographic microscopy for inspection of micro and nanostructured surfaces," *Opt. Las. Eng.* **46**, 499–507 (2008).
32. C. Remmersmann et al., "Phase noise optimization in temporal phase-shifting digital holography with partial coherence light sources and its application in quantitative cell imaging," *Appl. Opt.* **48**, 1463–1472 (2009).
33. P. Kolman and R. Chmelík, "Coherence-controlled holographic microscope," *Opt. Express* **18**, 21990–22003 (2010).
34. F. Dubois and C. Yourassowsky, "Full off-axis red-green-blue digital holographic microscope with LED illumination," *Opt. Lett.* **37**, 2190–2192 (2012).
35. T. Slabý et al., "Off-axis setup taking full advantage of incoherent illumination in coherence-controlled holographic microscope," *Opt. Express* **21**, 14747–14762 (2013).
36. L. Repetto, E. Piano, and C. Pontiggia, "Lensless digital holographic microscope with light-emitting diode illumination," *Opt. Lett.* **29**, 1132–1134 (2004).
37. W. Bishara et al., "Lensfree on-chip microscopy over a wide field-of-view using pixel super-resolution," *Opt. Express* **18**, 11181–11191 (2010).
38. G. Biener et al., "Combined reflection and transmission microscope for telemedicine applications in field settings," *Lab Chip* **11**, 2738–2743 (2011).
39. I. P. Ryle, S. McDonnell, and J. T. Sheridan, "Lensless multispectral digital in-line holographic microscope," *J. Biomed. Opt.* **16**, 126004 (2011).
40. P. Petruck, R. Riesenberg, and R. Kowarschik, "Partially coherent light-emitting diode illumination for video-rate in-line holographic microscopy," *Appl. Opt.* **51**, 2333–2340 (2012).
41. T. Pitkäaho, M. Niemelä, and V. Pitkäkangas, "Partially coherent digital in-line holographic microscopy in characterization of a microscopic target," *Appl. Opt.* **53**, 3233–3240 (2014).
42. B. Perucho and V. Micó, "Wavefront holoscopy: application of digital in-line holographic for the inspection of engraved marks in progressive addition lenses," *J. Biomed. Opt.* **19**, 016017 (2014).
43. V. Mico et al., "Spatially-multiplexed interferometric microscopy (SMIM): converting a standard microscope into a holographic one," *Opt. Express* **22**, 14929–14943 (2014).
44. V. Mico, Z. Zalevsky, and J. García, "Super-resolution optical system by common-path interferometry," *Opt. Express* **14**, 5168–5177 (2006).
45. V. Mico, Z. Zalevsky, and J. García, "Common-path phase-shifting digital holographic microscopy: a way to quantitative imaging and super-resolution," *Opt. Commun.* **281**, 4273–4281 (2008).
46. V. Mico, J. Garcia, and Z. Zalevsky "Quantitative phase imaging by common-path interferometric microscopy: application to super-resolved imaging and nanophotonics," *J. Nanophoton* **3**, 031780 (2009).
47. P. Gao et al., "Parallel two-step phase-shifting digital holograph microscopy based on a grating pair," *J. Opt. Soc. Am. A* **28**, 434–440 (2011).
48. P. Gao et al., "Parallel two-step phase-shifting point-diffraction interferometry for microscopy based on a pair of cube beamsplitters," *Opt. Express* **19**, 1930–1935 (2011).
49. M. Shan et al., "Parallel two-step spatial carrier phase-shifting common-path interferometer with a Ronchi grating outside the Fourier plane," *Opt. Express* **21**, 2126–2132 (2013).
50. I. Yamaguchi and T. Zhang, "Phase-shifting digital holography," *Opt. Lett.* **22**, 1268–1270 (1997).
51. T. Zhang and I. Yamaguchi, "Three-dimensional microscopy with phase-shifting digital holography," *Opt. Lett.* **23**, 1221–1223 (1998).
52. T. Kreis, *Handbook of Holographic Interferometry: Optical and Digital Methods*, Wiley-VCH Verlag GmbH & Co. KGaA, Weinheim (2005).
53. G. Popescu et al., "Diffraction phase microscopy for quantifying cell structure and dynamics," *Opt. Lett.* **31**, 775–777 (2006).
54. P. Bon et al., "Quadriwave lateral shearing interferometry for quantitative phase microscopy of living cells," *Opt. Express* **17**, 13080–13094 (2009).
55. B. Kemper et al., "Simplified approach for quantitative digital holographic phase contrast imaging of living cells," *J. Biomed. Opt.* **16**, 026014 (2011).
56. M. Born and E. Wolf, *Principles of Optics*, 7th ed., Cambridge University, Cambridge, UK (1999).
57. P. Langehanenberg, G. V. Bally, and B. Kemper, "Application of partially coherent light in live cell imaging with digital holographic microscopy," *J. Mod. Opt.* **57**, 709–717 (2010).
58. Y. Awatsuji, M. Sasada, and T. Kubota, "Parallel quasi-phase-shifting digital holography," *Appl. Phys. Lett.* **85**, 1069–1071 (2004).
59. T. Tahara et al., "Parallel phase-shifting digital holographic microscopy," *Biomed. Opt. Express* **1**, 610–616 (2010).

Biographies for the authors are not available.

Letter Vol. 42, No. 5 / March 1 2017 / Optics Letters 927

Optics Letters

Superresolved spatially multiplexed interferometric microscopy

José Ángel Picazo-Bueno,[1] Zeev Zalevsky,[2] Javier García,[1] and Vicente Micó[1,*]

[1]Department de Óptica y de Optometría y Ciencias de la Visión, Facultad Física, Universidad Valencia, C/Doctor Moliner 50, Burjassot 46100, Spain
[2]School of Engineering, Bar-Ilan University, Ramat-Gan 52900, Israel
*Corresponding author: Vicente.Mico@uv.es

Received 11 January 2017; accepted 31 January 2017; posted 6 February 2017 (Doc. ID 284440); published 23 February 2017

Superresolution capability by angular and time multiplexing is implemented onto a regular microscope. The technique, named superresolved spatially multiplexed interferometric microscopy (S2MIM), follows our previously reported SMIM technique [Opt. Express 22, 14929 (2014), J. Biomed. Opt. 21, 106007 (2016)] improved with superresolved imaging. All together, S2MIM updates a commercially available non-holographic microscope into a superresolved holographic one. Validation is presented for an Olympus BX-60 upright microscope with resolution test targets. © 2017 Optical Society of America

OCIS codes: (090.1995) Digital holography; (100.2000) Digital image processing; (100.6640) Superresolution; (180.3170) Interference microscopy.

https://doi.org/10.1364/OL.42.000927

Optical imaging systems are restricted in both axial and transversal resolution due to diffraction [1]. Such limitation was first introduced by Ernst Abbe who explained the role of numerical aperture (NA) and illumination wavelength (λ) concerning the resolving power in microscopy. In terms of spatial frequencies, every optical system has a bandpass truncation that limits the transversal resolution (ρ) to a value of $\rho = k\lambda/\mathrm{NA}$, g NA being the numerical aperture of the imaging system defined as $\mathrm{NA}_{\mathrm{illum}} + \mathrm{NA}_{\mathrm{lens}}$ and k being equal to 0.82 for coherent imaging systems having circular apertures [2,3]. For plane wave illumination ($\mathrm{NA}_{\mathrm{illum}} = 0$) and for air-immersed imaging systems, the maximum theoretical NA equals to 1, meaning that ρ can go down to a minimum value of $\sim\lambda$. However, it is habitual in microscopy to use lower NA values because these lenses provide attractive additional properties (longer working distances, larger fields of view, reduced prices, etc.). Thus, optical superresolution (SR) relates with the capability to overcome the resolution limit imposed by diffraction without changing the NA value of the lenses [4].

Abbe also pointed out that ρ can be increased by tilting the illumination with respect to the optical axis [1]. Ueda and Sato applied this concept to holography by recording a multi-exposed hologram composed of coherent addition of several bandpass images of the input object which were sequentially obtained under different oblique illuminations [5]. This illumination procedure is similar to the one provided by structure illumination for SR in digital holographic microscopy (DHM) [6,7], and it has been widely applied in combination with interferometric recording in both digital holography [6–17] and DHM [18–26] as a strategy to achieve SR imaging.

Recently, we have reported on a non-complex and low-cost way to convert a commercially available regular microscope into a holographic one with only minimal modifications [27,28]. The technique, named spatially multiplexed interferometric microscopy (SMIM), implements a common-path interferometric setup [19] into a real microscope embodiment where (1) the broadband light source is replaced by a coherent one, (2) a one-dimensional (1D) diffraction grating is properly inserted at the microscope embodiment, and (3) a clear region at the input plane is saved for reference beam transmission. SMIM upgrades a regular microscope into a holographic one with off-axis holographic recording with Fourier filtering [27] or slightly off-axis recording with a phase-shifting (P-S) algorithm [28].

In this contribution, we report on the additional capability of merging SMIM with SR imaging by angular multiplexing, thus allowing S2MIM (initials incoming from superresolved SMIM). Taking the basic layout proposed by SMIM [27,28], SR enables a resolution gain factor of 2 based on tilted beam illumination achieved by lateral displacement of the coherent source to a set of off-axis positions (from 4 to 9, depending on the desired object's spectrum coverage [12]) which are implemented sequentially using time multiplexing. In addition, the SMIM technique recovers the complementary spatial-frequency content provided by each tilted illumination. All this information is used to generate a SA expanding the cutoff frequency of the system and, thus, allowing SR imaging. All together, this letter validates S2MIM as a low-cost, simple, and versatile way of implementing SR and DHM into a regular upright non-holographic microscope.

SMIM [27,28] can be summarized through Figs. 1(a) and 1(b), where a coherent source (laser diode [27] or a SLD [28]) replaces the broadband light, the input plane is divided into three [27] or two [28] regions for spatial multiplexing of the field of view (FOV), and a 1D diffraction grating is inserted

0146-9592/17/050927-04 Journal © 2017 Optical Society of America

928 Vol. 42, No. 5 / March 1 2017 / Optics Letters Letter

somewhere in the microscope embodiment. The first permits holographic recording, the second is needed for clear reference beam transmission, and the third defines the holographic recording mode to be used (off-axis [27] and slightly off-axis [28]). Thus, the 1D grating [Fig. 1(b)] provides three replicas at the output plane and by properly selecting its period and position, the clear transparent area [*R* at Fig. 1(a)] overlaps with the sample area [*O* at Fig. 1(a)] forming an image plane hologram at the CCD plane. From it, the complex amplitude distribution of the transmitted bandpass image is retrieved by off-axis holographic recording and Fourier filtering [27] or slightly on-axis holographic recording and a P-S algorithm [28]. This procedure has been considered [27,28] for on-axis illumination using different lenses (5X, 10X, and 20X infinity corrected objectives), and now it is extended to off-axis illuminations for SR.

The main drawback of SMIM is the FOV restriction imposed by the need to transmit a clear transparent reference beam. As a consequence, modest/low NA objectives, which usually provide larger FOVs than higher NA ones, are additionally restricted in FOV. But, is it possible to increase the NA value (and thus the resolution) without modifying a given optical imaging configuration in SMIM? In such a case, and for a given microscope lens, the FOV is penalized (one-third [27] or half [28] of the available one), but the resolution will be improved in that limited FOV. As a result, a modest/low NA lens under S2MIM will present a useful FOV comparable to the FOV provided by a higher NA lens without SMIM and with a resolution limit similar to the one provided by this higher NA lens. For instance, a 5X/0.15NA objective has a FOV which is usually twice the one provided by a 10X/0.30NA lens. When applying SMIM, the useful FOV of the 5X/0.15NA lens is reduced to one-half (assuming the method reported in [28]), thus equaling the one provided by the 10X/0.30NA lens without SMIM. After applying S2MIM to the 5X/0.15NA objective, its resolution limit in the useful FOV will approach the one provided by the 10X/0.30NA lens without SMIM.

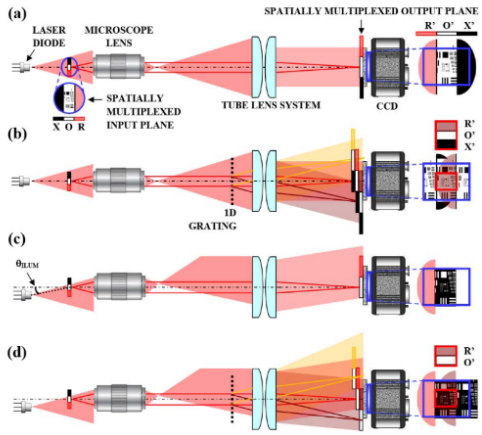

Fig. 1. S2MIM layout visualized through different cases: (a), (b) on-axis illumination without and with 1D grating, respectively, defining the regular SMIM mode, and (c), (d) off-axis illumination without and with 1D grating, respectively, showing a tilted beam illumination case for S2MIM. The blue and red rectangles will be introduced afterward.

To validate this target, we have implemented a mix between both previously reported SMIM configurations: a laser diode illuminates the input object (as in [27]), and the spatial multiplexing is defined as one-third of the available one (as in [27]), but the holographic recording is implemented by using slightly off-axis configuration and a P-S algorithm (as in [28]). In addition, two experiments are included for two different low NA microscope lenses (a 2X/0.05NA and a 5X/0.15NA Olympus objectives), each one of them using different components: (1) a VCSEL source (1 mW optical power, 850 nm) and a DVD laser diode source (5 mW optical power, 650 nm), and (2) a 1D Ronchi-ruled grating of 80 and 50 lp/mm period for the 2X and 5X objectives, respectively.

SR is implemented by displacing the illumination source to several positions out of the optical axis. Figure 1(c) represents one of these situations where the *O* region becomes illuminated with a tilted beam, so a complementary portion of the object's spectrum will be diffracted on-axis passing through the imaging lens aperture. The only restriction is that the illumination angle θ_{illum} will be above the one defined by the objective's NA. In addition, one side of the multiplexed FOV passes (the one incoming from *R*), so it is possible to overlap them at the CCD plane with the proper diffraction grating [Fig. 1(d)]. This process is repeated sequentially in time for four off-axis positions of the illumination source, thus recovering four additional pupils containing complementary spatial-frequency information of the object's spectrum, which are then used to generate an expanded SA from which a SR image is obtained as its Fourier transform [12,23].

Figure 1 also includes the output plane transversal distributions for the depicted cases: (a) the output plane distribution divided into three slots (R', O', and X') when on-axis illumination and no grating are considered, (b) the overlapping of the three regions by the 1D grating, (c) an off-axis illumination case where a bandpass image of the object (O') is accessible, and a clear reference beam (R') is at its side, and (d) the overlapping between O' and R' as a consequence of the 1D grating. The blue rectangle represents a complete FOV coverage by the sensor area, but it is enough to cover only the central red rectangle where overlapping is produced. This case will be our implementation case when using a commercial grade CCD camera (Basler A312f, 582 × 782 pixels, 8.3 μm pixel size, 12 bits/pixel).

Our first experimental implementation involves a 5X/0.15NA lens and a USAF resolution test target. Figure 2 shows the direct intensity imaging mode without the 1D grating (cases a and b) and the recorded interference when the diffraction grating is added (cases c and d). On one hand, we can see as the experimental resolution limit (Group 8-Element 1 or G8-E1: 256 lp/mm or 3.91 μm) perfectly matches with its theoretical value ($\rho = 3.55$ μm or 281 lp/mm) since the subsequent element (G8-E2: 287 lp/mm or 3.48 μm) remains unresolved. On the other hand, the interference period is too large and will not allow a Fourier filtering procedure to retrieve the complex amplitude of the transmitted bandpass image. Thus, a phase-shifting method is needed. As example, Visualization 1 presents the whole set of recorded slightly off-axis holograms from which a P-S algorithm (20 frames full cycle) is applied. In addition, the unblocked USAF test is overlapping at the

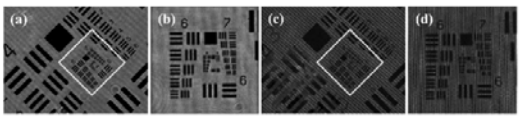

Fig. 2. S2MIM for the 5X/0.15NA objective: (a) a full frame image without grating (regular intensity imaging mode), (b) a magnified image of the central part marked with a solid line white rectangle, (c) full frame image with the grating, and (d) the same magnified ROI as in (b). Visualization 1 (4.7 MB) corresponds to (d).

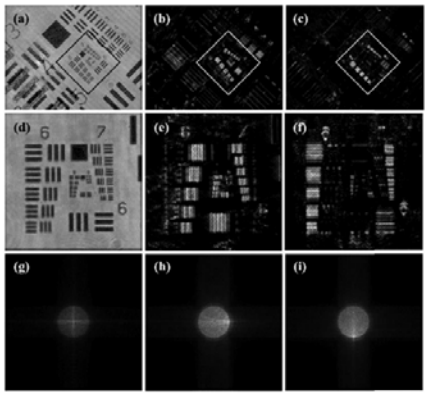

Fig. 3. S2MIM process for the 5X/0.15NA objective when considering three different illuminations: (a), (d), and (c) full frame images after a P-S algorithm for on-axis, horizontal, and vertical off-axis illuminations, respectfully; (b), (e), and (h) the central magnifications of (a), (d), and (g), respectfully; and (c), (f), and (i) the coherent apertures incoming from (b), (e), and (h), respectively.

lower left corner of Fig. 3(b), but this fact does not disturb the central part where S2MIM is validated.

Figure 3 includes three examples of the retrieved bandpass images after the P-S procedure: the left-central-right columns represent the on-axis, one horizontal and one vertical tilted beam illuminations, respectively. Note that Fig. 3(d) is equivalent to Fig. 2(c), but contains complex amplitude distribution. As a result, three elementary apertures (lower row) are retrieved and used to generate a SA coming from their coherent addition and guided by a visual image quality criterion [11] or by correlation operation with the overlapping areas between elementary apertures [22,25]. This process takes into account the equalization of three different factors for each recovered bandpass image in order to get a high-quality superresolved image: (1) a global constant phase factor [$\exp(iC)$, C being a constant] coming from mismatches in the optical path traveled for each tilted beam, (2) a quadratic phase factor [$\exp(i2\pi(ax^2 + by^2)/\lambda)$ being the coefficients (a, b) proportional to the misfocus] coming from small curvature errors of the sequential illuminations, and (3) a linear phase factor [$\exp(i2\pi(cx + ey)/\lambda)$ being the coefficients (c, e) proportional to the tilted illumination angle] needed to shift back each aperture to its original position in the object's spectrum.

Finally, Fig. 4 includes the results of the generated SA [Fig. 4(a)] which defines a higher cutoff frequency and yields in a SR image [Fig. 4(b)]. In comparison with the low-resolution image [Fig. 4(d) being the same than Fig. 3(d)] which corresponds with the inverse Fourier transform of the central aperture [solid white line circle at Fig. 4(a)], we can see that the last resolved element after S2MIM is G9-E1 corresponding with 512 lp/mm (or 1.95 μm). This element defines a new resolution limit related with a resolution gain factor of around 2 (from 3.91 to 1.95 μm). Compared with the image provided by a 10X/0.30NA Olympus lens under the same on-axis illumination conditions [Fig. 4(c)], we can see that both have the same resolution limit, thus validating our previous calculations. In addition, Figs. 4(b) and 4(d) include a three-dimensional (3D) view of the retrieved phase distributions just to strength that the complex amplitude is accessible, and Fig. 4(e) presents the plots along the vertical dashed lines placed at the red-green insets in Figs. 4(b) and 4(d) to clearly show the resolution improvement at both intensity and phase distributions.

The second experiment involves a 2X/0.05NA Olympus objective with a VCSEL diode as illumination. Now, the input

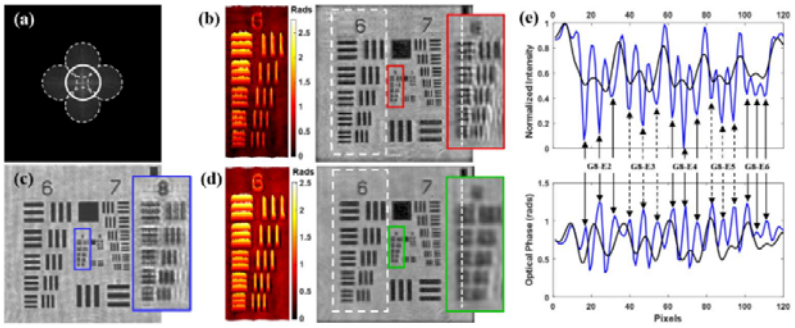

Fig. 4. Final result for the 5X/0.15NA objective: (a) the generated SA coming from the addition of four additional off-axis apertures (dashed white circles), (b) the superresolved image provided by S2MIM with a magnified portion (red rectangle) and a 3D plot of the phase distribution (dashed white rectangle), (c) the image provided by a 10X/0.30 objective using SMIM with on-axis illumination with the same area magnified (blue rectangle) for comparison, (d) the same visualizations as in (b), but for a conventional SMIM image, and (e) the plots for S2MIM (blue line) and SMIM (black line) along the dashed white lines included in the magnified ROIs at (b) and (d) considering intensity (up) and phase (down) distributions.

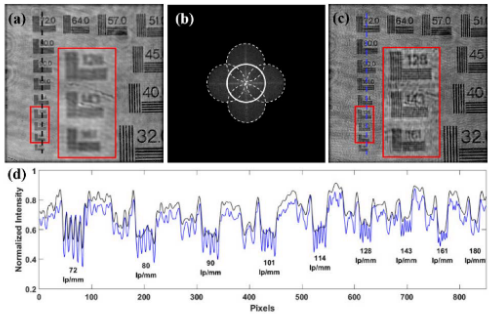

Fig. 5. Final result for the 2X/0.05NA lens: (a) the conventional low-resolution image provided by SMIM, (b) the SA coming from the addition of four additional off-axis apertures, (c) the SR image provided by S2MIM, and (d) the plots along the vertical lines at (a)–(c), respectively.

object is a NBS 1963A resolution target with elements ranging from 1 to 180 lp/mm. Figure 5 includes only the final results concerning (a) the conventional image obtained with regular SMIM and corresponding with the central pupil [solid white circle at Fig. 5(b)], (b) the generated SA, (c) the SR image provided by S2MIM, and (d) the plots along the vertical dashed lines included at Fig. 5(a) [black line] and Fig. 5(c) [blue line] to clearly show resolution improvement by identifying the five horizontal bars of each element. Although the element corresponding with 161 lp/mm (6.2 μm period) is barely resolved, we can see that the experimental resolution limit (the theoretical one is $\rho = 13.94$ μm) is improved from 72 lp/mm (13.9 μm period) to 143 lp/mm (7 μm period), once again validating a gain factor in a resolution of 2. In addition, Figs. 5(a) and 5(c) include insets where the elements marked with a red rectangle are magnified showing that the element's bars are not resolved with conventional SMIM, but they are using S2MIM.

In summary, previously reported SMIM has been improved with SR capability. Updating a regular microscope with coherent sensing capabilities [27–39] is an interesting alternative to commercially available holographic microscopes, depending on the application. However, the useful FOV becomes restricted as a consequence of using SMIM [27,28]. When a reasonable resolution limit is pursued, the usage of medium NA lenses can severely limit the allowable FOV. Instead of this, we can relax the NA parameter to get a higher FOV and apply S2MIM to improve the resolution limit. In other words, the FOV limitation is removed by doubling the resolving power. Experimental validations have been provided for two different low NA objectives. Nevertheless, the method is theoretically applicable to higher NA lenses at the expense of lower FOVs. Possibly the biggest restriction of the method is the use of a time multiplexing approach meaning that it is not possible to apply S2MIM for dynamic samples.

Funding. Ministerio de Economía y Competitividad (MINECO) (FIS2013-47548-P); European Regional Development Fund (ERDF).

REFERENCES

1. E. Abbe, Arch. Mikrosk. Anat. **9**, 413 (1873).
2. M. Born and E. Wolf, *Principles of Optics*, 7th ed., (Cambridge University, 1999).
3. Y. Cotte, M. F. Toy, E. Shaffer, N. Pavillon, and C. Depeursinge, Opt. Lett. **35**, 2176 (2010).
4. Z. Zalevsky and D. Mendlovic, *Optical Super Resolution* (Springer, 2002).
5. M. Ueda and T. Sato, J. Opt. Soc. Am. **61**, 418 (1971).
6. P. Gao, G. Pedrini, and W. Osten, Opt. Lett. **38**, 1328 (2013).
7. J. Zheng, P. Gao, B. Yao, T. Ye, M. Lei, J. Min, D. Dan, Y. Yang, and S. Yan, Photonics Res. **2**, 87 (2014).
8. S. A. Alexandrov, T. R. Hillman, T. Gutzler, and D. D. Sampson, Phys. Rev. Lett. **97**, 168102 (2006).
9. C. Yuan, H. Zhai, and H. Liu, Opt. Lett. **33**, 2356 (2008).
10. M. Paturzo, F. Merola, S. Grilli, S. De Nicola, A. Finizio, and P. Ferraro, Opt. Express **16**, 17107 (2008).
11. V. Mico and Z. Zalevsky, J. Biomed. Opt. **15**, 046027 (2010).
12. L. Granero, V. Micó, Z. Zalevsky, and J. García, Appl. Opt. **49**, 845 (2010).
13. J. Zhao, X. Yan, W. Sun, and J. Di, Opt. Lett. **35**, 3519 (2010).
14. L. Granero, Z. Zalevsky, and V. Micó, Opt. Lett. **36**, 1149 (2011).
15. A. Hussain and A. A. Mudassar, Opt. Commun. **285**, 2303 (2012).
16. V. Micó, C. Ferreira, and J. García, Opt. Express **20**, 9382 (2012).
17. L. Granero, C. Ferreira, Z. Zalevsky, J. García, and V. Micó, Opt. Lasers Eng. **82**, 104 (2016).
18. C. J. Schwarz, Y. Kuznetsova, and S. R. J. Brueck, Opt. Lett. **28**, 1424 (2003).
19. V. Mico, Z. Zalevsky, P. García-Martínez, and J. García, Opt. Express **12**, 2589 (2004).
20. V. Mico, Z. Zalevsky, and J. García, Opt. Express **14**, 5168 (2006).
21. Y. Kuznetsova, A. Neumann, and S. R. J. Brueck, Opt. Express **15**, 6651 (2007).
22. V. Mico, Z. Zalevsky, C. Ferreira, and J. García, Opt. Express **16**, 19260 (2008).
23. J. Bühl, H. Babovsky, A. Kiessling, and R. Kowarschik, Opt. Commun. **283**, 3631 (2010).
24. C. Yuan, G. Situ, G. Pedrini, J. Ma, and W. Osten, Appl. Opt. **50**, B6 (2011).
25. M. Kim, Y. Choi, C. Fang-Yen, Y. Sung, R. R. Dasari, M. S. Feld, and W. Choi, Opt. Lett. **36**, 148 (2011).
26. A. Calabuig, V. Mico, J. Garcia, Z. Zalevsky, and C. Ferreira, Opt. Lett. **36**, 885 (2011).
27. V. Micó, C. Ferreira, Z. Zalevsky, and J. García, Opt. Express **22**, 14929 (2014).
28. J. A. Picazo-Bueno, Z. Zalevsky, J. García, C. Ferreira, and V. Micó, J. Biomed. Opt. **21**, 106007 (2016).
29. G. Popescu, T. Ikeda, R. R. Dasari, and M. S. Feld, Opt. Lett. **31**, 775 (2006).
30. C. Maurer, A. Jesacher, S. Fürhapter, S. Bernet, and M. Ritsch-Marte, J. Microsc. **230**, 134 (2008).
31. D. Fu, S. Oh, W. Choi, T. Yamauchi, A. Dorn, Z. Yaqoob, R. R. Dasari, and M. S. Feld, Opt. Lett. **35**, 2370 (2010).
32. X. Cui, J. Ren, G. J. Tearney, and C. Yang, Opt. Express **18**, 16685 (2010).
33. B. Kemper, A. Vollmer, C. E. Rommel, J. Schnekenburger, and G. von Bally, J. Biomed. Opt. **16**, 026014 (2011).
34. V. Chhaniwal, A. S. G. Singh, R. A. Leitgeb, B. Javidi, and A. Anand, Opt. Lett. **37**, 5127 (2012).
35. N. T. Shaked, Opt. Lett. **37**, 2016 (2012).
36. K. Lee and Y. Park, Opt. Lett. **39**, 3630 (2014).
37. I. Frenklach, P. Girshovitz, and N. T. Shaked, Opt. Lett. **39**, 1525 (2014).
38. S. Karepov, N. T. Shaked, and T. Ellenbogen, Opt. Lett. **40**, 2273 (2015).
39. D. Roitshtain, N. A. Turko, B. Javidi, and N. T. Shaked, Opt. Lett. **41**, 2354 (2016).

Letter Vol. 43, No. 5 / 1 March 2018 / Optics Letters 1007

Optics Letters

Hilbert–Huang single-shot spatially multiplexed interferometric microscopy

José Ángel Picazo-Bueno,[1] Maciej Trusiak,[2] Javier García,[1] Krzysztof Patorski,[2] and Vicente Micó[1,*]

[1]Departamento de Óptica y de Optometría y Ciencias de la Visión, Facultad de Física, Universitat de Valencia, C/Doctor Moliner 50, Burjassot 46100, Spain
[2]Warsaw University of Technology, Institute of Micromechanics and Photonics, 8 Sw. A. Boboli St., 02-525 Warsaw, Poland
*Corresponding author: vicente.mico@uv.es

Received 12 December 2017; revised 15 January 2018; accepted 18 January 2018; posted 19 January 2018 (Doc. ID 315559); published 21 February 2018

Hilbert–Huang single-shot spatially multiplexed interferometric microscopy (H2S2MIM) is presented as the implementation of a robust, fast, and accurate single-shot phase estimation algorithm with an extremely simple, low-cost, and highly stable way to convert a bright field microscope into a holographic one using partially coherent illumination. Altogether, H2S2MIM adds high-speed (video frame rate) quantitative phase imaging capability to a commercially available nonholographic microscope with improved phase reconstruction (coherence noise reduction). The technique has been validated using a 20×/0.46 NA objective in a regular Olympus BX-60 upright microscope for static, as well as dynamic, samples showing perfect agreement with the results retrieved from a temporal phase-shifting algorithm.

OCIS codes: (100.5070) Phase retrieval; (180.3170) Interference microscopy; (170.0180) Microscopy; (120.2650) Fringe analysis; (170.3880) Medical and biological imaging.

https://doi.org/10.1364/OL.43.001007

Nowadays quantitative phase imaging (QPI) of biological specimens is a very useful tool for accurate analysis in medical diagnosis [1–3]. QPI is usually achieved by digital holographic microscopy (DHM), a technique that combines into a single platform high-quality imaging provided by microscopy, whole-object wavefront recovery ensured by holography, and numerical processing capabilities yielded by computers [4,5]. DHM allows visualization of phase samples using a noninvasive (no need for stained samples), full-field (nonscanning), real-time (on-line control), noncontact (no sample damage), and static (no moving components) operating principle.

In connection with this fact, today there is a growing interest in proposing new DHM configurations with improved capabilities in terms of simplicity, accuracy, robustness, price, and ease of use [6–22]. Among those methods, spatially multiplexed interferometric microscopy (SMIM) proposes a noncomplex and low-cost way to convert a commercially available regular microscope into a holographic one with only minimal modifications [19,20]. SMIM is based on a common-path interferometric layout and the modifications consist of (1) the replacement of the broadband light source by a coherent one, (2) the proper insertion of a one-dimensional (1D) diffraction grating in the microscope embodiment, and (3) saving a clear region at the input plane for reference beam transmission. The SMIM has been validated under an off-axis holographic recording with Fourier filtering [19] or slightly off-axis recording with a phase-shifting (P-S) algorithm [20]. In Ref. [21], SMIM is merged with super-resolution capabilities to overcome its main drawback: the field of view (FOV) restriction imposed by the need to transmit a clear transparent reference beam for holographic recording.

The recently proposed single-shot Hilbert–Huang phase microscopy (S2H2PM) method is composed of a fast, accurate, and robust QPI technique employing a single hologram [23]. The S2H2PM is based on the Hilbert–Huang transform (HHT). Huang's part—empirical mode decomposition (EMD)—originally employs adaptive dissection of analyzed 1D nonstationary and nonlinear signal into a set of so-called intrinsic mode functions representing signal features in different scales [24]. Efficiently managing this set of sub-signals (discarding spurious and preserving informative ones), one can develop a capable signal processing tool. Moreover, each empirical mode oscillates around zero which makes them perfectly suited for a further Hilbert transform phase and amplitude demodulation based on the analytic signal concept [24]. Recently, HHT was generalized into two-dimensional (2D), substantially enhanced in terms of both time consumption and accuracy extending its capabilities especially onto fringe pattern analysis, e.g., in phase microscopy [23,25–29]. As a result, S2H2PM uses an adaptive image-domain fringe filtering based on 2D enhanced fast EMD (first part of the 2D HHT) and 2D Hilbert spiral transform [30] with precise phase demodulation aided by the local fringe direction map estimation [29] (second party of the 2D HHT).

The S2H2PM retrieves sample phase distribution, regardless of the tilt angle between both interferometric beams and

0146-9592/18/051007-04 Journal © 2018 Optical Society of America

1008 Vol. 43, No. 5 / 1 March 2018 / Optics Letters Letter

without the need to apply a temporal P-S algorithm. This capability is very appealing since it optimizes the space-bandwidth product of the system while allowing real-time imaging only limited by the sensor acquisition frame rate. In a few words, S2H2PM [23] improves and overcomes the limitations of previously introduced Hilbert transform for phase demodulation [25,26] regarding (1) a 1D operating principle needing perpendicular fringes to the analyzed direction; (2) reduced flexibility in the type of fringes to be analyzed (sinusoidal, with no nonlinearities, not closed or significantly bent, having a certain fringe period close to off-axis configuration); and (3) uniform and constant hologram background. The S2H2PM technique [23] surpasses all of those limitations by using an adaptive 2D fringe pattern filtering employing empirical decomposition [27,28] and modified automatic selective reconstruction [29]. Only sharply extracted regions of each informative mode containing well-denoised fringes are preserved in the localized fringe filtering process.

In this contribution, we combine SMIM with a modified version of the S2H2PM algorithm into a single platform. Several major advancements are incorporated into the processing path of the S2H2PM technique. The modifications are aimed at increasing robustness and versatility of the reported scheme. The S2H2PM starts with adaptive filtering over the single fringe pattern (hologram, interferogram, etc.), and we propose the use of an automatic masking algorithm based on variational image decomposition (VID) [31] and Otsu thresholding. Other steps, i.e., local fringe direction map estimation, phase unwrapping, and further filtering, are modified accordingly and will be described in the experimental validation section. The result, named Hilbert–Huang single-shot SMIM (H2S2MIM), takes all the advantages of SMIM regarding an extremely simple, cost-effective, highly stable, and fast way to convert a standard microscope into a holographic one, in addition to the ones incoming from the modified version of S2H2PM and related to a robust and single-shot operational principle, even when partially coherent illumination is used in SMIM. This perfect combination equips a commercially available nonholographic microscope with accurate QPI capabilities and allows fast dynamic sample analysis only limited by the frame rate of the camera sensor.

The experimental validation of the proposed H2S2MIM method is implemented using the embodiment of a BX60 Olympus microscope, as in previous SMIM Refs. [19–21]. For the sake of simplicity, Fig. 1 depicts a scheme of the approach, where the main components of the microscope setup are taken into account. A superluminescent diode ([SLD] from Exalos, Model EXS6501-B001, 10 mW of optical power, a 650 nm central wavelength, a 6 nm spectral bandwidth) illuminates the input plane, where the useful FOV is spatially multiplexed into object/sample (O) and reference/clear (R) regions. The objective (Olympus UMPlanF infinity corrected 20×/0.46NA) and the tube lens system magnify the input plane spatially multiplexed distribution at the output port of the microscope, where a charge-coupled device (CCD) camera (Basler A312f, 582 × 782 pxs, 8.3 μm px size, 12 bits/px) is placed. In this way, conventional (nonholographic) imaging is recorded, but a 1D diffraction grating (Ronchi ruled grating, 20 lp/mm period) is introduced in the analyzer insertion slot just before the tube lens to allow output plane replicas and, thus, interferometric recording. Issues about proper selection of the 1D grating can be found in Ref. [20].

Using this optical layout, the microscope objective provides an infinity conjugated image which is brought into focus by the tube lens. By following the ray tracing at Fig. 1 of the on-axis (solid line) object (black) and reference (red) rays at the center of both O-R input plane regions, the 0th order of the 1D grating does not disturb the conventional imaging mode. However, the −1st diffraction order provides a shifted replica at the output plane allowing the overlapping at the lower CCD half-area of the conventional object beam, named O′(0th), with the reference beam coming from the −1st grating's diffraction order, named R′(−1st). Something similar happens at the upper CCD half-area when considering the conventional (nondiffracted) reference beam ray tracing, named R'(0th), with the object beam coming from the +1st grating's diffraction order, named O′(+1st). In order to clearly show this FOV duplicity at the output plane, Fig. 1 contains the output distribution coming from a 90 μm diameter microbead as an input object. However, the selected region for final reconstruction comes from the lower CCD half-area, that is, O′(0th) + R′(−1st), due to practical reasons (grating order efficiency, FOV constrictions at the input plane and vignetting issues).

Experimental validation of H2S2MIM has been divided into three parts. The first one involves a calibration stage in which a microbead of 90 μm in diameter is used to show the whole process step by step. This microbead is the one included at Fig. 1 so in the experimental results (see Fig. 2), we will only include the region of interest (ROI) marked with the white square at Fig. 1. To allow comparison, the sample must be static at least in the time where the P-S process is implemented. For the P-S procedure, the grating is placed on a motorized linear translation stage (Newport, model ESP300). A grating motion step of 2.5 μm between consecutive holograms is applied, meaning that 20 images integrate a full P-S cycle according to the grating's period. Nevertheless,

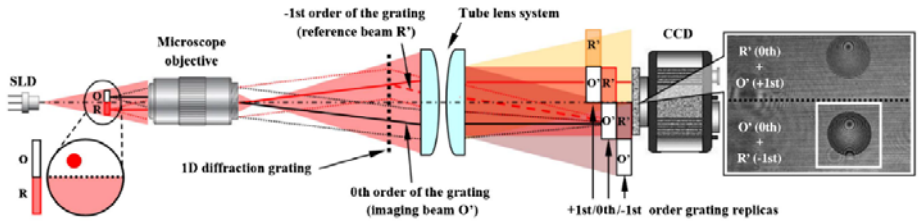

Fig. 1. Optical layout and ray tracing for H2S2MIM. Reconstructions come from the lower half of the CCD area where the O′(0th) + R′(−1st) beams overlap.

80 images are recorded in order to perfectly select the frames integrating the full P-S cycle and to minimize uncertainty errors in phase determination.

Figure 2(a) presents a single hologram (first frame of the full P-S video movie, Visualization 1), while Fig. 2(b) includes its Fourier transform (FT) showing overlapping of the different hologram diffraction orders (marked with white circles), so P-S is needed for complex amplitude retrieval; Fig. 2(c) presents a complex amplitude pupil retrieved after P-S algorithm application; Fig. 2(d) shows the intensity image of the bead obtained as inverse FT operation from Fig. 2(c); and Figs. 2(e)–2(f) present the 2D phase distribution in wrapped and unwrapped visualization modes, respectively. The results provided by the H2S2MIM method are included at Figs. 2(g) and 2(h) concerning 2D wrapped and unwrapped phase distributions. Finally, Fig. 2(i) presents a cross section of the retrieved phase profiles coming from the P-S and H2S2MIM methods in blue and red colors, respectively. Aside from the background differences, the H2S2MIM method perfectly matches the result provided by P-S technique.

The second validation compares reconstructions incoming from H2S2MIM method with a conventional P-S algorithm for more complex, but still static, samples. Two different types of prostate cancer cells (PC-3 and LnCaP cell lines) are used. Both types of cells were cultured in an RPMI 1640 medium with 10% fetal bovine serum, 100 U/ml Penicillin and 0.1 μg/ml streptomycine at standard cell culture conditions (37°C in 5% CO_2 in a humidified incubator). Once the cells reach a confluent stage, they were released from the culture support and centrifuged. The supernatant fluid is discarded by centrifugation, and the cells are resuspended in a cytopreservative solution and mounted in a microscopy slide.

Figure 3 presents in (a)–(d) the useful FOV (lower CCD half-area) provided by the proposed technique. In addition, these single images are the first frames, respectively, of two video movies (Visualization 2 and Visualization 3) containing

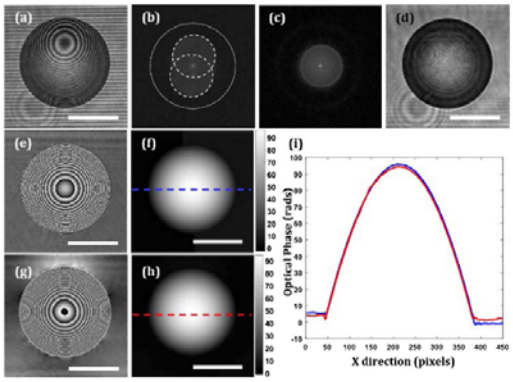

Fig. 2. Calibration results for a 90 μm sphere: (a) single slightly off-axis interferogram (first frame of the full P-S sequence Visualization 1, 3.25 MB); (b) the FT of (a); (c) the complex pupil retrieved by a P-S algorithm; (d) the intensity image; (e)–(f) and (g)–(h) phase visualization modes from P-S and H2S2MIM, respectively (lateral scales represent optical phase in rads); and (i) the comparison plot of the 3D phase profiles at (f) and (h). The scale bars at the lower right corners are 50 μm, approximately.

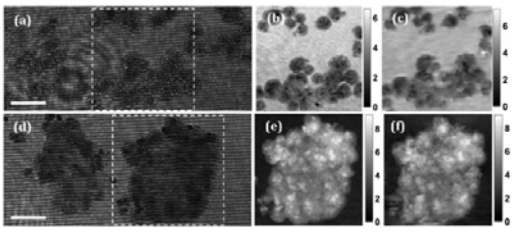

Fig. 3. Experiments with prostate cancer cells: (a) and (d) full available FOVs; (b) and (e) 2D unwrapped phase distribution incoming from the P-S algorithm; and (c) and (f) the distribution from H2S2MIM. Reconstructions from the white solid-line ROIs in (a) and (d). The lateral scale represents the optical phase in radians, and the scale bars are 50 μm, approximately.

the whole phase-shifted hologram sets. The 2D unwrapped phase distributions incoming from P-S and H2S2MIM algorithms are included through Figs. 3(b)–3(e) and Figs. 3(c)–3(f), respectively, for the ROIs marked with white solid-line squares at Figs. 3(a)–3(d). One can notice again that the values of the lateral scales coming from P-S and H2S2MIM are in perfect agreement.

Finally, maybe the most interesting capability of H2S2MIM relates to its single-shot operation principle. To validate this capability, we present a third experimental verification of the proposed method considering a sample integrated by two 45 μm diameter beads flowing in a 100 μm thickness counting chamber filled with water. Figure 4 includes the first frames of full video movies (Visualization 4 and Visualization 5) considering the ROIs (not the full available FOV) containing the 45 μm diameter beads and regarding (a) the recorded set of slightly off-axis holograms and (b) the retrieved 2D unwrapped phase distribution from H2S2MIM. Note that it is impossible to retrieve accurate bead phase information using a single hologram, since the diffraction orders are overlapping at spectral domain and no Fourier filtering can be applied. Hence, the single-shot working capability provided by H2S2MIM enables accurate QPI analysis of dynamic samples.

The modification of our previously reported H2S2PM algorithm [22] especially enables efficient analysis of the microbeads (extremely difficult case from the single-fringe-pattern analysis

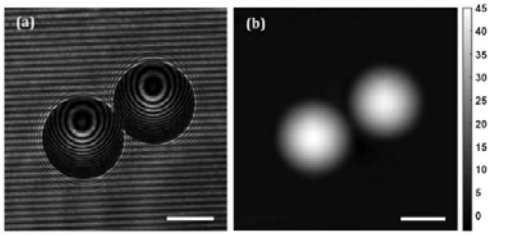

Fig. 4. Dynamic experimental validation of H2S2MIM using 45 μm flowing beads: (a) the first frame of the whole recorded P-S sequence (Visualization 4, 1.36 MB) and (b) the same (Visualization 5, 0.25 MB) concerning 2D unwrapped phase distribution retrieved from H2S2MIM. The lateral scale represents the optical phase in rads. The scale bars at lower right corners are 25 μm, approximately.

point of view). In both Figs. 2(a) and 4(a), one can observe that (1) the beads introduce a spurious circular diffraction pattern outside the bead region, making unidirectional carrier fringes difficult to analyze near the bead borders; (2) the fringes in the bead region have very significant spatially varying period and orientation; and (3) there are cumbersome fringe discontinuities alongside the border of the beads (discontinuous transition between background and bead shape coding fringes). Efficient phase demodulation of cumbersome bead holograms is possible due to the state-of-the-art modifications of the S2H2PM technique. The VID technique is used to extract a hologram background with a sharply edged bead region, and Otsu binarization is applied to complete the novel automatic masking procedure. In this way, we could accurately analyze both the bead region and carrier fringe region.

Significant spatial variation of the fringe period in the bead region is compensated for with a robust adaptive EMD technique [28]. However, global parameters based on the mean amplitude and the mean spectral energy are introduced into mode reconstruction scheme, resulting in an increased signal-to-noise ratio of the reconstructed holograms. This is a crucial advancement enabling bead analysis.

The S2H2PM utilizes Hilbert spiral phase transform (HST) [30] for the phase demodulation of an adaptively bandpass filtered fringe pattern with a zero mean value (local oscillation around zero is ensured using the EMD). The neuralgic part of the HST is an estimation of the local fringe direction map to accommodate for cumbersome fringe orientation variations (in the bead case—full 2π variability—the most troublesome case of closed fringes). We use a fringe direction estimator introduced in Ref. [23] and enhance it, employing EMD adaptive filtering of the very noisy first-estimate direction map. In this way, we obtain both accuracy and smoothness of the automatically estimated fringe direction map.

The modified HST algorithm generates phase map modulo 2π to be unwrapped. A previously used scheme [32] failed in the studied cumbersome cases mainly due to fringe discontinuities. We have applied a recently proposed iterative phase unwrapping technique based on the transport of an intensity equation [33]. It searches for a Poissonian smooth solution, which is its main advantage over the previous scheme [32] being very prone to local errors (especially in noisy areas with fringe discontinuities, e.g., beads borders, cell merger region, etc.) and their disastrous propagation. In this way a novel modified S2H2PM technique for one-stop-shop hologram quantitative phase determination is defined and implemented.

In summary, we have reported on a robust and single-shot principle working under partially coherent illumination for QPI in regular nonholographic microscopes. The method, named H2S2MIM, raises from a modification of our previously introduced S2H2PM method [23] applied to SMIM configuration [19–21]. H2S2MIM provides an extremely simple, cost-effective, highly stable, and fast way to convert a standard microscope into a holographic one working in a single illumination shot for QPI. Experimental validation has been presented and, although only a single microscope objective has been considered, the proposed method perfectly applies to other microscope lenses as SMIM does.

Funding. Secretaría de Estado de Investigación, Desarrollo e Innovación (SEIDI) (FIS2013-47548-P); Narodowe Centrum Nauki (NCN) (2017/25/B/ST7/02049); WUT statutory funds.

Acknowledgment. The authors want to thank Dr. José Antonio López-Guerrero from the Fundación Instituto Valenciano de Oncología-FIVO for PC-3 biosample preparation as well as Juan Martinez Carranza and Maria Cywinska for providing phase unwrapping and VID codes.

REFERENCES

1. M. K. Kim, *Digital Holographic Microscopy: Principles, Techniques, and Applications*, 1st ed. (Springer, 2011).
2. N. T. Shaked, Z. Zalevsky, and L. L. Satterwhite, eds., *Biomedical Optical Phase Microscopy and Nanoscopy* (Academic, 2012).
3. G. Popescu, *Quantitative Phase Imaging of Cells and Tissues* (McGraw-Hill Biophotonics, 2011).
4. B. Kemper and G. von Bally, Appl. Opt. **47**, A52 (2008).
5. M. K. Kim, SPIE Rev. **1**, 018005 (2010).
6. P. Bon, G. Maucort, B. Wattellier, and S. Monneret, Opt. Express **17**, 13080 (2009).
7. G. J. Tearney and C. Yang, Opt. Express **18**, 16685 (2010).
8. D. Fu, S. Oh, W. Choi, T. Yamauchi, A. Dorn, Z. Yaqoob, R. R. Dasari, and M. S. Feld, Opt. Lett. **35**, 2370 (2010).
9. F. Merola, L. Miccio, M. Paturzo, A. Finizio, S. Grilli, and P. Ferraro, Opt. Lett. **36**, 3079 (2011).
10. B. Kemper, A. Vollmer, C. E. Rommel, J. Schnekenburger, and G. von Bally, J. Biomed. Opt. **16**, 026014 (2011).
11. V. Chhaniwal, A. S. G. Singh, R. A. Leitgeb, B. Javidi, and A. Anand, Opt. Lett. **37**, 5127 (2012).
12. A. S. G. Singh, A. Anand, R. A. Leitgeb, and B. Javidi, Opt. Express **20**, 23617 (2012).
13. N. T. Shaked, Opt. Lett. **37**, 2016 (2012).
14. P. Girshovitz and N. T. Shaked, Opt. Express **21**, 5701 (2013).
15. R. Guo, B. Yao, P. Gao, J. Min, J. Han, X. Yu, M. Lei, S. Yan, Y. Yang, D. Dan, and T. Ye, Appl. Opt. **52**, 3484 (2013).
16. B. Bhaduri, C. Edwards, H. Pham, R. Zhou, T. H. Nguyen, L. L. Goddard, and G. Popescu, Adv. Opt. Photonics **6**, 57 (2014).
17. S. Karepov, N. T. Shaked, and T. Ellenbogen, Opt. Lett. **40**, 2273 (2015).
18. D. Roitshtain, N. A. Turko, B. Javidi, and N. T. Shaked, Opt. Lett. **41**, 2354 (2016).
19. V. Mico, C. Ferreira, Z. Zalevsky, and J. García, Opt. Express **22**, 14929 (2014).
20. J. A. Picazo-Bueno, Z. Zalevsky, J. García, C. Ferreira, and V. Micó, J. Bio. Opt. **21**, 106007 (2016).
21. J. Á. Picazo-Bueno, Z. Zalevsky, J. García, and V. Micó, Opt. Lett. **42**, 927 (2017).
22. T. D. Yang, H. J. Kim, K. J. Lee, B. M. Kim, and Y. Choi, Opt. Express **24**, 9480 (2016).
23. M. Trusiak, V. Mico, J. Garcia, and K. Patorski, Opt. Lett. **41**, 4344 (2016).
24. N. E. Huang, Z. Sheng, S. R. Long, M. C. Wu, W. H. Shih, Q. Zeng, N. C. Yen, C. C. Tung, and H. H. Liu, Proc. R. Soc. London A **454**, 903 (1998).
25. T. Ikeda, G. Popescu, R. R. Dasari, and M. S. Feld, Opt. Lett. **30**, 1165 (2005).
26. G. Popescu, T. Ikeda, C. Best, K. Badizadegan, R. R. Dasari, and M. S. Feld, J. Biomed. Opt. **10**, 060503 (2005).
27. M. Trusiak, K. Patorski, and M. Wielgus, Opt. Express **20**, 23463 (2012).
28. M. Trusiak, M. Wielgus, and K. Patorski, Opt. Laser Eng. **52**, 230 (2014).
29. M. Trusiak, Ł. Służewski, and K. Patorski, Opt. Express **24**, 4221 (2016).
30. K. G. Larkin, J. Opt. Soc. Am. A **18**, 1871 (2001).
31. X. Zhu, Z. Chen, and C. Tang, Opt. Lett. **38**, 275 (2013).
32. M. A. Herráez, D. R. Burton, M. J. Lalor, and M. A. Gdeisat, Appl. Opt. **41**, 7437 (2002).
33. J. Martinez-Carranza, K. Falaggis, and T. Kozacki, Appl. Opt. **56**, 7079 (2017).

IOP Publishing Journal of Optics
J. Opt. 21 (2019) 035701 (8pp) https://doi.org/10.1088/2040-8986/ab000e

Opposed-view spatially multiplexed interferometric microscopy

José Ángel Picazo-Bueno and Vicente Micó

Departamento de Óptica y de Optometría y Ciencias de la Visión, Facultad de Física, Universidad de Valencia, C/Doctor Moliner 50, Burjassot 46100, Spain

E-mail: vicente.mico@uv.es

Received 21 August 2018, revised 5 December 2018
Accepted for publication 18 January 2019
Published 31 January 2019

Abstract

The capability for simultaneous recording of light which is transmitted and reflected by a sample has big potential in microscopy. In this paper, we introduce opposed-view spatially multiplexed interferometric microscopy (OV-SMIM) as the combination of transmission and reflection (transflective) imaging modalities into a digital holographic microscopy platform. The implementation is in virtue of wavelength multiplexing for allowing simultaneous retrieval of quantitative phase information of the inspected sample. OV-SMIM generalizes a SMIM concept and provides an extremely simple, low cost and highly stable way to convert a bright field microscope into a holographic one with the functionality of transflective imaging. Experimental validation is presented for a regular Olympus BX-60 upright microscope considering chromium coated patterns and microbeads.

Keywords: multiplexed holography, digital image processing, digital holographic microscopy, reflective im

(Some figures may appear in colour only in the online journal)

1. Introduction

Since it was first evident [1–3], digital holographic microscopy (DHM) has becoming a powerful and versatile tool in many significant fields of biophotonics, life sciences and medicine [4–6]. Among other interesting capabilities, such as polarization microscopy imaging [7], aberration lens compensation [8], particle tracking [9] and extended depth of field imaging [10], just to cite a few, DHM is used for quantitative phase imaging (QPI) of biological specimens [5, 6, 11]. QPI retrieves a sample image that is usually interpreted as a map of path-length shifts associated with the essentially transparent specimen. QPI contains valuable information about a combination of both the local thickness [12] and refractive index distributions [13] of the sample. For this reason, QPI has become a successful, widely-used and powerful method in biological research [14].

Over the last 10 years, new and novel simplified, cost-effective, accurate and robust DHM architectures have been reported in scientific literature [15–29]. Inside them [24, 27–29], spatially-multiplexed interferometric microscopy (SMIM) relates to a common-path interferometric configuration implemented in a commercially available regular microscope where three minimal modifications are implemented: (i) the broadband light source is replaced by a coherent one, (ii) a one-dimensional (1D) diffraction grating is properly inserted at the microscope embodiment, and (iii) a clear region at the input plane is saved for reference beam transmission. SMIM has been successfully validated considering off-axis holographic recording with Fourier filtering [24], using slightly off-axis recording with a phase-shifting (P-S) algorithm [27], with superresolution capabilities to overcome the field of view (FOV) restriction [28], and in combination with Hilbert-Huang phase microscopy for allowing a single-shot operational principle even outside the off-axis holographic recording regime [29]. But all of those references work in the transmission imaging mode.

Here, we report for the first time on the inclusion of reflective imaging to SMIM. Although the reflective mode in DHM has been previously reported [4, 23, 30–32], it is usually implemented by external reintroduction of a reference beam at the recording plane. In this contribution, we report for the first time on reflective SMIM as a common-path reflective interferometric scheme adapted to a regular microscope for inspection of opaque samples. Moreover, reflective SMIM

can be considered as single imaging modality or in parallel to transmission SMIM because different illuminations (wavelength multiplexing) are used for the reflection/transmission schemes. Both together, transmission and reflection imaging modes define opposed-view SMIM (OV-SMIM) and generalize the SMIM concept with additional capabilities regarding the type of samples to be inspected while retaining the simplicity of SMIM regarding a robust, cost-effective and highly stable working principle for QPI in non-holographic microscopes.

OV imaging modality is a relatively recent technique applied to DHM [33–36]. Refractive index profiles were measured by OV-DHM considering single illumination wavelength with two digital sensors to allow a single-shot operation principle [33] or by using a single digital sensor sequentially recording the two required holograms [34], thus preventing single exposure capability. Darkfield imaging has also been improved in terms of contrast and signal-to-noise ratio by OV-DHM [35], and, finally, OV-DHM was proposed for autofocusing enhancement and FOV improvement in DHM [36], although this method is restricted only to transmission imaging mode and sequentially in time. Our OV-SMIM concept joins together all of the previous advantages regarding the single-shot operational principle, coherent recording in both transmission and reflection imaging modes, simplicity in the experimental implementation, and the capability of measuring the refractive index profile of the sample.

2. System description

The experimental setup is included in figure 1 where two diode-coupled sources illuminate the object in transflective mode (red/green laser diodes for reflection/transmission configurations, respectively). Red (635 nm) and green (520 nm) illuminations are taken, respectively, from fiber optic coupled diodes (Blue Sky Research, SpectraTec 4 and OSI Laser Diode, TCW RGBS-400R). Both beams provide simultaneous transflective illumination of the same FOV that is spatially multiplexed into three regions. We have selected the configuration included in [24] for SMIM since we need three regions of interest (ROIs) for: (i) the sample to be imaged (white ROI in figure 1), (ii) the reference beam for the transmission arm (green ROI in figure 1), and (iii) the reference beam for the reflective configuration (black ROI in figure 1). Transmission imaging mode is achieved as in previously reported SMIM methods but now the blocked ROI at the input plane (black rectangle in figure 1) prevents additional replicas at the output plane when considering transmission configuration (named X-ROI in figure 2) and it is used as mirror surface for reference beam back-reflection when considering the reflective arm (named R-ROI in figure 2).

This spatially multiplexed FOV is depicted in detail in figure 2 where the three regions are identified as R-O-X (referring to the reference, the object and the X-blocking areas, respectively). The O-ROI is centered on-axis while the R and X ones are at its sides. This 3-ROIs FOV is imaged and magnified by the microscope system generating R′-O′-X′ at

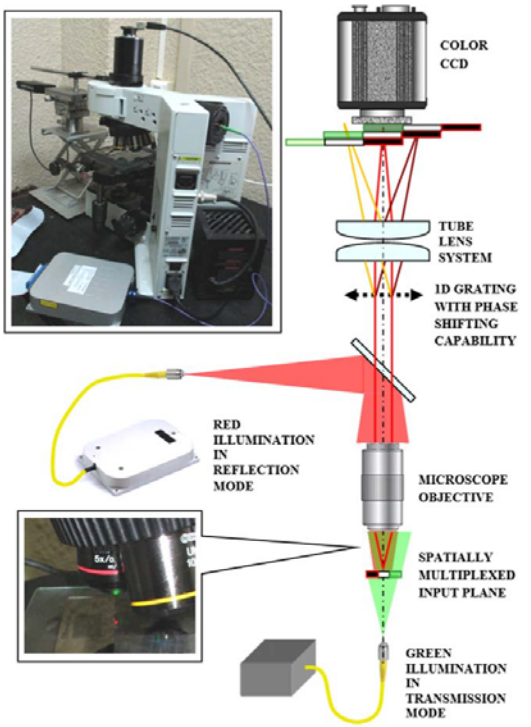

Figure 1. Pictures and scheme of the proposed OV-SMIM where the main SMIM components are identified.

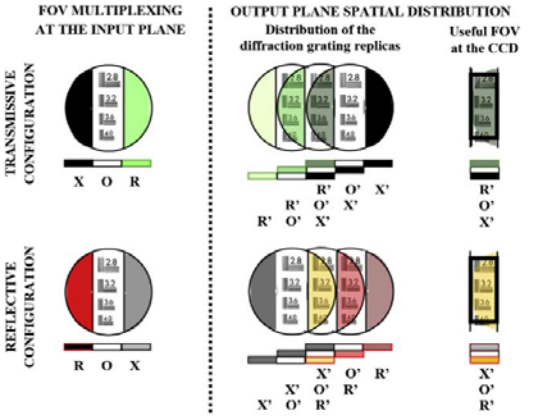

Figure 2. FOV multiplexing at the input/output planes in OV-SMIM for transmission (upper row) and reflection (lower row) imaging modes.

the output plane where the digital sensor is placed (Mightex USB3.0 SMN-C050-U, 2560 × 1920 pixels, 2.2 × 2.2 μm pixel pitch). As in previous SMIM methods, interferometric recording is achieved by introducing a 1D diffraction grating (Ronchi ruling grating, 40 lp/mm period) at one of the

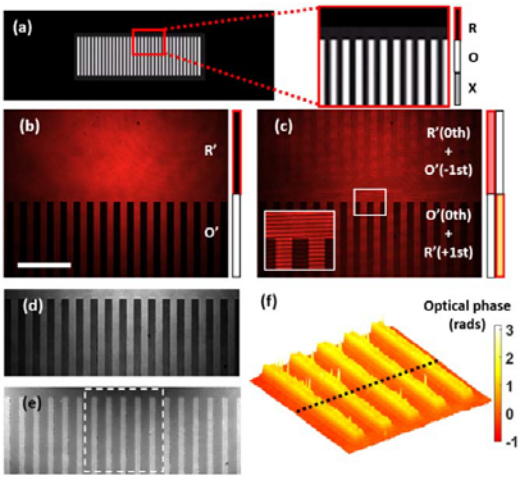

Figure 3. Experimental validation of OV-SMIM: reflective imaging mode. (a) Identification of the 3 ROIs, (b) direct image of the grating, (c) reflective hologram, (d) retrieved intensity image, (e) retrieved phase distribution, and (f) 3D view of the square area in (e). Scale bar in (b) is 200 μm.

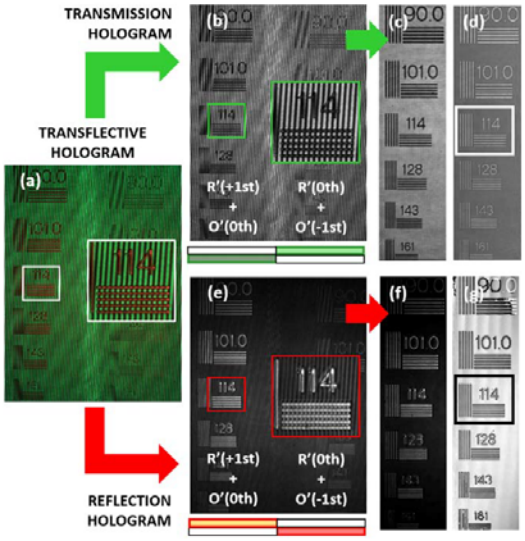

Figure 4. Experimental validation of OV-SMIM: transflective imaging mode with a resolution test target. (a) Transflective hologram, (b) hologram in transmission mode, and (c), (d) the retrieved intensity and phase images, respectively. Images (e)–(g) are equivalent to (b)–(d) but considering the hologram in reflection mode.

polarization slots of the microscope embodiment just before the tube lens system. In SMIM, the basic grating's period must be properly selected according to the illumination wavelength in order to overlap the different ROIs at the recording plane. The interferometric configuration can be designed to be off-axis [24] or slightly on-axis [27, 28], so Fourier filtering or P-S algorithm, respectively, are applied to retrieve the complex amplitude distribution incoming from the O′-ROI. Here, we have selected temporal P-S procedure where a motorized linear translation stage (Newport, model ESP300) provides the 1D grating shift (25 holograms integrate the full P-S cycle).

3. Experimental validation

The experimental validation of the proposed OV-SMIM has been divided in two parts, both using the embodiment provided by a BX60 Olympus microscope. As first implementation, reflective SMIM is proposed as a novel implementation imaging modality in SMIM when reflective/opaque samples need to be inspected (no transmission image is considered).

Experimental results are presented through figure 3 where a 1D Ronchi ruling grating (20 lp/mm period) is used as reflective sample. The three ROIs are clearly identified from figure 3(a) where the R-ROI is defined by the reflective coating fame of the grating. A 5X/0.15NA objective lens images the grating onto the digital sensor that only records the ROIs coming from R′ and O′. The direct image without (intensity image) and with (hologram) the 1D grating for the interferometric recording are presented in figures 3(b) and (c), respectively. Then, the P-S algorithm is applied and the retrieved results concerning intensity and 2D phase are included figures 3(d) and (e), respectively. In addition, figure 3(f) includes a 3D view of a grating area (white dashed square in figure 3(e)) coming from the retrieved quantitative phase values.

Then, transflective imaging validation is achieved by first using a NBS 1963A resolution test target and secondly a microbeads sample. NBS results are included in figures 4 and 5. Figure 4(a) shows the transflective hologram that is separated by direct demosaicing in the two color-coded holograms. The transmission hologram (figure 4(b)) allows us to retrieve the complex amplitude distribution of the transmitted light from which, besides a conventional bright field intensity imaging (figure 4(c)), the transmitted phase information (figure 4(d)) is available. In addition, reflective imaging mode (figure 4(e)) retrieves the complex amplitude distribution of the reflected light from which, besides a conventional dark-field intensity image (figure 4(f)), topographical information can be retrieved from the reflected phase distribution (figure 4(g)). The insets in figures 4(a)–(c) show interference fringes for clarity.

Figure 5 focuses on the reconstruction of the test target element marked with the white/black rectangles at figures 4(d)–(g), respectively, and corresponding with 114 lp/mm. The results represent the 2D (figures 5(a) and (b)) and 3D (figures 5(c) and (d)) views of the test element coming from the transmission/reflection arms, respectively, as well as two comparison plots (figures 5(e) and (f)) concerning a

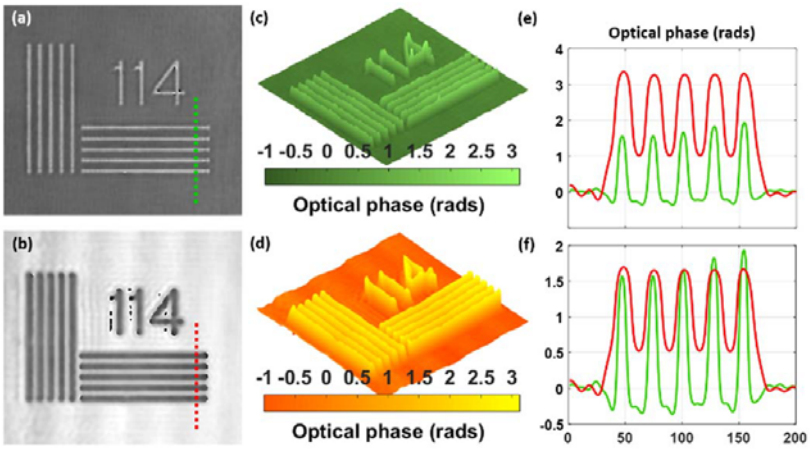

Figure 5. Experimental validation of OV-SMIM: transflective imaging mode with a resolution test target. (a), (b) and (c), (d) are the 2D and 3D views of the retrieved phase images, respectively. (e) The plot of the retrieved phase profiles along the lines in (a) and (b), while (f) includes the comparison once the reflective phase is compensated from twice the optical path.

vertical section along the horizontal bars of the test element (dashed green and red lines in figures 5(a) and (b)). Figure 5(e) shows the directly retrieved phase values where one can notice as the reflective arm provides twice the real values since light is twofold travelling the same optical path in air. Once this fact is compensated, the real phase values are included in figure 5(f). Notice also as the resolution limit is worse (width at half height of the bars profiles) for the reflective arm than for the transmission one since red illumination provides poorer resolution than the green one.

Finally, we have performed a third experiment involving a sample containing water-immersed micro spheres of 45 μm in diameter. In this case, we have used a 10X/0.30NA objective lens to get higher imaging performance and we have placed a mirrored-surface on one side of the FOV acting as X/R ROIs for transmission/reflection arms, respectively. This mirrored surface simultanously blocks the light from one side of the sample in the transmission imaging mode (X area in figure 2) while allows reference beam back reflection for the reflective imaging configuration (R area in figure 2).

The aim of the bead's experiment is to validate both imaging arms from a quantitative point of view using a more complex sample. Figure 6 shows the experimental results regarding (a) the transflective hologram; (b) and (c) the 3D views of the thickness profiles incoming from the phase values retrieved by the transmission and reflection arms, respectively; and (d) a comparative thickness plot incoming from the color coded solid lines at (b) and (c). The height profiles included throughout figure 6(d) are obtained after removing the wavelength dependence and considering optical path equalization between reflection and transmission modes. Leaving aside some backgroud noise mainly coming from phase unwrapping errors, figure 6(d) shows that both retrieved height profiles are in perfect agreement from one to the other. Again, one can notice the worse resolution limit

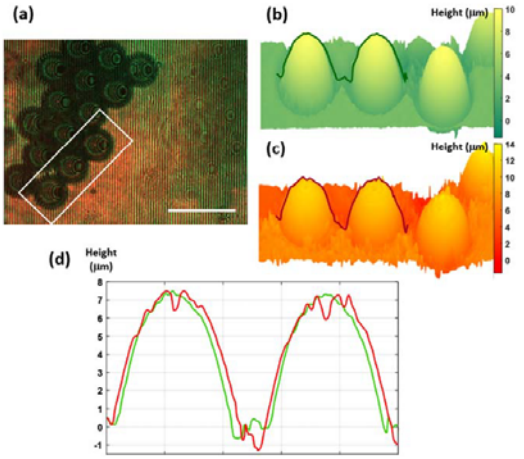

Figure 6. Experimental validation of OV-SMIM: transflective imaging mode with a microbeads sample. (a) Transflective hologram, (b), (c) 3D views of the thickness profiles incoming from the phase distributions retrieved by transmission and reflection, respectively, and (d) comparative thickness plot along the solid lines included in (b) and (c). Scale bar in (a) is 100 μm.

(width at half height of the beads profiles) for the reflective arm because of the red illumination wavelength.

4. Discussion

We have conducted a brief quantitative analysis to theoretically validate the obtained results. It is not our aim to develop here the mathematical equations involving optics for metals (one can consult advanced text books, such as, for instance, Born & Wolf) but only use the work provided by other

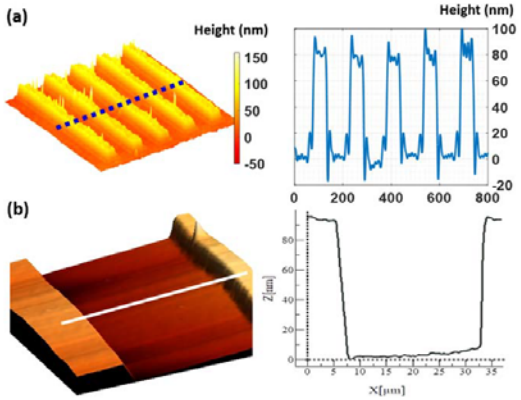

Figure 7. Thickness analysis of the grating's profile: (a) plot of the retrieved height values by using reflective SMIM and (b) AFM images of the grating.

authors. According to the website https://refractiveindex.info, which is based on [37], the phase change introduced by the reflection in the chrome layer is $\Phi_t = -161.507° = 3.4644$ rads.

Then, the phase difference ($\Delta\varphi$) between our two interferometric beams (the one reflected in the metallic layer and the one incoming from the glass substrate) can be calculated as

$$\Delta\varphi = \varphi_{glass} - \varphi_{metal} = \frac{2\pi}{\lambda}2t + \pi - \Phi_t \qquad (1)$$

where t is the metallic layer thickness. Here, the π rads value included at equation (1) is a consequence of the phase step in reflected light at dielectric interfaces (air-glass in our case), and, from equation (1), the thickness value of the chrome layer deposition can be calculated as

$$t = \frac{\lambda}{4\pi}(\Delta\varphi + \Phi_t - \pi). \qquad (2)$$

In order to know the retrieved height value from our reflective SMIM configuration, we have converted into a thickness profile the retrieved phase information. Thus, the 3D phase profile of figure 3(f) is plotted again as the height profile in figure 7(a), anda plot of the grating's relief along the blue dotted line in the 3D views is considered for the comparison. We have estimated a $\Delta\varphi_{mean} \cong 1.3$ rads that, according to equation (2), yields in a thickness value of $t_{mean} = 82$ nm.

This thickness value is compared against AFM characterization of one of those gratings profiles. AFM measurements were performed with a Cervantes Multimode AFM microscope in tapping mode using silicon with a natural resonance frequency of 300 KHz and with an equivalent constant force 40 Nm^{-1}. The scan rate was adjusted during the scanning of each image (0.1–1 Hz, 512 samples/line). The results are included in figure 7(b) showing a 3D rendered profile of the inspected area and a profile (plot along the white line) of the sample. As we can see from the AFM measurement, the metallic thickness is around 85 nm showing high concordance with the previously obtained t_{mean} value.

A similar analysis can be derived from the NBS test case through the plots included in figure 5(f). But it is not our aim to again compute a quantitative analysis rather than provide simultaneous agreement and concordance between both imaging modes in transflective SMIM. This is fully validated by comparing phase values.

Finally, quantitative validation for the beads sample is analyzed. Microbeads are a commonly used sample to calibrate DHM layouts but there are cumbersome issues to take into account. Thus, spherical aberration, diffraction at the bead borders, and the bead section the lens is imaging make the analysis awkward. But maybe the most important one is the NA of the lens used for imaging, since the whole bead phase profile will be retrieved only in the case of using a 1.0 NA objective. Otherwise, lower NA lenses will limit the captured cone of light being focused by the bead and the reconstruction will be related to two spherical caps which are not full hemispherical caps, so the whole bead diameter cannot be retrieved from the measured phase values. Since we are using a 0.3 NA lens, the light from the outer parts (borders) of the bead will not be captured by the lens, preventing phase steps at the beads borders and avoiding retrieving the whole bead diameter.

In our case, we are using polystyrene beads having a refractive index value of 1.6 at 520 nm (the transmission illumination wavelength, λ_G) [38]. The beads are static but water-immersed ($n_{medium} = 1.336$ at λ_G from [39]) inside the counting chamber. Then, the phase value φ considering the whole bead diameter ($\phi = 45$ μm) is $\varphi = 2\pi\ \Delta n\ \phi/\lambda_G = 143.5$ rads, approximately, being $\Delta n = n_{sample} - n_{medium}$. But this value will be retrieved only from a 1.0 NA objective lens (collection angle of 90°). Since we are using a 0.3 NA lens (collection angle of 17.45°), the retrieved phase values will be lower. Assuming a proportional reduction (something inaccurate but valid as a hand-waving approximation), the retrieved phase value should be 27.8 rads for the used objective. This value is not far from the one retrieved by the transmission imaging mode and it can be translated to thickness profile in virtue of

$$\Delta t = \frac{\lambda_G}{2\pi\ \Delta n}\Delta\varphi \qquad (3)$$

resulting in 8.6 μm of effective thickness instead of the theoretical 45 μm value.

However, we have measured 24 rads for the beads in the transmission mode meaning that the effective thickness is around 7.4 μm from equation (3) (see figure 6(d), green curve). This value is a bit below the expected one (8.6 μm) due to the previously commented limitations/assumptions.

But the most significant issue is that with this value, it is possible to calculate the refractive index value of the bead material from the two simultaneous holographic measurements. Thus, from the phase delays retrieved by the

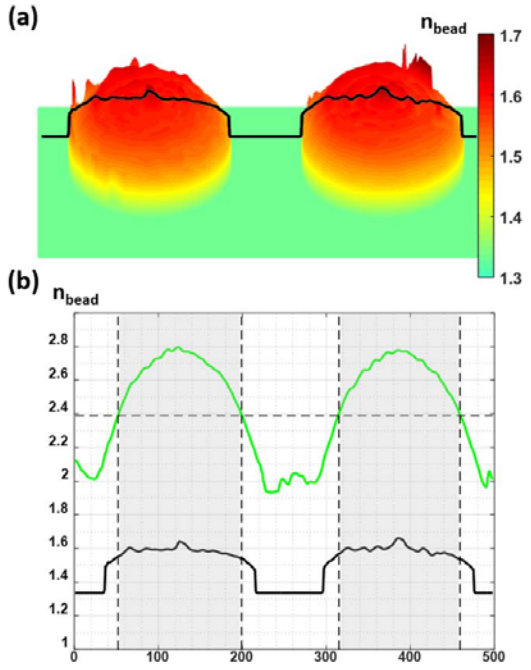

Figure 8. Refractive index distribution analysis: (a) refractive index spatial distribution coming from equation (6), and (b) plot along the central line in (a) for averaged refractive index value calculation. Note that the green curve just acts as an illustrative bead position and it is not representative of real refractive index values.

transmission

$$\Delta\varphi_G(x, y) = \frac{2\pi}{\lambda_G}(n_b^G - n_w^G)d(x, y) \quad (4)$$

and reflection

$$\Delta\varphi_R(x, y) = 2\frac{2\pi}{\lambda_R}n_w^R\frac{d(x, y)}{2} \quad (5)$$

ports, it is possible to retrieve the refractie index spatial distribution of the inspected sample ($n_b^G(x, y)$) for the transmission wavelength as

$$n_b^G(x, y) = \frac{\lambda_G}{\lambda_R}\frac{\Delta\varphi_G(x, y)}{\Delta\varphi_R(x, y)}n_w^R + n_w^G \quad (6)$$

where $\Delta\varphi_G$ and $\Delta\varphi_R$ are the measured phase distributions by transmission and reflection, respectively, λ_G and λ_R are the illumination wavelengths used in transmission and reflection, respectively, and n_w^R is the refractive index of the acuous medium for the reflection wavelength. Also, d(x,y) represents the bead height in equations (4) and (5). Note that (x,y) mean spatial distributions of some variables at the equations.

Equation (6) is plotted in figure 8 showing the refractive index profile coming from the combination of the information retrieved by reflective imaging mode ($\Delta\varphi_R$) and that incoming from the transmission imaging mode ($\Delta\varphi_G$). The resulting refractive index spatial distribution is shown in figure 8(a), where the area outside the beads has been masked down to avoid spureous random values and fixed to a value of 1.336 (refractive index value of the water for the G wavelength).

Finally, figure 8(b) includes a plot along the black line included in figure 8(a) in order to calculate an averaged refractive index value of the beads ($\langle n_b^G \rangle$). One can notice as the plot tends to be planar in the area where the beads are reconstructed, meaning that the refractive index value is unique. But we need to decide which is the useful bead extension for computing the refractive index value. For this, figure 8(b) also includes a scaled height profile of the beads (scaled version of the green plot at figure 6(d)) in order to clearly identify the beads position (this green curve does not represent refractive index values). Then, we have considered the full width at maximum height (FWMH) of the height profile as criterion for computing the averaged refractive index value. These two FWMH areas are represented by two shadowed rectangles in figure 8(b), and the averaged result is $\langle n_b^G \rangle = 1.59$; a value that is really close to the theoretical one ($n_{bead} = 1.6$ for the G illumination wavelength).

5. Conclusions

In summary, we have incorporated reflective imaging modality to our previously presented SMIM concept. This capability (i) expands the range of samples that can be analyzed by SMIM (not only transmissive but also reflective/opaque samples), (ii) generalizes the SMIM concept in the sense of completeness, and (iii) can be implemented in parallel with transmission imaging as well as individually. Together, the proposed OV-SMIM provides an extremely simple, cost-effective, highly stable and fast way to convert a standard microscope into a holographic one working in transflective mode for QPI. Experimental results have been presented first under reflective imaging mode in SMIM where quantitative analysis shows perfect matching between theory and experiments, and second using the transflective imaging mode for a resolution test target as well as for microbeads where the retrieved phase values for the transmissive and the reflective imaging modes are in perfect agreement with each other. Quantitative analysis has been validated for the reflective imaging mode in virtue of the comparison with AFM measurement and for the tranflective imaging mode by computing the refractive index value of the bead material.

But maybe the main drawbacks of OV-SMIM come from the FOV limitation and the specific chamber requirement for transflective imaging. Regarding the first one, the useful FOV is limited to around one third of the available one. However, this is not a critical restriction since it is common in microscopy that the digital FOV defined by the sensor will be smaller than the optical FOV provided by the microscope system. Thus, those areas falling outside the digital FOV can be used as reference ROIs for the interferometric recording. Moreover, superresolution capabilities can be implemented for improving the FOV/resolution ratio [28], as well as it being adapted for a single-exposure working principle

[24, 29]. Also, concerning the second, customized chambers are nowadays developed for specific applications, such as DHM [23], fluorescence microscopy [40], light-sheet microscopy [41] and optofluidic imaging [42]. Here, our aim is to provide an OV-SMIM proof of principle validation and not to manufacture a specific chamber for its application. Nevertheless, it is completely feasible in light of previous developments [23, 40–42].

Acknowledgments

This work was supported by the Spanish Ministerio de Economía y Competitividad and Fondo Europeo de Desarrollo Regional (FIS2017-89748-P). The authors want to thank Dr Alejandra Soriano Portillo from the Instituto de Ciencia Molecular (ICMol) for AFM characterization of the diffraction grating.

ORCID iDs

Vicente Micó https://orcid.org/0000-0001-9457-1960

References

[1] Zhang T and Yamaguchi I 1998 Three-dimensional microscopy with phase-shifting digital holography *Opt. Lett.* **23** 1221
[2] Cuche E, Marquet P and Depeursinge C 1999 Simultaneous amplitude-contrast and quantitative phase-contrast microscopy by numerical reconstruction of Fresnel off-axis holograms *Appl. Opt.* **38** 6994
[3] Dubois F, Joannes L and Legros J-C 1999 Improved three-dimensional imaging with a digital holography microscope with a source of partial spatial coherence *Appl. Opt.* **38** 7085
[4] Kemper B and von Bally G 2008 Digital holographic microscopy for live cell applications and technical inspection *Appl. Opt.* **47** A52
[5] Kim M K 2011 *Digital Holographic Microscopy: Principles, Techniques, and Applications* (New York: Springer)
[6] Shaked N T, Zalevsky Z and Satterwhite L L 2012 *Biomedical Optical Phase Microscopy and Nanoscopy* 1st edn (Oxford: Academic)
[7] Colomb T, Dürr F, Cuche E, Marquet P, Limberger H G, Salathé R-P and Depeursinge C 2005 Polarization microscopy by use of digital holography: application to optical-fiber birefringence measurements *Appl. Opt.* **44** 4461
[8] Colomb T, Kühn J, Charrière F, Depeursinge C, Marquet P and Aspert N 2006 Total aberrations compensation in digital holographic microscopy with a reference conjugated hologram *Opt. Express* **14** 4300
[9] Sheng J, Malkiel E and Katz J 2006 Digital holographic microscope for measuring three-dimensional particle distributions and motions *Appl. Opt.* **45** 3893
[10] Ferraro P, Grilli S, Alfieri D, Nicola S D, Finizio A, Pierattini G, Javidi B, Coppola G and Striano V 2005 Extended focused image in microscopy by digital holography *Opt. Express* **13** 6738
[11] Popescu G 2011 *Quantitative Phase Imaging of Cells and Tissues* (New York: McGraw-Hill)
[12] Marquet P, Rappaz B, Magistretti P J, Cuche E, Emery Y, Colomb T and Depeursinge C 2005 Digital holographic microscopy: a noninvasive contrast imaging technique allowing quantitative visualization of living cells with subwavelength axial accuracy *Opt. Lett.* **30** 468
[13] Rappaz B, Marquet P, Cuche E, Emery Y, Depeursinge C and Magistretti P 2005 Measurement of the integral refractive index and dynamic cell morphometry of living cells with digital holographic microscopy *Opt. Express* **13** 9361
[14] Bhaduri B, Edwards C, Pham H, Zhou R, Nguyen T H, Goddard L L and Popescu G 2014 Diffraction phase microscopy: principles and applications in materials and life sciences *Adv Opt Photon* **6** 57
[15] Bon P, Maucort G, Wattellier B and Monneret S 2009 Quadriwave lateral shearing interferometry for quantitative phase microscopy of living cells *Opt. Express* **17** 13080
[16] Cui X, Ren J, Tearney G J and Yang C 2010 Wavefront image sensor chip *Opt. Express* **18** 16685
[17] Fu D, Oh S, Choi W, Yamauchi T, Dorn A, Yaqoob Z, Dasari R R and Feld M S 2010 Quantitative DIC microscopy using an off-axis self-interference approach *Opt. Lett.* **35** 2370
[18] Merola F, Miccio L, Paturzo M, Finizio A, Grilli S and Ferraro P 2011 Driving and analysis of micro-objects by digital holographic microscope in microfluidics *Opt. Lett.* **36** 3079
[19] Kemper B, Vollmer A, Rommel C E, Schnekenburger J and von Bally G 2011 Simplified approach for quantitative digital holographic phase contrast imaging of living cells *J. Biomed. Opt.* **16** 026014
[20] Chhaniwal V, Singh A S G, Leitgeb R A, Javidi B and Anand A 2012 Quantitative phase-contrast imaging with compact digital holographic microscope employing Lloyds mirror *Opt. Lett.* **37** 5127
[21] Singh A S G, Anand A, Leitgeb R A and Javidi B 2012 Lateral shearing digital holographic imaging of small biological specimens *Opt. Express* **20** 23617
[22] Shaked N T 2012 Quantitative phase microscopy of biological samples using a portable interferometer *Opt. Lett.* **37** 2016
[23] Shaked N T, Zhu Y, Badie N, Bursac N and Wax A 2010 Reflective interferometric chamber for quantitative phase imaging of biological sample dynamics *J. Biomed. Opt.* **15** 030503
[24] Mico V, Ferreira C, Zalevsky Z and García J 2014 Spatially-multiplexed interferometric microscopy (SMIM): converting a standard microscope into a holographic one *Opt. Express* **22** 14929
[25] Karepov S, Shaked N T and Ellenbogen T 2015 Off-axis interferometer with adjustable fringe contrast based on polarization encoding *Opt. Lett.* **40** 2273
[26] Roitshtain D, Turko N A, Javidi B and Shaked N T 2016 Flipping interferometry and its application for quantitative phase microscopy in a micro-channel *Opt. Lett.* **41** 2354
[27] Picazo-Bueno J Á, Zalevsky Z, García J, Ferreira C and Micó V 2016 Spatially multiplexed interferometric microscopy with partially coherent illumination *J. Biomed. Opt.* **21** 106007
[28] Picazo-Bueno J Á, Zalevsky Z, García J and Micó V 2017 Superresolved spatially multiplexed interferometric microscopy *Opt. Lett.* **42** 927
[29] Picazo-Bueno J Á, Trusiak M, García J, Patorski K and Micó V 2018 Hilbert–Huang single-shot spatially multiplexed interferometric microscopy *Opt. Lett.* **43** 1007
[30] Kemper B, Stürwald S, Remmersmann C, Langehanenberg P and von Bally G 2008 Characterisation of light emitting diodes (LEDs) for application in digital holographic microscopy for inspection of micro and nanostructured surfaces *Opt. Lasers Eng.* **46** 499

[31] Castañeda R and Garcia-Sucerquia J 2018 Single-shot 3D topography of reflective samples with digital holographic microscopy *Appl. Opt.* **57** A12
[32] Reichelt S and Zappe H 2005 Combined Twyman–Green and Mach–Zehnder interferometer for microlens testing *Appl. Opt.* **44** 5786
[33] Lin Y-C and Cheng C-J 2010 Determining the refractive index profile of micro-optical elements using transflective digital holographic microscopy *J. Opt.* **12** 115402
[34] Zheng J, Gao P, Shao X and Nienhaus G U 2017 Refractive index measurement of suspended cells using opposed-view digital holographic microscopy *Appl. Opt.* **56** 9000
[35] Faridian A, Pedrini G and Osten W 2014 Opposed-view dark-field digital holographic microscopy *Biomed Opt Express* **5** 728
[36] Zheng J, Gao P and Shao X 2017 Opposite-view digital holographic microscopy with autofocusing capability *Sci. Rep.* **7** 4255
[37] Johnson P B and Christy R W 1974 Optical constants of transition metals: Ti, V, Cr, Mn, Fe, Co, Ni, and Pd *Phys. Rev.* B **9** 5056
[38] Sultanova N, Kasarova S and Nikolov I 2009 Dispersion properties of optical polymers *Acta Phys. Pol.* A **116** 585
[39] Kedenburg S, Vieweg M, Gissibl T and Giessen H 2012 Linear refractive index and absorption measurements of nonlinear optical liquids in the visible and near-infrared spectral region *Opt. Mat. Express* **2** 1588
[40] Mangeol P and Peterman E J G 2016 High-resolution real-time dual-view imaging with multiple point of view microscopy *Biomed Opt Express* **7** 3631
[41] Wu Y *et al* 2017 Reflective imaging improves spatiotemporal resolution and collection efficiency in light sheet microscopy *Nat. Commun.* **8** 1452
[42] Bianco V, Mandracchia B, Marchesano V, Pagliarulo V, Olivieri F, Coppola S, Paturzo M and Ferraro P 2017 Endowing a plain fluidic chip with micro-optics: a holographic microscope slide *Light Sci App* **6** e17055

Research Article | Vol. 27, No. 4 | 18 Feb 2019 | OPTICS EXPRESS 5655
Optics EXPRESS

Single-shot slightly off-axis digital holographic microscopy with add-on module based on beamsplitter cube

J. A. PICAZO-BUENO,[1] M. TRUSIAK,[2] AND V. MICÓ[1,*]

[1] *Departamento de Óptica y de Optometría y Ciencias de la Visión, Universidad de Valencia, C/Doctor Moliner 50, Burjassot 46100, Spain*
[2] *Warsaw University of Technology, Institute of Micromechanics and Photonics, 8 Sw. A. Boboli St. 02-525, Warsaw, Poland*
[*] *vicente.mico@uv.es*

Abstract: Slightly off-axis digital holographic microscopy (SO-DHM) has recently emerged as a novel experimental arrangement for quantitative phase imaging (QPI). It offers improved capabilities in conventional on-axis and off-axis interferometric configurations. In this contribution, we report on a single-shot SO-DHM approach based on an add-on module adapted to the exit port of a regular microscope. The module employs a beamsplitter (BS) cube interferometer and includes, in addition, a Stokes lens (SL) for astigmatism compensation. Each recorded frame contains two fields of view (FOVs) of the sample, where each FOV is a hologram which is phase shifted by π rads with respect to the other. These two simultaneously recorded holograms are numerically processed, in order to retrieve complex amplitude distribution with enhanced quality. The tradeoff is done in the FOV which becomes penalized as a consequence of the simultaneous recording of the two holograms in a single snapshot. Experimental validation is presented for a wide variety of samples using a regular Olympus BX-60 upright microscope. The proposed approach provides an optimized use of the imaging system, in terms of the space-bandwidth product, in comparison with off-axis configuration; allows the analysis of fast-dynamic events, owing to its single-shot capability when compared with on-axis arrangement; and becomes easily implementable in conventional white-light microscopes for upgrading them into holographic microscopes for QPI.

1. Introduction

Digital holographic microscopy (DHM) combines into a single platform high-quality imaging, whole-object wavefront recovery and numerical processing capabilities provided by, respectively, microscopy, holography and computers [1]. As consequence, DHM allows quantitative measurement of the complex amplitude distribution (especially phase information) of the light field that is passing through or is reflected by an inspected sample [2]. For this reason, DHM has becoming in a significant quantitative phase imaging (QPI) technique with strong potential in the bio-field [3–5] where visualization of biosamples using non-invasive (no need to use stains/dyes for contrast enhancement), wide-field (scanning-less technique), real-time (on-line monitoring), non-destructive (no sample damage) and static (no moving components) methods are highly demanded [6–16].

DHM is classically implemented using two opposite interferometric layouts [1]. On one hand, off-axis configuration reintroduces at the recording plane a reference beam which is tilted regarding the imaging beam. This configuration is capable of retrieving whole object wavefront in a single exposure because it is based on the spatial filtering of one of the diffraction orders at the Fourier domain [17]. The single-shot operational principle is really useful for evaluation of, for instance, dynamic processes in live cell imaging while the influence of external vibrations in the measurements becomes minimized. However, the

Research Article | Vol. 27, No. 4 | 18 Feb 2019 | OPTICS EXPRESS 5656
Optics EXPRESS

spectral extension of the reconstructed image can be severely limited due to the overlapping between the different diffraction orders at the Fourier domain. For a full separation of the twin imaging terms from the dc term at the Fourier domain, it is needed both a carrier frequency equal to at least three times the highest spatial frequency of the object wave and a digital sensor bandwidth at least four times the one of the object wave [18]. Essentially, the pixel characteristics of the digital camera define the relations of the extension and separation of the different diffraction orders [19] which can yield in significant information loss as a consequence of the space-bandwidth product deterioration [20]. On the other hand, on-axis interferometric configuration proposes an in-line geometry where the angle between reference and object beams is set to zero [21]. As a result, the spatial frequency bandwidth of the interferograms becomes narrower in comparison with off-axis modality and on-axis methods provide full optimization of the space–bandwidth product [19] up to a maximum achievable resolution imposed by the camera pixel size for collimated illumination [22]. However, the on-axis scheme needs at least three phase-shifted interferograms that are usually recorded sequentially in time for the complete elimination of the zero order and the twin image terms. Thus, it is not suitable for the analysis of moving samples or dynamic processes.

As a consequence of those pros and cons, a significant number (only a few are included here) of different approaches have been proposed along the past years in order to improve the complex amplitude retrieval in DHM for both off-axis [23–31] and on-axis [32–40] geometries. For instance, off-axis holography has evolved in the sense of improving processing time [25,28] as well as multiplexing different degrees of freedom [29,31]. And on-axis methods have mainly progressed to provide single shot operational principle [32,33,36–38]. In addition, the retrieved phase distribution from the off-axis arrangement has been recently proposed for helping in the in-line phase retrieval algorithm yielding in a hybrid phase retrieval mixed solution for fast, efficient and accurate QPI in DHM [41–44].

Halfway between on-axis and off-axis holographic arrangements, there is a new intermediate implementation mainly developed during the last decade. Instead of full or non-existent overlapping between the different terms at the Fourier domain described in, respectively, on-axis and off-axis layouts, it is possible to define an interferometric configuration allowing overlapping of the DC autocorrelation term with the real/twin image terms but non-overlapping between the two cross-correlation terms. This is easily achieved by controlling the angle between both interferometric beams. Thus, the whole complex amplitude distribution of the object is retrieved by eliminating the central DC term and applying conventional spatial filtering at the Fourier domain [18,24,45]. This arrangement is commonly named as slightly off-axis digital holographic microscopy (SO-DHM) and it proposes an intermediate solution because: i) it only needs two interferograms for phase retrieval, thus optimizing the acquisition rate in comparison with the on-axis layout, and ii) it relaxes the space-bandwidth product requirements of the digital sensor in comparison with off-axis configuration [18,36,46–56]. However, SO-DHM needs two independent measurements of the complex field for removing the DC term allowing access to the complex amplitude distribution of the real image term. Typically, these two images are sequentially recorded in time [18,36,49–55] but single-exposure capability has also been reported by using wavelength multiplexing [46,48], in virtue of the single-shot Hilbert transform operation [47] or with field of view (FOV) multiplexing using a non-polarizing beam splitter (BS) cube [56].

In this manuscript, we present single-shot SO-DHM approach based on a BS interferometric add-on module directly adapted to a conventional white-light microscope that enables to convert it into a holographic one. Single-exposure holographic principle in slightly off-axis geometry is achieved by FOV multiplexing using a BS cube interferometer. Thus, the digital camera records two interferograms in a single-shot that are phase shifted by π rads one to each other. This π rads phase step directly raises when using a BS cube interferometer as background arrangement because the reflected beam at the BS exhibits exactly a phase shift of π rads regarding the transmitted one [57,58]. These two simultaneously recorded SO-DHM

Research Article | Vol. 27, No. 4 | 18 Feb 2019 | OPTICS EXPRESS 5657
Optics EXPRESS

holograms are processed using an algorithm based on the subtraction of the two FOVs for eliminating the DC order term [48]. As a result, the spatial frequency distribution of the real image term can be filtered and centered at the Fourier domain and a final inverse digital FT retrieves the complex amplitude distribution of the sample. This algorithm is implemented with the images provided by an add-on module based on a BS interferometer with astigmatism compensating capabilities. The module is compact, robust and it is adapted to the exit port of a regular upright microscope with the added value to convert it into a holographic microscope working in a single illumination shot with low cost components.

2. System analysis

2.1 Layout description

The proposed single-shot SO-DHM approach has been validated using a regular Olympus BX-60 upright microscope. Figure 1 presents a picture of the microscope where the main modifications are depicted for clarity. Essentially, a fiber coupled green diode laser (OSI Laser Diode, TCW RGBS-400R) replaces the white light illumination provided by the mercury lamp of the microscope lamphouse allowing coherent illumination for the holographic recording. Light passes through a linear polarizer (P) to adjust the intensities of both replicas provided by the BS in order to achieve the most similar fringe contrast on both FOVs (this is a critical point in the reconstruction process). The trinocular head of the microscope has been removed just to avoid unwanted spurious reflections, so a tube lens (TL) has been added to maintain the infinity corrected imaging mode. The TL (f' = 120 mm) is just placed at the circular dovetail mount of the microscope trinocular port.

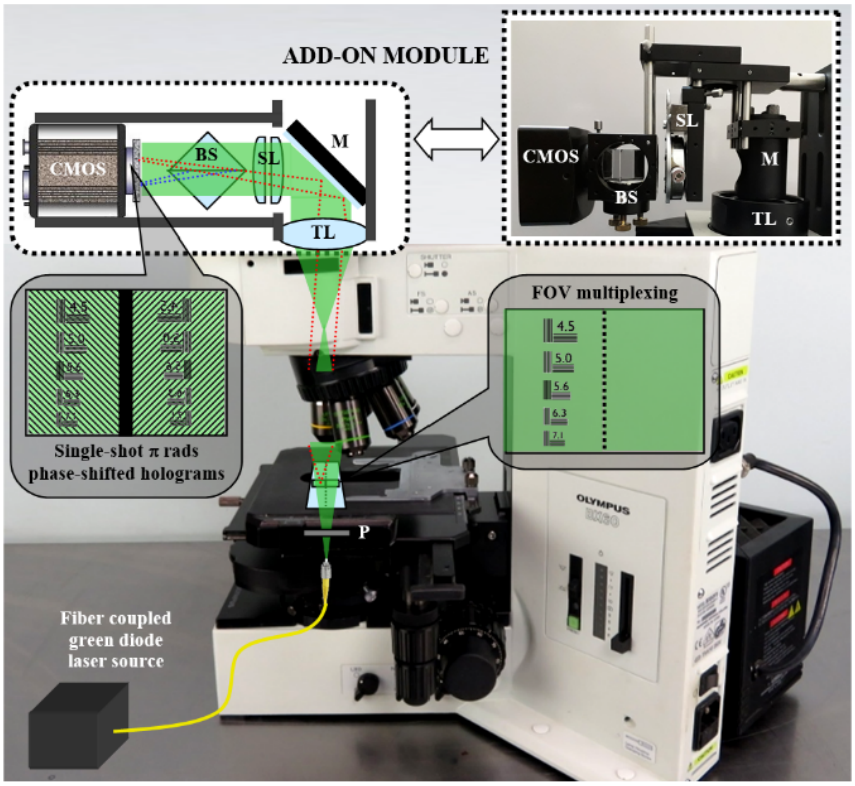

Fig. 1. Scheme of the proposed add-on module for single-shot SO-DHM in a regular non-holographic microscope. TL – tube lens, M – mirror, SL – Stokes lens, BS – beam splitter, P – linear polarizer, and CMOS – digital camera. A representative raytracing is included showing image duplication for the object ROI.

Research Article | Vol. 27, No. 4 | 18 Feb 2019 | OPTICS EXPRESS 5658
Optics EXPRESS

Then, a labmade add-on module is assembled and mounted at the output port of our modified microscope. It consist of a 45° elliptical mirror (M) mounted into beam steering mirror assembly (Qioptiq) that folds the light path into the horizontal direction towards the Stokes lens (SL), beam splitter (BS) and digital camera (CMOS). Leaving aside the SL (it will be deeply analyzed in next section), the BS (polarizing cube with 25.4 mm side) is placed in a non-conventional way, that is, rotated 45° regarding the position for splitting an incoming beam into two orthogonally separated ones. In this position, it defines a common-path interferometric configuration providing two simultaneous slightly off-axis holograms with a π rad phase step between them [56–61]. This operational principle enables single-shot capability for QPI in SO-DHM at the expense of the FOV reduction. The BS is mounted onto a tilting platform (Qioptiq) including three screws for fine adjustment and alignment. Finally, a CMOS imaging device (Mightex USB3.0 monochrome camera, 2560x1920 pixels, 2.2 μm pixel size, 14 fps) is placed behind the BS for recording of the slightly off-axis holograms. Additional opto-mechanical components (Thorlabs, Linos and Newport) assemble all the components into a single add-on module fixed at the microscope's output port.

2.2 Astigmatism compensation

The use of a BS in a non-conventional way introduces some aberrations that are critical to be compensated for high quality imaging. In particular, it introduces a non-negligible amount of tilt (prismatic effect) and astigmatism. The tilt effect can be easily compensated by slightly moving the sample at the input plane. But astigmatism compensation needs a more complex device/procedure. Note that, to the best of our knowledge, this is the first time that astigmatism is taken into account in manuscripts involving the use of a BS for interferometric recording since it was not treated before in previous references (only in [59] it is briefly discussed tilt aberration introduced by the BS cube).

The astigmatism introduced by the rotated BS can be easily seen in virtue of the case of a thickness plane-parallel plate that becomes tilted [62,63]. Depending on the illumination vergence, the amount of astigmatism can be significant enough to fully destroy image quality especially the fine sample details. Nevertheless, it can be compensated digitally [64] and with specially designed optical components such as unsymmetrical corrector [62] or variable/adjustable astigmatism compensators [65,66]. We have selected the second option since: i) it is a low-cost device that can be easily implemented at the lab, and ii) it means optical compensation of the astigmatism thus reducing the processing time of the algorithmic stage.

The solution implemented here for astigmatism compensation consists of a SL made by two pure cylindrical lenses of equal but opposite powers which are assembled onto a Risley prism mount. The lenses can be rotated one respect to the other thus varying the resulting astigmatic power from 0 (the axes of the cylindrical lenses are coincident) to the addition in absolute value of the individual cylinders (the axes of the two cylindrical lenses are crossed). And the orientation of the generated astigmatism can be adjusted by global rotation of the whole assembly. Thus, any astigmatism orientation can be optically compensated up to a maximum value of two times the cylindrical power of one of the single lenses integrating the SL. Moreover, the SL does not introduce spherical power since, regardless the orientation of the cylindrical lenses, its mean sphere power is theoretically zero (close to zero due to practical reasons). The SL was proposed by G. G. Stokes in 1849 [67] with the purpose of not to compensate but to measure astigmatism. Nowadays, it is a device used in diary practice for optometric refractive error measurement and it has been applied to different applications such as to improve image quality in eye fundus camera [65], as an adaptive astigmatism-correcting device for eyepieces [66,68], for improving visual acuity measurements [69], and to correct astigmatism at oblique incidence in a wide-angle optical models of the human eye [70].

Figure 2 includes a picture of the labmade SL used in the experiments as well as its experimental characterization using the automatic lensmeter (Topcon CL-300) for power

Research Article | Vol. 27, No. 4 | 18 Feb 2019 | OPTICS EXPRESS 5659
Optics EXPRESS

measuring. Since we have used a Risley prism mount for assembling the two cylindrical lenses of powers ± 1.50 D, the relative rotation angle between lenses is determined in prism diopters [outer scale in the Risley prism mount – see Fig. 2(a)]. Nevertheless, it is easy to translate these values into angular degrees following the expression

$$\theta = 90 - \cos^{-1}\left(\frac{tg^{-1}\left(\frac{\Delta}{100}\right)}{2(n-1)\alpha}\right) \quad (1)$$

being θ the rotation angle between the axis of the cylindrical lenses having their axes equally oriented at the beginning, Δ the prism diopters read at the Risley prism mount scale, n the refractive index value of the prisms removed from the mount (n = 1.523) and α the prism apex angle (8 degrees).

Thus, calibration of the SL is performed by varying the angle between both lenses, reading the prism diopters at 0.5Δ steps and computing the corresponding values for the rotation angle according to Eq. (1). The angle between lenses is changed by twisting the Risley rotating knob [black arrow in Fig. 2(a)]. Note also as the Risley prism mount has some marks at the outer part corresponding to the angular scale ranging from 0 to 180 degrees at 5 degrees steps. So, it is also possible to identify some control points in the calibration since, for instance, 5Δ and 10.5Δ coincide with 20° and 45°, respectively.

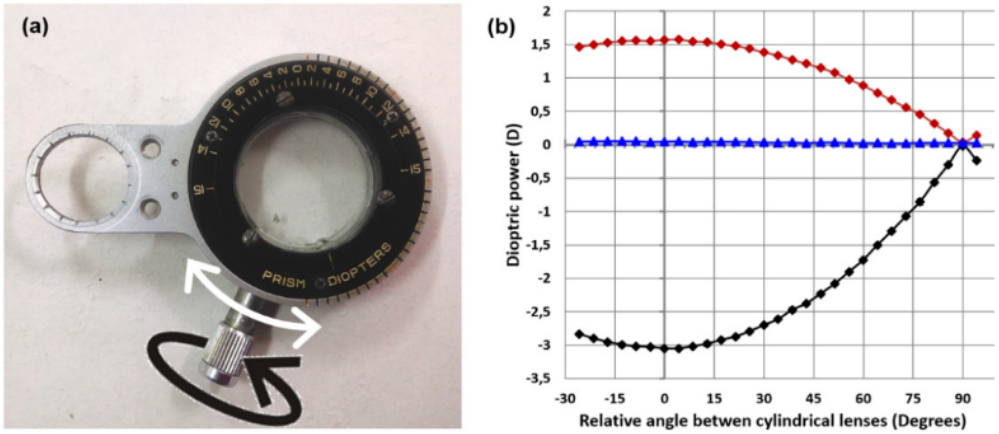

Fig. 2. SL characterization based on a Risley prism mount: (a) the labmade SL composed by two regular cylindrical lenses of equal but opposite powers (± 1.50 D), and (b) the generated cylindrical (black plot), spherical (red plot) and spherical equivalent (blue plot) powers versus relative rotation between lenses. The black/white arrow in (a) represents, respectively, how the angle between lenses and the orientation of the generated astigmatism can be changed.

Figure 2(b) shows the values for the spherical (S), the cylindrical (C) and the spherical equivalent (M = S + C/2) components versus the relative angle between cylindrical lenses. We have only considered a relative rotation angle of 90° (± 45° per each cylindrical lens) but the curve is symmetrical every 90° [65,66]. As expected, C (black plot) ranges from –3.00 D to 0 D and S (red plot) varies from + 1.50 D to 0 D making M (blue plot) close to 0 D for all the positions (M_{mean} = 0.03 D). So negligible spherical defocus will be introduced by the SL lens and astigmatism introduced by the rotated BS can be compensated until –3.00 D. Note that higher (or lower) astigmatic power can be generated by selecting cylindrical lenses with higher (or lower) powers.

Just as a proof of concept, Fig. 3 includes an experimental demonstration of the astigmatism influence and its optical compensation by the SL. We have used a resolution test

Research Article | Vol. 27, No. 4 | 18 Feb 2019 | OPTICS EXPRESS 5660
Optics EXPRESS

(USAF target) and a 10X/0.30NA microscope lens to illustrate the example. We have only included the central area and not the whole FOV of the images to clearly focus onto the smallest test's details. When the BS is inserted into the add-on module and rotated around 45° to its working position as BS interferometer, the USAF image is significantly distorted. Figures 3(a) and 3(b) include the aberrated images when, respectively, the vertical and horizontal bars of the resolution test are brought into focus by using the microscope focus adjustment knob. Obviously, the horizontal and vertical bars cannot be resolved due to the presence of the astigmatism. Then the SL is inserted into the add-on module and manually tuned to its best position for astigmatism compensation. The resulting image is included in Fig. 3(c) where no astigmatism aberration is observed. This result is compared against the image provided without the add-on module [Fig. 3(d)] and the central parts magnified for clarity. The main outcome from Fig. 3 is that resolution is preserved since the last resolved element (Group 9 – Element 2) is the same in both astigmatic-free images.

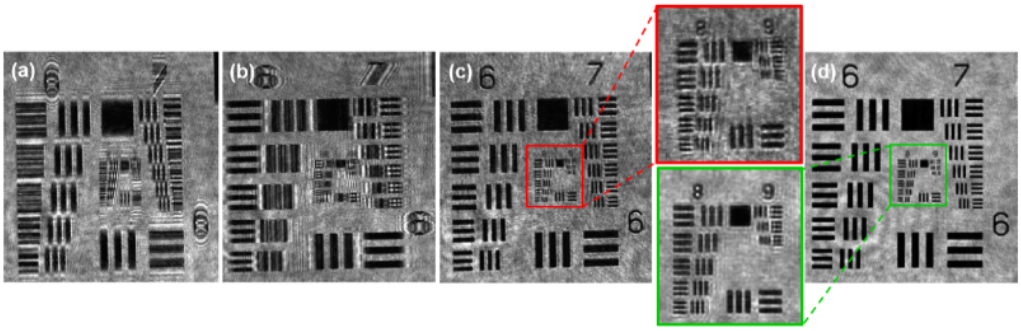

Fig. 3. Astigmatism influence in a BS interferometer: (a) and (b) images obtained after BS inclusion in rotated position where vertical and horizontal bars of the test are focused respectively; (c) image free of astigmatism after the SL is inserted in the add-on module; and (d) direct image without the add-on module for comparison.

2.3 Reconstruction procedure

Using the layout presented in Fig. 1, single-shot SO-DHM can be implemented in a regular non-holographic microscope. Because of the intrinsic characteristic of a BS interferometer, the two single-shot recorded holograms exhibit a phase step difference of π rads [57,58]. So considering that the input FOV is multiplexed into two equal areas, one for the sample and the other for the reference, the output plane recorded distribution will contain two anti-phase shifted holograms in the form of:

$$\begin{aligned} I_1(x,y) &= |O(x,y)|^2 + |R(x,y)|^2 + O(x,y)R^*(x,y) + O^*(x,y)R(x,y) \\ I_2(x,y) &= |O(x,y)|^2 + |R(x,y)|^2 - O(x,y)R^*(x,y) - O^*(x,y)R(x,y) \end{aligned} \quad (2)$$

being $|O|^2$ and $|R|^2$ the auto-correlation/DC terms of, respectively, the object and the reference waves, and OR^* and O^*R the cross-correlation terms in the form of real and twin imaging terms, respectively. Note as the sign of the auto-correlation terms are opposite between I_1 and I_2 because of the factors $\exp(i\pi)$ and $\exp(-i\pi)$ of the two π rads phase shifted holograms.

For the reconstruction process, we have implemented a subtraction algorithm [48] where the DC term can be eliminated by digital computation of the intensity difference in the form of:

$$I_1(x,y) - I_2(x,y) = 2O(x,y)R^*(x,y) + 2O^*(x,y)R(x,y) \quad (3)$$

Research Article | Vol. 27, No. 4 | 18 Feb 2019 | OPTICS EXPRESS 5661
Optics EXPRESS

Please note that upon subtraction amplitude of two information carrying terms doubled while DC component canceled out. Since we are in slightly off-axis mode (the carrier frequency of the experimental layout can be adjusted by rotating the BS cube in the add-on module), the two retrieved cross-correlation terms are not overlapping between them so the real image term can be filtered out in the Fourier domain making available the complex amplitude distribution of the real image term. However and before computing Eq. (3), fine digital matching of both images from a spatial point of view must be performed in terms of centering of both FOVs that are going to be subtracted. Otherwise, no correct recovery of the sample's spatial distribution will be performed. This process can be easily implemented using correlation operation of the two FOV halves after astigmatism compensation and before entering the reference beam for the holographic recording. The latter can be easily done by blocking the side corresponding with the reference path of the BS, thus allowing only the transmission of the imaging path.

In order to show the whole reconstruction process and to analyze the advantages of the proposed method, we present the experimental results obtained when a resolution test (NBS 1963A target) is considered as input object. We have moved from USAF to NBS since it contains large clear areas surrounding the resolution elements and this fact is needed for the reference beam transmission as well as to provide a wide area for standard deviation (STD) analysis. Figure 4 includes: Fig. 4(a) the direct image without the add-on module, Fig. 4(b) the distorted image when the BS is introduced, Fig. 4(c) the image free of astigmatism after the SL is inserted, and Fig. 4(d) the recorded hologram when the reference beam is introduced. Insets show 180 lp/mm element for astigmatism compensation and interferometric fringes for clarity.

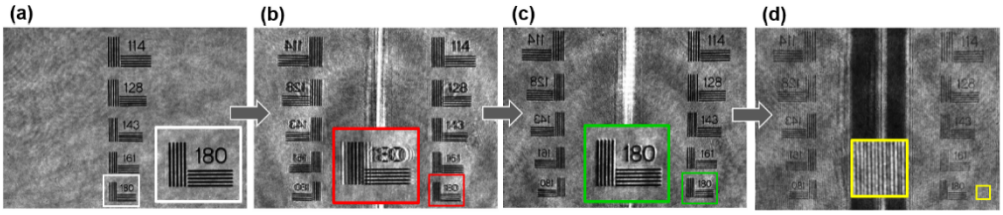

Fig. 4. Recording sequence in the proposed single-shot SO-DHM method: (a) direct image without the add-on module, (b) astigmatic image generated by the BS, (c) astigmatism-free image using SL, and (d) the single-shot SO recorded hologram.

Then, the proposed reconstruction method is illustrated through Fig. 5 (upper row labelled as 1) in comparison with the results obtained by considering conventional filtering at the Fourier domain (lower row labelled as 2), that is, without computing Eq. (3) and taking only into account one of the two FOVs. For each row, Fig. 5(a) presents the hologram, Fig. 5(b) its Fourier transform, and Fig. 5(c) the filtered spatial-frequency pupil which is used to retrieve Fig. 5(d) the intensity and Fig. 5(f) the phase distributions of the input sample. In addition, Fig. 5(e) includes a plot along the normalized intensity profile of one of the resolution test elements (114 lp/mm) and Fig. 5(g) shows the retrieved phase background image of the clear area marked with a solid line white rectangle in Fig. 5(f). Comparison of Figs. 5(a1)-5(a2) images clearly shows how background is eliminated so the DC term will not take part in the reconstruction process. This fact is made evident also when looking at Figs. 5(b1)-5(b2) and Figs. 5(c1)-5(c2) images since the $|O|^2$ contribution is readily observable at Figs. 5(b2)-(c2) while avoided at Figs. 5(b1)-(c1). Also, it can be noted that the spectra of real and twin images are separated from each other at Figs. 5(b1)-5(b2) images.

The question arises: what will we expect from both reconstructions? Obviously, a noisier and poorer quality image coming from the second row in comparison with the one obtained by the proposed system (first row). This statement is confirmed by plotting the recovered intensity images Figs. 5(d1)-5(d2) through the white dashed lines and by computing the STD

Research Article | Vol. 27, No. 4 | 18 Feb 2019 | OPTICS EXPRESS 5662
Optics EXPRESS

values in a background area [white rectangle in Fig. 5(f)] at the retrieved phase images Figs. 5(f1)-5(f2). The plots are included in Figs. 5(e1)-5(e2) and its comparison demonstrates that conventional filtering is mainly noise while the proposed method perfectly identifies the 5 vertical bars as well as the 4 dips coming from the number "114". And the phase background images are presented in Figs. 5(g1)-5(g2) where the proposed system provides a background smoother than the conventional procedure. This fact is confirmed also by computing the STD value of the images since it is reduced by around 40% (STD values included at Fig. 5).

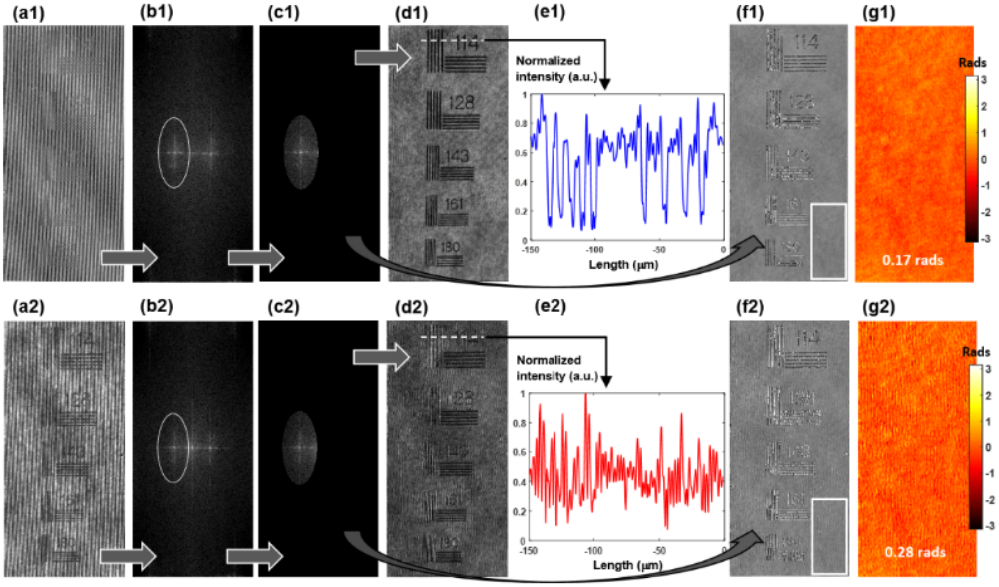

Fig. 5. Comparison results between the proposed system (upper row labelled as 1) and the conventional Fourier filtering method (lower row labelled as 2). Each row includes: (a) the hologram, (b) its Fourier transform, (c) the filtered spatial-frequency pupil, (d) the retrieved intensity image, (e) the plot of the normalized intensity profile marked with the dashed white line in (d), (f) the retrieved phase distribution, and (g) the retrieved phase background image coming from the solid line white rectangle in (f) including the STD value.

3. Experimental results on phase samples

3.1 Static biosamples

Our system has been tested with different lines (PC-3, LnCaP and RWPE-1) of prostate cancer cells prepared following the same procedure. The cells were cultured in RPMI 1640 medium with 10% fetal bovine serum, 100U/ml Penincillin and 0.1ug/ml Streptomycine at standard cell culture conditions (37°C in 5% CO2 in a humidified incubator). Once the cells reach a confluent stage, they were released from the culture support and centrifuged. The supernatant fluid is discarded by centrigutation and the cells are resuspended in a cytopreservative solution and mounted in a microscopy slide. Figure 6 shows the experimental results where the different cell lines are placed in different rows. Thus, PC-3 cells are included in the upper row (labelled as 1), LnCaP cells are in the central row (labelled as 2), and RWPE-1 cells are presented in the lower row (labelled as 3). Note that we have not included the whole rectangular FOV retrieved as in Fig. 5 but only a squared area as in Fig. 3 for optimizing the figure artwork.

At the different columns, Fig. 6 includes: Fig. 6(a) the subtraction hologram coming from Eq. (3), Fig. 6(b) its Fourier transform without DC term contribution, Fig. 6(c) the filtered pupil at the Fourier domain, Fig. 6(d) the retrieved phase distribution after inverse Fourier transform of the filtered aperture [with spectrum shifting to the center], and Fig. 6(e) the 3D view of the unwrapped phase distribution with quantitative scale bar. In addition, Fig. 6(f)

Research Article | Vol. 27, No. 4 | 18 Feb 2019 | OPTICS EXPRESS 5663
Optics EXPRESS

includes the same 3D view but retrieved from conventional Fourier filtering method for comparison with Fig. 6(e). One can notice as noise dominates the retrieved 3D phase profile using conventional tools whereas the proposed system allows perfect visualization of the cells regardless the number of cells in the analyzed FOV (increasing from up to down).

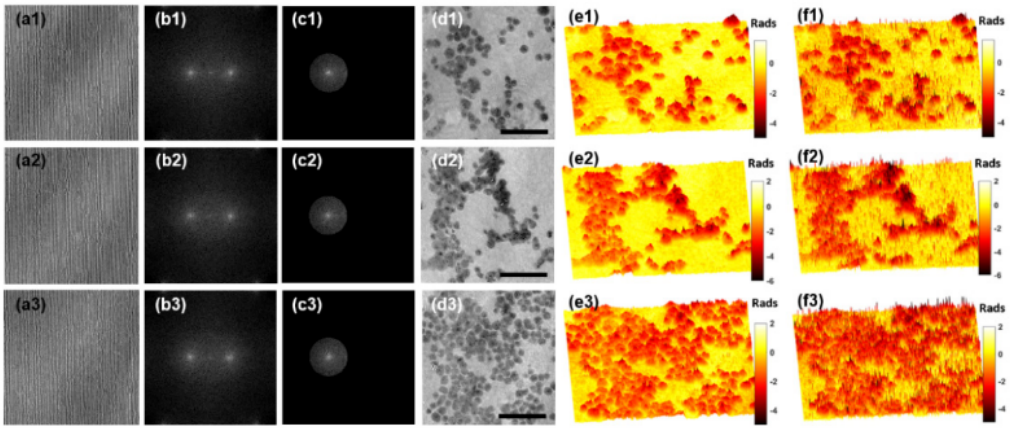

Fig. 6. Experimental results conducted on static biosamples: upper/central/lower rows are labelled as 1/2/3, respectively, and include PC-3/LnCaP/RWPE-1 cell lines, respectively. Each row includes: (a) the subtraction hologram ($I_1 - I_2$), (b) its Fourier transform, (c) the filtered spatial-frequency pupil, (d) the retrieved phase distribution, (e) the 3D plot of the unwrapped phase distribution included in (d), and (f) the same 3D view but considering the conventional Fourier filtering method. Black scale bars in (d) column are 100 µm.

3.2 Dynamic sample

Once SO-DHM was experimentally validated for static biosamples in previous section, our aim here is to demonstrate its validity for real-time measurement of dynamic objects. This is probably the most interesting capability of single-shot SO-DHM. Aimed at this, we have conducted an additional experiment where microbeads (Polybead Microspheres, standard monodisperse polystyrene microspheres) of 90 µm mean diameter are now imaged by a 20X/0.46NA objective lens. The microspheres are flowing in a 100 µm thickness chamber filled with water.

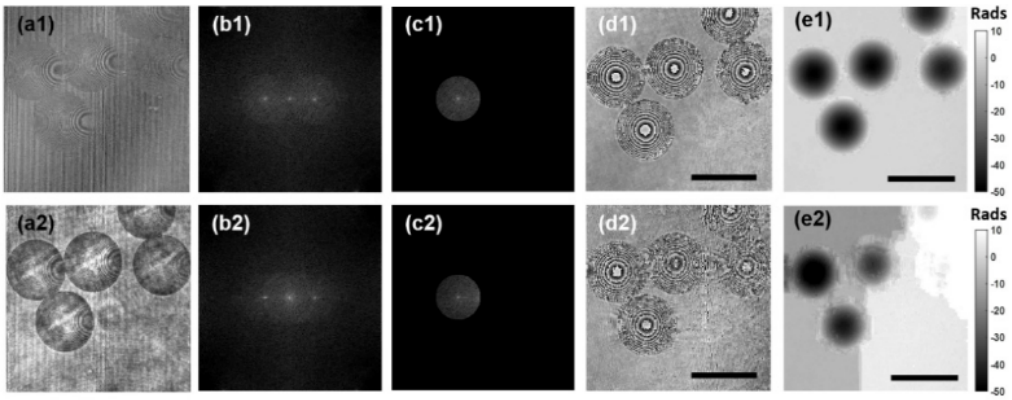

Fig. 7. Experimental results for dynamic microbeads: single frame analysis. Results coming from the proposed system are included in the upper row (labelled as 1) and the ones from conventional Fourier filtering method in the lower one (labelled as 2). Each row includes: (a) the hologram, (b) its Fourier transform, (c) the filtered spatial-frequency pupil, (d) the retrieved wrapped phase distribution, and (e) the 2D view of the unwrapped phase distribution included in (d). Black scale bars in (d)-(e) images are 100 µm.

Research Article | Vol. 27, No. 4 | 18 Feb 2019 | OPTICS EXPRESS 5664
Optics EXPRESS

Figure 7 presents the experimental results coming from the proposed system (upper row) and the conventional one (lower row). As in previous figure, Fig. 7(a) includes the hologram, Fig. 7(b) its Fourier transform, Fig. 7(c) the filtered aperture, Fig. 7(d) the retrieved wrapped phase distribution, and Fig. 7(e) the unwrapped phase distribution. Note that it is impossible to retrieve the beads accurate phase information using a single hologram with conventional tools since the DC term overlaps with the twin imaging terms at spectral domain. Thus, the retrieved phase distribution becomes very noisy making impossible a correct phase unwrapping. Hence the single-shot working capability provided by SO-DHM enables accurate QPI analysis of dynamic samples. Moreover, the spectrum at Fig. 7(b1) is perfectly marking the circular coherent aperture of the objective lens for both cross-correlation terms meaning that the DC is efficiently removed (only remains a single central spot probably coming from the auto-correlation term $|R|^2$ and from general slight imperfections of the subtraction procedure).

Finishing the single frame analysis, Fig. 8 includes the first frames corresponding with Fig. 8(a) the movie of the recorded set of single shot slightly off-axis holograms (see Visualization 1), Fig. 8(b) the movie representing the subtraction hologram derived from Eq. (3) (see Visualization 2), and Fig. 8(c) the retrieved 3D unwrapped phase profile of the microbeads flowing into the counting chamber (see Visualization 3). We have not included the results incoming from conventional Fourier filtering because, as previously stated, no accurate phase information is retrieved due to phase unwrapping errors.

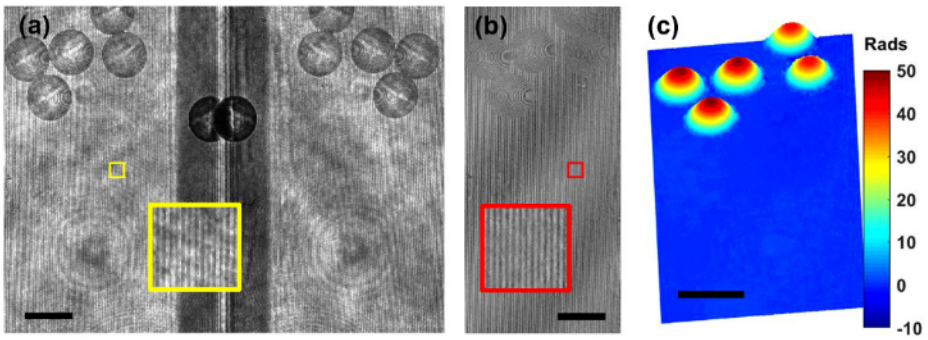

Fig. 8. Experimental results for dynamic microbeads: movie validation. (a) The recorded set of single-shot SO holograms with FOV multiplexing (see Visualization 1), (b) the movie from the subtraction holograms (see Visualization 2), and (c) the 3D view of the retrieved unwrapped phase distribution by single-shot SO-DHM (see Visualization 3). Black scale bars are 100 µm and insets show interferometric fringes for clarity.

4. Discussion and conclusions

Mainly over the last decade, new and novel simplified, cost-effective, accurate and robust DHM architectures have appeared in the scientific literature [71–85]. Among them, the idea of quantitative coherent sensing with regular microscopes appears as very attractive [71–73,75,78–85]. For instance, SMIM concept [80,83–85] was proposed by our group as a common-path interferometric configuration where minimal modifications are required to convert a regular microscope into a holographic one. The SMIM has been successfully validated considering off-axis holographic recording with Fourier filtering [80], using almost on-axis recording with phase-shifting algorithm [83], with superresolution capabilities to overcome the FOV restriction [84], and in combination with Hilbert-Huang phase microscopy for allowing single-shot operational principle even outside off-axis holographic recording regime [85]. Following in this line, we have presented a new and low-cost way to convert a regular microscope into a holographic one based on FOV multiplexing but with the new insights coming from: i) the use of a BS interferometer, ii) which is implemented under

Research Article Vol. 27, No. 4 | 18 Feb 2019 | OPTICS EXPRESS 5665
Optics EXPRESS

slightly off-axis configuration and iii) integrated into a robust add-on module including optical astigmatism compensation.

On one hand, the use of BS interferometers has been previously reported in the literature [48,56–65] but none of those references deal with the astigmatism introduced when the BS cube is rotated 45° for allowing interferometric replicas. Here, we have deeply analyzed it and proposed an optical compensation strategy based on a SL which is fully integrated into the same add-on interferometric module. According to the relative position of the cylindrical lenses in the SL, we have estimated a total amount of astigmatism equivalent to 0.25 D which is enough for destroying image quality in a microscope, especially at resolution limit (smallest details). Note that the dioptric power (inverse of its focal length) of the TL is 8.33D so the total power of the TL with the astigmatism is 8.58D which means an aberrated focal length of 116.5 mm. This distance is 3.5 mm away from the non-aberrated focal length (120 mm), so the amount of defocus is noticeable.

And on the other hand, SO-DHM has also been proposed as QPI method [18,36,46–56] but single-shot operational principle in SO-DHM is not quite common and requires more complex approaches, such as the use of additional wavelengths [46,48] or the reintroduction of an external reference beam [47], or simply applies to different fields such as lensless microscopy [56]. To the best of our knowledge, this is the first time that single-shot SO-DHM has been implemented in a standard microscope with an external add-on module based on a BS interferometer.

Nowadays, SO-DHM has becoming in an appealed approach for observing dynamic events. The lower the number of recordings, the better the reconstruction in terms of acquisition time and reconstruction errors. The former allows analysis of faster dynamic events ultimately limited by the recording time of a single snapshot. The latter implies that no differences exist between recordings since environmental conditions (thermal/mechanical vibrations, light fluctuations, etc.) are constant in a single snapshot. In that sense, single-shot SO-DHM provides superior performance than classical on-axis interferometry where at least two consecutive holograms are needed. Although parallel phase-shifting DHM has been proposed using different strategies such as modified Hartmann masks [86], micro polarizers attached pixel by pixel to a digital sensor [87], and based on a parallel-quadrature simultaneous phase-shifting method using two identical CCD sensors [88], those techniques are cost-effective from both temporal (computationally demanding) and economically (duplicating some components in the setup). The proposed add-on module is simple, cost-effective and minimally time consuming from an algorithmic point of view.

The experiments included along this paper compare the images retrieved by the proposed single-shot SO-DHM module against conventional Fourier filtering considering a single hologram in slightly off-axis configuration. The comparison shows better performance with improved QPI capabilities when using the proposed technique. Nevertheless, it is possible to increase the carrier frequency in the hologram and move to full off-axis architecture by further rotation of the BS cube. This procedure will recover accurate QPI but it will restrict even more the useful FOV since the central useless area will become enlarged as well as it will endanger the space-bandwidth product of the system. In addition, it is possible to apply a smaller filtering window in the slightly off-axis configuration so the DC term will be prevented in the reconstructed image and better accuracy in QPI will be achieved. However, this procedure will produce resolution limitation as a consequence of the low pass filtering at the Fourier domain, so the reconstruction will be blurred and information will be lost.

Although the proposed method has been validated using an upright microscope configuration, implementation using inverted systems can also be possible and will be a challenge for future works. This possibility will open the door to living cell/tissue culture investigations which are usually performed under inverted microscopes and that have become in a very useful tool in cellular and molecular biology because of their multiple benefits (excellent procedure for studying the normal physiology and biochemistry of cells, the effects

Research Article | Vol. 27, No. 4 | 18 Feb 2019 | OPTICS EXPRESS 5666
Optics EXPRESS

of drugs and toxic compounds on the cells, and mutagenesis and carcinogenesis, drug screening and development, and providing a high consistency and reproducibility of the results). Moreover, the use of partially coherence illumination for image quality improvement (coherence noise reduction) can also be a notable field to be explored.

Finally, the proposed method is theoretically valid to any study performed in the field of DHM/QPI provided that the FOV multiplexing will be satisfied. Thus, the only requirement is to defined a special chamber where the sample to be analyzed will be on one side (half FOV) leaving clear/transparent the other half FOV for reference beam transmission. If this condition is accomplished, then the proposed method is theoretically applicable to any DHM/QPI study which is actually carried under conventional DHM/QPI.

In summary, single-shot SO-DHM has been presented and validated into a regular upright microscope by means of a compact, robust and cost-effective add-on module which is directly placed at the microscope's output port. The add-on module is based on a BS interferometer for the recording of two simultaneous holograms that are shifted π rads one to each other. The add-on module also includes a SL for astigmatism compensation caused by the rotation of the BS. The two holograms are numerically processed for removing the DC term thus allowing the retrieval of the complex amplitude distribution by simple filtering procedure at the Fourier domain. Experiments are reported using different types of samples: resolution test targets are used for calibration and in order to show the whole process step by step, prostate cancer cells show the potential of the method for QPI, and flowing microbeads validate the method for dynamic regime. The main limitations of the proposed method are the FOV reduction as consequence of the spatial multiplexing needed for the recording of the two holograms in a single frame and practical troubles coming from the correct alignment of the added optical elements (mainly SL, BS cube and object illumination) which can yield in poorer quality QPI reconstructions.

Funding

Spanish Ministerio de Economía, Industria y Competitividad and the Fondo Europeo de Desarrollo Regional under the project FIS2017-89748-P and the National Science Center Poland (NCN) (Grant 2017/25/B/ST7/02049) - Statutory Funds Warsaw University of Technology.

References

1. M. K. Kim, "Principles and techniques of digital holographic microscopy," SPIE Rev. **1**, 018005 (2010).
2. B. Kemper and G. von Bally, "Digital holographic microscopy for live cell applications and technical inspection," Appl. Opt. **47**(4), A52–A61 (2008).
3. P. Ferraro, A. Wax, and Z. Zalevsky, eds., *Coherence light microscopy – Imaging and quantitative phase analysis* (Springer, 2011).
4. M. K. Kim, *Digital Holographic Microscopy: Principles, Techniques, and Applications* (Springer, 2011).
5. N. T. Shaked, Z. Zalevsky, and L. L. Satterwhite, *Biomedical Optical Phase Microscopy and Nanoscopy* (Oxford Academy, 2012).
6. C. Mann, L. Yu, C. M. Lo, and M. Kim, "High-resolution quantitative phase-contrast microscopy by digital holography," Opt. Express **13**(22), 8693–8698 (2005).
7. P. Marquet, B. Rappaz, P. J. Magistretti, E. Cuche, Y. Emery, T. Colomb, and C. Depeursinge, "Digital holographic microscopy: a noninvasive contrast imaging technique allowing quantitative visualization of living cells with subwavelength axial accuracy," Opt. Lett. **30**(5), 468–470 (2005).
8. P. Ferraro, S. Grilli, D. Alfieri, S. De Nicola, A. Finizio, G. Pierattini, B. Javidi, G. Coppola, and V. Striano, "Extended focused image in microscopy by digital Holography," Opt. Express **13**(18), 6738–6749 (2005).
9. T. Ikeda, G. Popescu, R. R. Dasari, and M. S. Feld, "Hilbert phase microscopy for investigating fast dynamics in transparent systems," Opt. Lett. **30**(10), 1165–1167 (2005).
10. F. Charrière, A. Marian, F. Montfort, J. Kuehn, T. Colomb, E. Cuche, P. Marquet, and C. Depeursinge, "Cell refractive index tomography by digital holographic microscopy," Opt. Lett. **31**(2), 178–180 (2006).
11. P. Ferraro, L. Miccio, S. Grilli, M. Paturzo, S. De Nicola, A. Finizio, R. Osellame, and P. Laporta, "Quantitative Phase Microscopy of microstructures with extended measurement range and correction of chromatic aberrations by multiwavelength digital holography," Opt. Express **15**(22), 14591–14600 (2007).

Research Article | Vol. 27, No. 4 | 18 Feb 2019 | OPTICS EXPRESS 5667
Optics EXPRESS

12. B. Kemper, A. Bauwens, A. Vollmer, S. Ketelhut, P. Langehanenberg, J. Müthing, H. Karch, and G. von Bally, "Label-free quantitative cell division monitoring of endothelial cells by digital holographic microscopy," J. Biomed. Opt. **15**(3), 036009 (2010).
13. M. F. Toy, S. Richard, J. Kühn, A. Franco-Obregón, M. Egli, and C. Depeursinge, "Enhanced robustness digital holographic microscopy for demanding environment of space biology," Biomed. Opt. Express **3**(2), 313–326 (2012).
14. F. Pan, S. Liu, Z. Wang, P. Shang, and W. Xiao, "Digital holographic microscopy long-term and real-time monitoring of cell division and changes under simulated zero gravity," Opt. Express **20**(10), 11496–11505 (2012).
15. D. Boss, J. Kühn, P. Jourdain, C. Depeursinge, P. J. Magistretti, and P. Marquet, "Measurement of absolute cell volume, osmotic membrane water permeability, and refractive index of transmembrane water and solute flux by digital holographic microscopy," J. Biomed. Opt. **18**(3), 036007 (2013).
16. J. Á. Picazo-Bueno, D. Cojoc, F. Iseppon, V. Torre, and V. Micó, "Single-shot, dual-mode, water-immersion microscopy platform for biological applications," Appl. Opt. **57**(1), A242–A249 (2018).
17. E. Cuche, P. Marquet, and C. Depeursinge, "Spatial filtering for zero-order and twin-image elimination in digital off-axis holography," Appl. Opt. **39**(23), 4070–4075 (2000).
18. N. T. Shaked, Y. Zhu, M. T. Rinehart, and A. Wax, "Two-step-only phase-shifting interferometry with optimized detector bandwidth for microscopy of live cells," Opt. Express **17**(18), 15585–15591 (2009).
19. L. Xu, X. Peng, Z. Guo, J. Miao, and A. Asundi, "Imaging analysis of digital holography," Opt. Express **13**(7), 2444–2452 (2005).
20. D. Claus and D. Iliescu, "Optical parameters and space-bandwidth product optimization in digital holographic microscopy," Appl. Opt. **52**(1), A410–A422 (2013).
21. I. Yamaguchi and T. Zhang, "Phase-shifting digital holography," Opt. Lett. **22**(16), 1268–1270 (1997).
22. T. E. Agbana, H. Gong, A. S. Amoah, V. Bezzubik, M. Verhaegen, and G. Vdovin, "Aliasing, coherence, and resolution in a lensless holographic microscope," Opt. Lett. **42**(12), 2271–2274 (2017).
23. D. Carl, B. Kemper, G. Wernicke, and G. von Bally, "Parameter-optimized digital holographic microscope for high-resolution living-cell analysis," Appl. Opt. **43**(36), 6536–6544 (2004).
24. N. Pavillon, C. Arfire, I. Bergoënd, and C. Depeursinge, "Iterative method for zero-order suppression in off-axis digital holography," Opt. Express **18**(15), 15318–15331 (2010).
25. H. Pham, H. Ding, N. Sobh, M. Do, S. Patel, and G. Popescu, "Off-axis quantitative phase imaging processing using CUDA: toward real-time applications," Biomed. Opt. Express **2**(7), 1781–1793 (2011).
26. B. Bhaduri and G. Popescu, "Derivative method for phase retrieval in off-axis quantitative phase imaging," Opt. Lett. **37**(11), 1868–1870 (2012).
27. T. Slabý, P. Kolman, Z. Dostál, M. Antoš, M. Lošťák, and R. Chmelík, "Off-axis setup taking full advantage of incoherent illumination in coherence-controlled holographic microscope," Opt. Express **21**(12), 14747–14762 (2013).
28. B. Sha, X. Liu, X.-L. Ge, and C.-S. Guo, "Fast reconstruction of off-axis digital holograms based on digital spatial multiplexing," Opt. Express **22**(19), 23066–23072 (2014).
29. I. Frenklach, P. Girshovitz, and N. T. Shaked, "Off-axis interferometric phase microscopy with tripled imaging area," Opt. Lett. **39**(6), 1525–1528 (2014).
30. X. He, C. V. Nguyen, M. Pratap, Y. Zheng, Y. Wang, D. R. Nisbet, R. J. Williams, M. Rug, A. G. Maier, and W. M. Lee, "Automated Fourier space region-recognition filtering for off-axis digital holographic microscopy," Biomed. Opt. Express **7**(8), 3111–3123 (2016).
31. M. Rubin, G. Dardikman, S. K. Mirsky, N. A. Turko, and N. T. Shaked, "Six-pack off-axis holography," Opt. Lett. **42**(22), 4611–4614 (2017).
32. Y. Awatsuji, M. Sasada, and T. Kubota, "Parallel quasi-phase-shifting digital holography," Appl. Phys. Lett. **85**(6), 1069–1071 (2004).
33. Y. Awatsuji, T. Tahara, A. Kaneko, T. Koyama, K. Nishio, S. Ura, T. Kubota, and O. Matoba, "Parallel two-step phase-shifting digital holography," Appl. Opt. **47**(19), D183–D189 (2008).
34. P. Gao, B. Yao, N. Lindlein, K. Mantel, I. Harder, and E. Geist, "Phase-shift extraction for generalized phase-shifting interferometry," Opt. Lett. **34**(22), 3553–3555 (2009).
35. P. Gao, I. Harder, V. Nercissian, K. Mantel, and B. Yao, "Phase-shifting point-diffraction interferometry with common-path and in-line configuration for microscopy," Opt. Lett. **35**(5), 712–714 (2010).
36. N. T. Shaked, T. M. Newpher, M. D. Ehlers, and A. Wax, "Parallel on-axis holographic phase microscopy of biological cells and unicellular microorganism dynamics," Appl. Opt. **49**(15), 2872–2878 (2010).
37. P. Gao, B. Yao, I. Harder, J. Min, R. Guo, J. Zheng, and T. Ye, "Parallel two-step phase-shifting digital holograph microscopy based on a grating pair," J. Opt. Soc. Am. A **28**(3), 434–440 (2011).
38. T. D. Yang, H.-J. Kim, K. J. Lee, B.-M. Kim, and Y. Choi, "Single-shot and phase-shifting digital holographic microscopy using a 2-D grating," Opt. Express **24**(9), 9480–9488 (2016).
39. C. Tian and S. Liu, "Phase retrieval in two-shot phase-shifting interferometry based on phase shift estimation in a local mask," Opt. Express **25**(18), 21673–21683 (2017).
40. J. Li, L. Zhong, S. Liu, Y. Zhou, J. Xu, J. Tian, and X. Lu, "An advanced phase retrieval algorithm in N-step phase-shifting interferometry with unknown phase shifts," Sci. Rep. 7(1), 44307 (2017).

Research Article | Vol. 27, No. 4 | 18 Feb 2019 | OPTICS EXPRESS 5668
Optics EXPRESS

41. C. Ozsoy-Keskinbora, C. B. Boothroyd, R. E. Dunin-Borkowski, P. A. van Aken, and C. T. Koch, "Hybridization approach to in-line and off-axis (electron) holography for superior resolution and phase sensitivity," Sci. Rep. **4**(1), 7020 (2014).
42. L. Orzó, "High speed phase retrieval of in-line holograms by the assistance of corresponding off-axis holograms," Opt. Express **23**(13), 16638–16649 (2015).
43. F. Wang, D. Wang, S. Panezai, L. Rong, Y. Wang, and J. Zhao, "Imaging on the surfaces of an uneven thickness medium based on hybrid phase retrieval with the assistance of off-axis digital holography," Opt. Commun. **401**, 59–65 (2017).
44. F. Wang, D. Wang, L. Rong, Y. Wang, and J. Zhao, "Single-shot dual-wavelength in-line and off-axis hybrid digital holography," Appl. Phys. Lett. **112**(9), 091903 (2018).
45. N. Pavillon, C. S. Seelamantula, J. Kühn, M. Unser, and C. Depeursinge, "Suppression of the zero-order term in off-axis digital holography through nonlinear filtering," Appl. Opt. **48**(34), H186–H195 (2009).
46. J. Han, P. Gao, B. Yao, Y. Gu, and M. Huang, "Slightly off-axis interferometry for microscopy with second wavelength assistance," Appl. Opt. **50**(17), 2793–2798 (2011).
47. L. Xue, J. Lai, S. Wang, and Z. Li, "Single-shot slightly-off-axis interferometry based Hilbert phase microscopy of red blood cells," Biomed. Opt. Express **2**(4), 987–995 (2011).
48. P. Gao, B. Yao, J. Min, R. Guo, J. Zheng, T. Ye, I. Harder, V. Nercissian, and K. Mantel, "Parallel two-step phase-shifting point-diffraction interferometry for microscopy based on a pair of cube beamsplitters," Opt. Express **19**(3), 1930–1935 (2011).
49. J. Min, B. Yao, P. Gao, R. Guo, B. Ma, J. Zheng, M. Lei, S. Yan, D. Dan, T. Duan, Y. Yang, and T. Ye, "Dual-wavelength slightly off-axis digital holographic microscopy," Appl. Opt. **51**(2), 191–196 (2012).
50. C. S. Guo, B. Y. Wang, B. Sha, Y. J. Lu, and M. Y. Xu, "Phase derivative method for reconstruction of slightly off-axis digital holograms," Opt. Express **22**(25), 30553–30558 (2014).
51. R. Guo, B. Yao, J. Min, M. Zhou, X. Yu, M. Lei, S. Yan, Y. Yang, and D. Dan, "LED-based digital holographic microscopy with slightly off-axis interferometry," J. Opt. **16**(12), 125408 (2014).
52. M. Shan, M. E. Kandel, H. Majeed, V. Nastasa, and G. Popescu, "White-light diffraction phase microscopy at doubled space-bandwidth product," Opt. Express **24**(25), 29033–29039 (2016).
53. H. Bai, Z. Zhong, M. Shan, L. Liu, L. Guo, and Y. Zhang, "Interferometric phase microscopy using slightly-off-axis reflective point diffraction interferometer," Opt. Lasers Eng. **90**, 155–160 (2017).
54. Z. Zhong, H. Bai, M. Shan, Y. Zhang, and L. Guo, "Fast phase retrieval in slightly off-axis digital holography," Opt. Lasers Eng. **97**, 9–18 (2017).
55. Y. Yang, Z.-J. Cheng, H.-M. Zhao, Q.-Y. Yue, and C.-S. Guo, "Quantitative phase imaging system with slightly-off-axis configuration and suitable for objects both larger and smaller than the size of the image sensor," Opt. Express **26**(13), 17199–17208 (2018).
56. M. León-Rodríguez, J. A. Rayas, R. R. Cordero, A. Martínez-García, A. Martínez-Gonzalez, A. Téllez-Quiñones, P. Yañez-Contreras, and O. Medina-Cázares, "Dual-plane slightly off-axis digital holography based on a single cube beam splitter," Appl. Opt. **57**(10), 2727–2735 (2018).
57. J. A. Ferrari and E. M. Frins, "Single-element interferometer," Opt. Commun. **279**(2), 235–239 (2007).
58. W. Qu, O. C. Chee, Y. Yu, and A. Asundi, "Characterization and inspection of microlens array by single cube beam splitter microscopy," Appl. Opt. **50**(6), 886–890 (2011).
59. W. Qu, K. Bhattacharya, C. O. Choo, Y. Yu, and A. Asundi, "Transmission digital holographic microscopy based on a beam-splitter cube interferometer," Appl. Opt. **48**(15), 2778–2783 (2009).
60. P. Gao, B. Yao, J. Min, R. Guo, J. Zheng, and T. Ye, "Parallel two-step phase-shifting microscopic interferometry based on a cube beamsplitter," Opt. Commun. **284**(18), 4136–4140 (2011).
61. H. Gabai and N. T. Shaked, "Dual-channel low-coherence interferometry and its application to quantitative phase imaging of fingerprints," Opt. Express **20**(24), 26906–26912 (2012).
62. J. Braat, "Analytical expressions for the wave-front aberration coefficients of a tilted plane-parallel plate," Appl. Opt. **36**(32), 8459–8467 (1997).
63. X. Zhong, T. Wang, J. Yan, and G. Jin, "Aberrations correction of tilted plane-parallel plate in convergent rays," Appl. Opt. **54**(7), 1758–1764 (2015).
64. T. Colomb, E. Cuche, F. Charrière, J. Kühn, N. Aspert, F. Montfort, P. Marquet, and C. Depeursinge, "Automatic procedure for aberration compensation in digital holographic microscopy and applications to specimen shape compensation," Appl. Opt. **45**(5), 851–863 (2006).
65. J. Arines and E. Acosta, "Low-cost adaptive astigmatism compensator for improvement of eye fundus camera," Opt. Lett. **36**(21), 4164–4166 (2011).
66. J. Arines and E. Acosta, "Adaptive astigmatism-correcting device for eyepieces," Optom. Vis. Sci. **88**(12), 1524–1528 (2011).
67. G. G. Stokes, *On a mode of measuring the astigmatism of a defective eye* in Mathematical and Physical Papers (Cambridge University, 1883), Vol. 2, pp. 172–175.
68. J. P. Foley and C. Campbell, "An optical device with variable astigmatic power," Optom. Vis. Sci. **76**(9), 664–667 (1999).
69. E. A. Villegas, E. Alcón, and P. Artal, "Optical quality of the eye in subjects with normal and excellent visual acuity," Invest. Ophthalmol. Vis. Sci. **49**(10), 4688–4696 (2008).
70. G. J. Wang, O. Pomerantzeff, and M. M. Pankratov, "Astigmatism of oblique incidence in the human model eye," Vision Res. **23**(10), 1079–1085 (1983).

Research Article | Vol. 27, No. 4 | 18 Feb 2019 | OPTICS EXPRESS 5669

Optics EXPRESS

71. P. Bon, G. Maucort, B. Wattellier, and S. Monneret, "Quadriwave lateral shearing interferometry for quantitative phase microscopy of living cells," Opt. Express **17**(15), 13080–13094 (2009).
72. X. Cui, J. Ren, G. J. Tearney, and C. Yang, "Wavefront image sensor chip," Opt. Express **18**(16), 16685–16701 (2010).
73. D. Fu, S. Oh, W. Choi, T. Yamauchi, A. Dorn, Z. Yaqoob, R. R. Dasari, and M. S. Feld, "Quantitative DIC microscopy using an off-axis self-interference approach." Opt. Lett. **35**(14), 2370–2372 (2010).
74. F. Merola, L. Miccio, M. Paturzo, A. Finizio, S. Grilli, and P. Ferraro, "Driving and analysis of micro-objects by digital holographic microscope in microfluidics," Opt. Lett. **36**(16), 3079–3081 (2011).
75. B. Kemper, A. Vollmer, C. E. Rommel, J. Schnekenburger, and G. von Bally, "Simplified approach for quantitative digital holographic phase contrast imaging of living cells," J. Biomed. Opt. **16**(2), 026014 (2011).
76. V. Chhaniwal, A. S. G. Singh, R. A. Leitgeb, B. Javidi, and A. Anand, "Quantitative phase-contrast imaging with compact digital holographic microscope employing Lloyd's mirror," Opt. Lett. **37**(24), 5127–5129 (2012).
77. A. S. G. Singh, A. Anand, R. A. Leitgeb, and B. Javidi, "Lateral shearing digital holographic imaging of small biological specimens," Opt. Express **20**(21), 23617–23622 (2012).
78. N. T. Shaked, "Quantitative phase microscopy of biological samples using a portable interferometer," Opt. Lett. **37**(11), 2016–2018 (2012).
79. N. T. Shaked, Y. Zhu, N. Badie, N. Bursac, and A. Wax, "Reflective interferometric chamber for quantitative phase imaging of biological sample dynamics," J. Biomed. Opt. **15**(3), 030503 (2010).
80. V. Mico, C. Ferreira, Z. Zalevsky, and J. García, "Spatially-multiplexed interferometric microscopy (SMIM): converting a standard microscope into a holographic one," Opt. Express **22**(12), 14929–14943 (2014).
81. S. Karepov, N. T. Shaked, and T. Ellenbogen, "Off-axis interferometer with adjustable fringe contrast based on polarization encoding," Opt. Lett. **40**(10), 2273–2276 (2015).
82. D. Roitshtain, N. A. Turko, B. Javidi, and N. T. Shaked, "Flipping interferometry and its application for quantitative phase microscopy in a micro-channel," Opt. Lett. **41**(10), 2354–2357 (2016).
83. J. A. Picazo-Bueno, Z. Zalevsky, J. García, C. Ferreira, and V. Micó, "Spatially multiplexed interferometric microscopy with partially coherent illumination," J. Biomed. Opt. **21**(10), 106007 (2016).
84. J. A. Picazo-Bueno, Z. Zalevsky, J. García, and V. Micó, "Superresolved spatially multiplexed interferometric microscopy," Opt. Lett. **42**(5), 927–930 (2017).
85. J. A. Picazo-Bueno, M. Trusiak, J. García, K. Patorski, and V. Micó, "Hilbert-Huang single-shot spatially multiplexed interferometric microscopy," Opt. Lett. **43**(5), 1007–1010 (2018).
86. P. Bon, G. Maucort, B. Wattellier, and S. Monneret, "Quadriwave lateral shearing interferometry for quantitative phase microscopy of living cells," Opt. Express **17**(15), 13080–13094 (2009).
87. T. Tahara, K. Ito, T. Kakue, M. Fujii, Y. Shimozato, Y. Awatsuji, K. Nishio, S. Ura, T. Kubota, and O. Matoba, "Parallel phase-shifting digital holographic microscopy," Biomed. Opt. Express **1**(2), 610–616 (2010).
88. B. Das, C. S. Yelleswarapu, and D. Rao, "Parallel-quadrature phase-shifting digital holographic microscopy using polarization beam splitter," Opt. Commun. **285**(24), 4954–5960 (2012).

Journal of Biomedical Optics

BiomedicalOptics.SPIEDigitalLibrary.org

Single-shot two-frame π-shifted spatially multiplexed interference phase microscopy

Maciej Trusiak
Jose-Angel Picazo-Bueno
Krzysztof Patorski
Piotr Zdańkowski
Vicente Mico

SPIE.

Maciej Trusiak, Jose-Angel Picazo-Bueno, Krzysztof Patorski, Piotr Zdańkowski, Vicente Mico, "Single-shot two-frame π-shifted spatially multiplexed interference phase microscopy," *J. Biomed. Opt.* **24**(9), 096004 (2019), doi: 10.1117/1.JBO.24.9.096004.

Journal of Biomedical Optics 24(9), 096004 (September 2019)

Single-shot two-frame π-shifted spatially multiplexed interference phase microscopy

Maciej Trusiak,[a,*] Jose-Angel Picazo-Bueno,[b] Krzysztof Patorski,[a] Piotr Zdańkowski,[a] and Vicente Mico[b,*]
[a]Warsaw University of Technology, Institute of Micromechanics and Photonics, Warsaw, Poland
[b]Universitat de Valencia, Departamento de Óptica y Optometría y Ciencias de la Visión, Burjassot, Spain

Abstract. Single-shot, two-frame, π-shifted spatially multiplexed interference microscopy (π-SMIM) is presented as an improvement to previous SMIM implementations, introducing a versatile, robust, fast, and accurate method for cumbersome, noisy, and low-contrast phase object analysis. The proposed π-SMIM equips a commercially available nonholographic microscope with a high-speed (video frame rate) enhanced quantitative phase imaging (QPI) capability by properly placing a beam-splitter in the microscope embodiment to simultaneously (in a single shot) record two holograms mutually phase shifted by π radians at the expense of reducing the field of view. Upon subsequent subtractive superimposition of holograms, a π-hologram is generated with reduced background and improved modulation of interference fringes. These features determine superior phase retrieval quality, obtained by employing the Hilbert spiral transform on the π-hologram, as compared with a single low-quality (low signal-to-noise ratio) hologram analysis. In addition, π-SMIM enables accurate *in-vivo* analysis of high dynamic range phase objects, otherwise measurable only in static regime using time-consuming phase-shifting. The technique has been validated utilizing a 20 × /0.46 NA objective in a regular Olympus BX-60 upright microscope for QPI of different lines of prostate cancer cells and flowing microbeads. [DOI: 10.1117/1.JBO.24.9.096004]

Keywords: digital holographic microscopy; interference microscopy; quantitative phase imaging; phase retrieval; fringe analysis.

Paper 190159R received May 15, 2019; accepted for publication Jul. 30, 2019; published online Sep. 14, 2019.

1 Introduction

Among a suite of modern microscopy techniques, quantitative phase imaging (QPI)[1–3] stands out as a vividly blossoming and extremely capable label-free approach. It provides a unique means for imaging cells and tissues, merging beneficial features established at the core of microscopy,[1] interferometry and holography,[4] and numerical computations. Using the refractive index as an intrinsic contrast agent,[5] QPI numerically converts the holographically encoded complex optical field of microobjects into a nanoscale-precise subcellular-specific 2-D/3-D/4-D map of the examined transparent specimen.[6,7] Impressive details can be imaged, e.g., via superresolution approaches,[8] even in live organisms, without severe photo-damage. Application-oriented QPI research provided recently outstanding solutions in numerous exciting biomedical fields, i.e., in neuroscience, methods such as digital holographic microscopy (DHM),[9] spatial light interference microscopy (SLIM),[10] and optical diffraction tomography (ODT);[11] in cell/tissue biology, ODT,[11] SLIM,[10] transport of intensity,[12] Fourier ptychography,[13] and quadriwave interferometry;[14] and in cancer diagnosis, DHM[15] and diffraction phase microscopy,[16,17] to name only some approaches. It is also worth showcasing the importance of in-flow quantitative phase measurements.[18,19]

The QPI setup stability and simplicity can be enhanced using common-path strategies,[20] while partial coherence may be employed to decrease speckle noise.[21] Among those methods, spatially multiplexed interferometric microscopy (SMIM) proposes a straightforward and low-cost way to convert a commercially available regular microscope into a holographic one with only minimal modifications.[22,23] SMIM is based on a common-path interferometric layout; the modifications consist of saving a clear region at the input plane for a reference beam, providing a coherent light source, and properly inserting diffraction grating. In this paper, we significantly advance this technique and propose an extremely robust and capable QPI method using a laser diode source, beam-splitter, and phase retrieval algorithm to upgrade a wide-field microscope into a versatile holographic one.

All QPI solutions are full-field optical techniques relying on the virtue of storing object information in an optical complex amplitude, which is subsequently encoded in a digital image. The characteristic quasi-periodic intensity pattern—the hologram (I)—is generated upon interference of object and reference beams, which are clearly distinguishable in coherent (holographic) coding. The hologram comprises a sum of three fundamental intensity components: background (incoherent sum of intensities of interfering beams I_1 and I_2), noise (uncorrelated and/or structured, N), and coherent interference fringes constituted by a cosine function modulated in phase (θ) and amplitude $[2(I_1I_2)^{1/2}]$:

$$I = I_1 + I_2 + 2\sqrt{I_1 I_2}\cos\theta + N. \quad (1)$$

Phase distribution (θ) is of interest and is represented as a local shape of the period and orientation variations of fringes. Therefore, an extremely important step of each full-field QPI method comprises the fringe pattern (hologram) phase demodulation understood as phase map decoding from the registered intensity distribution.

There are two fundamental QPI architectures with respect to the phase demodulation strategy employed: on-axis with temporal phase shifting-based phase demodulation[24] and off-axis with

*Address all correspondence to Maciej Trusiak, E-mail: m.trusiak@mchtr.pw.edu.pl; Vicente Mico, E-mail: vicente.mico@uv.es

Fourier transform (FT)-based phase retrieval.[25] The on/off axis term refers to the inclination angle between object and reference beams, which is significantly increased in the off-axis case to produce high spatial frequency carrier. Thus, it provides separation of the otherwise overlapped object terms and autocorrelation peak in the center of Fourier domain to facilitate spectral filtering. Both approaches are somewhat promoted and penalized: on-axis recording, despite being very accurate and well optimized in terms of the detector space-bandwidth product, has limited time resolution due to the need of phase-shifting sequence recording. The off-axis approach aided by the FT can quickly analyze dynamic events in a single-shot manner (phase is retrieved from a single hologram). However, it requires a sufficiently high hologram spatial carrier frequency limiting the space-bandwidth product and imposing constraints on phase details of imaged biostructures, as generally an object should be low pass banded with respect to the carrier frequency. Objects introducing strong phase shifts (high phase dynamic range) are therefore especially ponderous. It is worth emphasizing that third configuration emerged recently, namely the slightly off-axis regime. It attempts space-bandwidth product optimization by means of full spectral separation of conjugated object lobes, while leaving the autocorrelation term partially overlapped with information carrying terms.[26,28]

The recently proposed Hilbert–Huang single-shot SMIM (H2S2MIM) method[29] combines the advantages of the common-path SMIM layout with single frame hologram analysis using the Hilbert–Huang phase microscopy (H2PM) algorithm.[30] Together with superresolution technique,[26] they embody two main advancements of the classical SMIM method: single-shot operational principle even outside off-axis holographic recording regime[29] and the capability of overcome the field of view (FOV) restriction.[31] The H2PM works in two steps: (1) it filters out hologram background using the two-dimensional (2-D) empirical mode decomposition (EMD) and (2) performs phase demodulation of background-filtered hologram using Hilbert spiral transform (HST). The H2PM accepts a very wide range of holograms recorded in various architectures—from on-axis to off-axis with special emphasis on slightly off-axis regimes[26,28]—regardless of the local shape of interference fringes. It provides unique flexibility in terms of optical setup design and expands the suite of measurable objects into high phase dynamic range ones. Phase details can be successfully imaged under low carrier spatial frequency, and generally it enables accurate phase estimation of holograms with overlapped spectrum.[30] The Hilbert–Huang transform exhibits phase demodulation errors; however, in very challenging cases when high noise levels originated in a highly scattering sample it merged with low contrast of interference fringes caused by low coherence or mismatch in intensities or polarizations of interfering beams. These phenomena contribute to a significant decrease of the hologram signal-to-noise ratio (SNR) and preclude accurate, single-shot phase estimation of problematic yet interesting biosamples. Therefore, there is a need to fill this gap and enable accurate analysis of low signal-to-noise holograms recorded using the SMIM paradigm.

We propose a single-shot two-frame π-shifted spatially multiplexed interference microscopy (π-SMIM) to overcome the limitations imposed by highly scattering samples resulting in low SNR of recorded holograms. The π-SMIM adds high-speed (video framerate) accurate and robust QPI capability to a commercial nonholographic microscope with enhanced phase reconstruction by properly placing a beam-splitter to record in a single-shot two holograms mutually phase shifted by π radians. Although we have previously reported on a single-shot approach for QPI using a beam-splitter interferometric architecture,[32] the method here presented is conceptually different from the previous one in the following sense. The previous approach[32] was targeted to provide an external add-on module to be adapted into the exit port of a regular microscope in order to update it with coherence sensing capabilities. This external module is based on a beam-splitter cube interferometer working in slightly off-axis configuration, but the approach[32] does not imply internal modifications of the microscope as one needs in SMIM. As a consequence, the beam-splitter interferometer introduces a nonnegligible amount of astigmatism that must be compensated using a Stoke lens device, which is included in the add-on module itself. Here, the beam-splitter is inserted in the microscope embodiment [as the one-dimensional (1-D) diffraction grating in SMIM technique is inserted], that is, in the collimated beam light path meaning that no astigmatism is introduced, and no need for complex compensating devices is required. So, the technique reported in this paper is related with an SMIM improvement and cannot be packaged as an add-on module to be easily coupled in a conventional white-light microscope for upgrading it into holographic microscope for QPI. Moreover, the significant enhancement of phase demodulation efficiency is achieved using the two complementary hologram recording and subtraction schemes.

2 System Description

2.1 *Experimental Layout*

Figure 1 shows the optical implementation of the proposed π-SMIM method highlighting its working principle, with the main modifications depicted for clarity. Essentially, a fiber-coupled red diode laser (OSI Laser Diode, TCW RGBS-400R,

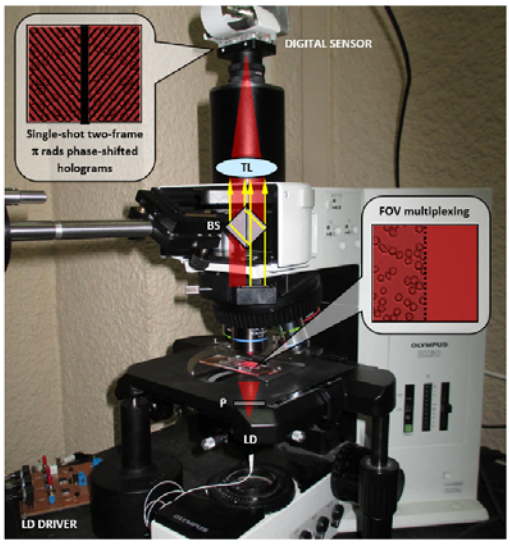

Fig. 1 Upright microscope updated with π-SMIM capability. TL, tube lens; BS, beam splitter; P, linear polarizer; LD, laser diode.

635 nm) replaces the white light illumination provided by the mercury lamp. Light passes through a linear polarizer (P) to adjust the intensities of both replicas provided by the BS. This is a critical point in the reconstruction process, since the more similar the fringe contrast of the two single-shot π-shifted holograms, the better the reconstructed phase image. The trinocular head of the microscope has been removed to avoid unwanted spurious reflections, so a tube lens (TL) has been added to maintain the infinity corrected imaging mode. The TL ($f' = 100$ mm) is just placed at the circular dovetail mount of the microscope trinocular port.

The BS (polarizing cube, 25.4 mm side) is inserted within the microscope embodiment into the collimated light path between the objective and TL. It is placed in a nonconventional way, that is, rotated 45 deg regarding the position for splitting an incoming beam into two orthogonally separated ones. In this position, it defines a common-path interferometric configuration providing two simultaneous slightly off-axis holograms with a π radians phase step between them.[32,34] This capability enables single-shot low-quality hologram phase demodulation at the expense of the FOV reduction. The BS is mounted onto a tilting platform including different screws for fine adjustment and alignment. Finally, a CMOS imaging device (Ximea MQ042MG-CM USB3.0) is placed at the microscope output's port for recording the π-SMIM holograms.

A number of dual-channel interference-based phase imaging techniques/setups were introduced in the literature.[35–40] They mainly differ in the optical configuration employed and strategy for phase retrieval. In Ref. 35, the off-axis configuration with low-coherence source and optical path difference minimization strategy was proposed. In Ref. 36, different off-axis configuration with beam-splitter for QPI was introduced. The authors of Ref. 37 report the use of Wollaston prism in an external module based on lateral phase shifting interferometer. The work in Ref. 38 extends concept of Ref. 37 by introducing a white-light, phase-shifting, polarization-driven standalone QPI module. The authors of Ref. 39 proposed to employ Wollaston prism and additional 4F imaging system and 1-D Hilbert transform for phase retrieval with rather obvious limitations (mainly scanning and loosing correlation between scans). The authors of Ref. 40 introduced off-axis configuration for QPI based on the retro reflectors. Although several dual-channel approaches were reported in the literature (i.e., Refs. 35–40), our proposed configuration is unique and novel in terms of inserting the BS into a regular biological microscope in its collimated beam path and enabling efficient phase demodulation in slightly off-axis[26–28] and quasi on-axis regimes. Experimental results introduced in Sec. 2.2 will corroborate this statement successfully.

2.2 *Algorithm Implementation*

Two recorded holograms constitute the two halves of the camera FOV and can be modeled as

$$I_R = I_1 + I_2 + 2\sqrt{I_1 I_2}\cos\theta + N, \tag{2}$$

$$I_L = I_1 + I_2 + 2\sqrt{I_1 I_2}\cos(\theta + \pi) + N, \tag{3}$$

where L denotes the left half and R denotes the right half of the hologram (see inset in Fig. 1). Upon subsequent subtractive superimposition of the left and right holograms (left and right half of the registered image), a π-hologram is generated with boosted SNR due to eliminated background and improved amplitude modulation of interference fringes. It can be modeled as

$$I_\pi = I_R - I_L = a + 4\sqrt{I_1 I_2}\cos\theta + N_{\mathrm{RL}}, \tag{4}$$

where a denotes π-hologram residual background term (in theoretically ideal case $a = 0$ as a consequence of identical background present in left and right holograms) and N_{RL} denotes π-hologram noise. A similar approach of data enhancement through two interferograms subtraction was reported to improve the amplitude demodulation process in interferometric full-field vibration studies[41] and for volumetric imaging using structured illumination microscopy and optical sectioning.[42] In this paper, we introduce two-frame scheme for phase map calculation improvement.

The phase demodulation is performed using the HST.[43] The analytic π-hologram (A_π) is calculated having its real part defined as π-hologram (I_π) and imaginary part as the HST of π-hologram designated as

$$\mathrm{HST}(I_\pi) = -i\exp(-i\beta)F^{-1}\left[\mathrm{SPFF}\left(4\sqrt{I_1 I_2}\cos\theta\right)\right], \tag{5}$$

$$A_\pi = I_\pi + i\mathrm{HST}(I_\pi), \tag{6}$$

where β is the local fringe orientation map,[43–45] SPF denotes spiral phase function, F and F^{-1} denote forward and inverse FT, respectively. The analytic π-hologram grants easy access to the phase map of interest

$$\theta = \mathrm{angle}(A_\pi) = a\tan\left[\frac{\mathrm{HST}(I_\pi)}{I_\pi}\right], \tag{7}$$

where the angle is a Matlab (MathWorks, Natick, Massachusetts) function computing the argument map of complex valued image. Phase unwrapping using the transport of intensity method[46] completes the phase demodulation path.

Prior to the subtraction of left and right holograms, it is highly recommended to numerically refine optically predefined alignment of both left and right holograms (find correct scale and rotation angle) using the feature matching function from the Matlab environment. To facilitate, the viewpoint on our strategy exemplifying left and right holograms are presented in Figs. 2(a) and 2(b), respectively. Holograms were recorded investigating prostate cancer cells from line LNCaP using the proposed π-SMIM method. The π-hologram is shown in Fig. 2(c). Some residual background (a) can be observed in Fig. 2(d) as a consequence of uneven background illumination in the FOV. We propose to decompose the π-hologram using the enhanced fast empirical mode decomposition (EFEMD)[47] like it is conducted in the first part of the H2PM for single hologram phase analysis.[29,30] Sum of first two modes is designated as the adaptively filtered π-hologram, whereas other decomposition components form the π-hologram background, Fig. 2(d), to be eliminated in filtering. Merging optically generated two holograms subtraction with numerically employed additional filtering a very robust π-SMIM phase retrieval scheme is composed.

From the computational load point of view, the demonstrated π-SMIM technique is the same as H2PM enabling complete phase demodulation under 1 s on a regular PC (CPU 2.6 GHz RAM 16 GB).

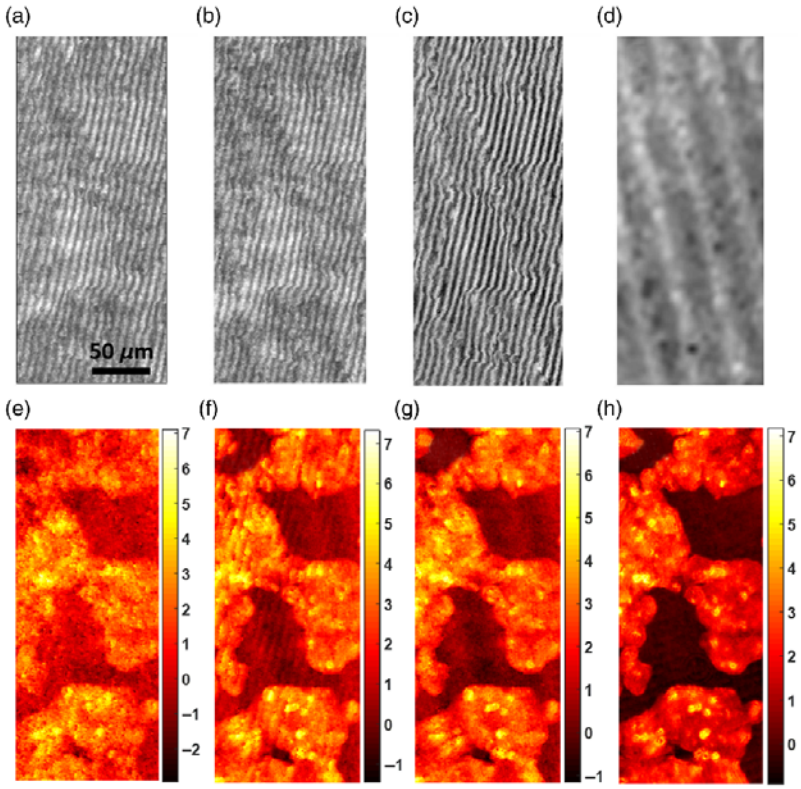

Fig. 2 Demonstration of the π-SMIM working principle: (a) left hologram, (b) right hologram, (c) π-hologram, (d) its background term. (e)–(h) Phase maps calculated using single hologram, π-hologram, filtered π-hologram, and phase-shifting sequence, respectively. Scale bars in (e)–(h) represent optical phase shift values in radians.

3 Experimental Results

3.1 *Validation of the π-SMIM Working Principle*

Experimental validation of the proposed approach has been divided into three sections. The aim of the first one is to provide a detailed implementation of the working principle and comparative analysis with other previously established techniques (recently established H2S2MIM and temporal phase-shifting approach).

Figure 2 shows the results considering prostate cancer cells. The cells were cultured in RPMI 1640 (GIBCO, Invitrogen, Life Technologies, California) medium with 10% fetal bovine serum, 100 U/ml Penicillin, and 0.1 μg/ml Streptomycin at standard cell culture conditions (37°C in 5% CO_2 in a humidified incubator). After the cells reach a confluent stage, they are released from the culture support and centrifuged. The supernatant fluid is discarded and cells are resuspended in a cytopreservative solution and mounted in a slide using the ThinPrep® 2000 system (Hologic, Marlborough, Massachusetts). The cells (LNCaP line) included in Fig. 2 are isolated from a needle aspiration biopsy of the left supraclavicular lymph node of a Caucasian male with confirmed diagnosis of metastatic carcinoma.

The π-hologram (partial) background rejection and (full) amplitude modulation amplification obtained upon subtractive superimposition of the two simultaneously recorded holograms [readily noticeable in Fig. 2(c) in comparison with Figs. 2(a) and 2(b)] are the main features determining superior quality of the phase retrieval using the π-hologram in comparison with single hologram analysis (right or left). This fact is corroborated by comparing four phase maps, Figs. 2(e)–2(h), obtained using different techniques.

The phase map obtained from just the left hologram is presented in Fig. 2(e) with general low quality and noisy appearance. The phase map calculated using the π-hologram is shown in Fig. 2(f). It compares favorably with single hologram phase map as it exhibits richer cellular details; however, the periodic artifact significantly deteriorating its quality can be observed. The origin of this artifact can be traced back to the uneven background of the π-hologram. After the EFEMD-based background correction [subtracting Fig. 2(d) from Fig. 2(c)] the retrieved phase map, Fig. 2(g), is now free of the periodic error. On the optical table, we assembled the Mach–Zehnder digital holographic microscope, performed reference measurement of the optical path delay introduced by studied sample and presented the "ground-truth" outcome in Fig. 2(h). Six phase-shifted

holograms were captured and the advanced iterative algorithm was employed for the reference phase map retrieval.[48] With established reference phase map, the root mean square errors for single hologram, π-hologram, and filtered π-hologram cases can be computed and rounded to 0.86, 0.56, and 0.52 rad, respectively. Assessing the retrieved phase quality, the RMS analysis quantitatively indicates the superiority of the proposed π-SMIM technique over single hologram H2S2MIM and highlights the importance of the residual background removal using the EFEMD-based additional filtering.

3.2 *Validation of the π-SMIM: Samples with Variable Size and Density*

In this section, phase objects with different size and density are investigated. For the experimental validation, two biosamples are considered: prostate cancer cells coming from a different cell line (PC-3 initiated from a bone metastasis of a grade IV prostatic adenocarcinoma from a Caucasian male) and dry red blood cells. The former introduces a different sample sizing while the latter is a dense sample with clustered degenerated cells. They often result in difficult shape of interference fringes [Figs. 3(a) and 3(d)] precluding their efficient single-frame phase demodulation using classical FT approach. The π-SMIM enables accurate *in vivo* analysis of those problematic specimens alleviating the problem of significant local fringe shape variation (overlapped spectrum) and very low SNR. High visual quality phase maps calculated using the π-SMIM and presented in Figs. 3(c) and 3(f) advocate its robustness and versatility analyzing complicated size-variable [PC-3, Fig. 3(c)] and clustered [dry red blood cells, Fig. 3(f)] biosamples. Subcellular resolution is to be highlighted, Fig. 3(c).

3.3 *Validation of the π-SMIM: Dynamic Samples*

Last but not least, Fig. 4 shows the π-SMIM capability to study transient events. Probably this is the most attractive capability of the proposed technique since it enables real-time analysis of very challenging dynamic samples. Several microbeads flowing in the water-filled microchamber were investigated. Figure 4(a) shows the exemplifying two-channel hologram and Fig. 4(b) shows the final retrieved 3-D phase map (Video 1) and corresponding with the rectangular black dashed ROI included in Fig. 4(a). As expected, the phase profile of the flowing microbeads is successfully retrieved using the proposed π-SMIM concept regardless the low SNR of left and right holograms. It was ensured by virtue of the π-hologram generation, Fig. 4(c), and its further analysis for phase demodulation. The problem of complicated closed fringes in bead-areas coming from overlapped spectrum produced in quasi on-axis configuration, Fig. 4(d), is also successfully surpassed using the proposed π-SMIM method. We would like to showcase at this point that proposed technique can work not only in slightly off-axis regime, where separation of conjugated object lobes in Fourier domain is fulfilled, but also in quasi on-axis configuration with overlapped spectrum of two conjugated terms. Results presented in Fig. 4 prove this statement.

4 Discussion

Two main novelties reported in this contribution are to be highlighted. Beam splitter cube is directly introduced here in a straightforward manner to the commercially available bright field microscope upgrading it to an interferometric one (having provided the coherent light source first)—this is the first time to the best of the authors knowledge that the beam splitter and

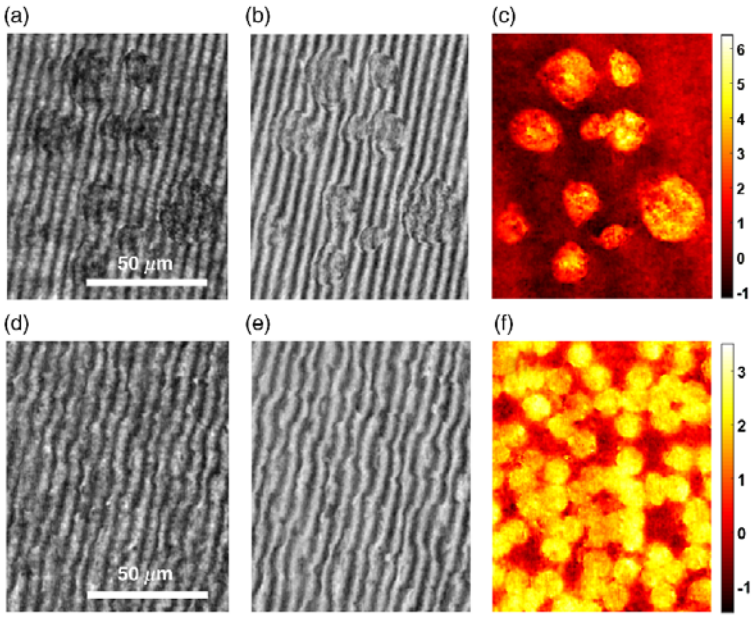

Fig. 3 (a)–(c) PC-3 cells and (d)–(f) red blood cells phase analysis for validation of the π-SMIM versatility and robustness: (a) and (d) holograms, (b) and (e) π-holograms, (c) and (f) phase maps. Scale bars in (c) and (f) represent optical phase values in radians.

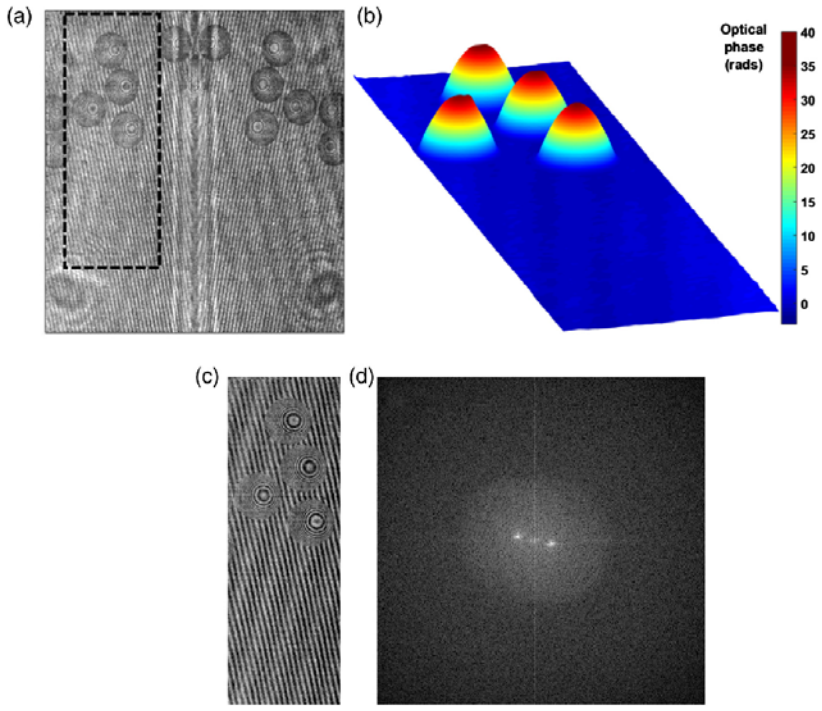

Fig. 4 Dynamic case: flowing beads phase analysis using the π-SMIM corroborating its high-speed imaging capabilities. (a) Example FOV, (b) successful phase reconstruction of the area within the black dashed rectangle (see Video 1 for full dynamic sequence), (c) π-hologram of selected region of interest, and (d) logarithmic modulus of the FT of the utilized π-hologram (overlapping conjugated complex amplitudes are clearly observable implying quasi on-axis regime). Three-dimensionally unwrapped phase profile of dynamic beads flowing into a water-filled counting chamber (Video 1, MOV, 1.15 MB [URL: https://doi.org/10.1117/1.JBO.24.9.096004.1]).

regular microscope are merged within the embodiment of the latter to enhance the capabilities of the microscope. Previous works in this line have reported on the use of diffraction gratings in SMIM technique (Refs. 22, 23, 29, and 31). The beam-splitter is working with the plane wave illumination, hence no additional spurious astigmatism is generated, as it was in the previous case in Ref. 32.

It is well-known that a tilted plane-parallel plate with collimated illumination (parallel rays) only causes a lateral displacement of rays without additional aberrations. But a tilted plane-parallel plate under nonparallel rays can cause a large amount of aberrations.[49,50] This was the case in Ref. 32 where convergent illumination passes the tilted BS cube; when examining the experimental images, it is evident it produced astigmatism.[32] Using the Stokes lens, an astigmatism of 0.25 diopters was measured which, according to theoretical calculations in the layout, corresponds with a Sturm interval of 3.5 mm, approximately. This is the separation between both focal lines due to the tilt of the BS. According to Eq. 4 in Ref. 51, the amount of astigmatism (A) introduced by a tilted plane-parallel plate when using convergent rays is given as

$$A = -\frac{t\theta^2(n^2-1)}{n^3}, \tag{8}$$

where t denotes the thickness of the plane-parallel plate (25.4 mm), θ is the rotation angle, and n is the glass index value at the illumination wavelength (1.52 assuming BK7 at 532 nm). Since $A \cong 3.5$ mm, the rotation angle of the BS cube can be computed from Eq. (8) yielding in $\theta \cong 35$ deg. This value is perfectly plausible since we started from an initial position where the BS was rotated 45 deg and then applied a small rotation to implement a slightly off-axis configuration. So, this quantitative analysis seems reasonable.

Nevertheless, and in order to qualitatively validate that the proposed approach does not generate additional spurious astigmatism due to the BS positioning, Fig. 5 includes a comparison between the intensity images produced by the former layout[32] and the actual one. Figure 5(a) presents the image produced without holographic recording and when no Stokes lens is considered in the layout of Ref. 32. Since the BS was placed in the convergent light path between the TL and the digital sensor, a non-negligible amount of astigmatism causes horizontal defocus in the recorded image. However, the BS is inserted in the collimated light path in the actual layout, leaving the system free of astigmatism. Figure 5(b) shows an intensity image free of astigmatism.

Second novelty is connected with the enhanced numerical phase retrieval scheme. The HST is applied for the phase

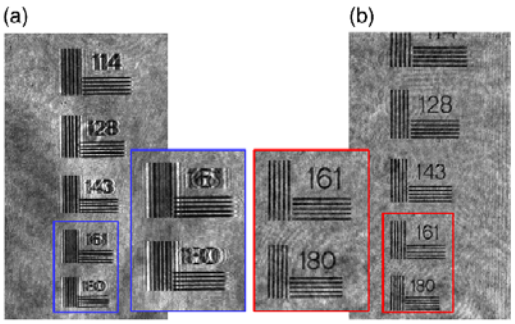

Fig. 5 Comparison between former[32] and actual layouts highlighting astigmatism avoidance: (a) image obtained with previous layout[32] and (b) image provided by the proposed layout.

demodulation of the π-hologram. Novelty resides in expanding the range of phase-objects to be examined by the HST. Employing the π-hologram generation strategy allows for analyzing phase maps otherwise encoded in cumbersome holograms of very low SNRs. Low SNR is understood here as combination of high noise, strong out of focus background and low contrast possibly caused by polarization, intensity or coherence mismatch. It is worth emphasizing that proposed π-SMIM technique exhibits the attractive ability to study in real-time dynamic phase objects with strong local phase variations (i.e., closed fringes in microbead area). Moreover, it provides an efficient means to demodulate holograms with low carrier frequency recorded in configurations ranging from quasi off-axis through slightly off-axis up to quasi on-axis architectures.

It is worth emphasizing that interferograms/holograms presented in Figs. 2–4 cannot be successfully analyzed using the FT due to rich spectrum versus too low carrier frequency, see Fig. 4(d) as an exemplifying quasi on-axis spectrum. In Ref. 32, the add-on module was proposed offering more room for appropriate data recording—the FT-based phase demodulation could be therefore possibly applied tilting the beam-splitter to create relatively high carrier frequency. The upper limit on carrier frequency is related also to the temporal coherence of the light source and utilizing broader spectra, i.e., SLDs, one may not be able to generate interference fringes in a large tilt regime. Additionally, in some cases of high dynamic range phase-objects (of rich spectrum), the FT method exhibits too limited bandwidth to provide efficient phase demodulation even with high carrier frequency employed. This manifests in partial overlapping of two information lobes (complex apertures) and autocorrelation term in Fourier domain in so-called slightly off-axis regime. In Ref. 32, it was proposed to subtract two BS-generated holograms removing autocorrelation term therefore eliminating described cumbersome overlap. This way FT phase demodulation could be introduced in Ref. 32 to a slightly off-axis regime once the central spectral term is removed. But the FT cannot be applied to the quasi on-axis case when the two complex apertures overlap due to a low carrier frequency; see, for example, the case studied in Fig. 4. This can happen while approaching the on-axis interferometric configuration or increasing the dynamic range of object introduced phase change. Dynamic range of phase increases when one is analyzing optically denser and richer structures or physically thicker ones (or both), e.g., microbeads in Fig. 4.

By employing beam-splitter, proposed biomedical QPI π-SMIM microscope generates two holograms shifted by π radians in a single shot. The holograms are in turn subtracted creating background-reduced and amplitude-enhanced differential hologram, so-called π-hologram. It is worth to highlight that this two-channel subtractive concept can be naturally used to enhance phase demodulation in full-field interferometric studies of technical objects, i.e., testing of MEMS/MOEMS (microlenses, micromembranes, etc.) and optical elements. Showcased versatility makes our approach scalable.

5 Conclusions

In this paper, we have proposed a new single-shot two-frame π-SMIM technique for upgrading a regular microscope into a versatile interference-based real-time phase imager with the ability to accurately study cumbersome micro-objects encoded in very low quality holograms (low carrier frequency, strong background and noise, low contrast, locally variable fringe shape, etc.). The π-SMIM hologram enhancement is conducted upon subtraction of two simultaneously recorded interference patterns generated by the beam-splitter at the expanse of FOV reduction. Robust phase retrieval is performed combining 2-D EMD numerical filtering and HST hologram demodulation. Unique features of the presented method were corroborated by successfully analyzing static (prostate cancer and red blood cells) and dynamic (flowing microbeads) highly scattering microsamples—quantitative evaluation was presented employing phase-shifting DHM as a reference method. As main outcome, π-SMIM enables accurate *in-vivo* analysis of noisy low-contrast high dynamic range phase objects, otherwise measurable only in static regimes using time-consuming phase-shifting.

Disclosures

The authors declare that there are no conflicts of interest related to this article.

Acknowledgments

This work has been partially funded by the National Science Center Poland (2017/25/B/ST7/02049), Faculty of Mechatronics Warsaw University of Technology statutory funds, Polish National Agency for Academic Exchange (PPN/BEK/2018/1/00511), and by the Spanish Ministerio de Economía, Industria y Competitividad Fondo Europeo de Desarrollo Regional (FIS2017-89748-P).

References

1. Y. Park, C. Depeursinge, and G. Popescu, "Quantitative phase imaging in biomedicine," *Nat. Photonics* **12**, 578–589 (2018).
2. G. Popescu, *Quantitative Phase Imaging of Cells and Tissues*, McGraw-Hill, New York (2011).
3. N. T. Shaked, Z. Zalevsky, and L. L. Satterwhite, *Biomedical Optical Phase Microscopy and Nanoscopy*, Academic Press, Oxford (2012).
4. D. Gabor, "A new microscopic principle," *Nature* **161**, 777–778 (1948).
5. F. Zernike, "How I discovered phase contrast," *Science* **121**, 345–349 (1955).
6. E. Cuche, F. Bevilacqua, and C. Depeursinge, "Digital holography for quantitative phase-contrast imaging," *Opt. Lett.* **24**, 291–293 (1999).
7. B. Kemper and G. von Bally, "Digital holographic microscopy for live cell applications and technical inspection," *Appl. Opt.* **47**, A52–A61 (2008).
8. Y. Cotte et al., "Marker-free phase nanoscopy," *Nat. Photonics* **7**, 113–117 (2013).

9. P. Marquet et al., "Digital holographic microscopy: a noninvasive contrast imaging technique allowing quantitative visualization of living cells with subwavelength axial accuracy," *Opt. Lett.* **30**, 468–470 (2005).
10. Z. Wang et al., "Spatial light interference microscopy (SLIM)," *Opt. Express* **19**, 1016–1026 (2011).
11. W. Choi et al., "Tomographic phase microscopy," *Nat. Methods* **4**, 717–719 (2007).
12. D. Paganin and K. A. Nugent, "Noninterferometric phase imaging with partially coherent light," *Phys. Rev. Lett.* **80**, 2586–2589 (1998).
13. J. Sun et al., "Single-shot quantitative phase microscopy based on color-multiplexed Fourier ptychography," *Opt. Lett.* **43**, 3365–3368 (2018).
14. P. Bon et al., "Quadriwave lateral shearing interferometry for quantitative phase microscopy of living cells," *Opt. Express* **17**, 13080–13094 (2009).
15. B. Kemper et al., "Investigation of living pancreas tumor cells by digital holographic microscopy," *J. Biomed. Opt.* **11**, 034005 (2006).
16. B. Bhaduri et al., "Diffraction phase microscopy: principles and applications in materials and life sciences," *Adv. Opt. Photonics* **6**, 57–119 (2014).
17. S. Uttam et al., "Early prediction of cancer progression by depth-resolved nanoscale mapping of nuclear architecture from unstained tissue specimens," *Cancer Res.* **75**, 4718–4727 (2015).
18. F. Merola et al., "Tomographic flow cytometry by digital holography," *Light Sci. Appl.* **6**, e16241 (2017).
19. V. Bianco et al., "Optofluidic holographic microscopy with custom field of view (FoV) using a linear array detector," *Lab Chip* **15**, 2117–2124 (2015).
20. V. Mico, Z. Zalevsky, and J. García, "Common-path phase-shifting digital holographic microscopy: a way to quantitative phase imaging and superresolution," *Opt. Commun.* **281**, 4273–4281 (2008).
21. J. M. Soto, J. A. Rodrigo, and T. Alieva, "Label-free quantitative 3D tomographic imaging for partially coherent light microscopy," *Opt. Express* **25**, 15699–15712 (2017).
22. V. Mico et al., "Spatially-multiplexed interferometric microscopy (SMIM): converting a standard microscope into a holographic one," *Opt. Express* **22**, 14929–14943 (2014).
23. J. A. Picazo-Bueno et al., "Spatially multiplexed interferometric microscopy with partially coherent illumination," *J. Biomed. Opt.* **21**, 106007 (2016).
24. K. Creath, "Phase-measurement interferometry techniques," *Prog. Opt.* **26**, 349–393 (1988).
25. M. Takeda, H. Ina, and S. Kobayashi, "Fourier-transform method of fringe-pattern analysis for computer-based topography and interferometry," *J. Opt. Soc. Am.* **72**, 156–160 (1982).
26. T. Ikeda et al., "Hilbert phase microscopy for investigating fast dynamics in transparent systems," *Opt. Lett.* **30**, 1165–1167 (2005).
27. N. T. Shaked et al., "Two-step-only phase-shifting interferometry with optimized detector bandwidth for microscopy of live cells," *Opt. Express* **17**, 15585–15591 (2009).
28. L. Xue et al., "Single-shot slightly-off-axis interferometry based Hilbert phase microscopy of red blood cells," *Biomed. Opt. Express* **2**, 987–995 (2011).
29. J. A. Picazo-Bueno et al., "Hilbert-Huang single-shot spatially multiplexed interferometric microscopy," *Opt. Lett.* **43**, 1007–1010 (2018).
30. M. Trusiak et al., "Quantitative phase imaging by single-shot Hilbert-Huang phase microscopy," *Opt. Lett.* **41**, 4344–4347 (2016).
31. J. A. Picazo-Bueno et al., "Superresolved spatially multiplexed interferometric microscopy," *Opt. Lett.* **42**, 927–930 (2017).
32. J. A. Picazo-Bueno, M. Trusiak, and V. Micó, "Single-shot slightly off-axis digital holographic microscopy with add-on module based on beamsplitter cube," *Opt. Express* **27**, 5655–5669 (2019).
33. J. A. Ferrari and E. M. Frins, "Single-element interferometer," *Opt. Commun.* **279**, 235–239 (2007).
34. P. Gao et al., "Parallel two-step phase-shifting microscopic interferometry based on a cube beamsplitter," *Opt. Commun.* **284**, 4136–4140 (2011).
35. H. Gabai and N. T. Shaked, "Dual-channel low-coherence interferometry and its application to quantitative phase imaging of fingerprints," *Opt. Express* **20**, 26906–26912 (2012).
36. H. Gabai et al., "Continuous wide-field characterization of drug release from skin substitute using off-axis interferometry," *Opt. Lett.* **38**, 3017–3020 (2013).
37. K. Lee and Y. Park, "Quantitative phase imaging unit," *Opt. Lett.* **39**, 3630–3633 (2014).
38. Y. Baek et al., "White-light quantitative phase imaging unit," *Opt. Express* **24**, 9308–9315 (2016).
39. N. T. Shaked, M. T. Rinehart, and A. Wax, "Dual-interference-channel quantitative-phase microscopy of live cell dynamics," *Opt. Lett.* **34**, 767–769 (2009).
40. P. Girshovitz and N. T. Shaked, "Compact and portable low-coherence interferometer with off-axis geometry for quantitative phase microscopy and nanoscopy," *Opt. Express* **21**, 5701–5714 (2013).
41. K. Patorski and M. Trusiak, "Highly contrasted Bessel fringe minima visualization for time-averaged vibration profilometry using Hilbert transform two-frame processing," *Opt. Express* **21**, 16863–16881 (2013).
42. K. Patorski, M. Trusiak, and T. Tkaczyk, "Optically-sectioned two-shot structured illumination microscopy with Hilbert–Huang processing," *Opt. Express* **22**, 9517–9527 (2014).
43. K. G. Larkin, D. J. Bone, and M. A. Oldfield, "Natural demodulation of two-dimensional fringe patterns. I. General background of the spiral phase quadrature transform," *J. Opt. Soc. Am. A* **18**, 1862–1870 (2001).
44. X. Yang, Q. Yu, and S. Fu, "A combined method for obtaining fringe orientations of ESPI," *Opt. Commun.* **273**, 60–66 (2007).
45. M. Trusiak, Ł. Służewski, and K. Patorski, "Single shot fringe pattern phase demodulation using Hilbert–Huang transform aided by the principal component analysis," *Opt. Express* **24**, 4221–4238 (2016).
46. J. Martinez-Carranza, K. Falaggis, and T. Kozacki, "Fast and accurate phase-unwrapping algorithm based on the transport of intensity equation," *Appl. Opt.* **56**, 7079–7088 (2017).
47. M. Trusiak, M. Wielgus, and K. Patorski, "Advanced processing of optical fringe patterns by automated selective reconstruction and enhanced fast empirical mode decomposition," *Opt. Lasers Eng.* **52**, 230–240 (2014).
48. Z. Wang and B. Han, "Advanced iterative algorithm for phase extraction of randomly phase-shifted interferograms," *Opt. Lett.* **29**, 1671–1673 (2004).
49. M. A. Habegger, "Astigmatism in light-deflector elements," *J. Opt. Soc. Am.* **60**, 326–331 (1970).
50. M. C. Simon, "Image formation through monoaxial plane-parallel plates," *Appl. Opt.* **27**, 4176–4182 (1988).
51. X. Zhong et al., "Aberrations correction of tilted plane-parallel plate in convergent rays," *Appl. Opt.* **54**, 1758–1764 (2015).

Biographies of the authors are not available.

PARTE III

RESUMEN DE LA TESIS

1. Introducción: microscopía holográfica digital aplicada a la formación de imágenes cuantitativas de fase

La capacidad de visualizar y analizar objetos transparentes de tamaño micrométrico de manera no invasiva ha sido uno de los retos principales de la *microscopía óptica* a lo largo del siglo XX. Para ello, se desarrollaron diversas técnicas de microscopía que convertían pequeñas diferencias de fase, inducidas por las variaciones en el índice de refracción de los objetos, en variaciones de intensidad, haciendo estos objetos visibles a simple vista. Entre todas las técnicas que se desarrollaron para este fin, destacan la *microscopía de contraste de fase* inventada por Zernike [Zernike-1942A, Zernike-1942B], y la *microscopía de contraste diferencial interferencial* de Nomarski [Nomarski-1952, Nomarski-1960].

Sin embargo, estas técnicas de microscopía solamente proporcionan información cualitativa del objeto, por lo que su análisis se limita a la simple visualización. No obstante, recientemente se han realizado diversos esfuerzos para lograr un análisis cuantitativo de los objetos mediante la modificación de estas técnicas [Gao-2011A, King-2008, Fu-2010]. A pesar de ello, estas técnicas requieren del empleo de elementos ópticos muy específicos que son muy delicados y costosos, cuya alineación es complicada, y en las que la obtención de información cuantitativa de fase no siempre es trivial. Por el contrario, existen otras técnicas de microscopía basadas en la *interferometría*, que proporcionan información cuantitativa de fase de una manera más sencilla y directa. Quizás la técnica por excelencia de este tipo de técnicas sea la *microscopía holográfica digital*.

La *microscopía holográfica digital* se basa en la combinación de *holografía digital* y *microscopía óptica*, y es una técnica que proporciona información cuantitativa de fase de manera no invasiva (sin tinciones), a tiempo real (una sola captura), sin contacto (sin necesidad de elementos que estén en contacto con el objeto), a campo completo (sin necesidad de escaneado) y estática (sin necesidad de elementos ópticos móviles). De esta manera, la *microscopía holográfica digital* permite el análisis cuantitativo de estructuras y procesos dinámicos que ocurren a nivel micrométrico y nanométrico mediante la obtención directa de la distribución de la amplitud compleja del campo eléctrico transmitido o reflejado por la muestra. La distribución de fase presente en esta amplitud compleja contiene información muy valiosa del objeto como puede ser su índice de refracción o su grosor. En el caso particular del análisis celular, esta información está relacionada con propiedades fundamentales como pueden ser la densidad física o la concentración química. Por tanto, esta técnica de microscopía puede ser muy útil para analizar ciertos tipos de procesos celulares a tiempo real y sin alterar sus condiciones naturales. La Figura 1

incluye un ejemplo de una imagen cuantitativa de fase de una muestra celular lograda mediante la *microscopía holográfica digital*, obtenida durante la tesis.

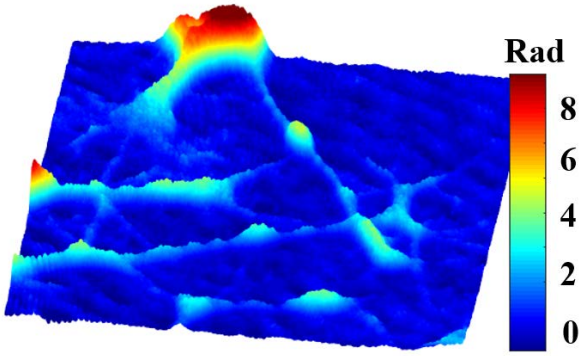

Figura 1. Perspectiva tridimensional de una imagen cuantitativa de fase de una muestra de neuronas del hipocampo obtenida mediante *microscopía holográfica digital*.

Por todo esto, el microscopio holográfico digital se ha convertido en un instrumento de microscopía utilizado en diversos campos del conocimiento como pueden ser la medicina, la biofotónica, la biología, o la biofísica, entre muchos otros. Entre todas aplicaciones al campo de la biología celular destacan: la monitorización y el análisis tridimensional de migraciones celulares [Dubois-2006B, Mann-2006, Daneshpanah-2007, Sun-2008, Choi-2009, Langeha-2009, Javidi-2010, Memmolo-2012, Merola-2012], el seguimiento cuatridimensional del movimiento de nanopartículas [Xu-2003, Antkowiak-2008, Warnasoo-2010], el contaje, registro y clasificación automático celular [Moon-2007, Mölder-2008, Seo-2010, Anand-2011, Liu-2011, Memmolo-2011, Mihailescu-2011, Moon-2012, Yi-2013], la caracterización de índices de refracción [Rappaz-2005, Lin-2010, Wang-2012], o el análisis y la manipulación de propiedades biomecánicas [DaneshPanah-2010, Cardenas-2011, Esseling-2012, Kemper-2013]. Por todo esto, la *microscopía holográfica digital* aplicada a la obtención de información cuantitativa de fase puede ser muy atractiva en áreas del conocimiento muy importantes como la investigación contra el cáncer [Mann-2005, Janeckova-2009, Wang-2010] o la reproducción asistida [Crha-2011, Memmolo-2011, Merola-2013].

2. Microscopía interferométrica por multiplexado espacial

En los últimos años se han realizado varios esfuerzos por desarrollar nuevas técnicas de *microscopía holográfica digital* con capacidades mejoradas en cuanto a la precisión, robustez, versatilidad, simplicidad y bajo coste [Bon-2009, Tearney-2010, Fu-2010, Merola-2011, Kemper-2011, Chhaniwal-2012, Singh-2012, Shaked-2012, Girshovitz-2013, Guo-2013, Bhaduri-2014, Karepov-2015, Roitshtain-2016, Yang-2016]. A tal efecto, se han desarrollado numerosos métodos para dotar de propiedades

holográficas a microscopios convencionales [Kemper-2008, Bon-2009, Cui-2010]. En consonancia con estos métodos, la *microscopía interferométrica por multiplexado espacial* o *SMIM* (del inglés Spatially Multiplexed Interferometric Microscopy) se presenta como una técnica estable, sencilla y económica de equipar un microscopio convencional de campo claro con propiedades holográficas [Micó-2014].

El principal objetivo de la técnica *SMIM* consiste en la implementación de una arquitectura interferométrica en el seno de un microscopio regular para la obtención de imágenes cuantitativas de fase mediante la técnica de *microscopía holográfica digital*. Para lograr esto, la técnica introduce unas sencillas modificaciones en el cuerpo del microscopio que hacen posible el registro holográfico. Estas modificaciones están encauzadas a la implementación de un interferómetro de camino común, empleando una estrategia de multiplexado espacial del plano objeto para la generación del haz de referencia.

Para ilustrar mejor los cambios introducidos en el microscopio por esta técnica, se ha incluido la Figura 2. Comencemos por considerar un microscopio regular cuyo esquema óptico y trazado de rayos se muestran en la Figura 2 (a), donde también se han señalado sus principales componentes ópticos. Siguiendo el esquema propuesto, una lámpara halógena ilumina el plano objeto en transmisión, donde se encuentra la muestra bajo análisis. A continuación, la luz difractada por el objeto es recogida por un objetivo de corrección infinita el cual, junto con una lente de tubo, forman una imagen del objeto en el plano imagen, donde se coloca un sensor digital para su registro. Así pues, el detector registra una imagen de intensidad del objeto, de modo que no se puede extraer información cuantitativa de fase a partir de ella.

Ahora bien, la técnica *SMIM* introduce tres sencillos cambios que dotan al microscopio de características holográficas [ver Figura 2 (b)]. Por un lado, la lámpara halógena, que proporciona iluminación incoherente, es reemplazada por una fuente de luz coherente (o parcialmente coherente) y con emisión divergente. Ejemplos de fuentes luminosas empleadas son los diodos láser o los diodos superluminiscentes. Por otro lado, el plano objeto se multiplexa espacialmente, esto es, se divide en varias regiones de igual tamaño, generalmente dos o tres. Suponiendo la situación en la que el plano objeto se divide en dos regiones, una de estas contendrá el objeto bajo análisis (denominada región objeto), mientras que la otra será un área clara, transparente, sin objeto, por la que viaja el haz incidente de iluminación sin sufrir modificación alguna, de manera que esta parte del haz puede considerarse como haz de referencia (denominada región referencia). En esta situación, ambos haces viajan en paralelo a través de los mismos componentes ópticos, pero sin interferir entre ellos, con lo que el microscopio se comportará como un microscopio regular que trabaja bajo iluminación coherente, pero cuyo campo de visión ha sido reducido a la mitad. Cabe destacar, no obstante, que esta reducción del campo de visión útil es la principal desventaja que presenta la técnica *SMIM*.

Finalmente, para permitir un registro holográfico, se inserta un elemento óptico que sea capaz de combinar espacialmente ambos haces. Este elemento puede ser una red de difracción o un cubo divisor de haz, entre otros. Supongamos que el elemento óptico introducido es una red de difracción de tipo sinusoidal [ver Figura 2 (b)]. Esta red producirá tres réplicas idénticas, salvo en intensidad, del haz incidente propagándose a lo largo de tres direcciones distintas, en función de la frecuencia espacial de la red. Una de ellas viajará siguiendo la dirección del haz incidente (orden 0 de difracción), mientras que las otras dos se propagarán en direcciones distintas formando un cierto ángulo con respecto al orden 0 (órdenes ±1 de difracción). El ángulo de propagación de estos haces está directamente relacionado con la frecuencia espacial de la red de difracción. De esta manera, es posible seleccionar una red de difracción con una frecuencia espacial tal que permita generar una superposición de estas réplicas adecuada en el plano imagen que permita un registro holográfico. Puesto que para la recuperación de fase es preciso la interferencia entre los haces objeto y referencia, la red de difracción debe ser escogida de tal manera que las imágenes generadas en el plano imagen por los distintos órdenes de difracción estén lateralmente separadas una distancia igual a la mitad del campo de visión total. Una frecuencia espacial demasiado grande evitará el solapamiento entre haces, mientras que una frecuencia demasiado pequeña hará que las regiones objeto de los distintos órdenes de difracción solapen entre sí. Por consiguiente, la configuración idónea es aquella en la que las regiones objeto, procedentes de las distintas replicas generadas por la red de difracción, interfieren con las regiones referencia procedentes de las réplicas contiguas, generando así dos interferogramas [ver Figura 2 (b)]. De estos interferogramas, uno de ellos se empleará para la recuperación de fase. Más concretamente, el patrón de interferencias seleccionado será aquél formado por la superposición coherente de la región objeto procedente del orden de difracción 0 con la región referencia del haz procedente del orden -1. Cabe destacar también, por otro lado, que tanto la posición axial de la red como su frecuencia espacial son determinantes a la hora de definir la configuración holográfica en el plano imagen, pasando de una configuración *en eje* cuando la red se inserta en o cerca del plano de Fourier del objetivo, a una configuración *fuera de eje* en los casos en los que la red se coloca lo suficientemente alejada de este plano.

Así pues, con estas tres modificaciones, la técnica *SMIM* implementa un interferómetro de camino común estable, simple y económico, capaz de generar interferogramas aptos para su registro y posterior obtención de imágenes cuantitativas de fase.

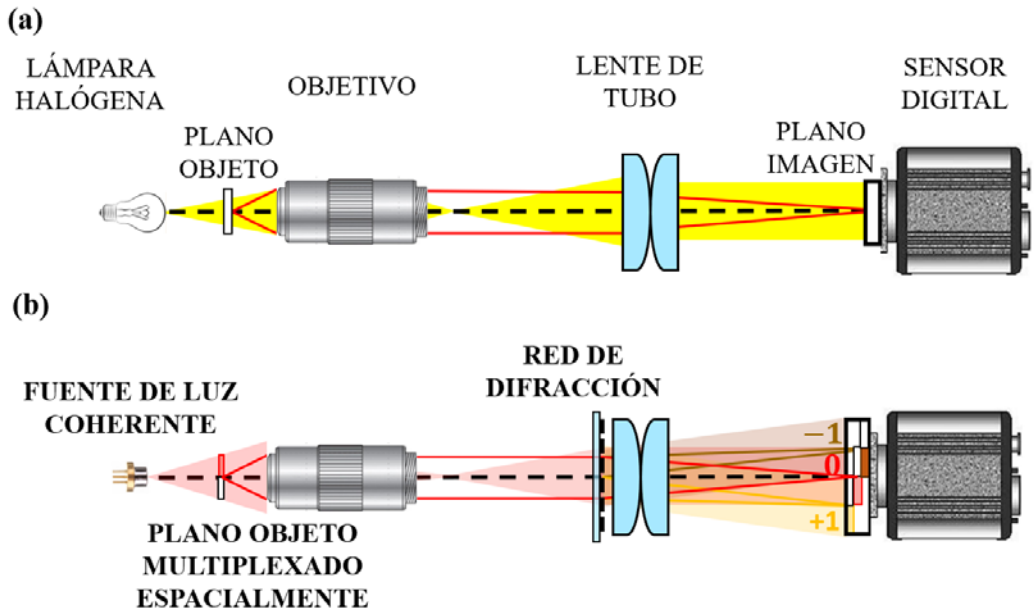

Figura 2. Implementación de la técnica *SMIM*, en la que se muestran los esquemas ópticos de un microscopio regular de campo claro antes (a) y después (b) de implementar la técnica. En (a) se han identificado los distintos elementos ópticos y los planos conjugados objeto e imagen del microscopio, mientras que en (b) se han remarcado en negrita los cambios introducidos por la técnica.

3. Objetivos de la tesis

El objetivo principal de la tesis ha sido el desarrollo y la mejora de la técnica de microscopía óptica denominada *microscopía interferométrica por multiplexado espacial* o *SMIM* (del inglés Spatially Multiplexed Interferometric Microscopy) que, tal y como hemos comentado anteriormente, implementa una serie de modificaciones sencillas al cuerpo de un microscopio convencional de campo claro para equiparlo con propiedades holográficas. De esta manera, el microscopio es capaz de obtener no sólo la información de intensidad, sino también la información de fase de la amplitud compleja del campo eléctrico de la onda difractada por el objeto bajo análisis.

Esta técnica de microscopía fue inicialmente propuesta por Micó y colaboradores [Micó-2006B, Micó-2008, Micó-2009, Micó-2014]. Los primeros esfuerzos en esta línea fueron llevados a cabo en mesa óptica [Micó-2006B, Micó-2008, Micó-2009], mientras que pocos años después realizaron la primera validación experimental de esta técnica en el cuerpo de un microscopio regular de campo claro [Micó-2014]. Siguiendo esta línea de investigación, la presente tesis doctoral ha centrado sus esfuerzos en mejorar esta técnica mediante el desarrollo y la implementación de numerosas estrategias enfocadas tanto a la mejora de la calidad de las imágenes cuantitativas de fase obtenidas como a la posibilidad de analizar procesos dinámicos.

Así pues, la mejora de la calidad de las imágenes recuperadas de fase ha sido llevada a cabo, por un lado, mediante la reducción de ruido coherente presente en estas y el rediseño del multiplexado espacial del campo de visión que permite obtener una mayor región de análisis [Picazo-Bueno-2016] y, por otro lado, mediante la aplicación de técnicas de superresolución basadas en la generación de una apertura sintética que han permitido compensar el efecto de la reducción del campo de visión necesario para la aplicación de la técnica mediante un incremento en la resolución espacial de las imágenes de fase obtenidas [Picazo-Bueno-2017].

Posteriormente, se ha implementado un sistema holográfico capaz de obtener información cuantitativa de fase en configuraciones de transmisión y reflexión, incrementando por tanto la cantidad de objetos susceptibles de ser analizados por esta técnica [Picazo-Bueno-2019A]. Además, ambos modos de formación de imagen han sido simultáneamente empleados para la obtención del índice de refracción de objetos homogéneos a partir de la información de fase obtenida por ambas modalidades.

Finalmente, se han desarrollado diversas estrategias para permitir el análisis de procesos dinámicos. En primer lugar, se ha implementado un método de recuperación de fase que se basa en la transformada de Hilbert-Huang, gracias a la cual se ha podido extraer información cuantitativa de fase a partir de una sola captura en una configuración holográfica *ligeramente fuera de eje* [Picazo-Bueno-2018B]. Por otro lado, se han desarrollado distintos dispositivos interferométricos basados en cubos divisores de haz que han permitido el análisis dinámico mediante la aplicación de métodos de sustracción de imágenes y posterior empleo del método de filtrado en Fourier [Picazo-Bueno-2019B], en caso de definir una configuración holográfica *ligeramente fuera de eje*, o de la transformada de Hilbert-Huang [Trusiak-2019], en caso de presentar una configuración *cuasi en eje*.

4. Metodología y resultados experimentales

A la vista de los objetivos propuestos durante la presente tesis doctoral, se han realizado una serie de validaciones experimentales que han servido para demostrar la viabilidad de los métodos de mejora propuestos en la técnica *SMIM*. Adicionalmente, con el fin de conseguir un mejor entendimiento y sentar las bases no solo teóricas sino también experimentales en *microscopía holográfica digital* (al fin y al cabo *SMIM* es una implementación específica de *microscopía holográfica digital*), se presenta un experimento inicial en el que se ha diseñado una plataforma formadora de imágenes multimodal que proporciona simultáneamente dos tipos de imágenes: por un lado, la plataforma genera imágenes de intensidad convencionales de campo claro mediante la iluminación incoherente del objeto por transmisión y, por otro lado, es capaz de registrar digitalmente hologramas y obtener información cuantitativa de fase a partir de estos [Picazo-Bueno-2018A].

Para ello, se ha implementado un sistema óptico cuyos elementos ópticos pueden englobarse en dos partes en función del propósito que tienen: los elementos formadores de imagen (principalmente un objetivo de inmersión en agua y una lente de tubo), comunes para ambas modalidades de imagen y, por otro lado, los elementos que conforman la disposición interferométrica situada detrás de la lente de tubo. Estos elementos (cubos divisores de haz, espejos, lentes convergentes, agujero estenopeico) están dispuestos de tal manera que generan una configuración interferométrica tipo Mach-Zehnder que produce un patrón de interferencias entre el haz imagen y un haz de referencia sintetizado a partir del haz imagen en el seno del interferómetro. Un registro holográfico en configuración *fuera de eje* ha permitido la aplicación de técnicas de filtrado en Fourier para la recuperación de fase, permitiendo así una obtención de la información de fase a partir de una sola captura, abriendo por tanto la posibilidad al análisis de procesos dinámicos.

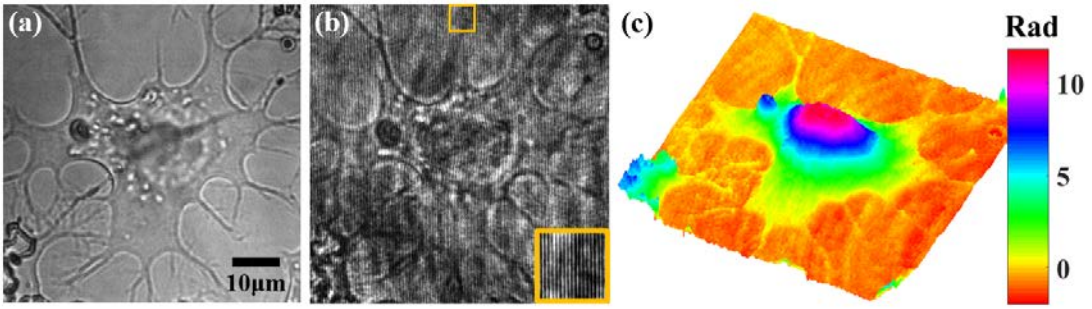

Figura 3. Resultados experimentales obtenidos a partir de la plataforma multimodal desarrollada en [Picazo-Bueno-2018A] para el caso de una muestra biológica.

La validación experimental de esta plataforma multimodal ha constado de tres etapas. En primer lugar, el dispositivo holográfico ensamblado ha sido calibrado mediante el empleo de diversos tipos de objetos sintetizados (microesferas, microestructuras cónicas) cuyas características geométricas y ópticas vienen dadas por los fabricantes. La formación de imágenes cuantitativas de fase de estos objetos ha permitido obtener experimentalmente el grosor de cada objeto (una vez conocido el material del que están formados), cuyo valor ha sido satisfactoriamente comparado con el teórico. Además, para demostrar la capacidad de análisis de procesos dinámicos del dispositivo holográfico, se ha llevado a cabo un experimento en el cual se le ha inducido un desplazamiento lateral y axial simulado a una muestra biológica compuesta de un conjunto de células neuronales del hipocampo fijadas (estáticas) a través del desplazamiento de la plataforma que las contiene, demostrando así la capacidad de análisis a tiempo real que posee dicho sistema. A continuación, se ha realizado una validación experimental de la plataforma multimodal en la cual se han formado simultáneamente imágenes tanto de intensidad de banda ancha como cuantitativas de fase, de una serie de muestras biológicas fijadas. La Figura 3 incluye un ejemplo de los resultados experimentales obtenidos durante este proceso, en la que se presenta una imagen de intensidad convencional (a) con iluminación blanca, un holograma generado por la plataforma holográfica (b) y una imagen en perspectiva de la información cuantitativa de fase recuperada a partir de (b). Para concluir la validación experimental, se ha demostrado la capacidad de análisis a tiempo real de este sistema óptico multimodal mediante la monitorización y el análisis de la actividad dinámica de una célula neuronal del hipocampo viva durante un intervalo temporal de 100 s. Este periodo de tiempo ha sido suficiente para apreciar una contracción de las paredes celulares a una velocidad promedio de unos 7.5 nm/s a lo largo de una dirección.

Sentadas las bases sobre *microscopía holográfica digital* [Picazo-Bueno-2018A], se ha llevado a cabo el desarrollo y la mejora de la técnica *SMIM* mediante la implementación de una serie de técnicas con diferentes capacidades. Como denominador común, todas las técnicas propuestas a lo largo de esta tesis han sido implementadas en el cuerpo de un microscopio regular compuesto de campo claro Olympus BX60, cuyo sistema formador de imágenes está formado por un objetivo con corrección infinita y una lente de tubo.

El primer sistema experimental basado en esta técnica fue desarrollado por Micó y otros [Micó-2014]. En dicho experimento, los autores dotaron de la capacidad de formación de imágenes de fase cuantitativas al mismo microscopio Olympus BX60 mediante la introducción de tres elementos en su esquema: 1) inserción de una fuente de luz coherente; 2) multiplexación espacial del campo de visión, dividiéndolo en tres regiones que sirvieran como región objeto, región de transmisión del haz de referencia y región de bloqueo; y 3) inserción de una red de difracción unidimensional. Sin

embargo, este sistema presentaba dos aspectos negativos: por un lado, las imágenes de fase que se obtenían presentaban una cantidad de ruido coherente considerable y, por otro, la región del plano objeto reservada para el objeto estaba demasiado limitada, ya que solamente se empleaba un tercio del campo de visión total que presentaba el sistema óptico.

Por este motivo, se ha realizado un experimento que mejora las capacidades de la técnica mediante la reducción del ruido coherente presente en las imágenes de fase y la ampliación de la región del plano objeto que contiene el objeto [Picazo-Bueno-2016]. El primer aspecto negativo se ha solventado mediante la sustitución de la fuente de iluminación coherente (diodo láser) empleada en [Micó-2014] por una fuente de luz parcialmente coherente (diodo superluminiscente). Esta fuente luminosa emite luz divergente con un alto grado de coherencia espacial, pero con una coherencia temporal reducida, de manera que evita así la presencia de ruido coherente procedente de los patrones de moteado o las múltiples reflexiones generadas en las distintas interfases aire-vidrio del microscopio, a la vez que permite interferencias en función de su longitud de coherencia. Por otro lado, la ampliación de la región objeto ha sido posible mediante una redistribución espacial del plano objeto menos restrictiva, que ha permitido aumentar la extensión de esta región pasando a ocupar la mitad del campo de visión total o disponible, en lugar de un tercio como en el caso anterior. Ahora bien, el empleo de una fuente de iluminación con una coherencia temporal reducida ha imposibilitado la implementación de una configuración holográfica *fuera de eje*, por lo que la recuperación de fase ha sido llevada a cabo empleando métodos de desplazamiento de fase que requieren de varios registros holográficos, eliminando así la posibilidad de análisis a tiempo real. Además, el multiplexado espacial realizado del plano objeto hace que el holograma usado para la recuperación de fase aparezca en el plano imagen desplazado con respecto al eje óptico del microscopio, forzando al desaprovechamiento de la mitad del sensor digital si se quiere seguir manteniendo la posición convencional de registro de imágenes (esto es, manteniendo el sensor alineado con el eje óptico del microscopio). La Figura 4 presenta el esquema óptico y el diagrama de rayos del dispositivo implementado, en la que adicionalmente se han incluido de una manera clara las distribuciones espaciales presentes en los planos objetos e imagen como consecuencia de la aplicación de la técnica.

Las modificaciones introducidas han sido implementadas y validadas experimentalmente empleando dos objetivos de microscopio con características distintas: un 10X/0.30NA y un 20X/0.46NA. En primer lugar, se ha realizado un proceso de calibración del sistema utilizando un test de resolución y unas microesferas. Este test se ha usado para comprobar que la aplicación de la técnica *SMIM* no genera una pérdida en la resolución espacial en las imágenes obtenidas, mediante la comparación entre las imágenes de intensidad obtenidas con la técnica

SMIM y las proporcionadas bajo condiciones de formación de imágenes convencionales, empleando la misma fuente luminosa. Por otro lado, las microesferas han servido para validar correctamente las imágenes cuantitativas de fase obtenidas por la técnica. Este proceso se ha llevado a cabo a través de una comparativa entre las distribuciones de fase obtenidas mediante la técnica propuesta y las proporcionadas por un sistema holográfico convencional basado en una arquitectura interferométrica tipo Mach-Zehnder con una configuración holográfica *fuera de eje* para recuperar la fase mediante procesos de filtrado en Fourier. Los resultados experimentales obtenidos muestran una alta concordancia entre ambas distribuciones de fase recuperadas. Una vez calibrado, el sistema propuesto ha sido validado experimentalmente mediante la formación de imágenes cuantitativas de fase de diferentes tipos de células fijadas (glóbulos rojos, espermatozoides y células de cáncer de próstata). Para finalizar, se ha realizado un estudio para cuantificar la reducción de ruido coherente lograda gracias al uso de una fuente de luz parcialmente coherente. Esta cuantificación ha sido llevada a cabo mediante un análisis de los valores de las desviaciones estándar obtenidos en las regiones sin objeto de las imágenes de fase recuperadas. La comparativa directa de estos valores se ha realizado solamente considerando las imágenes obtenidas para el test de resolución, ya que es el único objeto testeado en ambos sistemas. Los resultados experimentales muestran una reducción del ruido coherente en las imágenes de fase de un factor 10, reduciendo el valor de la desviación estándar de 0.31 a 0.033 rad por el simple hecho de emplear una fuente de luz parcialmente coherente en lugar de una iluminación coherente.

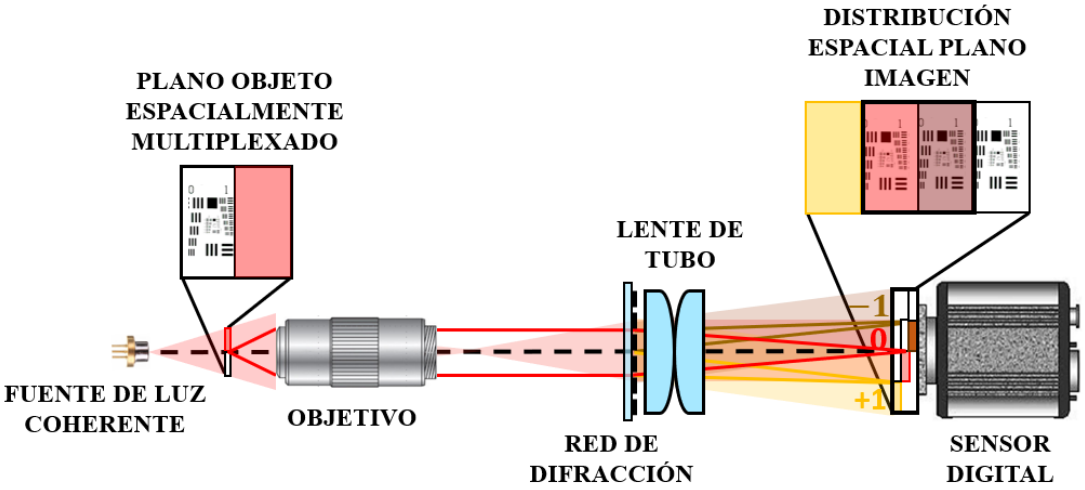

Figura 4. Esquema óptico propuesto para la aplicación de la técnica *SMIM* desarrollada en [Picazo-Bueno-2016].

Ahora bien, la principal desventaja de la técnica *SMIM*, que viene a ser la reducción de la región del plano objeto que contiene la muestra, sigue estando todavía vigente a pesar de la mejora propuesta en [Picazo-Bueno-2016] (de 1/3 a 1/2 del campo objeto). Esta reducción del campo de visión útil puede ser crítica a la hora de trabajar con objetivos de media/alta apertura numérica. Además, la aplicación de esta

técnica hace que los objetivos con baja apertura numérica, los cuales normalmente presentan menores aumentos y menores resoluciones espaciales pero mayores campos de visión que los objetivos de alta apertura numérica, se vean adicionalmente restringidos. Este hecho, aunque inevitable debido al modo de generación del haz de referencia, sí que puede ser compensado de alguna manera, por ejemplo, mediante la mejora de la resolución del sistema. De esta manera, si por ejemplo consideramos un objetivo de microscopio 5X/0.15NA y suponemos una ganancia de resolución del sistema de un factor 2, se obtendrán unas imágenes de características similares a las obtenidas empleando un objetivo 10X/0.30NA, similares en cuanto al área del campo de visión que contiene la muestra y en cuanto a la resolución que presenta el sistema. No obstante, este sistema tendrá todas las ventajas de emplear un objetivo con una menor apertura numérica, como puede ser un precio reducido o el aumento de la distancia de trabajo, parámetro que puede ser crucial dependiendo de la aplicación específica que se considere.

Por este motivo, en [Picazo-Bueno-2017] se ha presentado una técnica denominada *microscopía interferométrica por multiplexado espacial superresolvente* o *S2MIM* (del inglés Superresolved Spatially Multiplexed Interferometric Microscopy), basada en la aplicación de técnicas de superresolución sobre un esquema propuesto por la técnica *SMIM*. Esta técnica consiste en la generación de una apertura sintética a partir de la recuperación secuencial (multiplexado temporal) de diferentes porciones del contenido espacio-frecuencial (pasabanda) de la amplitud compleja no accesible mediante el registro holográfico realizado en condiciones convencionales (mediante iluminación en eje). Para obtener esta información espacio-frecuencial, la técnica *S2MIM* realiza una serie de registros holográficos (proceso de codificación) empleando distintas iluminaciones oblicuas. Estas iluminaciones forman un ángulo con respecto al eje óptico del sistema (multiplexado angular) que viene dado por las características del sistema. En este experimento se han obtenido cinco registros holográficos bajo condiciones de iluminación diferentes. Más concretamente, se ha realizado un registro holográfico con la iluminación en eje (convencional) y cuatro registros en los que la iluminación se encuentra fuera de eje colocada en cuatro posiciones laterales distintas, formando una cruz entre todas ellas. Puesto que se ha definido una configuración holográfica *ligeramente fuera de eje* y se utiliza un multiplexado temporal, se han empleado técnicas de desplazamiento de fase para recuperar cada pasabanda (proceso de decodificación). Una vez obtenidas las cinco pasabandas, se ha reposicionado el contenido espacio-frecuencial de estas pasabandas en el espectro del objeto mediante procesos computacionales (etapa de post-procesado digital), logrando así una apertura sintética [ver Figura 5] cuyo contenido espacio-frecuencial presenta una frecuencia de corte mayor que la inicial y, por tanto, cuya imagen obtenida a partir de esta nueva apertura presenta una mayor resolución.

La técnica *S2MIM* ha sido experimentalmente validada empleando dos objetivos de microscopio distintos (2X/0.05NA y 5X/0.15NA) y dos test de resolución diferentes (tipo NBS1963A y tipo USAF, respectivamente). La Figura 5 muestra los resultados experimentales obtenidos empleando un test de resolución tipo USAF cuya imagen ha sido obtenida mediante el objetivo 5X. En la Figura 5 se incluyen la imagen convencional de baja resolución [Figura 5 (a)], la apertura sintética generada mediante la técnica de superresolución [Figura 5 (b)], y la imagen superresuelta obtenida mediante *S2MIM* [Figura 5 (c)]. En ambos experimentos, los resultados experimentales han mostrado una ganancia en la resolución del sistema de un factor 2. Además, la imagen superresuelta generada para el test de resolución USAF por el 5X/0.15NA ha sido comparada con una imagen del mismo test obtenida con un objetivo 10X/0.30NA, demostrando que la aplicación de la técnica *S2MIM* a objetivos de baja apertura numérica es capaz de obtener, efectivamente, imágenes de características similares a las proporcionadas por objetivos de mayor apertura numérica.

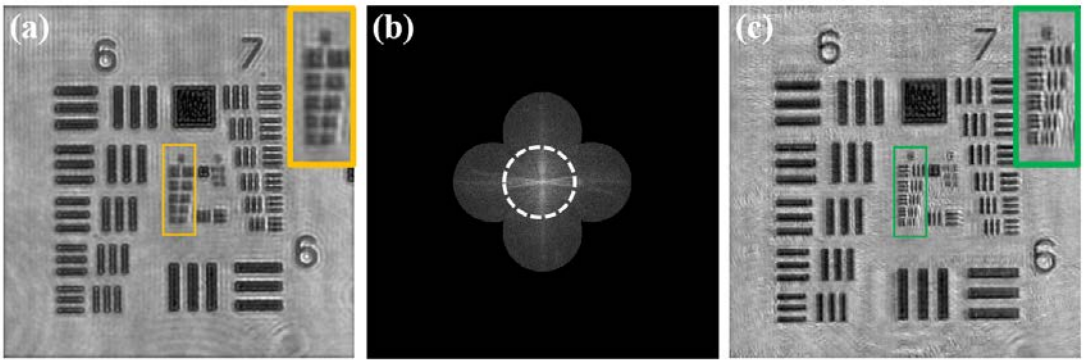

Figura 5. Resultados experimentales obtenidos por la técnica *S2MIM* en el caso de la formación de imágenes de un test de resolución tipo USAF mediante un objetivo 5X/0.15NA presentados en [Picazo-Bueno-2017].

Como hemos señalado anteriormente, el uso de fuentes de iluminación parcialmente coherente reduce significativamente la cantidad de ruido coherente presente en las imágenes cuantitativas de fase obtenidas mediante la técnica *SMIM* [Picazo-Bueno-2016]. Sin embargo, debido a que este tipo de fuentes luminosas presentan una coherencia temporal reducida, generalmente no permiten implementar una configuración holográfica *fuera de eje*, puesto que la diferencia de caminos ópticos entre el haz objeto y el de referencia necesaria para la ejecución de este tipo de configuraciones a menudo supera la longitud de coherencia de estas fuentes, evitando así el registro holográfico en una configuración de camino común. Por consiguiente, se deben definir otro tipo de configuraciones que sí permitan este registro, como pueden ser las configuraciones *ligeramente fuera de eje* o *cuasi en eje*. Estas configuraciones holográficas suelen ir acompañadas de la aplicación de métodos de desplazamiento de fase para la recuperación de fase, que normalmente requieren de varias capturas, eliminando así la posibilidad de un análisis dinámico a partir de

estas configuraciones. No obstante, recientemente se han desarrollado diversos métodos de recuperación de fase a partir de una sola captura basados en la aplicación de la transformada de Hilbert-Huang, los cuales permiten un análisis de procesos dinámicos incluso en las configuraciones holográficas anteriormente mencionadas [Trusiak-2012, Trusiak-2014, Trusiak-2016A].

Para dotar a la técnica *SMIM* de la capacidad de análisis de procesos dinámicos en situaciones de registros holográficos *ligeramente fuera de eje* o *cuasi en eje*, definidos cuando se emplea una fuente de iluminación parcialmente coherente, hemos desarrollado una técnica, denominada *microscopía interferométrica por multiplexado espacial de única exposición basada en la transformada de Hilbert-Huang* o *H2S2MIM* (del inglés Hilbert-Huang Single-Shot Spatially Multiplexed Interferometric Microscopy), que hace uso de la transformada de Hilbert-Huang para la recuperación de fase a partir de un solo registro holográfico empleando la técnica *SMIM* [Picazo-Bueno-2018B]. Al igual que en los casos anteriores, la técnica *H2S2MIM* ha sido implementada empleando mecanismos habituales de la técnica *SMIM*. Así, la iluminación de banda ancha del propio microscopio ha sido reemplazada por un diodo superluminiscente con emisión parcialmente coherente; se ha empleado el multiplexado espacial del plano objeto que divide éste en dos regiones iguales para la transmisión de los haces interferométricos (objeto y referencia); y finalmente, se ha insertado una red de difracción que, junto con un sensor digital, han permitido un registro holográfico en configuración *ligeramente fuera de eje*.

Para la recuperación de fase, se ha desarrollado un algoritmo robusto, rápido y preciso que hace uso de la transformada de Hilbert-Huang. Este algoritmo está fundamentalmente basado en un método de reconstrucción de fase desarrollado previamente en [Trusiak-2016], pero incluye algunas modificaciones para incrementar la robustez y versatilidad del mismo. Estas modificaciones están enfocadas al análisis de situaciones complejas desde un punto de vista de franjas interferenciales como es el caso de las microesferas (dirección y periodo de franjas variable, discontinuidades presentes en los bordes, etc.). Con todo, el método de recuperación de fase propuesto aquí empieza con la aplicación de un filtrado adaptativo sobre el holograma registrado. Dicho filtrado comienza con un proceso de enmascaramiento automático basado en la técnica de descomposición variacional de imágenes [Zhu-2013] y finaliza con la aplicación de una umbralización de la imagen del tipo Otsu. La aplicación de este filtrado consigue eliminar tanto el ruido (contenido espectral de alta frecuencia) como el fondo (contenido espectral de baja frecuencia) presentes en el holograma. Además, el método tiene en cuenta distintos parámetros globales para mejorar la relación señal ruido del holograma filtrado. A continuación, se aplica la transformada de Hilbert de fase espiral al holograma filtrado para la recuperación de fase. La parte más crítica de esta transformada consiste en la correcta estimación del mapa de direcciones locales de las franjas interferenciales. En este

trabajo, se ha empleado una versión modificada del estimador de direcciones incluido en [Trusiak-2016], en la que adicionalmente se emplea un filtro adaptativo basado en la técnica de descomposición de imágenes en modos empíricos. Finalmente, la completa recuperación de fase se lleva a cabo empleando un algoritmo iterativo de desenvoltura de fase (la transformada obtiene valores de fase comprendidos en un intervalo de 2π rad) basado en la ecuación de transporte de intensidad [Martínez-Carranza-2017].

La validación experimental de la técnica *H2S2MIM* ha constado de tres partes. En la primera etapa, se ha llevado a cabo un proceso de calibración de la técnica. La calibración se ha realizado mediante la comparativa entre las distribuciones de fase obtenidas por *H2S2MIM* y por métodos de desplazamiento de fase convencionales, para el caso de una microesfera. Posteriormente, se ha realizado un proceso de validación, en el cual se ha realizado una comparativa análoga a la anterior pero esta vez aplicada al caso de dos muestras biológicas distintas. Finalmente, se ha efectuado un análisis de un proceso dinámico en el que dos microesferas fluyen dentro de un medio acuoso. En la Figura 6 se incluyen tanto un holograma capturado en el instante inicial (a), como las distribuciones de fase recuperadas por la técnica en el primer (b) y en el último instante (c) del proceso (visión en perspectiva). Este análisis se ha desempeñado solamente mediante la técnica *H2S2MIM*, puesto que los métodos estándar de desplazamiento de fase no permiten la recuperación de fase a partir de una sola captura. Los resultados experimentales han mostrado que las distribuciones de fase obtenidas por ambos métodos concuerdan entre sí y que *H2S2MIM* permite la recuperación de fase a partir de una sola captura incluso cuando se implementa una configuración holográfica *ligeramente fuera de eje*.

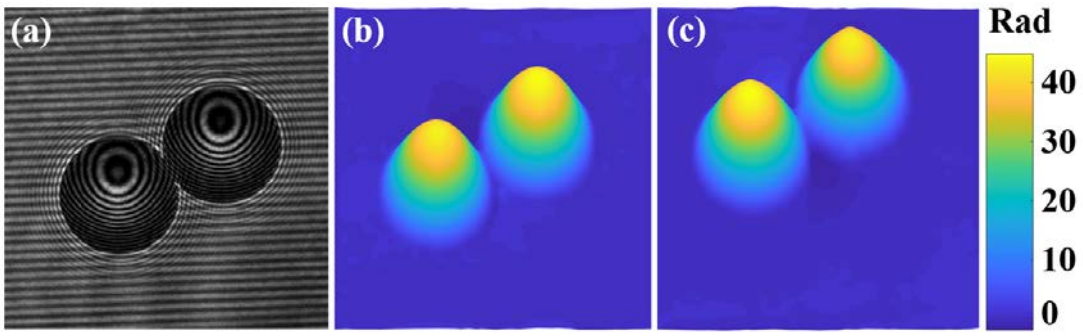

Figura 6. Resultados experimentales obtenidos mediante la técnica *H2S2MIM* propuesta en [Picazo-Bueno-2018B] para la demostración de la capacidad de análisis de procesos dinámicos.

Los experimentos realizados previamente han validado la técnica *SMIM* solamente para la modalidad de formación de imágenes por transmisión, reservando así el uso de la técnica para objetos transmisivos. Sin embargo, esta técnica también puede ser aplicable a otro tipo de objetos que no cumplan estas características como, por ejemplo, los objetos opacos, que solo pueden ser visualizados a partir de la luz

que se refleja en ellos. Por este motivo, hemos implementado un sistema basado en la técnica *SMIM* capaz de obtener no sólo imágenes cuantitativas de fase por reflexión, sino también simultáneamente por transmisión, permitiendo así una modalidad transflectiva de formación de imágenes [Picazo-Bueno-2019A].

La técnica propuesta, denominada *microscopía interferométrica por multiplexado espacial de visión opuesta* o *OV-SMIM* (del inglés Opposed-View Spatially Multiplexed Interferometric Microscopy), ha empleado dos fuentes de luz coherentes con distintas longitudes de onda y emisiones divergentes para la iluminación del objeto en transmisión y reflexión. Por otro lado, el plano objeto ha sido espacialmente multiplexado en tres regiones con el mismo tamaño. La región centrada con el eje óptico del microscopio ha contenido al objeto bajo análisis, mientras que las regiones contiguas a éste han tenido la misión de proporcionar haces de referencia para ambas modalidades de formación de imagen. Así pues, una de estas regiones ha constado de un área totalmente transparente, sin objeto, para permitir la transmisión de un haz de referencia, mientras que la otra ha contenido una superficie espejada que nos ha facilitado la obtención de un haz de referencia para la modalidad reflectiva, a la vez que ha bloqueado la luz incidente por transmisión. Finalmente, una red de difracción y un sensor de color digital han permitido el registro holográfico simultáneo de ambos hologramas multiplexados en longitud de onda empleando una configuración holográfica *ligeramente fuera de eje*. En la Figura 7 se muestra tanto el esquema óptico como el trazado de rayos del sistema propuesto. En este caso, hemos empleado un método de desplazamiento de fase para la recuperación de la amplitud compleja a partir de las dos modalidades de formación de imagen.

La validación experimental se ha llevado a cabo mediante el uso de un conjunto de microesferas y varios objetos con recubrimiento metálico. Para comenzar, y puesto que la modalidad formadora de imágenes por transmisión ya ha sido previamente calibrada y validada en los anteriores trabajos, se ha validado solamente la formación de imágenes por reflexión. En este experimento, se ha obtenido el espesor de la capa metálica (deposición de cromo) presente en una red de difracción a partir de imágenes cuantitativas de fase, y su valor ha sido satisfactoriamente comparado con el extraído a partir de las mediciones realizadas por un microscopio de fuerza atómica. A continuación, se ha validado la formación de imágenes transflectivas empleando un test de resolución y un grupo de microesferas. El test de resolución ha sido usado para comprobar la concordancia en los valores de fase obtenidos a partir de las modalidades de transmisión y reflexión. Los resultados experimentales han demostrado una alta concordancia en estos, puesto que ambas modalidades presentan valores similares una vez compensados los valores de fase obtenidos por reflexión (la luz viaja dos veces a lo largo del mismo camino óptico). El último experimento se ha desarrollado empleando un conjunto de microesferas inmersas en una solución acuosa. Los resultados experimentales han mostrado que, a

pesar de una incompleta reconstrucción de las microesferas debido, entre otros factores, al empleo de un objetivo de baja apertura numérica, los valores de grosor obtenidos por ambas modalidades son similares. Además, y pese a que los grosores obtenidos se alejan notablemente de los valores teóricos, ha sido posible calcular una estimación del índice de refracción promedio de las microesferas a partir de la obtención de imágenes transflectivas. Este valor ha sido satisfactoriamente comparado con el valor proporcionado por los fabricantes.

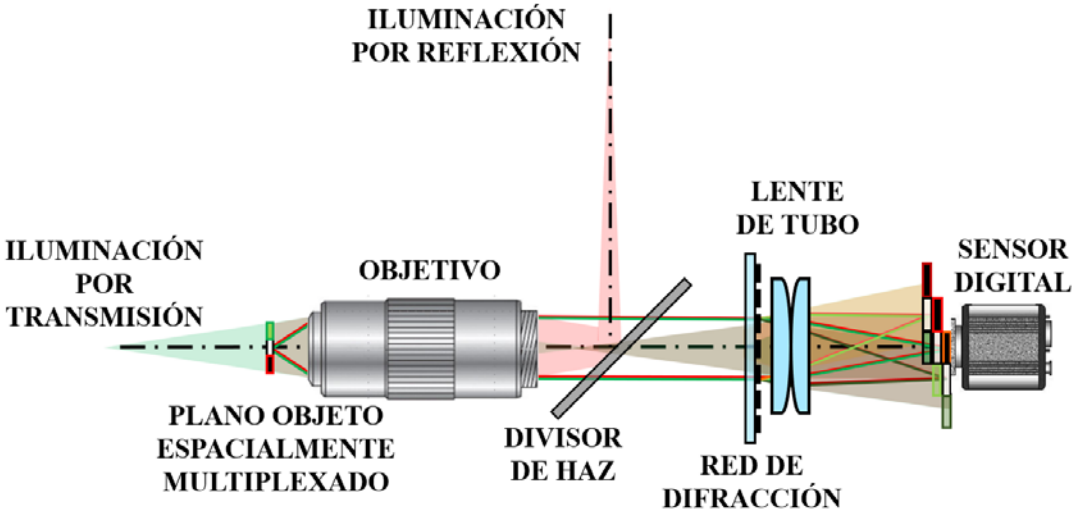

Figura 7. Esquema propuesto para la validación de la técnica *OV-SMIM* presentada en [Picazo-Bueno-2019A].

En las validaciones experimentales anteriores, la técnica *SMIM* ha equipado un microscopio regular con capacidades holográficas mediante la creación de una arquitectura interferométrica de camino común basada en el empleo de una de red de difracción para el registro holográfico. Este registro se ha realizado usualmente bajo configuraciones holográficas *ligeramente fuera de eje*, por lo que la recuperación de fase se ha llevado a cabo, o bien empleando técnicas de desplazamiento de fase [Picazo-Bueno-2016, Picazo-Bueno-2017, Picazo-Bueno-2019A], o mediante la aplicación de la transformada de Hilbert-Huang [Picazo-Bueno-2018B]. La primera técnica generalmente ha necesitado de varias capturas para la recuperación de fase, mientras que el algoritmo empleado en la segunda no ha sido trivial y ha requerido de una cierta experiencia para poder llevarlo a cabo. Así pues, en el experimento presentado en [Picazo-Bueno-2019B], se ha introducido un dispositivo holográfico en forma de módulo accesorio acoplado al puerto de salida del microscopio que ha permitido una recuperación de manera sencilla y a partir de una sola captura bajo condiciones holográficas *ligeramente fuera de eje*.

En cuanto al montaje experimental presentado en [Picazo-Bueno-2019B], se han introducido varios cambios en el microscopio para poder realizar el registro holográfico. En primer lugar, los cambios correspondientes con la iluminación y el multiplexado espacial del plano objeto han seguido la línea de la técnica *SMIM*, es decir, por un lado, la iluminación blanca se ha reemplazado por una fuente de luz coherente y, por otro lado, el plano objeto ha sido dividido en dos regiones para la transmisión de los dos haces interferométricos. En cuanto al dispositivo holográfico adaptado en el puerto de salida del microscopio, ha estado compuesto de un espejo, una lente de Stokes, un cubo divisor de haz en configuración interferométrica (rotado 45º con respecto a su posición convencional) y un sensor digital. La inserción del cubo divisor de haz de manera que su capa divisora se encuentre casi paralela con el eje óptico del microscopio ha generado dos interferogramas en configuración *ligeramente fuera de eje*, idénticos entre sí salvo por un desplazamiento en la fase de π rad. No obstante, tanto la posición axial (entre la lente de tubo y el sensor digital) como la inclinación del divisor de haz han introducido una cantidad considerable de astigmatismo (además de efecto prismático) que ha reducido considerablemente la calidad de la imagen. Para compensar este astigmatismo, se ha introducido una lente de Stokes formada por dos lentes cilíndricas (no introducen aberración esférica). Adicionalmente, se ha reemplazado la cabeza trinocular del microscopio por una lente de tubo, para evitar reflexiones indeseadas. Por otro lado, también se ha introducido un polarizador lineal entre la fuente de luz y el plano objeto para obtener una relación de intensidades semejante entre ambos interferogramas que permita la correcta aplicación de la técnica de sustracción de imágenes. La Figura 8 muestra el esquema óptico del microscopio después de la introducción de las modificaciones señaladas y del acoplamiento del dispositivo holográfico. El registro de dos interferogramas con intensidades similares en configuración *ligeramente fuera de eje* desfasados π rad entre sí hace posible la recuperación de fase a partir de una sola captura y de una manera sencilla, mediante la combinación de técnicas de sustracción de imagen y de filtrado en Fourier.

La validación experimental del dispositivo propuesto en [Picazo-Bueno-2019B] se ha dividido en tres fases: 1) una primera fase de calibración, en la que se ha empleado un test de resolución tanto para cuantificar la cantidad de astigmatismo introducido por el cubo divisor de haz como para mostrar todo el proceso de recuperación de fase, 2) una segunda etapa de validación en la que se han obtenido diversas imágenes cuantitativas de fase de diferentes tipos celulares, y 3) una tercera fase de implementación de la técnica para la formación de imágenes de fase de procesos dinámicos, en cuyo caso se han empleado un conjunto de microesferas fluyendo en el interior de un medio acuoso. A lo largo de todo el proceso de validación experimental, los resultados obtenidos mediante el método propuesto han sido comparados con aquellos extraídos a partir del filtrado en Fourier de uno de los hologramas generados por el dispositivo, mostrando una clara mejoría en la calidad

de las reconstrucciones debido a una notable disminución de ruido en las imágenes de fase. De este modo, se ha demostrado que la aplicación del método de sustracción de imágenes propuesto es capaz de recuperar la información de fase de manera precisa cuando trata con procesos dinámicos en situaciones en las que se implementa una configuración holográfica *ligeramente fuera de eje*.

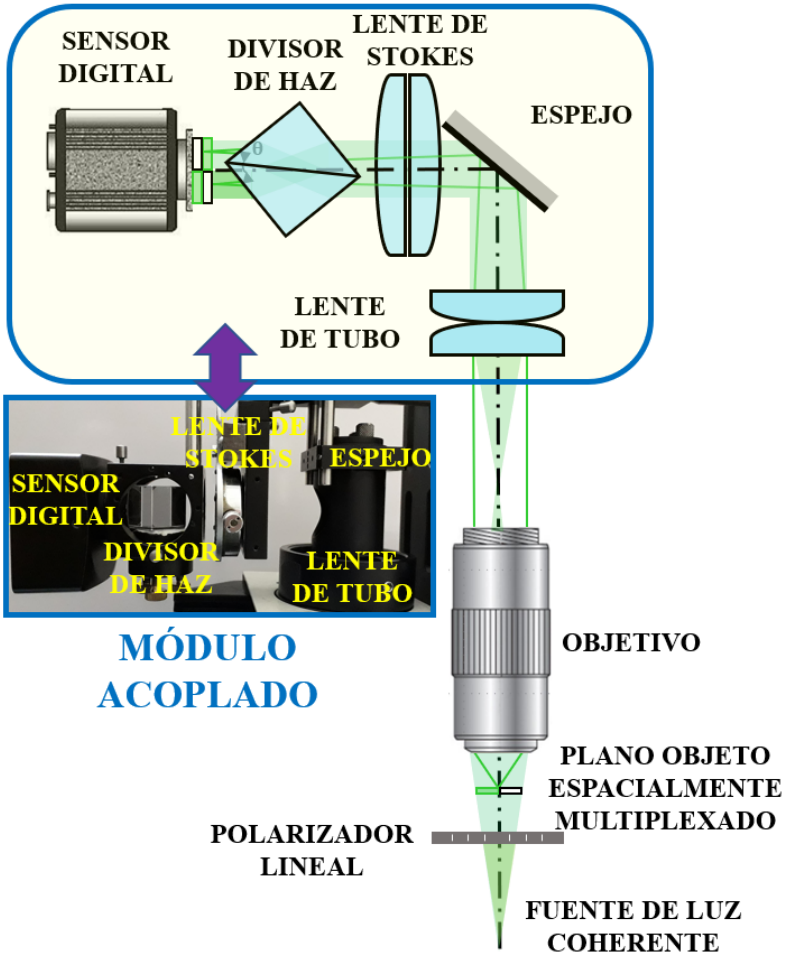

Figura 8. Esquema óptico del microscopio después de la inclusión del dispositivo holográfico propuesto en [Picazo-Bueno-2019B].

Sin embargo, como hemos señalado anteriormente, tanto la posición axial como la rotación del cubo divisor de haz presentado en [Picazo-Bueno-2019B] han introducido una cantidad importante de astigmatismo, por lo que se ha utilizado una lente de Stokes para su compensación, incrementando así la complejidad del dispositivo holográfico accesorio acoplado al microscopio. No obstante, cuando trabajamos con sistemas ópticos de corrección infinita, como es nuestro caso, se puede evitar la presencia de astigmatismo mediante la inserción del cubo divisor de haz en el interior del cuerpo del microscopio, concretamente en la región en la que los rayos viajan en paralelo, es decir, entre el objetivo de corrección infinita y la lente de tubo. Además, el método de recuperación de fase a partir de una sola captura presentado en

[Picazo-Bueno-2019B] requería de una configuración holográfica *ligeramente fuera de eje*, es decir, estaba limitada a situaciones en las que los órdenes -1 y +1 de difracción del holograma se encontraban solapando con el orden 0 de difracción, pero separados entre sí. Por todas estas razones, hemos desarrollado una última técnica denominada *microscopía interferencial de fase por multiplexado espacial basada en la captura de dos hologramas desfasados π rad* o *π-SMIM* (del inglés single-shot two-frame π-shifted Spatially Multiplexed Interference phase Microscopy) que introduce el cubo divisor de haz en el espacio infinito (entre objetivo y lente de tubo) y que emplea un algoritmo basado en la combinación de los métodos de sustracción de imágenes y de la transformada de Hilbert-Huang para la recuperación de fase. Con estas modificaciones, la técnica propuesta en [Trusiak-2019] ha permitido la formación de imágenes cuantitativas de fase de eventos dinámicos a partir de un solo registro holográfico de baja calidad empleando una configuración holográfica *cuasi en eje*.

Para implementar el método propuesto en [Trusiak-2019], se ha diseñado una arquitectura holográfica similar a las presentadas en [Picazo-Bueno-2016, Picazo-Bueno-2018B]. La diferencia fundamental con respecto a estas arquitecturas radica en la introducción de un cubo divisor de haz en el cuerpo del microscopio en lugar de una red de difracción para generar el registro holográfico [ver Figura 9]. Asimismo, también se han aplicado modificaciones presentadas en [Picazo-Bueno-2019B], como el reemplazo del trinocular por una lente de tubo para evitar reflexiones indeseadas, la introducción de un polarizador lineal entre la fuente y el plano objeto para controlar la intensidad de los haces interferométricos y la rotación de un ángulo de 45º con respecto a su posición convencional del cubo divisor de haz para generar el registro holográfico. Con todas estas modificaciones, el dispositivo propuesto por la técnica *π-SMIM* produce dos interferogramas con idénticas características que en el caso presentado en [Picazo-Bueno-2019B], pero con la única salvedad de que son registrados en configuraciones holográficas *cuasi en eje*.

En cuanto al método de recuperación de fase, hemos empleado un algoritmo de recuperación de fase basado en la combinación de las técnicas de sustracción de imagen [Picazo-Bueno-2019B] y de transformada de Hilbert-Huang [Picazo-Bueno-2018B], que permite la recuperación de fase a partir de un único holograma capturado en configuración *cuasi en eje*, permitiendo así el empleo de la técnica *π-SMIM* para el análisis de procesos dinámicos. El método de recuperación de fase se ha llevado a cabo en varias etapas: la primera de ellas ha consistido en la aplicación del método de sustracción de imágenes a los hologramas. A continuación, se ha implementado un método de filtrado de imagen basado en la descomposición de imágenes en modos empíricos denominado EFEMD (del inglés Enhanced Fast Empirical Mode Decomposition) aplicado anteriormente en [Picazo-Bueno-2018B], con el que se ha eliminado cualquier rastro de imagen de fondo, obteniendo así un holograma de mayor

calidad compuesto de dos de los modos extraídos de estas imágenes. Finalmente, para recuperar la información de fase se emplea un método basado en la transformada de Hilbert de fase espiral.

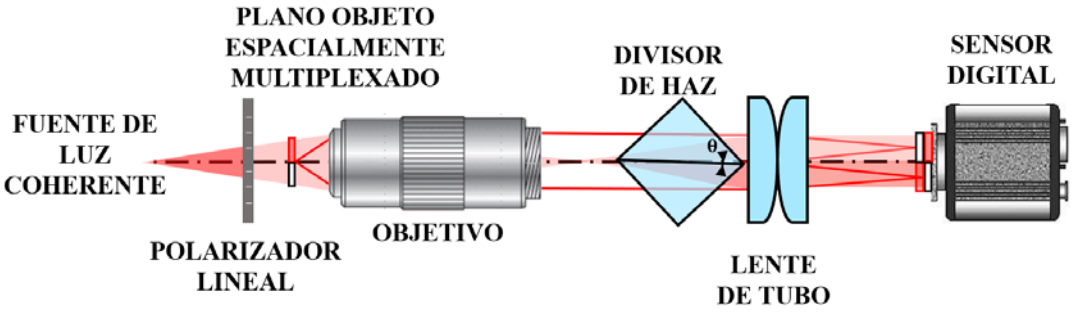

Figura 9. Esquema óptico del microscopio después de la aplicación de la técnica *π-SMIM* propuesta en [Trusiak-2019].

La validación experimental de la técnica desarrollada en [Trusiak-2019] también se ha dividido en tres fases. En una primera fase de calibración, se ha empleado un conjunto de células de un mismo tipo celular para comparar las imágenes de fase obtenidas a partir de la técnica propuesta con las proporcionadas por otros métodos de recuperación de fase, como el método de desplazamiento de fase y el método desarrollado en *H2S2MIM* [Picazo-Bueno-2018B]. Posteriormente, se ha realizado una segunda etapa de validación experimental en la que se ha demostrado la versatilidad y la robustez del método propuesto mediante la formación de imágenes cuantitativas de fase de dos tipos diferentes de muestras biológicas. Una de ellas estaba formada por células de un mismo tipo celular que presentaban distintos tamaños, mientras que la otra consistía en una muestra muy concentrada de glóbulos rojos. Para finalizar el proceso de validación experimental, se ha demostrado la capacidad para el análisis de eventos dinámicos de la técnica *π-SMIM* mediante el seguimiento del movimiento de unas microesferas inmersas en agua. Todas estas validaciones han demostrado que la técnica propuesta es capaz de formar imágenes cuantitativas de fase de procesos dinámicos a partir de un solo registro holográfico de baja calidad y con una configuración holográfica *cuasi en eje*.

5. Conclusiones y trabajos futuros

A raíz de los resultados experimentales obtenidos en la presente tesis, se puede concluir que la técnica *SMIM* es muy versátil y que puede ser implementada de múltiples maneras, de modo que se puede hacer uso de cada una de las disposiciones presentadas según el objetivo a perseguir. Esta técnica se ha basado en la *microscopía holográfica digital* para la obtención de imágenes cuantitativas de fase, por lo que se ha realizado un experimento preliminar que ha proporcionado un mejor entendimiento

experimental sobre la *microscopía holográfica digital*. Este experimento se ha basado en el desarrollo de una plataforma multimodal formadora de imágenes que ha proporcionado tanto imágenes de intensidad convencionales, mediante un sistema óptico que ha empleado iluminación de banda ancha, como imágenes cuantitativas de fase, a partir de registros holográficos obtenidos a partir de la implementación de una arquitectura interferométrica.

Posteriormente, se han desarrollado diferentes configuraciones experimentales basadas en la técnica *SMIM* que han mejorado en algún aspecto las anteriores versiones presentadas de la misma. Así pues, en la implementación de la técnica *SMIM* presentada en [Picazo-Bueno-2016], el uso de una fuente de iluminación parcialmente coherente en lugar de una fuente de luz totalmente coherente ha permitido mejorar significativamente la calidad de las imágenes de fase obtenidas, gracias a una reducción en un orden de magnitud de la presencia de ruido coherente en éstas con respecto a las presentadas en [Micó-2014]. Cabe destacar que el uso de fuentes de luz parcialmente coherentes tiene una especial relevancia cuando se implementan dispositivos interferométricos en el cuerpo de un microscopio, ya que estos presentan una gran cantidad de interfases aire-vidrio sin recubrimientos específicos que pueden llegar a producir múltiples reflexiones e introducir de esta manera patrones de interferencia indeseados que estropeen la imagen final. Además, también se ha diseñado una distribución espacial del plano objeto menos restrictivo que en [Micó-2014], agrandando así el área inspeccionada del objeto por la técnica. Sin embargo, la principal desventaja presentada por esta disposición tiene relación con la imposibilidad de análisis de procesos dinámicos. Puesto que la longitud de coherencia de la fuente luminosa empleada es reducida, este hecho generalmente imposibilita la implementación de una configuración holográfica *fuera de eje*, y debido al hecho de que normalmente se emplean métodos de desplazamiento de fase para la recuperación de fase en configuraciones distintas a esta, esto hace que se pierda la capacidad de análisis a partir de una sola captura. Así pues, la aplicación de la técnica *SMIM* presentada en [Picazo-Bueno-2016] puede ser muy interesante en situaciones en las que la obtención de una mejor relación señal ruido y un campo de visión más amplio sean más importantes que la capacidad de análisis a tiempo real.

Por otro lado, la técnica *S2MIM* ha equipado la técnica *SMIM* con la capacidad de obtener imágenes superresueltas [Picazo-Bueno-2017]. Esta técnica se ha basado en la aplicación de técnicas de superresolución por apertura sintética que han permitido mejorar la resolución del sistema óptico mediante estrategias de multiplexado temporal y angular, obteniendo así una ganancia en la resolución espacial de un factor 2. De esta manera, la técnica *S2MIM* ha compensado la reducción del campo de visión útil generada por la implementación de la técnica *SMIM* doblando el poder de resolución del sistema. Sin embargo, la principal desventaja de la técnica *S2MIM* ha sido su incapacidad para analizar procesos dinámicos, ya que las imágenes

superresueltas han sido obtenidas mediante la aplicación de estrategias de multiplexado temporal y de algoritmos de desplazamiento de fase y, por tanto, se han necesitado varias capturas holográficas para sus implementaciones.

En cuanto a la técnica *H2S2MIM*, ha superado los problemas correspondientes al empleo de fuentes de luz parcialmente coherente presentes en [Picazo-Bueno-2016] mediante la aplicación de un algoritmo robusto y preciso basado en la transformada de Hilbert-Huang para la recuperación de fase. De esta manera, *H2S2MIM* ha permitido la obtención de imágenes cuantitativas de fase a partir de un solo holograma en configuración *ligeramente fuera de eje* introduciendo unas sencillas modificaciones en el cuerpo de un microscopio regular. Por contrapartida, quizás la principal desventaja de la técnica haya sido la complejidad del algoritmo de recuperación de fase empleado.

Asimismo, la técnica *OV-SMIM* ha equipado a un microscopio óptico convencional con la capacidad de formación de imágenes cuantitativas de fase reflectivas y transflectivas mediante la implementación de un dispositivo interferométrico en el seno del microscopio. Esta técnica ha permitido extender el rango de aplicabilidad de la técnica *SMIM* a diferentes tipos de muestras, proporcionando de este modo completitud a la técnica *SMIM*. Además, la técnica *OV-SMIM* ha permitido la inspección de los valores de índice de refracción de muestras homogéneas. Sin embargo, la principal desventaja de esta técnica tiene que ver con la complejidad del multiplexado espacial del plano objeto, debido a la necesidad de lograr un haz de referencia para cada modalidad de formación de imagen (transmisión y reflexión). No obstante, este hecho puede no ser muy relevante hoy en día debido a la capacidad que presenta la industria para generar diseños personalizados de cámaras que contengan al objeto para aplicaciones específicas.

En relación con el dispositivo holográfico desarrollado en [Picazo-Bueno-2019B], éste ha permitido la obtención de imágenes cuantitativas de fase de procesos dinámicos a partir de una sola captura cuando se implementa una configuración holográfica *ligeramente fuera de eje*. Además, el módulo accesorio adaptado en el puerto de salida del microscopio ha permitido la modificación de la frecuencia portadora del haz de referencia de una manera más sencilla y versátil que en los casos en los que se utilizaba una red de difracción para generar las interferencias. Este hecho se ha conseguido con la simple rotación del cubo divisor de haz, permitiendo así todo tipo de configuraciones holográficas. Asimismo, el multiplexado espacial del plano objeto necesario para la implementación de la técnica es el menos restrictivo de todos los posibles multiplexados cuando tratamos con la técnica *SMIM*, debido a la necesidad de transmisión de un haz referencial (división del campo de visión en dos mitades). Sin embargo, quizás la mayor desventaja que ha presentado este dispositivo ha sido la necesidad de incluir en él una lente de Stokes para compensar el astigmatismo generado por el divisor de haz, incrementando así su complejidad. Otro

aspecto negativo a tener en cuenta cuando tratamos con cubos divisores de haz para la generación de interferencias es la región intermedia no útil que aparece entre interferogramas, la cual incrementa con el ángulo de rotación del cubo divisor de haz y con el aumento, llegando a cubrir toda la región sensible del sensor en situaciones extremas.

Finalmente, la técnica *π-SMIM* ha demostrado que se puede obtener información cuantitativa de fase a partir de una única captura holográfica de baja calidad en configuración *cuasi en eje*. Esta técnica ha combinado todos los aspectos positivos de las técnicas presentadas en [Picazo-Bueno-2018B , Picazo-Bueno-2019B], en cuanto a la aplicación del método de sustracción de imágenes, el multiplexado espacial y la facilidad para definir una configuración holográfica determinada [Picazo-Bueno-2019B], por un lado, y en cuanto a la recuperación de fase a partir de un único holograma en configuración *cuasi en eje* que se ha llevado a cabo a través de la aplicación de un algoritmo basado en la transformada de Hilbert-Huang [Picazo-Bueno-2019B], por otro lado. Además, la implementación de una configuración *cuasi en eje* permite una mejor optimización del ancho de banda espacio-frecuencial del holograma. Por contrapartida, la técnica *π-SMIM* también incluye las principales desventajas de las técnicas desarrolladas en [Picazo-Bueno-2018B, Picazo-Bueno-2019B], que son: la complejidad del algoritmo de recuperación de fase, la necesidad de un solapamiento perfecto entre interferogramas a la hora de realizar la sustracción de imágenes y la región espacial inútil presente entre los dos interferogramas.

En conclusión, todas las implementaciones y validaciones experimentales presentadas a lo largo de esta tesis han contribuido al desarrollo y la mejora de la técnica *SMIM*, demostrando su gran potencial y versatilidad para convertir un microscopio óptico convencional de campo claro en uno holográfico mediante la aplicación de unas pocas modificaciones sencillas y económicas generadas en el cuerpo del microscopio.

A la vista de los experimentos realizados y de las conclusiones extraídas de esta tesis, varias son las opciones de continuidad que se presentan. De entre una gran variedad de futuribles implementaciones y aplicaciones de la técnica *SMIM* aquí desarrollada, nombraremos a continuación algunas de ellas.

- La técnica *SMIM* puede ser implementada en conjunción con otras técnicas interferométricas basadas en multiplexado por longitud de onda, como la *microscopía holográfica digital por múltiple longitud de onda*, que soluciona el problema de ambigüedad de fase presentado a la hora de obtener información cuantitativa de fase de objetos con morfologías abruptas [Warnasoo-2007, Mann-2008]; la *superresolución por multiplexado de longitud de onda*, previamente empleada en holografía de

Gabor [Granero-2015] para obtener una mejora en la resolución; o la *microscopía holográfica sin lentes de iluminación múltiple y de única exposición*, que presenta un algoritmo iterativo de convergencia rápida con el que se mejora significativamente la relación señal-ruido en las imágenes cuantitativas de fase [Sanz-2015, Sanz-2017, Sanz-2018].

- Asimismo, la técnica *SMIM* puede ser combinada con otras técnicas de formación de imagen, como la *microscopía de fluorescencia* o la *microscopía convencional de campo claro*, trasladando así la idea propuesta en [Picazo-Bueno-2018A] implementada en mesa óptica al caso de un microscopio comercial. De esta manera, se pretendería obtener simultáneamente información complementaria a tiempo real de distintos procesos, hecho particularmente relevante cuando se lidia con procesos celulares.